POLITECNICO
MILANO 1863

NUMERICAL SOLUTION OF FLUID-STRUCTURE INTERACTION ARISING IN BLOOD PUMPS BASED ON WAVE MEMBRANES

Author:

Marco MARTINOLLI

MOX, Dipartimento di Matematica

Supervisor:

Prof. Christian VERGARA

LABS, Dipartimento di Chimica,
Materiali e Ingegneria Chimica

December 4, 2021

POLITECNICO DI MILANO

Abstract

Mathematical Models and Methods in Engineering

Dipartimento di Matematica

Doctor of Philosophy

Numerical Solution of Fluid-Structure Interaction Arising in Blood Pumps Based on Wave Membranes

by Marco MARTINOLLI

Wave Membrane Blood Pumps (WMBPs) are novel left ventricular assist devices in which blood propulsion arises from the progressive wave propagation along an oscillating immersed membrane.

The main purpose of this thesis is to numerically investigate the fluid-structure interaction between the blood and the wave membrane via three-dimensional simulations in the real pump domain to better understand the physical principle in WMBPs and analyze pump performance, both in terms of hydraulic power and hemocompatibility. The adopted numerical strategy is based on the unfitted Extended Finite Element Method (XFEM), which avoids remeshing by using a fixed background mesh for the fluid problem. A relaxed contact model was introduced to handle potential membrane-wall collisions in the pump, in case of high wave undulations.

The computational study was conducted in two different WMBP designs, the flat membrane pump design (Test I) and the J-shape membrane pump design (Test II). In both cases, the numerical solution was successfully validated against *in-vitro* experimental data. The numerical results highlighted the role of the membrane wave deformation in generating blood outflow despite an adverse pressure gradient and showed that, at identical operating conditions, the J-shape pump design outperformed the flat design. Specifically, the predicted hydraulic output increased when either the frequency or the amplitude of membrane oscillations were higher, with a limited increase in the fluid stresses, suggesting good hemocompatibility properties of the WMBP system. Thus, we tested a new operating point in the J-shape design, which achieved physiologic flow rate target at diastolic head pressure. Finally, a preliminary study over the secondary non axi-symmetric modes of membrane vibration was presented (Test III), taking full advantage of the three-dimensional nature of the computational simulations .

In conclusion, the proposed fluid-structure-contact model proved to be a reliable tool to predict the performance of WMBPs at different working conditions and support pump development in view of its application in the upcoming first-in-human trials.

Acknowledgements

Foremost, I would like to express my gratitude to my mentor Christian Vergara, for all your advices and your dedicated guidance during this research, and to my industrial supervisors Jacopo Biasetti, Luc Polverelli and François Cornat, for welcoming me in your vibrant work environment. Thank you to the whole ROMSOC consortium and particularly to Volker Mehrmann and Lena Scholz, who created a tight group of scientists from all over Europe, that was uniquely focused on the professional growth of its fellows.

I want to thank the people who actively contributed to my work. First of all, thanks to Stefano Zonca, for your support over the many technical issues experienced during these years. Thank you also to all the members of the simulation and membrane teams from the partner company, who shared with me every week the knowledge and the experience cultivated during their industrial mission. Thank you to Trevor Snyder and Charlotte Rasser, for their feedback and the cooperation shown during the publication process.

Thank you to all the many wonderful people I met during these years and supported me in the toughest times. Thank you to my hilarious colleagues from the MOX lab, an amazing group of people who formed a cheerful work environment that will be very hard to find elsewhere. In particular, thanks to Simone, Stefania, Nicolas, Simone, and Silvia; you have been my closest friends since the very beginning of this journey (because, yes, I was indeed in Rome with you!). You advised me, you motivated me, you always were there for me. Thank you. Many thanks to my colleagues and friends in Paris, and particularly to Sofia, Giuseppe, Laura, Nathalie, Alessia, Paul, Diego, and Francesca; you have been my anchor during my time abroad and helped me every time I needed. Finally, thanks to my crazy international community of ESRs. It has been an honor to be your representative, and I will always remember the various travels and workshops (and deliverables) we made together.

In conclusion, thank you to my family, who know me besides my smile and who always stood by my side, regardless of the borders or the pandemics which separated us during these years. You were there to celebrate my successes and to listen to my outbreaks. Just, thank, you.

Contents

List of Symbols

Ω	pump domain	
Ω^f	fluid domain	
Ω^m	membrane domain	
Ω^r	magnet ring domain	
Σ	fluid-structure interface	
Γ^{in}	inlet boundary	
Γ^{out}	outlet boundary	
Γ^w	wall boundary	
Γ^m	membrane holder surrogate boundary	
Γ^r	magnet ring boundary	
Γ_{cut}	artificial cut boundary	
$\mathbf{n}^f$	external fluid normal	
$\mathbf{n}^s$	external structure normal	
$\mathbf{n}^w$	external wall normal	
$\mathcal{T}_h$	background mesh	
$\mathcal{T}_h^m$	foreground membrane mesh	
$\mathcal{T}_h^r$	foreground magnet ring mesh	
$\mathcal{T}_h^f$	fluid cut-mesh	
$\mathcal{G}_h$	split elements set	
K	element	
P_i^K	sub-portion i of element K	
N^f	maximum number of fluid sub-portions in $\mathcal{T}_h$ mesh	
$\mathcal{F}_h^\Sigma$	set of cut-faces at interface Σ	
$\mathcal{F}_h^p$	set of fluid physical cut-faces	
$\mathcal{F}_h^s$	set of cut-faces with stabilization	
$\mathcal{F}_h^g$	set of faces with ghost-penalty	
h	mesh step	cm
t	time	s
T	total time	s
Δt	timestep	s
τ	period of oscillation	s
p	fluid pressure	$mmHg$
$\mathbf{u}$	fluid velocity	cm/s
$\mathbf{T}^f$	fluid Cauchy stress tensor	$dyne/cm^2$
$\mathbf{u}^*$	fluid convective velocity	cm/s
$\mathbf{d}$	structure displacement	cm
$\mathbf{d}^m$	membrane displacement	cm

$\mathbf{d}^r$	magnet ring displacement	cm
$\mathbf{T}^s$	solid Cauchy stress tensor	$dyne/cm^2$
$\widehat{\mathbf{T}}^s$	first Piola-Kirchhoff stress tensor	$dyne/cm^2$
ρ_f	blood density	g/cm^3
μ_f	blood viscosity	$dyne/cm^2$
ρ_m	membrane density	g/cm^3
E_m	membrane Young modulus	$dyne/cm^2$
ν_m	membrane Poisson ratio	
λ_m	membrane first Lamé parameter	$dyne/cm^2$
μ_m	membrane second Lamé parameter	$dyne/cm^2$
H	head pressure	$mmHg$
Q	flow volume rate	l/min
f	oscillation frequency	Hz
Φ	oscillation amplitude (stroke)	cm
φ	oscillation displacement function	cm
P^{in}	inlet pressure	$mmHg$
P^{out}	outlet pressure	$mmHg$
W	hydraulic power	W
Δ	contact gap distance	cm
χ	contact force	$dyne/cm^2$
ε_c	thickness of contact layer	cm
Ω^c	contact layer domain	
Γ^c	contact boundary	
γ_Σ	interface penalty parameter	
γ_{dg}	interior fluid-fluid penalty parameter	
γ_v	continuous interior penalty parameter - convection	
γ_{div}	continuous interior penalty parameter - divergence	
γ_p	continuous interior penalty parameter - pressure	
γ_g	ghost interior penalty parameter	
γ_c^0	contact penalty parameter	
γ	shear rate	s^{-1}
γ^{max}	maximum shear rate in time and space	s^{-1}
WSS	wall shear stress	Pa
σ^{scalar}	scalar representation of internal fluid stress	Pa
σ^{VM}	Von Mises solid stress	MPa

Chapter 1

Introduction & Motivations

1.1 The clinical context

1.1.1 Cardiac physiology

The heart is the key organ of the cardiovascular system that pumps blood through the body in order to ultimately supply oxygen to the destination tissues. In particular, the cardiac function is twofold: the right side of the heart is responsible for the blood oxygenation and the expulsion of carbon dioxide through the lungs (pulmonary circulation), while the left side is in charge of the pumping of blood throughout the body to reach for the other organs and tissues (systemic circulation). Thanks to the transport of blood cells, hormones and other nutrients, blood circulation plays a fundamental role in many physiologic processes in the human system. In particular, blood cells, that constitute 45% of blood, cover three functions depending on their type: (i) *red blood cells*, or erythrocytes, which represent the most part of blood cells, transport oxygen thanks to the hemoglobin and deliver it to the cells to satisfy their metabolic needs; (ii) *white blood cells*, or leukocytes, at the core of the immune system, protect the body from infectious pathogens or parasites; and (iii) *platelets*, or thrombocytes, are responsible for blood clotting at sites of injury of the vessels to prevent blood loss. The fluid part of the blood, said *plasma*, mostly composed of water, circulates dissolved nutrients, such as amino acids, glucose, and mineral ions, that will be absorbed by the target cells.

The internal cavity of the human heart is divided into four chambers, two *atria* (right and left atrium) and two *ventricles* (right and left ventricle), separated by cardiac valves that regulate the transition of blood. The atria receive blood from the veins returning to the heart, while the ventricles collect blood from the atria and eject it into the arteries. The atria and the ventricles are separated by a wall that does not allow blood exchanges, called *interatrial septum* and *interventricular septum*, respectively.

The blood circulation in the heart is represented in Figure 1.1. Specifically, the *right atrium* receives deoxygenated blood coming from the superior and inferior vena cava, while the *right ventricle* pushes it into the pulmonary arteries to enter in the lungs. The tricuspid valve and the pulmonary valve control the passage of blood from the right atrium to the right ventricle and from the right ventricle and the pulmonary artery, respectively. The oxygenated blood returns into the *left atrium* via the pulmonary
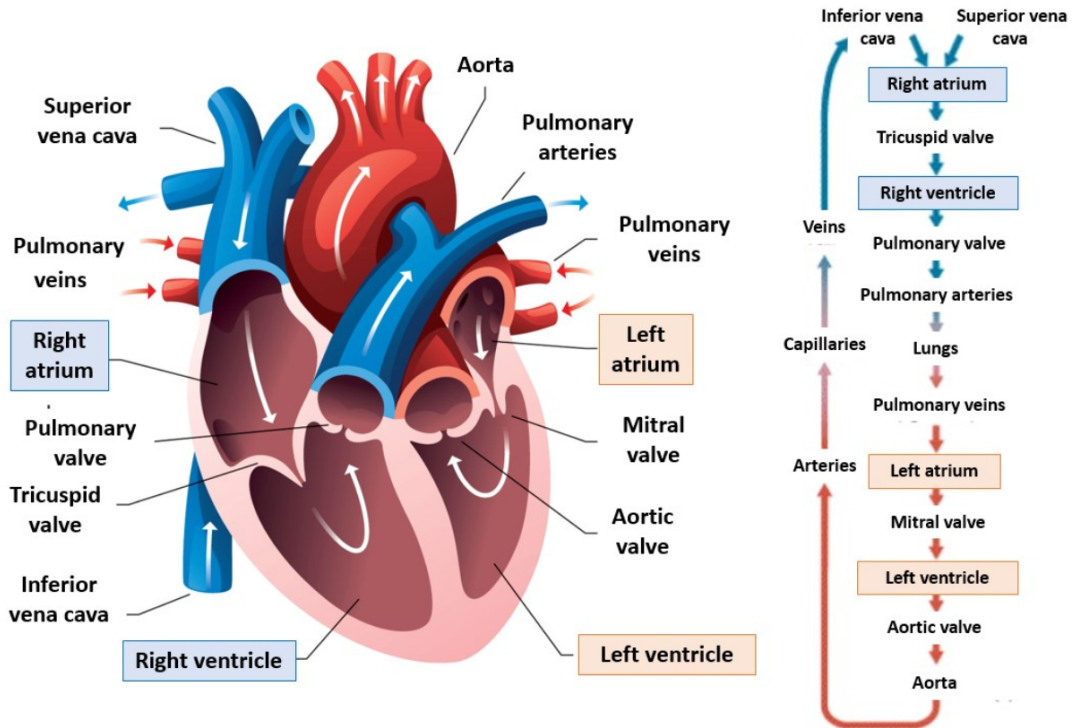
FIGURE 1.1: Anatomy of human heart (left) and schematic representation of blood circulation (right). Figures taken from [8] and [57].

veins and then the *left ventricle* (LV) pumps it into the *aorta* artery. On the left side of the heart, the mitral valve (or bicuspid valve) controls the filling of the left ventricle with the blood coming from the left atrium, while the aortic valve allows the release of blood from the left ventricle into the *aorta* artery. The oxygenated blood flows from the aorta (diameter: 2.5-3.5 *cm*) into an intricated network of smaller and smaller arteries until reaching the capillaries (diameter: 5-10 *μm*), where the oxygen and the nutrients are transferred to the recipient tissues. Afterwards, oxygen-depleted blood passes from the capillaries to larger veins and, eventually, goes back to the right atrium.

The pumping ability of the heart derives from the activity of contraction and relaxation of the cardiac muscle, said *myocardium*, during the cardiac cycle. Indeed, the mechanics of the myocardium provoke changes in the pressure inside the heart cavities, triggering the opening or the closure of the cardiac valves, thereby regulating the blood flow between the chambers. The contraction and the relaxation phases of the myocardium are referred to as *systole* and *diastole*, respectively. Figure 1.2 shows the time evolution of the atrial, ventricular and aortic pressures (Figure 1.2a) and the pressure-volume (PV) loop of the left ventricle during the heartbeat (Figure 1.2b). In particular, we can identify four phases in the hemodynamics inside the left heart:

1. *Isovolumic contraction*. It corresponds to the first phase of ventricular systole, when both the mitral and the aortic valves are still closed. Hence, the contraction of the left ventricle provokes a drastic increase in the ventricular pressure, without modifying the volume of the chamber.
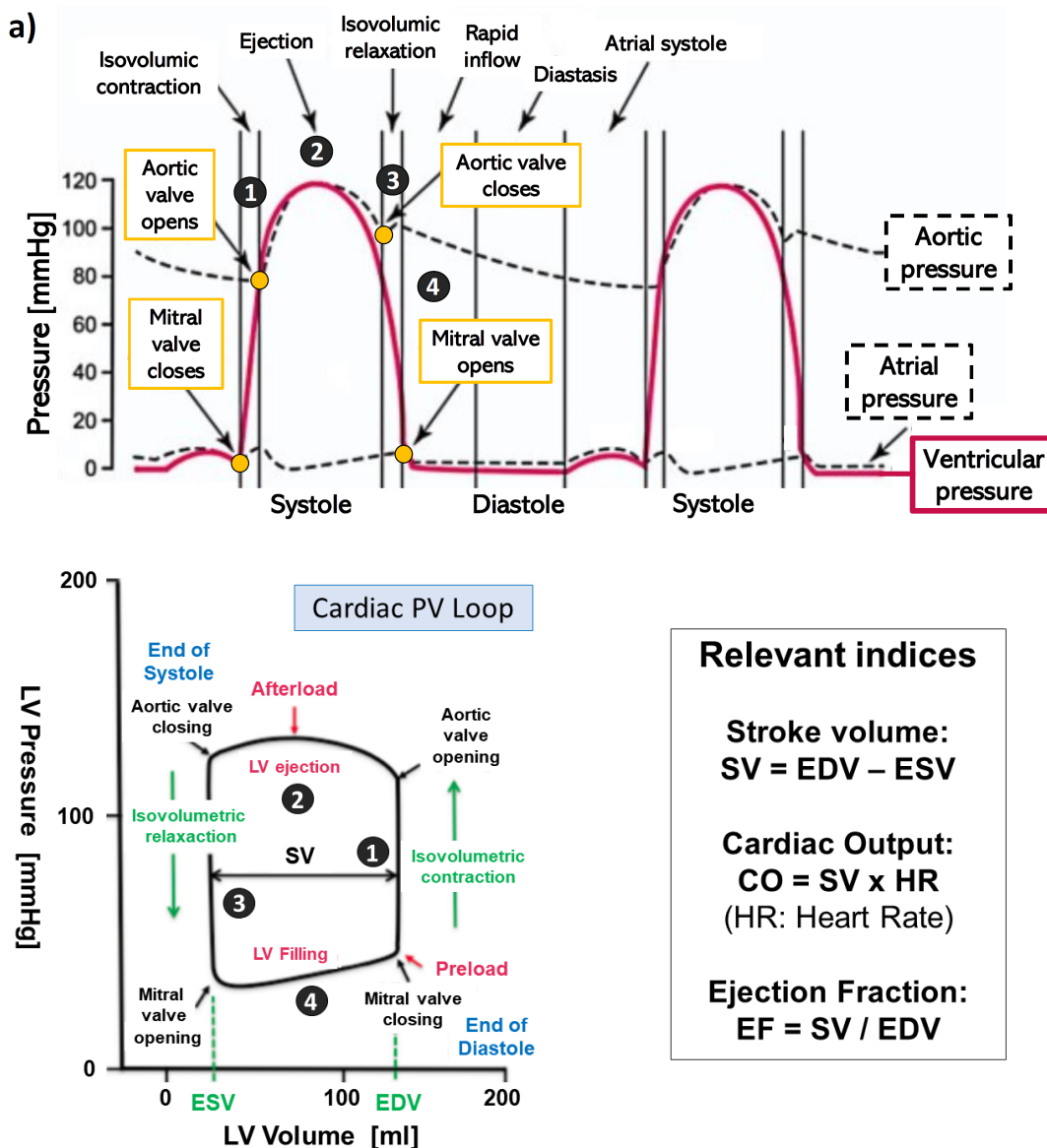
FIGURE 1.2: a) Phases of the cardiac cycle, with corresponding variations in ventricular pressure (red solid line) and atrial and aortic pressure (black dashed lines). Figure extracted from [140]. b) Pressure-Volume (PV) loop of the Left Ventricle (LV) during the cardiac cycle and relevant cardiac function indices. Plot adapted from [56].

2. *Ventricular ejection.* As the ventricular pressure exceeds the aortic pressure ($\sim$ 80 mmHg), the aortic valve opens, initiating the blood ejection from the left ventricle into the aorta. The contraction carries on after the opening of the valve, leading to a further increase in the pressure in both the left ventricle and the aorta. When the active contraction of the ventricle ends, the ventricle volume reaches its minimum value, called *End-Systolic Volume* (ESV). Afterwards, the ventricular pressure starts decreasing, leading to retrograde flow from the aorta that causes the closure of the aortic valve.

3. *Isovolumic relaxation.* After the end of the ventricular systole, the left ventricle starts to relax. Since the valves are again both closed, the relaxation does not lead to changes in volume, but to a rapid drop of the intraventricular pressure.

4. *Ventricular filling*. When the ventricular pressure gets lower than the atrial pressure (∼ 0-10 mmHg), the mitral valve opens, starting the filling of the left ventricle chamber. Around 70% of ventricular filling occurs during this initial phase (*rapid inflow*). As ventricular diastole goes on, the passive filling of the ventricular chamber gets slower (*diastasis*), before being newly accelerated by the active contraction of the left atrium (*atrial systole*), that pushes residual blood into the ventricle. At the end of diastole, the volume in the left ventricle is maximum and equal to the so-called *End-Diastolic Volume* (EDV).

The same mechanisms apply to the right heart as well. However, the myocardium wall in the left ventricle region is almost two times thicker than the one right ventricle, owing to the higher hydraulic resistance that it has to overcome to pump blood throughout the whole body [250]. Indeed, the values of pressure in the left heart are approximatively five times higher than in the right heart.

This multi-step cardiac activity results in a *pulsatile* blood flow signal, that repeats at each heartbeat. Figure 1.3 represents the aortic flow waveform during the cardiac cycle: after the aortic valve opens, the aortic flow rapidly rises until reaching its peak at more than 20 l/min; then, as the ventricular pressure decreases, blood ejection decelerates and eventually the aortic flow becomes negative, causing the closure of the aortic valve. During diastole, the flow is almost null. The volume of blood pumped from the left ventricle per beat is named *stroke volume* (SV), which corresponds to the difference between the EDV and ESV. At rest conditions, SV amounts to around 90-110 ml [187]. The *cardiac output*, corresponding to the volume of blood ejected per minute, is computed as the product of stroke volume and *heart rate*, i.e. the number of heartbeats per minute (bpm). In healty conditions, the cardiac output at rest amounts to 5.08 l/min, with variations of 1-2 l/min depending on age, gender and body surface area (BSA) [45].
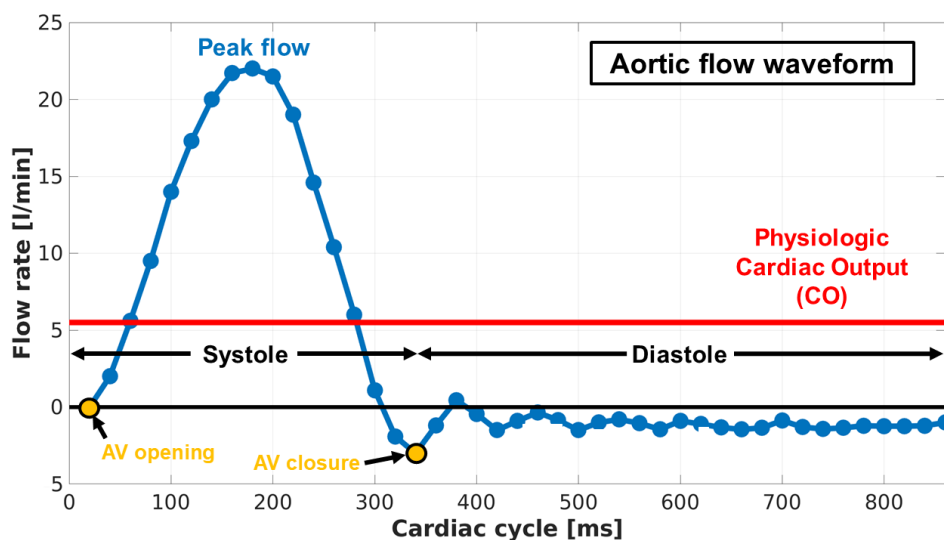

FIGURE 1.3: Aortic flow waveform during cardiac cycle. Physiologic value of average cardiac output is highlighted in red. AV - Aortic Valve. Figure adapted from [173].

1.1.2   Heart failure

Heart failure (HF) is a global pathological cardiac condition in which a structural or functional abnormality of the heart does not allow to reach the physiologic blood flow rates, that are required to meet the matabolic demands of the body [277, 253]. Nowadays, HF is one of the most common causes of morbidity and mortality worldwide [172] and the most prominent cause of hospitalizations and death in the United States [94]. HF has affected 40 million people worldwide [44] and, given the progressive ageing of the population, the number of cases is predicted to constantly increase in the next decades [253, 176]. For instance, the projections from the American Heart Association [157] show that at least 8 millions people in US will suffer of heart failure by 2030, accounting for an increase in prevalence of 46%. Such heart dysfunction is particularly common in the developed countries, characterized with higher life expectancy, older population, and bad nutritional lifestyle [295], where it represents a major health care cost [94].

The most common causes for HF include coronary artery disease, previous myocardial infarction, valvular heart disease, cardiomyopathy and myocardatis [47, 232]. Unless these diseases lead to cardiac arrest or death, they typically imply a reduction in the stroke volume. In the initial stages of these diseases, the heart tries to compensate for the cardiac output by increasing the frequency of contraction (tachicardia), and thereby the heart rate, or the diastolic filling [238]. When such correction mechanisms are no longer effective, cardiac output decreases drastically leading to HF [238]. The prognosis for HF patients is poor, with lower survival rates than most cancers [99].

The *ejection fraction* (EF), that compares the ejected blood volume with respect to the total blood volume in the chamber, is the primary criterion to characterize the type of HF [94, 253, 295]. Referring to Figure 1.2b, the EF can be computed as the ratio between between the stroke volume (SV) and the end-diastolic volume (EDV). HF with *preserved ejection fraction* (HFpEF) shows physiologic values of ejection fraction, *i.e.* around 50-70% [188]. HFpEF, also referred to as diastolic HF, indicates an impaired left ventricul filling or suction capacity during diastole. When the ejection fraction is lower than 40%, HF is defined as with *reduced ejection fraction* (HFrEF). HFrEF is also named systolic HF because it implies an insufficient contraction of the myocardium, that prohibits to correctly pump oxygenated blood out to the body. Recent studies [232] introduced a third class of HF, the *mid-range ejection fraction* (HFmEF), with an intermediate ejection fraction between 40 and 50%, that have primarily mild systolic dysfunction, but with features of diastolic dysfunction. Even though the diagnosis of HFpEF and HFmEF is more challenging than the diagnosis of HFrEF, they represent more than the half of the cases of HF. Hence, other diagnostic criteria, such as the observation of high levels of natriuredic peptides or concomitant morbidities, can be employed to identify HFpEF and HFmEF conditions [93].

The severity of cardiac dysfunction and HF is defined according to the Interagency Registry for Mechanically Assisted Circulatory Support (INTERMACS) [152], created in 2005, that defines a classification of patients profiles affected by HF, depending on symptoms (such as significant fatigue, dyspnea, or peripheral edema) and clinical signs (such as elevated jugular venous pressure, pulmonary crackles, or abnormalities

Class	Descriptor	INTERMACS profile	Time frame for intervention
1	"Crash and burn"	Hemodynamic instability in spite of increasing doses of catecholamines and/ or critical hypoperfusion of target organs despite MCS; patients in critical cardiogenic shock	Necessary within hours
2	"Sliding on ionotropes"	Intravenous ionotrope support with acceptable blood pressure but rapid deterioration of kidney function, nutritional state, or signs of congestion	Necessary within days
3	"Dependent stability"	Hemodynamic stability with dependency on low or intermediate doses of ionotropic agents due to hypotension, worsening symptoms, or progressive kidney failure	Elective within weeks to months
4	"Resting symptoms"	Temporary discontinuance of ionotropic agents is possible, but patient presents to medical attention with frequent symptoms	Elective within weeks to months
5	"Exertion intolerant"	Stable at rest without ionotropic agents but major limitation in any level of physical activity; clinical signs of moderate fluid retention and some level of kidney dysfunction	Variable, depending on nutrition, organ function, activity level
6	"Walking wounded"	Stable at rest without ionotropic agents and minor limitation in physical activity; clinically without signs of fluid retention or kidney dysfunction	Variable, depending on nutrition, organ function, activity level
7	"Placeholder"	NYHA class II or III symptoms without current or recent fluid overload and hemodynamic instability	Transplantation or circulatory support may not currently be indicated

FIGURE 1.4: Interagency Registry for Mechanically Assisted Circulatory Support (INTERMACS) classification. Figure taken from [94].

in electrocardiogram) [232, 34]. Figure 1.4 reports the details of the INTERMACS classification from level 1 to level 7, in order of decreasing severity of the heart dysfunction. Clinicians refer to the INTERMACS to decide the quality and timeliness of intervention for the patients with HF. Indeed, in case of less severe chronic HF (INTERMACS 4-7), treatment can be initially limited to lifestyle adjustments or pharmacological therapies, e.g., angiotensin-converting enzyme (ACE) inhibitors, angiotensin II type I receptor blockers (ARBs), β-blockers, and diuretics [232]. However, the severity of the symptoms of chronic patients tends to worsen over time despite optimal therapy, especially in case of precipitant factors (*e.g.*, infection, hypertension or ventricular arrhythmias [232]). It has been estimated that 0.5-5% of patients with chronic HF are completely refractory to medical treatment (*refractory chronic heart failure*) [191, 181]). This may result in progression to higher INTERMACS classes (INTERMACS 1-3) and, ultimately, to *end-stage chronic heart failure*, or simply *advanced heart failure* (AHF), with a 1-year mortality rate over 50% [181]. AHF patients are characterised by advanced structural heart disease and pronounced symptoms of heart failure at rest or upon minimal physical exertion. For these patients or, alternatively, in case of *acute heart failure* (INTERMACS 1), more advanced replacement therapies are required, such as heart transplantation or mechanical circulatory support systems [94, 183].

1.2 Left Ventricular Assist Devices

1.2.1 Heart transplantation

Despite the notable advances in medical treatments and prevention, Heart Transplantation (HT) remains the most promising and widely accepted long-term treatment for end-stage HF [18]. Indeed, the 5-year survival for heart transplantation patients who receive successful immunosuppressive therapy amounts to 70–80% [162] and the median survival post-transplant is 10 years [6]. It also significantly improves quality of life, exercise capacity, and return to work, compared with other conventional treatments [232].

However, the access to this surgical therapeutic option is limited for two reasons. First, the availability of healthy donor hearts is very poor, while there is an increasing number of transplant candidates. Indeed, in the most recent years, only 4500-5500 transplants were performed per year in the world [162], corresponding to less than 2% of the estimated 300000 patients with AHF who could benefit of cardiac transplantation [94]. Second, patients with end-stage chronic HF need to satisfy strict selection criteria for HT, that are based on age, lifestyle (*e.g.*, drug or alcohol abuse, bad nutrition), and clinical conditions (common controindications are active infections, cardiovascular diseases, pulmonary hypertension, renal dysfunction, or cancer) [232]. Due to older population and the increasing rate of co-morbidities, the number of not eligible patients is increasing over the years [6].

Eligible candidates with refractory chronic HF are inserted in waiting lists for cardiac transplantation. However, more than 60% of patients are transplanted in high-urgency status, typically for acute HF, leaving little chances for candidates listed for less urgent transplantation [232]. Therefore, a median waiting time of 16 months was estimated by Eurotrasplant [268], while mortality of patients in the waiting list is 21% at 6 months and 47% at 1 year [6].

After cardiac transplantation, patients have a 1-year survival rate close to 90% [162]. However, the main risk of HT consists in organ rejection, that can either occur during the first 24 hours (early graft dysfunction), primarily caused by pre-existing donor heart disease or allograft injury, or after weeks to years (late graft dysfunction), due to acute cellular-mediated or antibody-mediated rejection [145]. Moreover, the patient may undergo severe long-term complications due to the immunosuppressive therapy subsequent to HT, such as infections, hypertension, renal failure, malignancies, and cardiac allograft vasculopathy [145].

1.2.2 Mechanical Circulatory Support Devices

The various limitations of heart transplantation led to the search of alternative or helping approaches to treat acute and advanced HF [181]. Mechanical Circulatory Support (MCS) devices have been designed to take over, totally or partially, the blood pumping ability of the failed heart, by mechanically propelling blood into the aorta. In

this way, MCS devices unload the failing ventricle and maintain sufficient end-organ perfusion.

MCS systems are divided in two main categories, *non-durable devices*, for short-term support (hours-days), and *durable* devices, for mid- or long-term support (weeks-months-years) [190].

Non-durable MCS devices are typically used in patients with acute and rapidly deteriorating HF (INTERMACS level 1) to temporarily stabilize hemodynamics and end-organ perfusion. The most common examples of non-durable MCS systems are:

- the *Intra-Aortic Baloon Pump* (IABP) [82, 265]. It is a percutaneous device, based on a intra-aortic counterpulsation balloon that inflates and deflates at a specified rate to assist blood ejection and reduce the workload on the left ventricle. The expected increase in cardiac output is between 0.5 and 1 l/min [73]. IABP is indicated for patients recovering from cardiac infarction, recent heart surgery or acute myocarditis [214, 252].

- the *Extracorporeal Membrane Oxygenation* (ECMO) [164, 84]. When ECMO are used to treat HF (Veno-Arterial configuration, VA ECMO), the deoxygenated blood is taken from a central vein via an outflow cannula, it passes through an extracorporeal pump and an oxygenator system, and finally it returns into a central artery by means of an inflow cannula. In this way, VA ECMO bypasses completely the pulmonary circulation and provides both hemodynamic and respiratory support [189]. Alternatively, the Veno-Venous configuration of ECMO (VV ECMO) can selectively sustain the respiratory function in case of respiratory failure [84].

Other prototypes of non-durable MCS systems are the Impella pump (CardiacAssist) [204, 72] and TandemHeart (ABIOMED) [297, 135]. Thanks to their short-term cardiac support, these short-term MSC devices allow for a full clinical evaluation of the patient's conditions and can be used as *Bridge-to-Decision* (BTD), giving the time to consider a potential transition to durable MSC devices or HT [295].

Instead, durable MSC devices are mostly implanted in patients with advanced chronic heart failure. Indeed, the majority of VAD implants are performed in patients with INTERMACS levels from 1 to 3, while the ones with INTERMACS from 4 to 7 are generally considered to be stable enough to be rather listed for HT [94]. Nonetheless, the INTERMACS registry, that serves as central repository for MCS clinical outcome data, shows better outcomes in LVAD patients having a higher INTERMACS class (levels 4-6) with a 1-year survival at 93% [232]. Moreover, recent trials [96, 271] showed that earlier implantation of durable MSC devices in less severely ill patients had better outcomes than in those patients continuing on medical therapy.

Durable MSC systems are generally divided in two main categories:

1. *Total Artificial Hearts* (TAHs) [80, 75]. TAHs are pneumatically-powered devices that are designed to permanently replace the cardiac apparatus. As a consequence, their application requires the explantation of patient's native ventricles and valves. TAHs are generally composed of two large artificial ventricles, which are equipped with mechanical disc valves to regulate flow
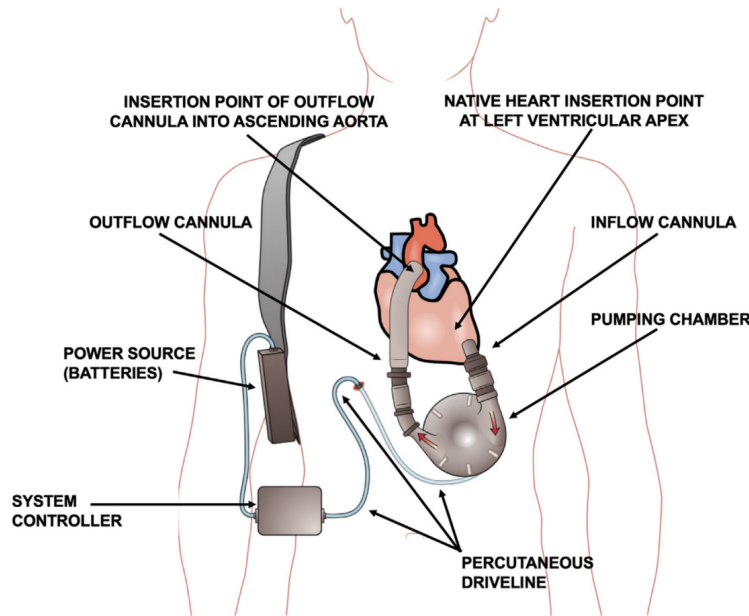
FIGURE 1.5: Standard components of an intracorporeal left ventricular assist device. Figure taken from [94].

direction, and percutaneous drivelines attached to an external pump [77]. They offer biventricular support and work in pulsatile flow regime, but their large size makes the implantation accessible only to patients with appropriate chest size [75]. For instance, CardioWest (Syncardia), that is the only TAH available in the United States, does not fit in many men and most women [18].

2. *Ventricular Assist Devices* (VADs) [6, 18]. VADs, or blood pumps, are implantable devices that can temporarily or permanently support either one or both heart ventricles. Most of VADs specifically target the left ventricle and are thereby called *Left Ventricular Assist Devices* (LVADs). LVADs are implanted at the apex of the left ventricle (*i.e.* its bottom part), where they gather the blood from the left ventricle into the pump chamber via an inflow cannula; then, they mechanically eject it through a flexible outflow cannula into the ascending aorta. Right Ventricular Assist Devices (RVADs) can similarly support the right ventricle. RVADs are often employed in case of potential reversibility of the right ventricle failure, that has shown to largely influence survival to and from HT [151, 94]. Finally, in case of biventricular failure or persisting right ventricle failure after LVAD implantation, Biventricular Assist Devices (BiVADs) may be indicated [136]. VADs functioning is usually monitored and controlled by an external *system controller*. Furthermore, a set of batteries transmits the input current to to the controller and the pump actuator via a *percutaneous driveline*. The overall structure of an implantable blood pump is shown in Figure 1.5.

Despite recent attempts to improve TAHs in terms of smaller size (Bivacor [284]) or physiologic output (RealHeart [228], Carmat [207, 169]), in the last decades LVADs have proved to be less invasive, more reliable and with minor risk of post-implant complications [18, 181]. Hence, the use of TAHs is very limited and specifically

selected for patients with irreversible biventricular cardiac failure [77].

Thanks to their high reliability and the small size, LVADs can be used in a wide spectrum of treatments, depending on the health state of the patient and on the severity of the heart disease. In particular, LVADS are employed as:

- *Bridge to Transplantation* (BTT): LVADs (or BiVAD) can be implanted in patients in the waiting list for HT, that have a cardiac function that is too unstable to await a suitable donor heart. In these patients, LVAD treatment has showed to improve quality of life, survival-to-transplantation rates, and post-transplant survival [295, 162].

- *Bridge to Recovery* (BTR): in some conditions, the functional improvement of the left ventricle during LVAD treatment permits to achieve cardiac recovery and to eventually remove the device. This outcome occurs more likely in younger patients with an acute but reversible cause of HF, such as acute myocarditis or cardiomyopathy [94].

- *Bridge to Candidacy* (BTC): patients that are initially not eligible for HT due to transient dysfunctions may change their candidacy status thanks to LVAD implantation and ultimately be inserted in the waiting list. Indeed, LVAD treatment may permit to recover end-organ functionality, improve right ventricle activity, and relieve hypertension, which are potential causes for patients ineligibility to HT [162, 232].

- *Destination Therapy* (DT): LVADs can be employed as permanent solution for patients with end-stage heart failure who are ineligible for HT. Indeed, non-transplant-eligible patients with LVAD reach a survival of 80% at 1 year and 70% at 2 years [232]. Such positive results have open an increasing interest in LVADs treatment as an alternative to HT. Indeed, as shown in Figure 1.6, the relative employment of LVADs a DT grew from 2% in 2008 to 49% in 2017 [295].

1.2.3   LVADs history and classification

1.2.3.1   Birth of MCS devices

The earliest efforts in MCS development are represented by the *Cardio-Pulmonary Bypass* (CPB) [134], an extracorporeal pump that temporarily circulates and oxygenates blood while bypassing the heart and the pulmonary system. The original propotype of CPB was proposed in 1885 by Maximilian Von Frey, but its employment was limited by the lack of a proper anticoagulation medical treatment. After several animal trials during the first half of the 20th century, CBP was successfully used in 1953, for the first time in a human patient, during an open-heart surgery to repair an atrial septal defect [74].

The increasing interest in CBP and in open-heart surgery in the 1950s led to the development of more advanced MCS devices. Initially, the research was focused on TAHs, that could permanently replace the cardiac apparatus. The first TAHs
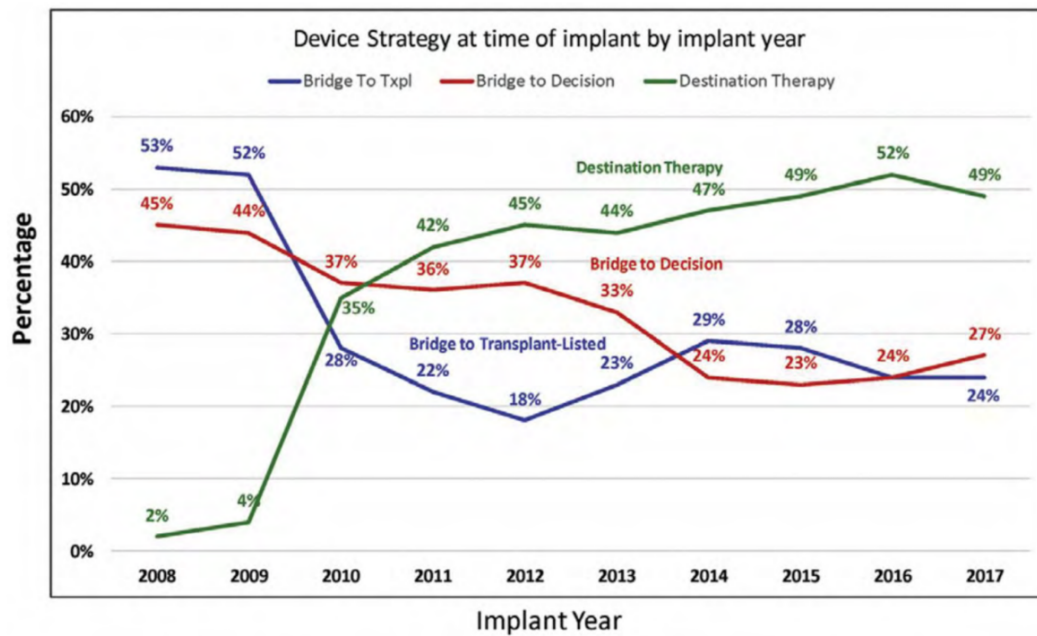
FIGURE 1.6: Devices strategy in MCS systems from 2008 until 2017. Figure extracted from [295].

were developed and tested in animals in 1950 by Kolff in the Unites States [78], and by Liotta in Argentina [79], In the following years, also alternative solutions for short-term support were investigated. For instance, the percutaneous intra-aortic counterpulsation baloon pump was proposed in 1962 by Moulopoulos [211] and implanted for the first time in 1967 for about 7 hours, until stabilization of the patient's conditions. Furthermore, Debakey performed in 1966 the first mid-term implantation of a paracorporeal VAD, in a patient with cardiac arrest following aortic valve replacement [175]. It was a pneumatically-driven VAD used as BTR to wean the patient from CBP and wait for the heart recovery. It was employed for 10 days until discharge of the patient.

After the first cardiac transplantation, perfomed in 1967 in South Africa [46], an increasing interest for BTT devices spread among clinicians, in order to support the patients with AHF waiting for suitable donor hearts. Therefore, starting in the late 1960s, many technological industries and research centers collaborated to develop the first VAD prototypes. Further motivated by the awareness of lack of donor hearts and of the contraindications to HT, the following decades were marked by significant technological advancements in device design and functioning.

1.2.3.2 First generation LVADs

The tight collaboration between medical industries and national research centers risen in the 1960s-1970s led to the development of the *first generation* of LVADs which includes *pulsatile volume displacement pumps*. These LVADs are equipped with inflow and outflow mechanical valves that allow to direct the blood dynamics inside the pump chamber in order to obtain a pulsatile output flow [6]. The pump

chamber, usually placed in the abdominal pocket, consists of a rigid case containing a membrane that separates blood and air. An external compressor cyclically changes the internal volume of the pump chamber through a pneumatically-driven expansion of the membrane, thereby propelling the blood by positive displacement (see Figure 1.7, left). The resulting stroke volume is fixed. Hence, the pump rate must be adjusted to modulate the LVAD output.

The first successful implantation of a long-term pulsatile flow LVAD was performed in 1988 [163]. A few years later, in 1994, a similar prototype, the Thoratec pneumatic VAD (pVAD), received for the first time the approval for BTT from the Food and Drug Administration (FDA) [94]. Subsequently, it has been in clinical use for over 20 years and implanted in overall 4000 patients [94]. With respect to other devices, pVAD allows patients to be discharged home with the device in place. This technology further evolved in HeartMate XVE (Thoratec Corp), or HeartMate I (HM1) [184], that quickly became the new LVAD standard for BTT worldwide for 25 years [94]. In 2001, the Randomized Evaluation of Mechanical Assistance for the Treatment of Congestive Heart Failure (REMATCH) trial [156] randomized 129 patients with AHF, who were not candidates for cardiac transplantation to receive either Optimal Medical Management (OMM) or HM1 implantation. This study showed that survival at 1 and 2 years was 52% and 23%, respectively, in the HM1 group, against 25% and 8% in the OMM cohort [247, 172]; also, HM1 group showed a reduction of 48% in risk of all cause mortality compared with OMM group [94]. Such results led to FDA approval of the HeartMate XVE as the first VAD for DT. Other examples of first generation LVADs are the AB5000 blood pump (ABIOMED) [251], implantable VAD (iVAD, Thoratec) [25], Novacor (World Heart) [272], and LionHeart LVD2000 (Arrow International) [202].

Even though they achieve a volume flow rate of up to 10 $^l/_{min}$, first generation LVADs are rarely used due to the large volume of the device, that makes implantation difficult and increase the risk of infections. For instance, the size of HM1 requires that the Body Surface Area (BSA) of the patient is higher than 1.8 m^2, thus excluding most children and small adults from potential application [172]. In addition, these devices show also high incidence of malfunction, many bearings, high working noise, and a lower pulsation than the one of the native heart [6]. The resulting durability of pulsatile LVADs reach 2 years.

1.2.3.3   Second generation LVADs

The *second generation* devices are *continuous flow* (CF) *axial rotary pumps*, where blood is propelled by a rotating impeller suspended in the blood flow path by mechanical contact bearings (Figure 1.7, right). These devices are defined axial flow blood pumps because the rotor imparts tangential velocity and kinetic energy to the blood, resulting in generation of a net pressure rise across the pump [172]. Rotary pump flow is directly proportional to rotor speed - around 6000-15000 rounds per minute (rpm) [181] - and inversely proportional to pressure difference between the inlet (*pre-load*) and outlet (*after-load*) [205]. With respect to pulsatile displacement pumps, second generation LVADs do not include inner valves and they eject blood
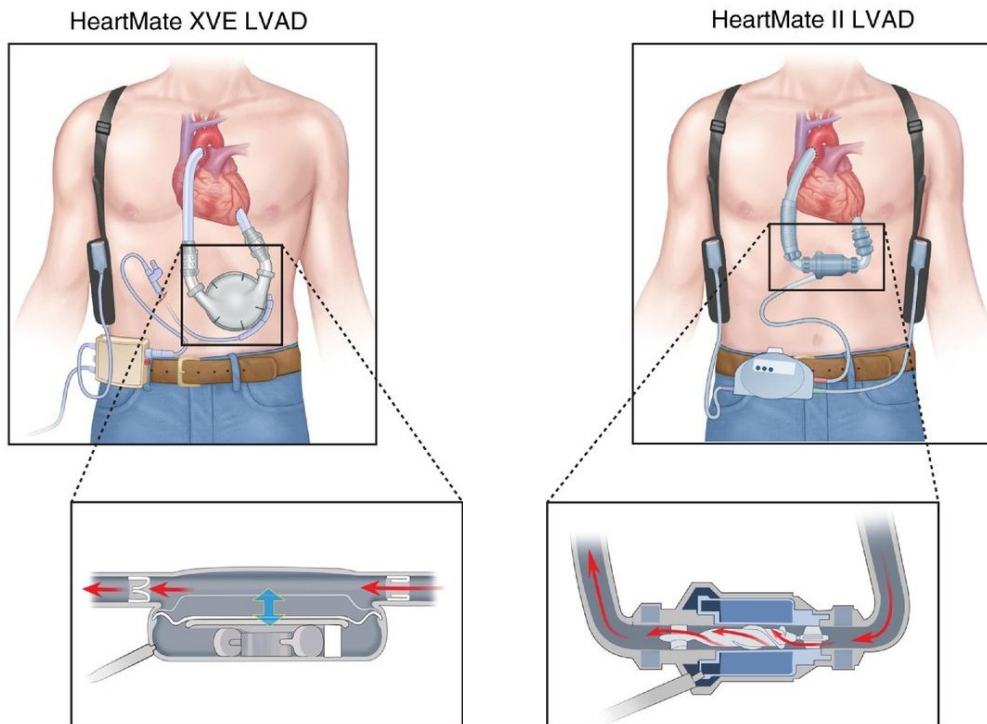
FIGURE 1.7: Comparison of a volume displacement (HeartMate XVE LVAD, left) and an axial flow rotary pump (HeartMate II LVAD, right). Figure comes from [246].

flow in a continuous regime. Axial pumps are characterized by a smaller size, that allows a simpler placement below the diaphragm or, more recently, in the preperitoneal space [3], with no need of creating an abdominal pump pocket during implantation (see Figure 1.7, right) [6]. This results in less surgery trauma, faster recovery and reduced risk of infections. Furthemore, they show lower energy requirements, lower operation noise, lower incidence of device failure and higher durability [6, 94].

The first example of CF pump is the *HemoPump*, developed in 1988 to treat cardiogenic shock [181]. It was a percutaneous catheter-mounted rotary pump that opened the research to more advanced CF pumps for medium- and long-term therapy. Hence, the first in-human implantation of a CF VAD, the DeBakey LVAD (MicroMed) [166], was held in 1998 for end-stage HF. HeartMate II (HM2, Thoratec) [137] is the most used axial flow LVAD, with a number of implantations up to 10 times higher than in other CF devices and counting over 10000 patients worldwide. Indeed it has received approval for BTT in 2008 and for DT in 2010 [181]. Clinical trials of HM2 showed significant improvement with respect to pulsatile HM1, with a 68% survival at one year (against 52%) and 58% survival at two years (against 24%) [94]. Other second generation LVADs are HeartAssist 5 (Micromed Cardiovascular) [67] and Jarvik 2000 FlowMaker (JarvikHeart) [302].

However, CF rotary pumps caused complications related to the exposition of blood to nonphysiologic high shear stresses. Indeed, the high speed of rotor and the narrow gaps (50-500 μm) may result to shear stresses higher than 1500 Pa, while physiologic thresholds are around 2-8 Pa [18]. Such stress conditions may end in blood trauma, e.g. degradation of Von Willebrand Factor (VWF) protein, platelet

activation, and hemolysis. Also, the presence of guide vanes facilitate blood clotting in area of stasis and, hence, pump thrombosis. Furthermore, the non-pulsatile ouput of CF LVADs leads to diminished pulsatility, increased pressure gradients on aortic valve and decreased compliance in smaller arteries [64]. Thus, with respect to first generation pulsatile devices, CF LVADs show a lower rate of left ventricular recovery and an increase in adverse events such as gastro-intestinal (GI) bleeding, aortic insufficiency, and stroke [6, 64, 179]. Thrombus formation is normally prevented via anticoagulation therapies, but increasing the risk of gastro-intestinal bleeding [183].

1.2.3.4   Third generation LVADs

The *third generation* of LVADs consists of CF *centrifugal rotary blood pumps*, that differ from the axial LVADs because they accelerate blood circumferentially, in a direction perpendicular to the flow coming in from the left ventricle (see Figure 1.8) [6]. In addition, unlike in second generation designs, the rotor is suspended in the blood flow path with non-contact bearing design, using either hydrodynamic levitation, like VentrAssist (Ventracor) [301], or magnetic levitation, like DuraHeart (Terumo) [210], or a hybrid system, like HVAD (HeartWare) [286]. Hydrodynamic levitation of the rotor derives from fluid lifting forces in thin blood layers separating the impeller from the pump housing; while magnetic levitation is achieved by employing permanent repelling magnets in the rotor and the pump housing. Thus, by avoiding any mechanical contact, these systems reduce shear stress, device wear, frictional dissipation and heat generation, thereby increasing device lifetime and reliability [6, 181]. As a result, even though centrifugal pumps are slighly larger than axial pumps, they are more suitable for long-term support, thanks also to lower speed of rotation (1800-4000 rpm), higher hydraulic efficiency, and lack of stationary vanes [181]. In addition, they present an anatomical suitable geometry that allows pericardial placement and, consequently, less invasive surgery [273].
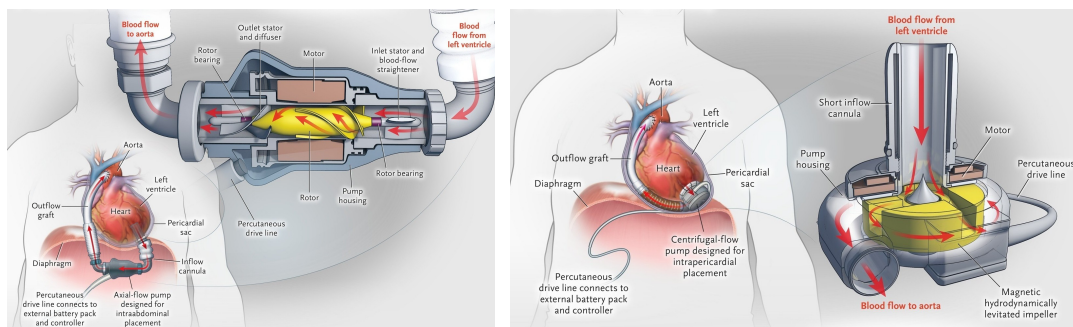

FIGURE 1.8: Comparison of structure and mechanics inside axial (left) and centrifugal (right) rotary pumps. Images taken from [246].

HVAD and HeartMate III (HM3, Thoratec) [41, 7, 227] are the most common third generation LVADs.

HVAD is deemed to be versatile and reliable device, also suitable for different clinical scenarios, including biventricular support. It reaches 10 L/min at low rotational speed, i.e. 2400 rpm [181]. It received approval for BTT in 2012, and for DT in

2017 [181]. Clinical performance of HVAD was studied in the HeartWare Ventricular Assist System as Destination Therapy of Advanced Heart Failure (ENDURANCE) trial [203, 218], where 446 patients were randomized to have either HVAD or HM2 treatment. In this study, HM2 patients underwent more LVAD malfunctions or failures requiring device replacement (16.2% vs. 8.8%), while the stroke rate was higher in the HVAD group (29.7% vs. 12.1%) [203]. Overall, HVAD appeared to be more durable than HM2.

HeartMate III presents a fully magnetically levitated rotor, with wide blood flow conduits and no mechanical bearings. Such design minimizes shear forces, wear on moving component and heat generation. In particular, HM3 introduces a CF pulsation algorithm to generate artificial pulse, by varying rotational speed from 3000 to 9000 rpm every 2 s [7, 181]. The artificial pulse mode prevents stasis and increases washing within the flow path of the blood pump [129]. As a result of the new engineering design and the artificial pulse algorithm, HM3 presents lower risk of gastro-intestinal bleeding, thrombosis, and aortic insufficiency, and may allow myocardial reverse remodeling [7, 239]. HM3 was approved in 2016 for BTT, and in 2018 for DT application [181]; but also short-term support with HM3 can be performed. In 2016, the Multicenter Study of MagLev Technology in Patients Undrergoing Mechanical Circulatory Support Therapy with HeartMate 3 (MOMENTUM 3) [200] showed a superior outcome in HM3 patients than in HM2 patients, with significant improvement in incidence of stroke, thrombosis, bleeding, and ventricular arrhythmias, and decreased hospitalization and care costs [199].

A recent study from EUROMACS [259] compared the performance of HVAD and HM3. In this study, the two LVADs showed similar survival, but HM3 cohort showed lower incidence of adverse events, such as stroke, pump thrombosis, and blood trauma. Driveline infections were more common in HM3 [199].

The classification of the LVADS is reported in Figure 1.9, which summarizes the strong and the weak points for each generation.

1.2.4 Limitations of LVAD application

Nowadays, the most common implanted LVADs to treat advanced HF are HeartMate II, HVAD and, more recently, HeartMate III. Indeed, they have shown important outcomes in ventricular function support and recovery, with a device durability that can last over 10 years [181]. However, despite the many technological advancements through the last fifty years, the incidence of LVAD-related complications and adverse events is still significantly high and can affect the long-term outcome of the patients. For this reason, their implantation is still limited to the most severe cases of acute and chronic refractory HF and patient selection is a crucial factor to determine the success of LVAD therapy. Indeed, independently of the surgical implantation approach, several risk factors have been identified for early mortality after LVAD implantation, such as advanced age, female gender, smoking, high body mass index, INTERMACS level 1 or 2, renal or liver failure, and other concomitant cardiac procedures [181, 220].

Generation	Pump qualities	Disadvantages	Examples
First	• Pulsatile flow • Volume displacement • Intra/extracorp. placement • Uni/bi-ventricular support • Mid/long-term support	• Large size • Need for high BMA • Percutaneous lead • Operation noise • Frequent malfunction	Thoratec pVAD Thoratec iVAD HeartMate XVE Novacor LionHeart
Second	• Rotary pump • Axial continuous flow • LVAD • Long-term support	• Contact bearings • Absent pulse • Thrombus formation • Percutaneous lead • Risk of ventr. suction	HeartMate II Jarvik 2000 DeBakey
Third	• Rotary pump • Centrifrugal continuous flow • LVAD • Non-contact bearings	• Intermediate size • Absent/low pulse • Percutaneous lead • Risk of ventr. suction	HeartMate III HVAD DuraHeart EvaHeart

FIGURE 1.9: Summary of characteristics, disadvantages and examples for each pump generation. Inspired on the review from [6].

The most common complications following LVAD application are bleeding, infection, right ventricular failure, and blood-related and neurological adverse events.

The risk of internal bleeding depends on the surgical technique and on the anticoagulant therapy, with very variable incidence going from 0 to 45% [181]. Bleeding can occur in different locations, such as at pump connections, grafts in the conduits, and on mucosal surfaces, particularly in the gastro-intestinal (GI) tract [183]. Rate of GI bleeding are higher in the upper GI tract, than in the lower GI tract. GI bleeding, with a reported incidence in CF LVADs of 6-35% [181], was very rare in first generation pulsatile pumps. Indeed, it is thought that the impellers in rotary CF pump degrade the Von Willebrand Factor (VWF) protein, causing the so-called Von Willebrand Syndrome, that increases the likelihood of GI bleeding [289]. However, in the recent years, the increasing experience with second and third generation devices led to a reduction in GI bleeding rates and consequent mortality [94].

The percutaneous driveline, which links the implanted pump with the external power source, constitutes a source of entry for bacteria from the external environment into LVAD interior [181]. Although the most common site of infection is the driveline cable itself, occurring in the 5-55% of cases, mostly during the first month, the infection can also develop in different locations of the LVAD circuit, such as the pump pocket or the cannulae [94]. In the latter cases, device explantation is mandatory, while antibiotics are administrated to suppress the infection. Possible non-durable MSC (*e.g.* Impella) could be considered for critical patients. Infections, ultimately leading to sepsis, represent the third most common cause of death of LVAD patients within the first year [183].

Right ventricular failure (RVF), occurring in 15-40% of LVAD patients [183], is the most undesired post-implant complication, because it is highly associated with increased peri-operative and short-term mortality [94, 181]. It results in septal

shift, increased right ventricle pre-load, and decreased right ventricle contractility, ultimately causing a decrease in the LVAD flow. When RVF emerges in the operating room, specific solutions, such as RVADs, BiVADs or TAHs, may be considered. The right ventricular stroke work index (RSWI) can be used to predict the likelihood of post-operative RVF from echocardiography results [94].

Another class of LVAD complications are the blood-related adverse events, also called hemocompatibility-related adverse events. In the context of LVADs, the term *hemocompatibility* generally refers to the clinical impact on blood of the biophysical interactions occurring at the device-blood interface [18]. Hemocompatibility-related adverse events are essentialy two:

- *Hemolysis*. It corresponds to the rupture of the red blood cells caused by intense stress conditions inside the blood pump. For instance, in CF rotary pumps high shear stress levels are generated by the impeller blades, especially at the tip and at the outer edge, where clearances are small and velocity is maximum [205]. The lysis of the erythrocytes' membrane leads to the release of the hemoglobin in plasma and, consequently, to poor oxygenation of the end-organ tissues. Large concentration of plasma-free hemoglobin can ultimately cause kydney dysfunction and multi-organ failure. While the physiologic range of stresses in the cardiovascular system is around 0.1-10 Pa [20], the reference thresholds found in literature for critical hemolysis are fixed at 150 Pa [160, 106] or 300 Pa [20]. Nonetheless, another essential factor for hemolysis mechanisms is the *exposure time* to stress. Indeed, it was shown that even peak stresses of 1000 Pa did not produce significant levels of hemolysis, provided that the exposure time was sufficiently short (*e.g.* below few milliseconds) [20]. Hemolysis incidence is around 10-18% in axial devices [241], while the employment of non-contact bearing technology had significantly reduced hemolysis rates in the third generation devices [205].

- *Pump thrombosis*. In the cardiovascular system, thrombosis represents the formation of clot (or thrombus) by platelets as part of the hemostatic mechanisms activated in case of vessel damage in order to prevent unnecessary bleeding. When these mechanisms are reproduced inside the pump chamber or in the LVAD cannulae, we refer to pump thrombosis. Pump thrombosis compromises the LVAD function and, in case of detachment from LVAD surfaces, the free thrombus can circulate in the blood stream and occlude a vessel (thromboembolism), potentially causing end-organ failure and death. Pump thrombosis originates from a complex and variegated set of biophisical processes, that are favored in regions with high shear stress, with flow recirculation or stasis, or at blood-contacting surfaces with low hemocompatibility. In particular, pump thrombi are divided in *red thrombi*, rich of erythrocites, that form in regions with flow stagnation, and *white thrombi*, rich of platelets, that are associated with turbolent flow [183]. The platelet potential for aggregation is thought to be activated at shear stress higher than 50 Pa [147, 106], while they tend to deposit in regions with low shear stress (*e.g.* below 0.1-1 Pa) [285]. Also, the Von Willebrand Factor protein, that mediates to platelet adhesion to pump walls, is activated at shear stress higher than 9-20 Pa [257, 106]. Pump thrombosis

has an incidence of 2-11% and requires LVAD replacement [94]. Continuous clinical monitoring together with an adequate anticoagulant therapy are fundamental to prevent pump thrombosis in CF devices.

Hemolysis and pump thrombosis are actually highly correlated and, for instance, pump thrombosis is monitored by controlling typical hemolysis biomarkers, such as plasma free hemoglobin concentration and haptoglobin [181].

Neurological LVAD-related adverse events include ischemic stroke, hemorrhagic stroke, transient ischemic attack. The INTERMACS annual report [165] indicates that the risk of stroke increases in case of prolonged term support, with an incidence of 7%, 11% and 17% at 6, 12 and 24 months, respectively. Another study showed that a systolic pressure higher than 100 mmHg is associated with a 2.5-fold higher risk of stroke, with an increase of 19% with every increment of 5 mmHg [183]. Analogously, the stroke risk significantly reduced when mean arterial pressure (MAP) was maintained below 90 mmHg [183].

Other adverse events to LVAD implantation are aortic regurgitation, ventricular arrhythmias, hyperthension, and device stoppage or malfunction [183, 94].
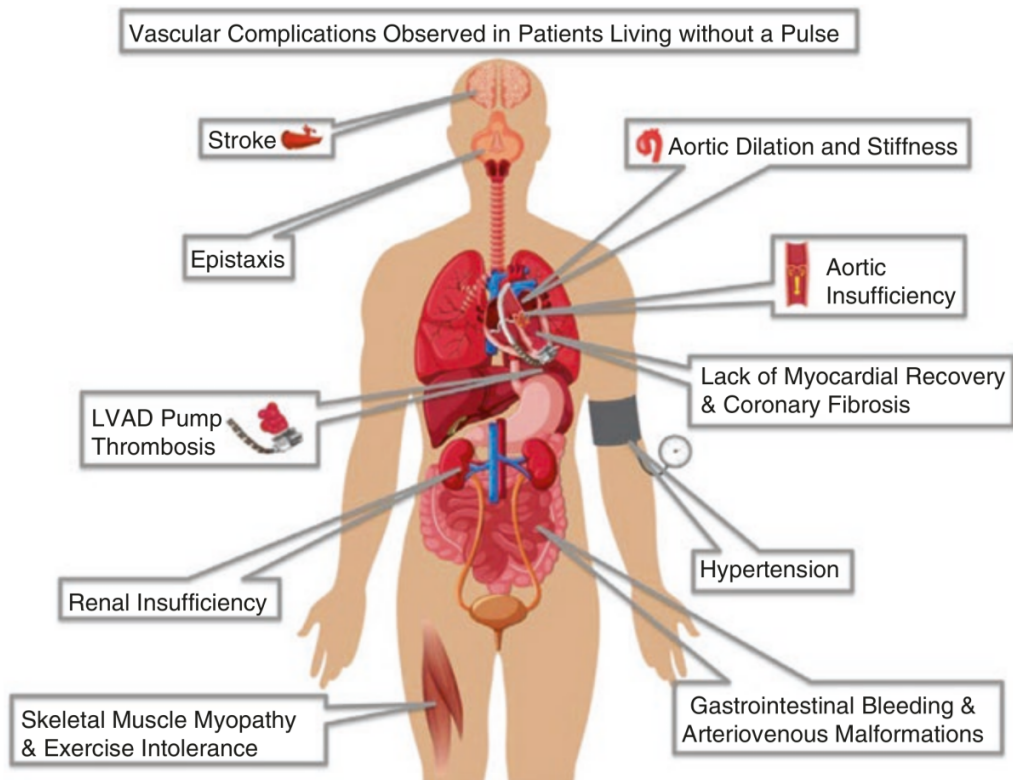

FIGURE 1.10: Potential vascular complications in patients with CF LVAD support. Figure taken from [39].

Thus, the control and the prevention of all such complications is very challenging in modern continuous-flow pump applications. Indeed, clinicians have to find the patient-specific optimal speed of rotation of the operating rotor: low velocity may result in continued HF, end-organ dysfunction, and pump thrombosis; while high speed can lead to hemolysis, right ventricle failure, ventricular arrhythmias, and

VWF syndome [94]. Furthermore, since most of these CF pumps are operated at a single fixed pump speed, their clinical use results in a reduction of patient pulse pressure, potentially favoring vascular complications [179], such as GI bleeding, pump thrombosis, aortic valve insufficiency and stroke (see Figure 1.10). In the recent years, LVAD companies have developed pulsation algorithms for rotary pumps, as for HeartMate III [7], with the aim of improving wash-out [18], but the LVAD pulsation algorithms currently used clinically do not restore a physiologic pulse [58]. Finally, current commercially available LVADs lack of systems for physiologic control to automatically adjust operating conditions depending on preload, afterload, intracardiac dynamics, or metabolic demands.

In the next generation of LVADs, hemocompatibility is thought to be the major way for improvement either by optimizing the pump design, as in EvaHeart 2 [313], or by proposing novel pulsatile flow mechanisms, as in TORVAD [126] and in WMBP [39]. Moreover, wireless solutions for LVAD functioning, with internal power source and a transdermic charging process, are under study, to significantly reduce the risk of infections [181].

1.3 Role of simulations in cardiovascular applications

1.3.1 Modeling approach in the cardiovascular system

Mathematical modeling and numerical simulations are valuable tools in the field of cardiovascular medicine, allowing to better understand the complex processes involved in cardiovascular diseases and support clinical decisions in treatments and surgical procedures [266, 238]. In particular, numerical simulations can represent for clinicians a non-invasive source of detailed quantitative information, that is complementary to the clinical data coming from medical imaging (*e.g.*, X-ray, computed tomography, magnetic resonance) and other diagnostic tests [238]. Indeed, a virtual representation of the blood dynamics in the heart or in a vessel, properly parametrized with respect to available patient data, allows to investigate potential critical regions characterized, *e.g.,* by high vorticity, turbolence, or anomalous wall shear stress [280]. Therefore, the numerical model can be a patient-specific predictive tool that can be employed to anticipate potential pathological conditions or optimize a personalized medical treatment [280].

Owing to the multiphysic and multiscale nature of the cardiovascular system, the related mathematical models are highly *coupled* and their solution can be very challenging. Typically, such coupled models are the result of the integration of multiple stand-alone core components that describe specific sub-parts of the system. For instance, modeling the blood dynamics in the arterial system requires to solve two sub-problems: the blood dynamics in the vessel (fluid sub-problem) and the deformations of the vessel itself (structure sub-problem). The coupling of these two sub-components rises from the mutual exchange of energy between the blood and the vessel wall at their interface: as the blood exerts pressure on the wall, the latter deforms due to the vessel compliance; as a consequence, the vessel accumulates

potential energy, that is then transmitted on the blood in the shape of kinetic energy [238]. Hence, this type of physical configuration can be mathematically described in the so-called *Fluid-Structure Interaction* (FSI) framework [149].

In cardiovascular FSI applications, blood is normally considered as a *Newtonian* fluid, i.e. with a linear relationship between internal forces and velocity gradients, even though it is well know that it displays some non-Newtonian properties (*e.g.*, shear-thinning viscosity, non-linear visco-elastic behavior of blood cell membranes, effect of aggregation and disaggregation of erythrocites, etc.) [283, 20]. Indeed, the non-Newtonian rheology of blood becomes relevant only in capillaries and smallest arteries [238], where the vessel diameter is similar to the size of the blood cells, or in low shear stress regimes (shear rate lower than 100 s^{-1}) [65, 2]. In other conditions, the Newtonian assumption is acceptable and the blood flow can be studied by means of the Navier-Stokes Equations. Instead, the vessel wall is generally modeled as an hyperelastic material, whose deformation depends on specific constituents such as collagen and elastin [153]. The blood velocity and pressure and the vessel deformations are finally coupled at the Fluid-Structure (FS) interface, where the continuity of the velocities (*kinematic coupling*) and of the normal stresses (*dynamic coupling*) is required [238, 31].

When we consider the heart function, the modeling process is even more complex due to the multiple intertwined physical processes that are involved in the cardiac system [266, 76]. Indeed, the mechanics of the myocardium, that guide the blood dynamics inside the heart chambers and its ejection throughout the body (fluid-structure coupling) [90, 201], derive from the electric stimulus along the cardiac tissue (electro-mechanic coupling) [244, 180], whose propagation depends itself on the spatial orientation of the cardiac cells (electrophysiology) [229, 306]. The combination of all these aspects lead to a Fluid-Structure-Electrophysiology Interaction (FSEI) model of the heart function [294]. In addition, a full model of the cardiac system should consider additional aspects such as the opening/closure dynamics of the heart valves [121, 111] and the perfusion of the heart itself [86, 219].

The numerical solution of such coupled systems can be particularly stiff, because the solution of the different sub-problems depend on each other. For instance, in the FSI cardiovascular problem described above, the displacement of the vessel changes the geometry of the fluid domain, while the blood stresses influence the vessel deformation, and viceversa. In hemodynamics, the numerical approaches for these coupled systems are either *partitioned* or *monolythical* [238]. In partitioned schemes [290], the fluid and structure sub-problems are solved separately, either in one step or iteratively. In fact, the physical coupling is relaxed so that the fluid-structure interface dynamics are splitted among the two problems and written in the form of suitable boundary conditions. Alternatively, the monolithic approach consists in directly solving the full coupled FSI problem, by applying an exact or inexact Newton method to the whole non-linear system [17]. The application of one method rather than the other depends on the specific problem at hand and on the computational framework at disposal.

For more details on cardiovascular mathematics, we refer the reader to [238].

1.3.2 Numerical simulations for cardiovascular medical devices

Computational simulations are playing an increasingly significant role in the industrial process for the development of biomedical devices, supporting the engineers in the optimization of device performance and reliability. Indeed, the *in-silico* approach represents a low-cost and less time-consuming alternative to *in-vitro* or *in-vivo* testings, which allows to predict device behavior under a variety of clinical conditions and consequently reduce the risks of device implantantion and failure. In this way, medical companies can integrate the input from simulations to shorten the process for regulatory approval and meet safety requirements, to eventually bring faster new treatments to patients.

In the following, we illustrate few examples of medical devices for cardiovascular medicine, whose development or implantation got benefit from the computational simulations.

Cardiac Resynchronization Therapy (CRT) is an established therapy for patients with moderate or severe HF with reduced ejection fraction (HFrEF) that present intra- and/or inter-ventricular conduction delay. The goal of CRT is to stimulate both the right and left ventricles by means of a *biventricular pacemaker*, to reduce the conduction delay and, ultimately, resynchronize the contraction between and within heart ventricles. However, recent studies highlighted that 40–50% of patients do not respond to CRT [171, 130] and that an effective reduction of conduction delay could be achieved only provided that the pacing protocol is well calibrated on the specific patient [83]. In this context, patient-specific simulations of the cardiac electromechanics coupled with a pacemaker model have shown to be useful tools for physicians to predict the patient response to CRT [212] and study the optimal device placement and settings [171].

The *Transcatheter Aortic Valve* (TAV) is a biological prosthesis that replaces the native aortic valve in patients with high-risk valve diseases. It is well known that the prosthesis positioning is the most indicative factor for possible complications, like paravalvular leaking or valve regurgitation [92]. However, clinicians cannot easily predict the optimal placement, due to the large inter-patient geometric variability and to the frequent presence of calcium deposits in pathological valves [186, 248]. Thus, having the possibility to virtually reproduce in specific patients the phases of TAV implantation allows to optimize device selection and implantation strategy in order to improve valve performance and ensure long-time durability [209, 28, 274, 55]. Among all, FSI simulations, which capture the mutual interaction between the the leaflets and the blood flow, ermeged to be the best numerical approach for such problems, because they give the opportunity to study both the loading on the valve leaflets as well as the variation of the flow patterns in the aortic root induced by the transcatheter valve [186, 185, 309, 19].

Stenosis is a common cardiovascular disease consisting in the narrowing of the lumen of the vessel due to the accumulation of fatty material such as cholesterol. In case of occlusion of coronary arteries, *Coronary Arterial Bypass Graft* (CABG) can be used to restore regular perfusion conditions by creating a new flow path around the stenoted coronary tract. Simulating the local hemodynamics can help to optimize the grafting

configuration so that critical factors, like flow vorticity and wall shear stress rate, are minimized and post-operative recurrence of the stenosis is avoided [237, 168]. Recent works [15, 16] showed that this kind of study can be made patient-specific without loss of efficiency, reconstructing the specific geometry via medical imaging and using POD-Galerkin reduced-order methods to decrease the computational cost of the simulation.

A last example is represented by the many numerical studies about *stent devices* and their medical applications. Stents, tipically applied in case of artery stenosis, are small mesh tubes made of plastic or metal, which are permanently inserted in the lumen of pathological vessels and inflated to reinstate regular physiological conditions. In most severe cases, *Drug-Eluting Stents* (DES) are employed to prevent potential reoccurence of stenosis by locally releasing a drug which chemically blocks restenosis processes. However, since the collection of clinical evidences of DES performance can be very expansive and poor, numerical simulations are valuable alternative tools to investigate the mechanics, the fluid dynamics and the pharmacodynamic processes involved in the device action and optimize the stent design accordingly [14, 292, 81].

1.3.3 State of the art of numerical studies in LVAD applications

In the field of LVAD development, numerical simulations play a major role in the design cycle, thanks to their ability to predict the device performance in terms of both hydraulic output and hemocompatibility. Indeed, the *in-silico* approach enables important functionalities for the LVAD development, such as agile testing of the pump designs, in-depth insight in the flow field, and prediction of the potential LVAD complications. Over time, numerical simulations emerged to be more time- and cost-effective than many *in-vitro* or *in-vivo* testings, overcoming a plurality of limitations in prototype building and experimental setup [20, 21]. For instance, Computational Fluid Dynamics (CFD) simulations allow to predict critical features within the flow field, like regions with flow recirculation or high shear stress, that may be difficult to detect experimentally in physical testings. These are typical factors that can cause energy losses and favor blood-related adverse events, like hemolysis and thrombosis. Thus, the LVAD development team can take advantage of the valuable information coming from simulation results to predict undesired dynamics and prevent them by properly adjusting the design of the pump.

More specifically, we can identify three main purposes of CFD modeling of LVAD:

1. predict the pressure vs. flow performance and the hydraulic efficiency of an LVAD for a specific design, to avoid potentially high costs for manufacturing (Sect. 1.3.3.1);

2. estimate the potential of hemolysis or pump thrombosis (Sect. 1.3.3.2);

3. optimize device design, operation or implantation, with respect to indices characterizing the pump hydraulic performance and/or hemocompatibility (Sect. 1.3.3.3).

1.3.3.1 Predicting hydraulic performance

The prediction of the hydraulic performance of the LVADs is one of the main advantages of numerical simulations, especially in the early phases of the development, because it allows virtual testing of new designs for a wide range of operating conditions, without need of fabricating the physical prototype [107].

The hydraulic performance of blood pumps is typically assessed by looking at two factors:

i. the *pump characteristic curves*, which represent the relationship between head pressure H and pump flow rate Q at fixed operating conditions (*e.g.*, at constant speed of rotation in a rotary blood pump). Such curves, also commonly called *HQ curves*, are used to determine the hemodynamic interaction of the device with the heart, because they describe the LVAD response to changes in pressure conditions at the pump outlet (after-load) or inlet (pre-load), potentially experienced during the cardiac cycle [131].

ii. the *hydraulic efficiency*, that corresponds to the ratio between the output power and the input power. For instance, in case of rotary blood pumps, the efficiency η is computed as:

$$\eta = \frac{W}{\mathbf{T} \cdot \omega} \tag{1.1}$$

where $W = H\,Q$ is the hydraulic power, while $\mathbf{T}$ and ω are the rotor torque and angular frequency, respectively. In case of small values of hydraulic efficiency, the energy is dissipated in vortical structures or backflows that penalize the device performance and durability, and thus the design should be reviewed. Although rotary pumps are usually very efficient ($\eta > 90\%$) in many industrial scenarios, the adaptations to their design for blood applications (*e.g.* smaller size for better implantation, larger gaps to reduce hemolysis, etc.) lead to an increase in friction losses and lower efficiency [267]. Hence, it was found that in most VADs the best values of hydraulic efficiency range from 40% to 70% [131].

In particular, the shape of the pump characteristic curve represents a fundamental design goal during the design process of a blood pump. Indeed, HQ curves are divided in two groups: *steep HQ curves*, with low pressure sensitivity, and *flat HQ curves*, with high pressure sensitivity. Figure 1.11 reports the examples of a steep HQ curve from the HeartMate II axial pump (left) and a flat HQ curve from the HVAD centrifugal pump (right). We remind the reader that in pump systems, since the head pressure corresponds to the adverse pressure difference between at the pump outlet or inlet, the generated flow must decrease as the head pressure increases. Specifically, steep HQ curves are more stable with respect to pre-load or after-load pressure perturbations, but span a smaller range of flow rates. Hence, the rotational speed of the impeller has to be actively increased to obtain a significant flow augmentation. Active physiologic speed control algorithms have been proposed by many authors [205, 133], but not transferred to clinical practice yet. On the contrary, flat HQ curves show high variations in pump flow to small changes of pump pressures. This behavior results in a passive adaptation of the flow output to the possible variations

in arterial or systemic circulation (passive control mechanism) [131] and in a higher
flow pulsatility [205], similarly to the way the native ventricle normally works. As a
consequence, the HQ curves provide also relevant information about the likelihood of
suction events or hyperthension [205, 133]. Previous work from Graefe et al. [131]
indicated that the pump characteristic curve can switch from steep to flat, depending
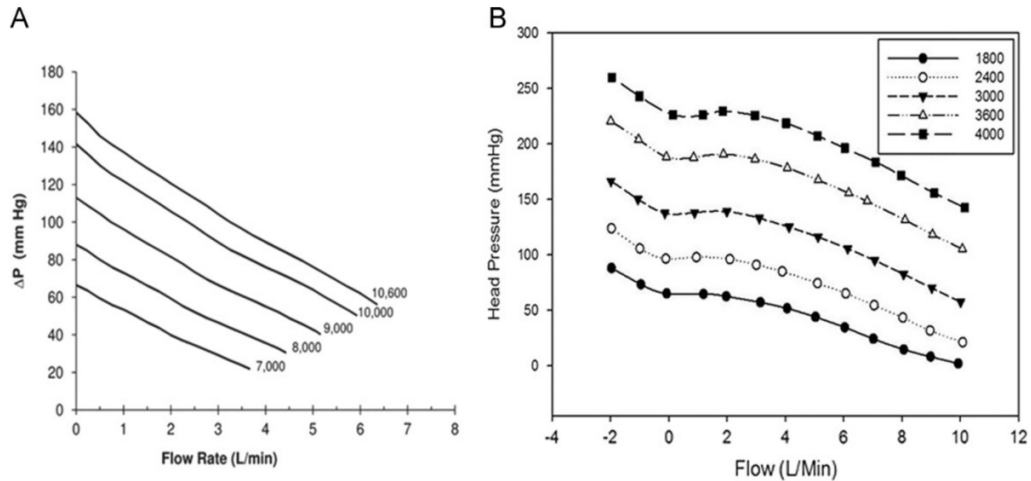on the design of the flow-guiding structures, such as the blades of the rotor.

FIGURE 1.11: Characteristic pump HQ curves of axial flow pump HeartMate II (left) and
centrifugal flow pump HVAD (right). Figure taken from [205].

In many computational studies [217, 62, 225], characteristic pump curves can play an
important role in the parametrization and the validation of the numerical approach.
Indeed, once the device is already fabricated, HQ curves are typically derived experi-
mentally by *in-vitro* testings, by exposing the device to different hydraulic resistances
and measuring the generated flow rate. In most cases, this is done in a *Mock circu-
latory loop*, a flow-loop system made of tubes and reservoires that is constructed to
mimic the human circulatory conditions.

In view of the model validation, the experimental HQ data curves can be compared
with the simulation results obtained at analogous hydraulic conditions, in order to
check that the numerical model reproduces well the pressure sensitivity of the device.
Such validation approach is represented in Figure 1.12, where the experimental and
CFD results are plotted together with a hdyraulic efficiency map, for the optimized
axial Streamline pump studied in [49]. A further example of model validation is
represented by [262], where they compared the numerical HQ results for different
turbolence models with experimental data and found out that the Stress-Blended
Eddy Simulation (SBES) turbulence model was more accurate than the standard k-ω
turbulence model. However, other authors [287, 275] suggest to additionally check
the velocity distribution by means of *particle image velocimetry*, by looking at the
flow field profiles in specific pump areas, such as at the entrance of the inlet or at the
leading edge of the spinning blades.

Although CFD simulations are excellent tools to predict hydraulic performance and
provide in-depth insight on the internal flow dynamics, they are also characterized by
high computational cost and simulations can last for long time in complex scenarios.
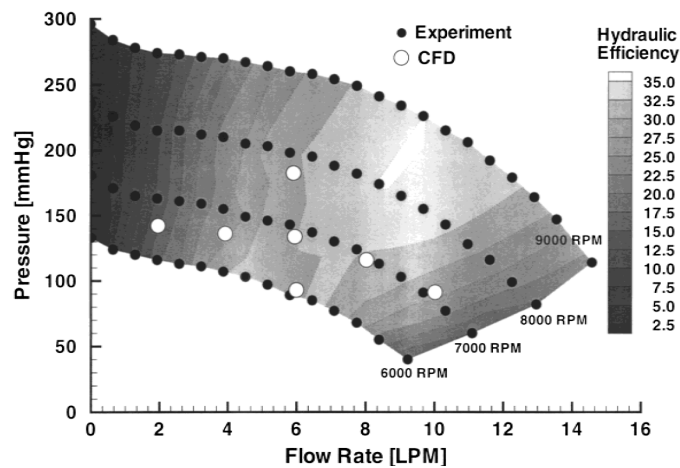However, in such cases, there exists an alternative computational approach based on

FIGURE 1.12: Plot of HQ experimental curves for different rotational speeds and CFD results from [49], with additional hydraulic efficiency indication.

lumped parameter models [300, 132] that are able to rapidly provide quantitative input-output information of the pump performance for different operating conditions. For instance, the computational cardiorespiratory simulator coupled with an LVAD model, proposed by Fresiello et al. [108], was used to test LVADs performance during physical exercise [132].

1.3.3.2 Modeling approach for hemocompatibility

Computational simulations enable also mathematical estimates of the blood damage generated in the blood pumps, in order to assess device hemocompatibility. As explained in Section 1.2.4, the main issues that undermine LVAD hemocompatibility are hemolysis and in-pump thrombosis, that are both linked to unphysiological hemodynamic-generated stresses in the flow field. As a matter of fact, the complex processes that cause blood damage are not fully understood and nowadays there are no established methods to obtain reliable and accurate evaluations of hemolysis or thrombosis in large-scale flows [131]. This is also partially due to the very high computational cost of simulating the effect of blood flow on the singles blood cells. Nonetheless, there exist alternative approaches that may be sub-optimal in evaluation accuracy, but that can provide valuable information on blood damage at manageble computational cost.

Hemolysis, corresponding to the rupture of the red blood cells, is the results of prolonged exposition of erythocites to extremely high stresses. This eventually leads to the release of hemoglobin in plasma and to a shorter lifetime of the erythrocytes. The ratio of plasma-free hemoglobin to the total hemoglobin defines the *Index of Hemolysis* (IH). A more clinically acceptable value is the *Normalized Index of Hemolysis* (NIH), that is calculated as

$$NIH = IH\,(1 - Hct)\,\kappa, \tag{1.2}$$

where *Hct* is the hematocrit, equal to 45% in physiologic condition, and κ is the hemoglobin content of blood, equal to 150 g/l in a healthy person.

It has been shown that the index of hemolysis is highly correlated with two main factors: the fluid stress σ_s and the exposure time to stress τ_s [29, 278]. Thus, a first investigation on the hemolysis risk in a blood pump can be directly carried over by deriving related quantities from the flow results of CFD simulations. The stress conditions in the pump can be analyzed by computing the maximum and the volumetric distribution of a suitable scalar representation σ_s of the instantaneous fluid stress tensor. In most numerical studies, this stress value, that should include both shear and extensional components [89], corresponds either to the fluid stress rate [223, 12] or to a measure of the internal structure stresses (via the so-called *Von Mises stress*) [30, 20, 106, 174]. Although there is no consensus in the LVAD community for a unique reference value, the standard critical threshold of blood stress for hemolysis ranges from 100 to 650 Pa [106, 127, 245]. Furthermore, some works [106, 223] proposed to estimate the residence time of blood cells, as surrogate quantity to exposure time τ_s, as the ratio between flow rate and the pump flow volume. However, this CFD-based approach is not exhaustive because blood trauma is related to the combination of these two quantities (that should not be studied independently) and to the stress history, i.e. the accumulated damage of the red blood cells during their transition through the pump [12, 20].

Empirical studies [29, 89, 278] indicated that the index of hemolysis *IH* can be predicted using a power law distribution, based on stress σ_s and exposure time τ_s:

$$IH = C\,\sigma_s^a\tau_s^b, \tag{1.3}$$

with *C*, *a* and *b* being constant parameters. For instance, the empirical values proposed by Taskin et al. [278], which minimized the difference against numerical results, were $C = 1.21 \cdot 10^{-5}$, $a = 2.004$ and $b = 0.747$.

Stress-based hemolysis models [223] can be derived by integrating in Eq. (1.3) in time and space the power law, with the scalar stress σ_s defined with respect to the *intantaneous shear rate G_f* as

$$\sigma_s = \mu_f\,G_f. \tag{1.4}$$

In the integration process, there are two different approaches, the Eulerian and the Lagrangian approach. In the former case, a convection-diffusion-reaction equation is solved to compute a linearized version of *IH* as a variable field in the flow domain; in the latter case, *IH* is integrated along simulated trajectories of particles passing from pump inlet to pump outlet. In principle, since it takes into account the stress history, the Lagrangian approach is preferred to the Eulerian one, provided that the number of valid pathlines is sufficiently high to span almost all pump domain [12, 106]. However, this method is computationally very expensive, while the Eulerian approach is more practicable and automatically computes the hemolysis index in the whole domain [279, 131].
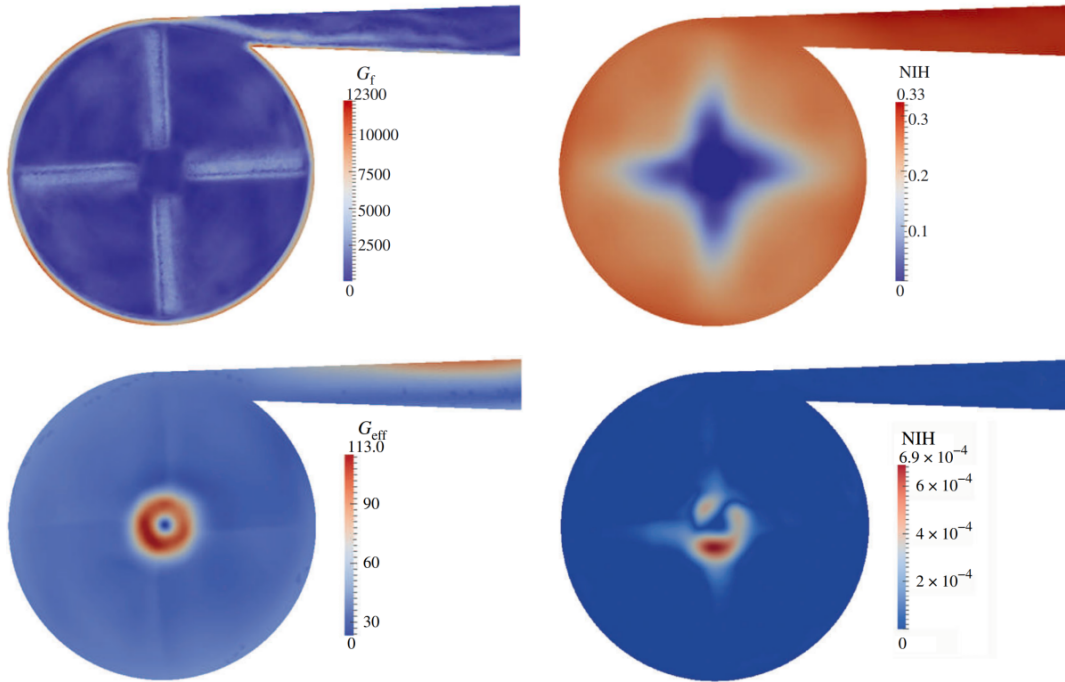
FIGURE 1.13: Shear rate and Normalized Index of Hemolysis in a simplified centrifugal blood pump domain using stress-based model (above) and strain-based model (below). Results are taken from computational work [223].

However, stress-based models rely on the assumption that the stress causes an instantenous deformation on the target red blood cells, that actually violates the viscoelastic nature of these cells [223, 296, 139]. Therefore, a more advanced hemolysis model is the *strain-based hemolysis model* [12, 20, 117], that considers actual cell deformation and cell aging. In this approach, the *effective shear rate* considers the viscoelastic deformation of the erythrocites, that are assumed to behave as droplets in high shear flow [13]. Hence, denoting by G_{eff} the effective shear rate, in strain-based models the scalar stress σ_s is computed as

$$\sigma_s = \mu_f \, G_{eff} = \mu_f \, \frac{2 \, f_1 \, D}{f_2 \, \left(1 - D^2\right)}, \qquad (1.5)$$

where μ_f is the blood viscosity, D is a geometric measure of droplet distortion, and f_1 and f_2 are experimentally-based constants [12].

Results of stress-based and strain-based hemolysis models can differ significantly. For example, a comparative study in a centrifugal blood pump [223] highlighted that stress-based hemolysis generally overestimates the blood damage. Indeed, at flow rate of 5 l/min, the maximum NIH is equal to 0.33 g/l when the instantaneous shear rate is considered, while it amounts to just 0.00069 g/l when the effective shear rate is adopted (see Figure 1.13). Moreover, the distribution of IH is also very different: in the stress-based model, the highest damage is located at the circumference of the pump chamber, where there are peaks of velocity and stress, even though for very short exposure times; instead, in the strain-based model, hemolysis index is higher at the center, where the angular velocity is lower, but the exposure time is much longer [223].

Although pump thrombosis is considered a more severe LVAD adverse event than hemolysis, because it can lead to stroke, pump-replacement surgery or, in case of thromboembolism, to sudden death, there are still many open questions about thrombogenicity and few established numerical methods to predict pump thrombosis [131]. Indeed, thrombosis is a complex phenomenon, that is still not completely understoood, in which a combination of interrelated biochemical and hemodynamic factors result in several cascade reactions causing platelet activation, deposition, aggregation, and stabilization [311]. In addition, experimental data on thrombus formation and deposition are very challenging, both in *in-vitro* and *in-vivo* testings [131]. Nevertheless, it is thought that the relation between flow patterns and thrombogenicity is the following: the potential for thrombus formation (Von Willebrand factor degradation, platelets activation, thrombin and fibrine production, etc.) is triggered in flow regions with high shear stress and long exposure time (as for hemolysis), while thrombus aggregation and deposition tend to occur in low shear and stagnation areas, on blood contacting surfaces with low hemocompatibility [20, 257, 235, 261].

Thus, numerical simulations recently emerged to be a promising approach to improve device thromboresistance by means of tailored design optimization. Several CFD studies [282, 178] aimed at identifying regions for potential thrombosis adhesion with locally stagnant flow and low stresses and compared the numerical results with experimental measurements. As for hemolysis, both Eulerian and Lagrangian approaches are possible to analyze the residence time within the pump [95, 208] and the pump design can be updated accordingly to maximize LVAD washout [192]. In particular, Girdhar et al. [123] introduced a new methodology, called *Device Thrombogenicity Emulation* (DTE), that combines *in-silico* and *in-vitro* approaches to optimize antithrombotic LVAD performance.

Modeling of thrombus formation and deposition mostly developed in simple scenarios. For instance: Wu et al. [312] numerically studied the Von Willebrand factor (VWF)-mediated platelet shear activation and deposition in an idealized stenosis; Osuna et al. [216] specifically studied the role of erythocites-thrombocites interactions in platelets margination and activation in the LVAD ouflow graft and in the aortic arch region; Goodman et al. [128] predicted thrombus growth and thromboembolizaton in low-shear devices, like hemodialyzers or blood oxygeneators. Such models are typically based on a system of coupled convection-diffusion reaction equations, that describe multiple biochemical processes to predict velocities, concentrations of thrombus agents, VWF and platelet activation rates, platelet transport and deposition. In these CFD studies, blood is treated as a mixture comprised of a fluid component and a porous solid component representing the growing thrombus. In particular, Antaki et al. [311, 310] applied an Eulerian approach for the first time in a real LVAD, the axial HeartMate II, to study specifically the processes of thrombus initiation, propagation, and stabilization. The patterns of deposition predicted with such model agreed well with the clinical observations [310].

1.3.3.3 CFD-based LVAD optimization

Starting in the 1990s with the first numerical studies carried out in simplified pump models [221, 230], CFD modeling has had an increasing impact in the development

process of rotary blood pumps, primarily in view of the optimization of the device design. Indeed, it has been estimated that the CFD-based design approach shortened the overall design time frame from an order of years to months [49]. Nevertheless, the optimization process of LVADs design can be very challenging because it can address multiple interdependent geometric parameters. In rotary blood pumps, the geometric features of interest can refer to the pump impeller, comprising its rotating blades, the rotor-bearing system, or the inflow and outflow grafts. Moreover, the optimization process is typically driven by multiple objective functions, often competing against each other, that address both the hydraulic performance and the hemocompatibility of the device. Notice that at the same time the variations of the geometric parameters has to be compliant with size constraints, that guarantee device miniaturization to facilitate device implantation.

The core of rotary blood pumps is the impeller, that converts mechanical power into hydraulic power, resulting in an increase in flow and head pressure. It is well known that the rotor spins at elevated velocities, that expose blood to non-physiologic shear stresses. For this reason, many numerical studies aimed at the optimization of geometric features of the impeller to improve hemocompatibility without losses in hydraulic performance. Among these works, we mention the following ones: Wiegmann et al. [303], Ozturk et al. [217], and Kannojiya et al. [160] investigated the influence of several design parameters (*e.g.* number of blades, blade width, blade angle, clearance gap, housing configuration) on the hemocompatibility of a centrifugal pump, looking at maximum stress, volumetric stress distribution, flow recirculations, and hemolysis index; Liu et al. [177] specifically studied the effect of the gap between the rotor blades and the housing of an axial pump, that has shown to highly influence local maximum velocity, shear stress, and exposure time; Wu et al. [308] proposed the introduction of a set of secondary blades located along the back of the rotor of miniature centrifugal blood pump intended for pediatric use, to reduce the retrograde flow in the back clearance gap; Fraser et al. [105] studied the effect of the impeller axial position in a magnetically levitated blood pump; and, finally, Ghadimi et al. [119] performed a shape optimization study on HeartMate III, by varying geometrical features such as inlet and outlet radius, blade angle distribution, or volute cross-section area distribution.

An innovative study from Girdhar et al. [123] performed a design optimization process driven exclusively by the maximization of the device thromboresistance. The authors used the Device Thrombogenicity Emulation (DTE) strategy that combines numerical simulations with experimental measurements by correlating the predicted hemodynamics with platelet activity coagulation markers. In a Lagrangian-based approach, the predicted cumulative stress was computed along many platelet trajectories and the related probability density function was derived to represent the 'thrombogenic footprint' of the device. Starting from the design of DeBakey LVAD, an iterative procedure finally led to an optimized antithrombotic design, called HeartAssist 5 LVAD, that minimized stress accumulation (see Figure 1.14). The platelet activity in HeartAssist 5 LVAD was found to be an order of magnitude lower than in initial DeBakey design, proving the potential of the novel DTE approach in reducing device thrombogenicity.

Other works focused specifically on the design of the rotor-bearing system. Second
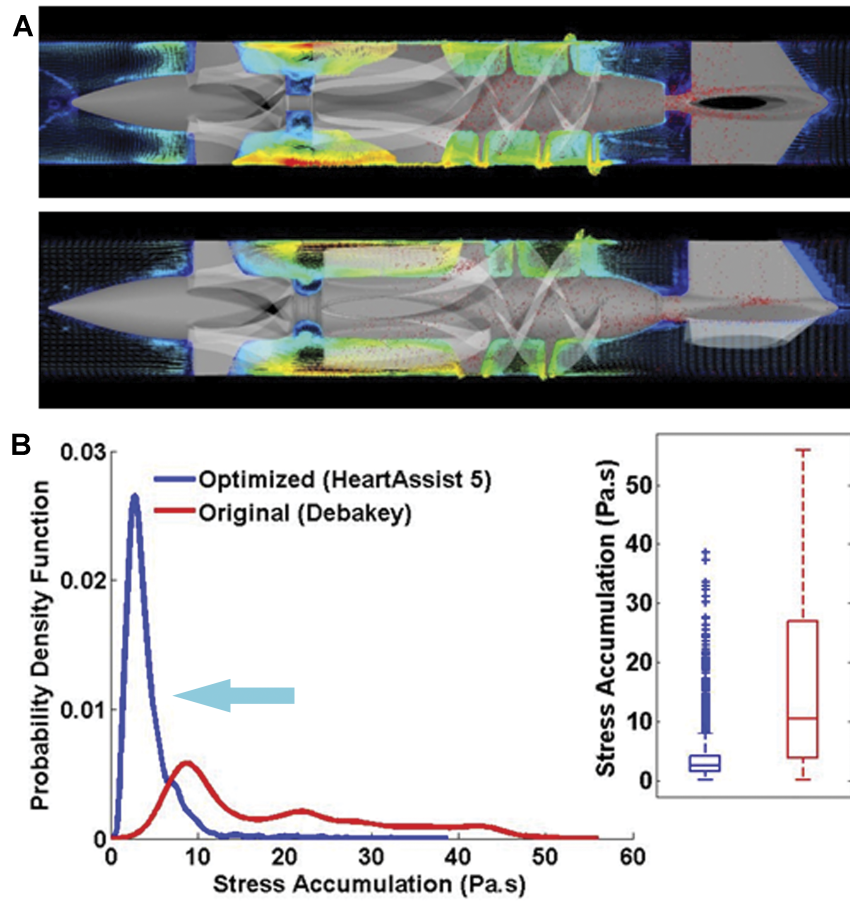
FIGURE 1.14: Comparative results of cumulative stress in DeBakey LVAD and DTE-optimized HeartAssist 5 LVAD. Figure taken from [123].

generation LVADs (typically axial rotary pumps) use contact bearings to balance the hydraulic load on the rotor, that may be due either axial or radial forces or to tilting. In third generation devices (typically centrifugal rotary pumps), a contactless bearing system is preferred and the hydraulic load is compensated by hydro-dynamic or magnetic bearing components. CFD modeling was a crucial tool to guide the transition from second to third generation LVADs. Burgreen et al. [49] studied a novel axial flow blood pump equipped with a magnetically suspended rotor. The main goal of the study consisted in improving hemocompatibility of blood-contacting surfaces, considering both insight on shear-induced hemolysis as well as surrogate functions describing thrombosis potential. The CFD-based design strategy involved closely coupling a Navier-Stokes solver to a parameterized geometry modeler and advanced mesh movement techniques. Song et al. [270] extended this study by analyzing the hydraulic loads under highly transient conditions. Indeed, the axial force on the rotor was estimated to vary from 3.5 to 5.5 N during the heartbeat [131]. A similar analysis has been subsequently carried over in centrifugal blood pumps by Salvatori and Della Gatta [249], who additionally discussed the effect of leakage flow, operating mode and wear conditions on axial thrust.

In addition to design optimization, another goal of numerical studies in LVAD systems is to investigate the interplay between the operation of modern continuous-flow

devices with the pulsatile-based cardiovascular system. A comparative study from Chen et al [62] analyzed the performance of four clinical CF VADs, two axial pumps and two centrifugal pumps, under clinically relevant pulsatile flow conditions. The axial VADs showed higher mean wall shear stress and scalar stress, but the residence time of the centrifugal VADs was much longer because of the larger volume of their pump chamber. At fixed pump speed, the hemolysis index was greater at low flow rate, due to longer exposure time to shear stress compared with at high flow rate. Scardulla et al. [255] performed patient-specific CFD simulations in the main arteries of the gastro-intestinal tract of LVAD patients, to study the hemodynamic alterations due to continuous-flow support in terms of wall shear stress and predict the potential of vessel bleeding.

Pulsation algorithms in CF LVADs, based on the modulation of rotor speed during the cardiac cycle, have been proposed and implemented clinically to improve vascular pulsatility and reduce related adverse events. However, computational studies addressed this specific topic to better understand the effectiveness of these algorithms in recreating artificial pulse. For instance, Liu et al. [179] developed a simulation platform for testing the effects of different speed patterns of CF LVADs on the ventricle and vascular system. The results showed that an asynchronous pattern effectively increased the vascular pulsatility, but a synchronous counterpulsation pattern reduced ventricular unloading and presented more physiologic hemodynamics. In another study from Chen et al. [63], an asynchronous pulsation algorithm was tested in the HVAD in relation to the potential variations in device hemocompatibility. The numerical outcomes did not highlight any differences in the time average hemolysis index with and without rotor speed modulation, indicating that HVAD in asynchronous mode is able to restore native pulsatility without any further increase of blood damage. Also HeartMate III operation was numerically studied in continuous and Artifical Pulse (AP) mode by Grinstein et al. [138]. The patient-specific simulations, obtained by the coupling with a lumped parameter model for the systemic circulation, showed that the AP modulation allowed to reach a peak flow rate of 9.84 $^l/_{min}$, but the overall cardiac output was 5.96 $^l/_{min}$, similarly to the one achieved in continuous mode. In addition, the AP mode significantly reduced blood stagnation in the ascending aorta: 48% of the blood was flushed out from the ascending aorta in continuous mode, while 60% was flushed under AP operation.

In conclusion, we mention the numerical studies that addressed the optimal implantation of LVADs, with the aim to reduce surgery and post-surgery complications. In particular, some computational works studied the influence of the position of the inflow cannula with the risk of blood stagnation and thrombosis, specifically considering the angulation of the cannula [1] or the implantation site [120]. Other studies focused on the anastomosis between the outflow cannula and the aorta. In particular, Prather et al. [235, 236] performed numerical FSI simulations coupled with Lagrangian particle tracking algorithm, to finally propose to adjust the LVAD outflow cannula to direct potential thrombi away from cerebral vessels. This type of approach has been estimated to reduce the risk of stroke by 50% [215]. Finally, Bonnemain et al. investigated the different effects of the cannulations in the ascending or descending aorta on the systemic circulation, using a 1D network [35], and on the local blood dynamics in the aortic arch, using a coupled 3D-1D model [34].

Chapter 2

Wave Membrane Blood Pumps

2.1 The partner LVAD company

The partner LVAD company of the project is a high-growth medtech company located in Clichy, France. Founded in 2012, it counts nowadays more than 50 employees, including experts in fluid mechanics, biology, electronics, mechanical engineering and manufacturing. Since its creation, the company has raised more than 80 million euros in funding, received numerous awards, and in 2021 it became part of the *French Tech 120 index*, a selection of 120 French startups with the potential to become global technology leaders in their sectors.

Its industrial activity involves the development of new mechanical circulatory support (MCS) technologies for a large spectrum of heart failure patients, based on a novel membrane-based pumping concept. The basic principle was inspired on the *vibrating membrane fluid circulator* proposed by Drevet in 2003 [91] and subsequently employed for general pumping applications at AMS R&D (France). The final aim is to employ a similar wave pumping technology (exclusive license agreement with AMS R&D in 2012) in the context of implantable left ventricular assist devices (LVADs), to overcome the limitations in hemocompatibility and pulsatility of state-of-the-art MCS devices.

The innovative pumping technology studied at the company was applied on the *Wave Membrane Blood Pumps* [38, 231], or WMBPs, patented in 2018 in the United States. A photograph of the main components of the physical device is reported in Figure 2.1, left, where the core component in white with the central hole is the elastic membrane and the two metal parts form the pump housing. WMBP is thought to present important advantages in terms of performance, size and costs, with respect to the competitors currently active in the fast-growing market of cardiac assist devices. Nonetheless, it is still not commercially available and the design of the pump is not completely finalized.

As a consequence, the R&D department of the LVAD company continuously aims at improving the performance of the pump, both in terms of hydraulic efficiency and hemocompatibility. *In-vitro* testings are frequently performed to assess the performance of WMBPs for different operating conditions of the device. There is a plurality of pump characterization benches available at the company, including the Mock circulatory loop (see Figure 2.1, right), for hydraulic and blood tests. Numerical
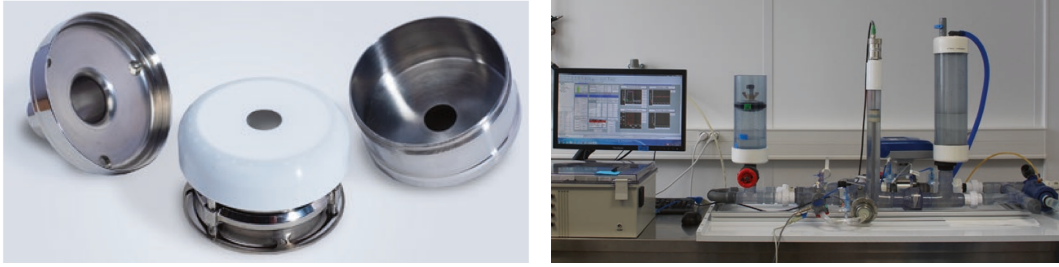
FIGURE 2.1: Photographs of the partially disassembled WMBP (left) and of the Mock circulatory loop used at the partner company (right). Pictures taken from [39].

simulations are typically performed in commercial software packages, like COMSOL, ANSYS Fluent and ADINA, to predict the behavior of the membrane or of the pump actuator and test potential alternative pump designs. In most cases, in order to save computational time, 2D axi-symmetric simulations are performed, taking advantage of the overall cilindrical symmetry of the device. Recently, very promising outomes in *in-vivo* implants of WMBPs have been achieved for long-term support in healthy sheep and for short-term support in sheep with ischemia-induced heart failure [36]. Hence, the partner company is currently finalizing the clinical system, by optimizing device durability, implantation and pulsation control algorithms, before moving to European clinical trials to obtain the Conformitè Europëenne (CE) marking [39, 36].

2.2 A new LVAD: Wave Membrane Blood Pump

2.2.1 A biomimetic membrane-based technology

Wave Membrane Blood Pump is an implantable pump that employs a new pumping mechanism based on the interaction of the blood flow with an undulating elastic membrane, resulting in forward propulsion of blood. Such membrane-based technology is said to be *biomimetic*, because it is inspired by the undulating motion of the tail of marine animals: indeed, the oscillations induced on the polymer membrane reproduce the swimming mode of most of fishes and marine mammals. However, the fluid-structure interaction mechanics are reversed: while marine animals propel themselves through water, in WMBPs the membrane is fixed at one end and propels blood towards the outlet. Being an LVAD application, the membrane has to overcome the adverse pressure difference existing between the left ventricle (inlet port) and the aorta (outlet port) of a failed heart. The blood flow path of a failed heart with WMBP support is depicted in Figure 2.2.

2.2.2 Device structure

The structure of the implantable WMBP, shown in Figure 2.3, can be divided in two main parts: the pump housing and the pump chamber.
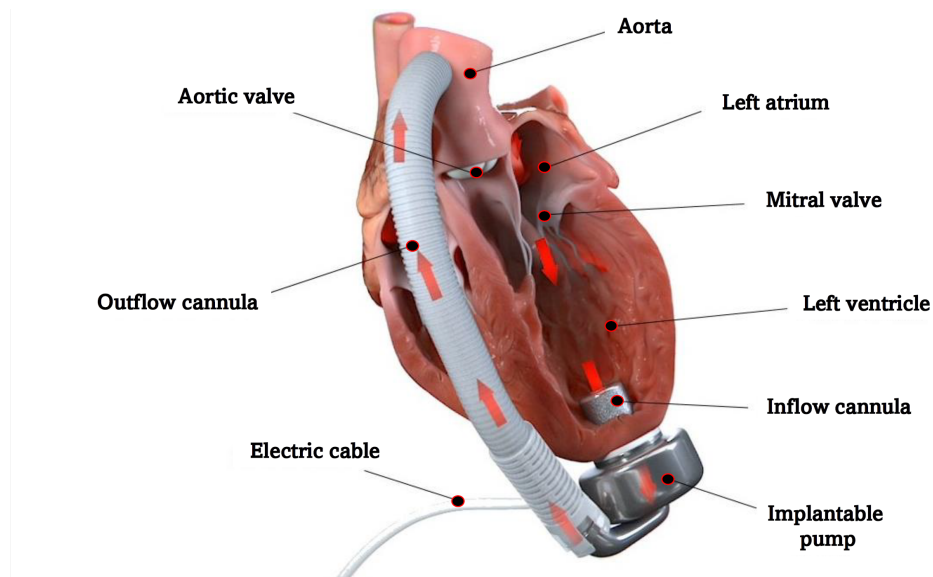
FIGURE 2.2: Representation of the implantable WMBP.

The pump housing, made of a biocompatible material (such as titanium), includes an *inflow cannula*, implanted at the apex of the left ventricle, and an *outflow cannula*, placed at the opposite side of the device and in fluid communication with the ascending aorta via an outflow graft.

The pump chamber has a cylindrical body (volume ~ 75 cm^3) and comprises:

- an *electro-magnetic actuator system*. The actuator sytem, located at the center of the pump chamber, is composed of a stationary part, consisting in the central stator and the electromagnetic coils, and a mobile part, corresponding to a *magnet ring*, which is suspended concentrically around the stator. The stator supports the whole apparatus, being connected with the pump housing via a fixation ring, and it hosts the electromagnet. The magnet ring is supposed to reciprocate the magnetic field generated by the actuator coils, moving rigidly up and down along the stator. A set of thin *suspension rings*, or spring rings, may be placed above and under the magnetic ring, in order to exert an elastic resistance to any radial deflections of the magnet to enforce an axially-constrained displacement.

- a *membrane assembly*. It is suspended within the flow channel, displaced concentrically along the pump longitudinal axis. The membrane assembly includes two different components: a rigid *membrane holder* and an elastomeric *wave membrane*. The membrane holder, located at the outer side of the membrane assembly, is directly connected with the magnet ring via a plurality of titanium posts. The flexible *wave membrane* is a discoidal elastic body along which the deformation waves can propagate from the membrane holder towards the outlet cannula. At the center, the wave membrane presents a circular orifice in proximity to the outlet channel.

Thus, the blood flow enters through the inlet cannula into the pump chamber, it flows around the actuator and then along the sides of the membrane holder, until reaching
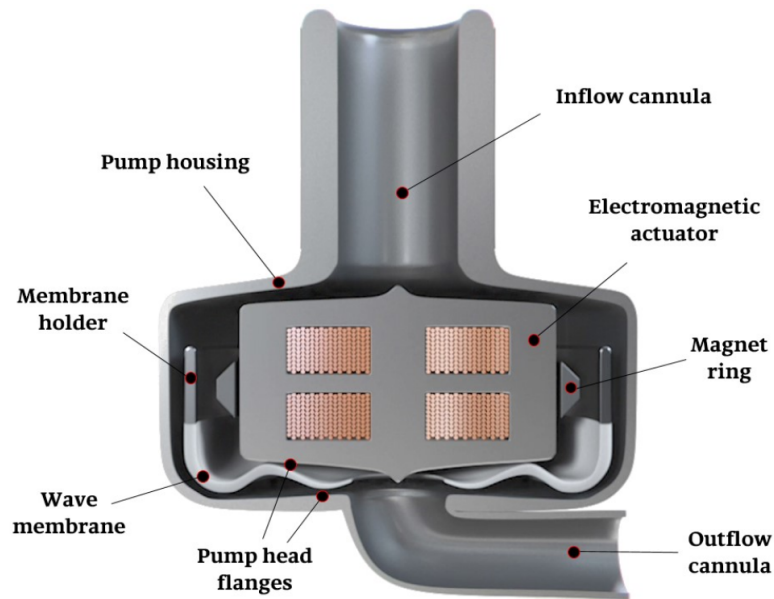
FIGURE 2.3: Cross-sectional view of the main components of the implantable WMBP, including inlet and outlet channel, the actuator assembly (stator, electromagnetic coils and magnet ring) and the membrane assembly (wave membrane and membrane holder).

a lower region of the pump, where the wave membrane is suspended. This narrow space of the flow channel is named *pump head* and the delimiting walls are called *pump head flanges*. Here, blood interacts with wave membrane and is finally expelled throughout the outflow cannula. Notice that the thickness of the wave membrane, as well as the gap distance between the pump head flanges, decreases in radial direction going towards the outlet cannula.

The pump device is coupled with an *external controller* and extracorporeal *power source* via a transcutaneous *electric cable*. The controller communicates with the electromagnetic actuator to set the operating points of the WMBP and keeps memory of pump performance. The power source consists of a set of external rechargeable batteries, which can be used to supply energy to both the electromagnetic coils and the controller for several hours. An *external programmer*, like a laptop or mobile device, is used by a clinician to configure pump working parameters, like amplitude, frequency or duty cycle of the electromagnet actuator. A scheme of the complete structure of the LVAD system is represented at Figure 2.4, as described in the patent of the device [38].

2.2.3   Wave membrane technology

The wave membrane technology of WMBPs is activated by an alternating current applied to the electromagnetic coils of the actuator. The latter generates a magnetic field with rapidly opposing poles, that drives the periodic oscillatory motion of the magnet ring, with a certain frequency and amplitude of oscillation. Since the membrane holder is mechanically engaged with the magnet ring, the excitation transits
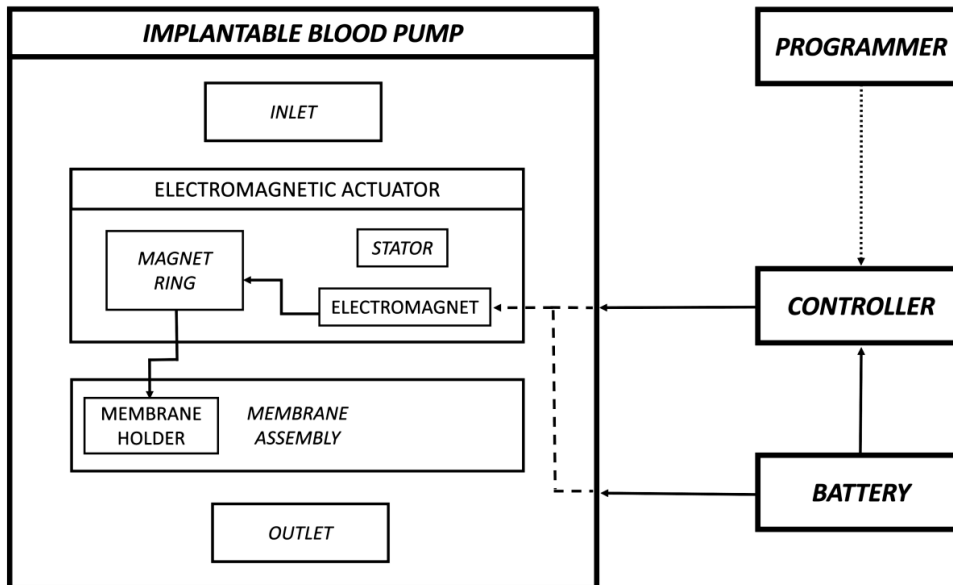
FIGURE 2.4: Functional scheme representing the interactions between the main components of the implantable WMBP.

from the actuator to the membrane assembly. As the membrane holder starts oscillating with the magnet ring, a wavelike displacement propagates in the wave membrane from the membrane holder towards the center, in direction of the outlet channel [101, 225]. The propagating deformation wave is accompanied by the damping effect of the surrounding viscous fluid, due to the shape of the pump head flanges. This results in an energy transfer from the membrane to the blood in the form of pressure gradient and fluid flow [91]. Indeed, the resulting pressure buildup in the pump head allows to push from the inlet towards the outlet channel. The characteristics of the generated pressure gradient and blood flow depend on the size and the shape of the membrane, the spacing between the pump head flanges, and the excitation parameters. Therefore, the pump works as an energy transducer, that converts electromechanical energy into hydraulic power.

Thanks to the transport effect of the deformation waves, WMBPs work as *valveless volume displacement pumps*. Indeed, as observed in Figure 2.5, during its progressive propagation, the wave membrane transports the blood that is enclosed in the volumes between the membrane undulations and the pump head flanges radially inward towards the outlet channel. These masses of blood transported by the membrane wave are referred to as *fluid pockets*. During its wave motion, the membrane may approach to the pump flanges close enough to isolate the fluid pockets propagating towards the outlet, thus minimizing any potential backflow towards the inlet. Therefore, this configuration between the wave membrane and the rigid walls covers a function similar to the one of mechanic valves in the first-generation pulsatile pumps. Notice that, under specific operating conditions, the membrane may in principle collide with the pump head flange, triggering potential contact dynamics; however, this point has still to be fully investigated.
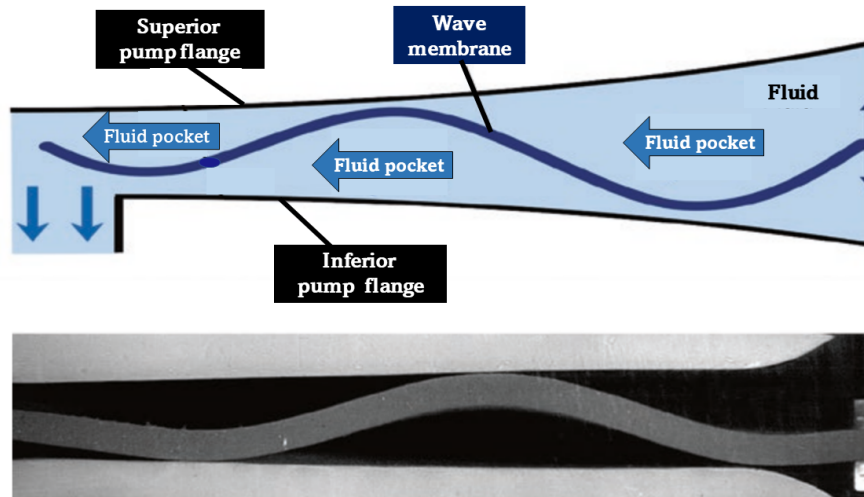
FIGURE 2.5: Fluid pocket propagation in pump head region of WMBPs. Figure adapted from [39].

2.3   Flat membrane and J-shape membrane designs

The design of the different components of the WMBP system has been revised multiple times, to optimize pump efficiency and reduce the risk of blood trauma. In particular, we can consider two different pump designs, showed in Figure 2.6, that differ mostly in the membrane geometry. The first design, Design A (Figure 2.6, left), presents a membrane assembly with a planar discoidal geometry and for this reason it is refered to as *flat membrane pump design* (or, concisely, *flat design*). The membrane holder (orange) has an annular shape, that runs along the external edge of the membrane disc. The remaining portion of the membrane disk (yellow) corresponds to the flexible wave membrane. The second pump design, Design B (Figure 2.6, right), that is more recent, shows a longer membrane holder that bends towards the inlet up to the magnet ring (grey). Owing to the shape of the cross-section of the membrane assembly, this design is called *J-shape membrane pump design* (or *J-shape design*).

The two designs present differences also in the flow channel (light blue), corresponding to the region between the internal pump housing and the external surface of the actuator (central hole). In Design A, the gap between the magnet ring and the actuator wall is thinner (smaller clearance) than in Design B. The enlargement of the clearance gap in the J-shape design allows to reduce risk of blood damage or thrombus formation in that region. The J-shape design presents larger flow channels, to accomodate for the longer membrane assembly, and smoother boundaries, especially nearby the membrane holder, to facilitate blood dynamics. The additional inlet cuspid in the upper part of Design B is thought to reduce the hydraulic resistance in the pump. The magnet ring is also smoother and larger in Design B.

The elongation of the membrane holder towards the inlet in the J-shape design was motivated by both hydraulic and hemocompatibility-related reasons. Indeed, the upper part of the J-shaped membrane holder should (i) work as a *flow separator*, distributing blood flow across the lower and upper sides of the membrane; (ii) reduce
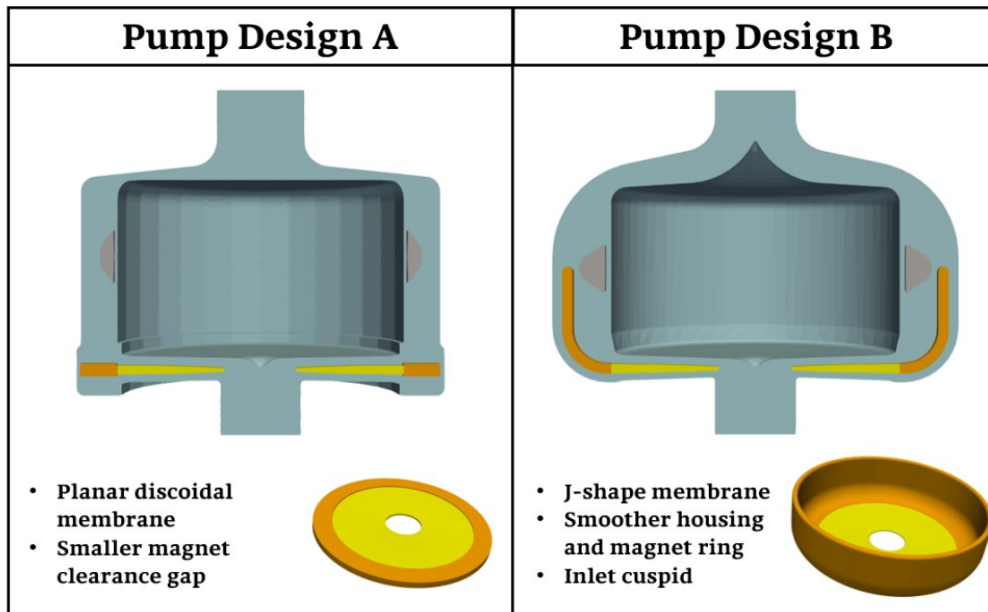
FIGURE 2.6: Comparison of flat membrane pump design (A) and J-shape membrane pump design (B), with focus on the different geometries of the membrane holder (orange). In yellow, the oscillating wave membrane.

flow recirculation near the magnet ring and the exposure time to high shear rates; and (iii) increase the resistance to retrograde flow to improve hydrodynamic output. The latter point was specifically investigated in *in-vitro* testings, measuring the hydraulic power for different heights of the membrane holder and different frequencies of oscillation (see Figure 2.7). The experimental results showed that the maximum hydraulic power of the pump increases with the height of the membrane holder at a non-linear rate, for each tested frequency of oscillation [231]. Thus, for instance, it is sufficient to employ a 18 mm-high membrane holder to increase the maximum hydraulic power from 1.42 W (with planar design) to 9.13 W at 120 Hz. This means also that it is possible to reach the same hydraulic output at lower frequency by switching to the J-shape design, thus potentially reducing blood shear rate and increasing fatigue life of the membrane. As a result, according to the company requirements, the range of potential frequencies of oscillation shifted from $60 - 120$ Hz in the flat design to $30 - 70$ Hz in the new J-shape design. Nevertheless, higher frequencies may still be tested in the J-shape design in case of desired augmented pump output, *e.g.* to reproduce systolic ejection. Instead, the stroke of oscillation, corresponding to twice the amplitude of oscillation, is generally between 1 to 2 mm for both designs.

2.4 Potential theurapeutic benefits of WMBPs

The wave membrane technology in WMBP is aimed at overcoming the current limitations of commercially available continuous-flow rotary blood pumps, by providing physiological pulsatile flow with a minimum risk of blood trauma.
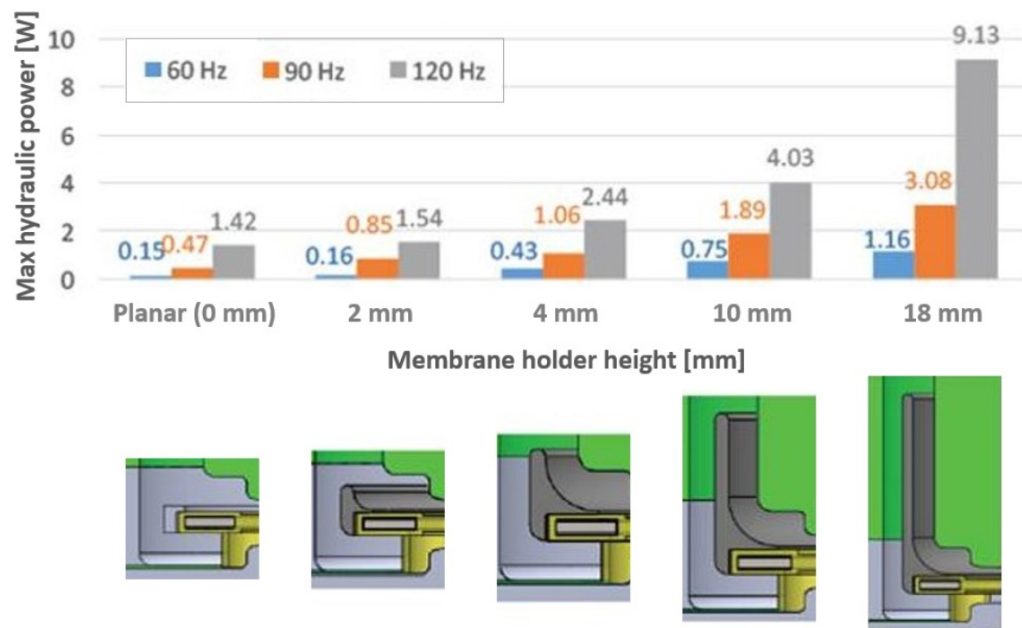
FIGURE 2.7: Measurements of the maximum hydraulic power of the pump for increasing heights of the membrane holder, from planar design to height of 18 mm, for three different frequency parameters (60 Hz, 90 Hz, 120 Hz). Experimental data come from the patent of the WMBP device [231].

WMBP is able to reproduce a wide range of physiologic flow rates, potentially enabling the possibility to reproduce the pulsatility of the native heart [101]. Indeed, pump performance can be modulated by the frequency at which the membrane operates, to genearate flows that can approach the flow rate of native heart during systole (see Figure 1.3) [269]. For example, Mock loop testings showed that WMBPs can achieve an output flow rate over 10 $^l/_{min}$ at 100 Hz, against a physiologic pressure difference of 80 mmHg across the pump [40].

In particular, flow pulsatility can be created by switching rapidly between levels of pump output. For instance, when working in synchronous mode, the pump flow rate can be increased during systole to reproduce the natural augmentation of the cardiac output in the ejection phase; while during diastole, the LVAD output can be decreased to limit backflow and avoid left ventricle suck down [37]. In order to regulate the blood flow in real time, the oscillation frequency can be controlled by a pulsation control algorithm, that is able to synchronize with the heartbeat by sensorless detection of the native ventricle systole [269]. Thanks to the low inertia of the wave membrane, the pump system presents a very short delay (~ 30 ms) to the change of operating parameters [37], allowing to adapt, almost instantaneously, the pump performance to fit patient-specific needs (both at rest and during exercise) [39].

The pulsatility mode in WMBPs was assessed in a Mock circulatory loop and compared with HeartMate II (HM2) and HVAD working in the same setup. As can be seen in Figure 2.8, both HM2 and HVAD pumps showed a decrease in both pulse pressure ΔP and maximum pressure curve slope $^{dP}/_{dt}|_{max}$, with respect to the values in the simulated circulatory system of a heart failure patient. This indicates a
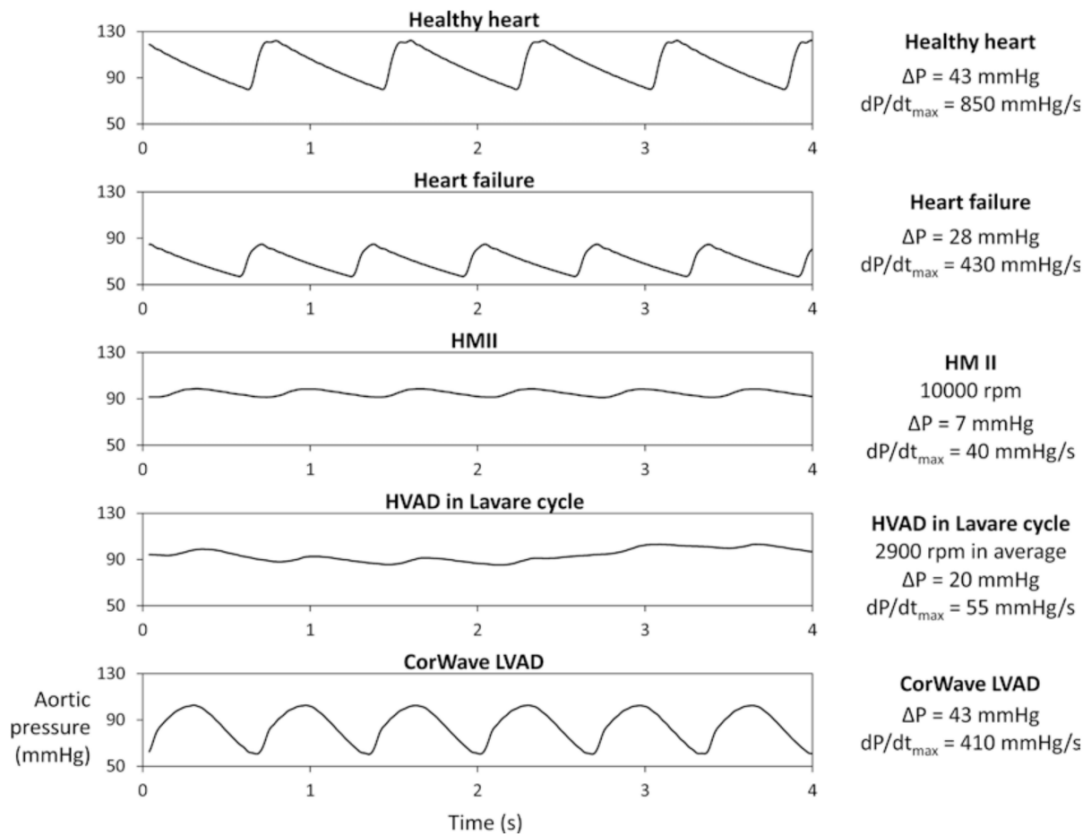
FIGURE 2.8: Comparison of aortic pressure Figure taken from [39].

dampening of the pulsatility in these CF LVADs, resulting in a pulse pressure smaller than 20 mmHg. Instead, WMBP restored a physiologic pulse pressure, that allows to potentially reduce typical risks of CF pumps, such as GI bleeding or renal complications [37]. The synchronization algorithm is being validated in *in-vivo* animal trials [39] and the study of other pulsatility algorithms, such as counter-pulsation or asynchronous mode, are under active investigation.

The potential improvement in hemocompatibility in WMBPs derives from two important differences with respect to the technology used in previous LVADs. Firstly, the wave membrane in WMBP replaces the high-speed impeller of second and third generation devices, thereby decreasing the levels of blood velocities and hydrodynamic-generated shear stress exerted on blood cells [6]. Indeed, it has been estimated that a centrifugal LVAD working at 7 l/min exposes approximately 70% of the blood volume to velocities higher than 2 m/s, considered to be the maximum physiologic blood speed in healthy conditions [260]. Instead, at equivalent flow conditions, only 1% of the blood volume in WMBPs exceeds such threshold on blood velocity [39]. Secondly, WMBPs lack of artificial mechanical valves, that were used in pulsatile first generation LVADs to direct blood flow and prevent backflows and that are known to cause significant blood trauma [6]. Indeed, during its motion, the membrane itself is able to approach to the pump flanges very closely (contact configuration), thereby closing the way to any potential backflow. In addition, the geometry of WMBPs was carefully designed to avoid regions of flow stagnation and recirculation, in order to prevent thrombus formation and dissipation [269]. Also, the transition of the pump

from low to high output in pulsatility mode has been carefully optimized to eliminate any increased blood damage compared to the average of the two in continuous mode [39].

As a result, the LVAD developed at the partner company is a promising product presenting important advantages in terms of both hydraulic and hemodynamic performance, size and costs, with respect to the competitors active in the fast-growing market of MCS devices. Nevertheless, there are still many aspects on the pump functioning that need to be fully understood and the synergy between experiments and simulations can be the key to improve device performance.

2.5   Previous studies on wave membrane technology

Due to the novelty and the uniqueness of the wave-generated pump concept, the number of experimental or numerical studies addressing the wave membrane technology is very poor.

In a work from 2002 by Feier et al. [101], an early LVAD prototype named *FishTail pump*, predecessor to WMBP, was tested in an *in-vivo* study for the first time. The FishTail pump employed a primitive version of the wave membrane technology of WMBPs – J. B. Drevet, co-autor of [101], is the inventor of the membrane pumping concept – , with the ability to generate both pulsatile and non-pulsatile flows. In [101], the pump was implanted in 6 swine animals for short-term support (3 hours) using non-pulsatile operation mode. The results demonstrated the potential of the novel pump concept, that showed slightly better hemodynamic performance than an extracorporeal centrifugal pump of the time (Biomedicus BP-80). However, the analysis on blood damage showed that the FishTail pump produced high levels of hemolysis, that needed to be addressed to improve clinical applicability.

A more similar pump device to WMBP is the *progressive wave pump*, developed at AMS R&D for general pumping applications and proposed in [225] in 2012 for potential use as cardiac support system. In this work, two different geometrical configurations, both axi-symmetric, are considered for the progressive wave pumps: a *discoidal design* and a new *tubular design* (see Figure 2.9). In the former case, similarly to what happens in the flat membrane design of WMBP, the actuator imparts transversal oscillations on the external circumference of the membrane disc, so that the generated waving motion pushes gently the blood cells from the periphery into the inner orifice of the membrane. In the latter case, the membrane has tubular shape and the direction of excitation is not radial, but axial. The discoidal design of progressive wave pump differs from WMBP for two main reasons: (i) in WMBPs, the inlet and the outlet channels are displaced with 180 degrees, while the prototype in Perschall's work shows an angle of 90 degrees, implying an undesirable flow deflection; (ii) the pump actuator of WMBP is magnetic, whereas progressive wave pumps employ a mechanic actuator.

The purpose of the study from Perschall et al. [225] was two-fold: i) on the one hand, a fluid-structure interaction (FSI) validation was performed on the existing discoidal design via comparison against real experimental data; ii) on the other
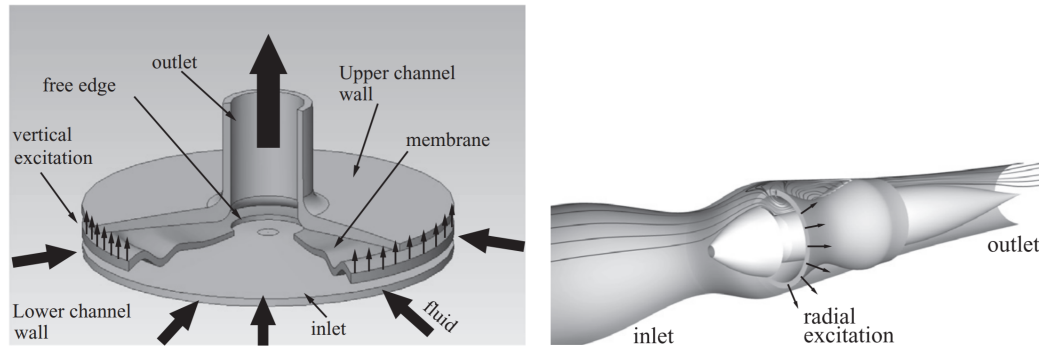
FIGURE 2.9: Discoidal (left) and tubular (right) design of progressive wave pumps. Illustrations taken from [225].

hand, the tubular configuration was virtually tested and optimized for potential VAD applicability. In the validation step, 2D axi-symmetric FSI simulations were carried out for different frequencies of membrane oscillation, using ADINA software package. The fluid (water) was assumed to be unsteady, laminar and Newtonian, while the membrane was modeled as an hyperelastic material with Saint-Venant-Kirchhoff stress-strain relationship. Hence, the fluid-structure dynamics were described by means of the coupling between the incompressible Navier-Stokes equations, written in the Arbitrary Lagrangian-Eulerian formulation, and a non-linear elastodynamic equations. The resulting coupled system was solved using a monolithic approach. As observed in Figure 2.10, although the numerical results overestimated the slopes of the experimental HQ curves, the relative difference between the tested frequencies was correctly numerically reproduced. In addition, the authors proposed a linear correction to apply to the predicted pressure values to find a better agreement with the data. Furthermore, a Design Of Experiment (DOE) method was applied to optimize the tubular design in view of LVAD application. Hence, geometric parameter (*e.g.* membrane length, thickness, axial stiffness and angles) were systematically varied to maximize volume flow rate, efficiency and minimize shear stress. The resulting tubular design, that was actually fabricated at AMS R&D, showed less flow recirculations, decreased hemolysis index and lower potential for platelet deposition.

There no exist other experimental or computational studies conducted in WMBPs to analyze the LVAD performance. Indeed, although the work from Scheffler et al. [256] involves a lumped parameter model to represent the WMBP, it specifically addresses the actuation mechanism that triggers the wave membrane undulations, without considering the hemodynamic output.

2.6 Objectives of the thesis

The main objective of this industrial thesis is to perform, for the first time, a computational study on the fluid-structure interactions (FSI) arising in the cutting-edge Wave Membrane Blood Pump, currently under development at the partner company. Given the novelty of this LVAD concept, there are still many aspects to investigate in the FSI dynamics to better understand how the wave propagation technology
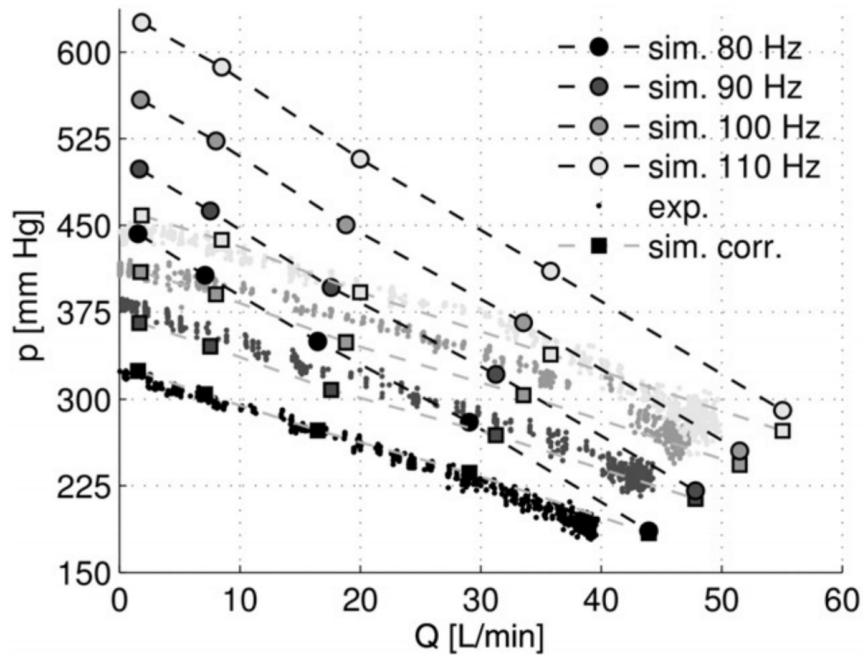
FIGURE 2.10: Validation analysis from [225], comparing experimental HQ curves (exp.) with simulation results (sim.) and simulation result with linear correction (sim. corr.).

works and what is the potential of the device in terms of hydraulic performance and hemocompatibility.

Another novelty of the project resides in the numerical approach adopted to carry over the three-dimensional FSI simulations, that is the Extended Finite Element Method (XFEM, [141, 51]). Indeed, this numerical method, that was developed quite recently and usually employed in rather simple scenarios or in two-dimensional geometries, is here applied for the first to solve a real three-dimensional industrial problem. XFEM is an unfitted mesh method that can be very computationally challenging in 3D applications, but has important advantages in terms of geometric flexibility and accuracy with respect to other more standard strategies The FSI model has been integrated with a contact model to study the potential contact dynamics between the membrane and the pump walls. The computational framework of the project is the LIFEV (LIbrary of Finite Elements) library [26] (`https://bitbucket.org/lifev-dev/lifev-release/wiki/Home`).

More specifically, the major goals of this study are:

0. The construction of an effective pipeline to reproduce computational meshes of real three-dimensional WMBP geometries;

1. the development and validation of the numerical model to solve the FSI simulations in such real three-dimensional WMBP domains;

2. a parametric analysis of the pump performance for different operating conditions of the WMBP device;

3. a comparative study between the flat and J-shape membrane pump designs (see Figure 2.6), in terms of hydraulic power and potential for hemocompatibility;

4. a preliminary investigation on vibrational non axi-symmetric modes of the wave membrane for certain operating conditions of the device.

Chapter 3

Mathematical and Numerical Method

3.1 Fluid-Structure Interaction model

3.1.1 Computational domain

Let Ω be the whole pump domain composed by the region occupied by the fluid and by the immersed structures. The two main oscillating structures are the membrane assembly domain $\Omega^m(t)$ and the magnet ring domain $\Omega^r(t)$. The membrane assembly is composed by the deformable wave membrane and the rigid membrane holder. As explained in detail in Section 2.2.3, as the magnet ring oscillates rigidly under the effect of the pump actuator, its displacement is mechanically transmitted to the membrane holder, via a system of supporting posts; since the membrane holder is properly enclosed in the wave membrane, the periodic excitation is transferred to the contiguous elastomeric part of the membrane assembly. Then, the fluid domain $\Omega^f(t)$ is determined as the complementary region to the union of the two structures, *i.e.*

$$\Omega^f(t) = \Omega \setminus (\Omega^m(t) \cup \Omega^r(t)). \tag{3.1}$$

Hence, the fluid domain changes in time due to the motion of the two structures. A cross-sectional representation of the computational domain is reported in Figure 3.1 for both the flat membrane pump design (left) and the J-shape membrane pump design (right), see Section 2.3 for a detailed description of the physical differences between the two designs. In particular, the boundaries Γ^{in} and Γ^{out} represent the pump inlet and outlet, respectively. Fluid boundary Γ^w corresponds to the housing wall (external fluid boundary) and the surface of the pump actuator (internal fluid boundary). Γ^m and Γ^r (in red) indicate the boundaries where the prescribed oscillations are assumed to occur, see below. Finally, boundary $\Sigma = \partial\Omega^m \setminus \Gamma^m$ is the fluid-structure interface, where no-slip and traction continuity conditions hold true.

In this work, we simplified the magnet-membrane interaction by omitting the membrane holder and the interconnecting fixation system and by assuming that the oscillation of the membrane assembly is directly imposed on the boundary Γ^m proximal to the actual location of the membrane holder (see Figure 3.2) [194]. Equivalently, we apply a displacement field $\boldsymbol{\varphi}$ on both membrane boundary $\Gamma^m \subset \partial\Omega^m$ and magnet boundary $\Gamma^r = \partial\Omega^r$ as a Dirichlet condition. Accordingly, for the fluid we prescribed a compatible Dirichlet data $\dot{\boldsymbol{\varphi}}$ on $\Gamma^m \cup \Gamma^r$. Notice that, since we are prescribing
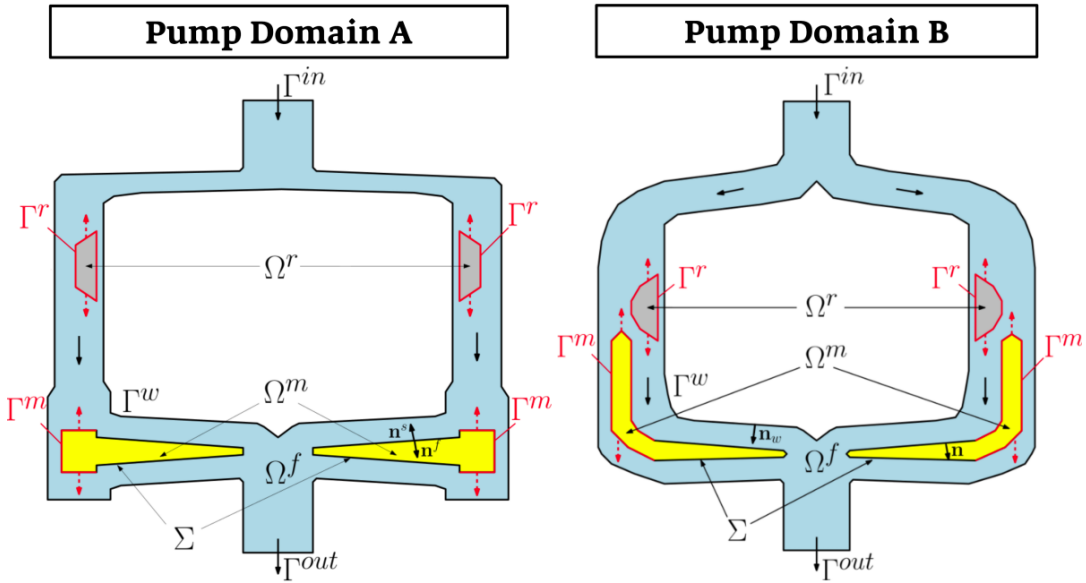
FIGURE 3.1: Computational domains for flat design (Pump Domain A) and J-shape design (Pump Domain B).

Dirichlet conditions with known data, we cannot prescribe any information about the interface tractions. The neglection of the fixation system is assumed to not influence significantly the global hemodynamics, given the small portion of the volume occupied in the pump. For the same reason, the pair of thin suspension rings above and below the magnet ring is also omitted from the computational domain.

3.1.2   Mathematical formulation of the FSI problem

The intertwined dynamics arising inside the Wave Membrane Blood Pumps (WMBP) can be mathematically described in the framework of Fluid-Structure Interface (FSI) modeling, where a system of Partial Differential Equations (PDEs) describes separately the behavior of the fluid and of the structures (membrane and magnet) in the respective domains, while proper coupling conditions define their interaction at the Fluid-Structure (FS) interface Σ. In this section, we neglect the effect of the potential contact dynamics between the wave membrane and pump walls, that will be specifically discussed in next section (Sect. 3.2).
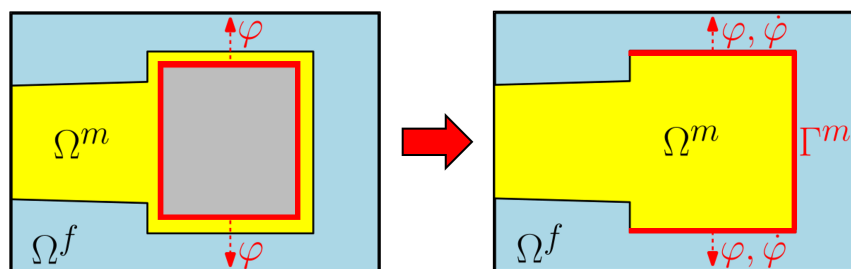
FIGURE 3.2: Replacement of the membrane holder (gray) with a surrogate condition applied on the boundary Γ^m (red) of the membrane assembly domain Ω^m.

We assumed the blood to be an incompressible, viscous and Newtonian fluid. In this work, the Newtonian approximation is justified by the characteristic size of the pump domain is much larger than the diameter of blood cells, apart from local (in space and time) exceptions in the contact region [238]. In addition, the shear rate observed in the simulations was generally higher than the reference threshold of 100 s^{-1}, over which the Newtonian assumptions is considered to be valid [65]. Denoting by ρ_f the fluid density and by μ_f the dynamic viscosity, we can then express the fluid Cauchy stress tensor as $\mathbf{T}^f(\mathbf{u}, p) = -p\mathbf{I} + 2\mu_f \mathbf{D}(\mathbf{u})$, with $\mathbf{D}(\mathbf{u}) = \frac{1}{2}(\nabla\mathbf{u} + \nabla\mathbf{u}^T)$, where $\mathbf{u}$ and p are the fluid velocity and pressure, respectively. Therefore, we used the Navier-Stokes equations to model the conservation of momentum and mass of blood, respectively. We remark that, since the Reynolds number in the pump varies between 200 to 2000 in space and time, there might be effects of transition to turbulence in the fluid dynamics that are neglected in this model.

The wave membrane is considered to be made of homogeneous and isotropic material, as in [225], with density ρ_m. We also assumed that the membrane undergoes infinitesimal linear deformations, so that we can apply Hooke's Law in the range of small displacements and write the first Piola-Kirchhoff tensor as $\widehat{\mathbf{T}}^s(\widehat{\mathbf{d}}^m) = \lambda_m(\widehat{\nabla} \cdot \widehat{\mathbf{d}}^m)\mathbf{I} + 2\mu_m \widehat{\mathbf{D}}(\widehat{\mathbf{d}}^m)$, where $\widehat{\mathbf{d}}^m$ is the membrane displacement and λ_m and μ_m are the Lamé parameters. The small deformation approximation is justified in our problem setting, because the observed normal strains are smaller than 5.5% and the tangential shears are smaller than 3% [194]. Notice that we used the $\widehat{\cdot}$ notation to refer to quantities defined in the Lagrangian configuration in the domain $\widehat{\Omega}^m = \Omega^m(0)$. We recall that the current configuration of the membrane domain $\Omega^m(t)$, as well as the Eulerian representation of the reference quantities, can be obtained by applying the Lagrangian map $\widehat{\mathcal{L}}(t) : \widehat{\Omega}^m \to \Omega^m(t)$. In particular, the solid Caucht stress tensor $\mathbf{T}^s$, that is the Eulerian counterpart of the first Piola-Kirchhoff tensor, is defined as $\mathbf{T}^s(\mathbf{d}^m) = J^{-1}\widehat{\mathbf{T}}^s(\widehat{\mathbf{d}}^m)\mathbf{F}^T$, with $\mathbf{F} = \nabla\mathbf{x}$ being the gradient of deformation and $J = \det\mathbf{F}$ its determinant. Nevertheless, we remark that in the small deformation regime we can assume that $\widehat{\mathbf{T}}^s = \mathbf{T}^s$ [122].

The magnet ring was modeled as a rigid structure, whose vertical movement has an impact on determining the fluid domain, velocity, and pressure. Hence, since we are not interested in the internal deformation or stresses, we solve a Laplacian problem in Ω^r to propagate the boundary condition into the internal nodes.

For a given $T > 0$, the fluid-structure interaction problem reads as follows:

Fluid-Structure Interaction Model in WMBP

For each time $t \in (0, T]$, find the fluid velocity $\mathbf{u}(t) : \Omega^f(t) \to \mathbb{R}^3$, the fluid pressure $p(t) : \Omega^f(t) \to \mathbb{R}$, the membrane deformation $\widehat{\mathbf{d}}^m(t) : \widehat{\Omega}^m \to \mathbb{R}^3$, and

the magnet ring displacement $\mathbf{d}^r(t) : \Omega^r(t) \to \mathbb{R}^3$, such that:

$$\rho_f \left(\partial_t \mathbf{u} + \mathbf{u} \cdot \nabla \mathbf{u}\right) - \nabla \cdot \mathbf{T}^f(\mathbf{u}, p) = \mathbf{0} \qquad \text{in } \Omega^f(\mathbf{d}), \qquad (3.2a)$$

$$\nabla \cdot \mathbf{u} = 0 \qquad \text{in } \Omega^f(\mathbf{d}), \qquad (3.2b)$$

$$\rho_m \partial_{tt} \widehat{\mathbf{d}}^m - \nabla \cdot \widehat{\mathbf{T}}^m(\widehat{\mathbf{d}}^m) = \mathbf{0} \qquad \text{in } \widehat{\Omega}^m, \qquad (3.2c)$$

$$\Delta \mathbf{d}^r = \mathbf{0} \qquad \text{in } \Omega^r, \qquad (3.2d)$$

$$\mathbf{u} = \partial_t \mathbf{d}^m \qquad \text{on } \Sigma(\mathbf{d}), \qquad (3.2e)$$

$$\mathbf{T}^f(\mathbf{u}, p)\, \mathbf{n}^f = -\mathbf{T}^s(\mathbf{d}^m)\, \mathbf{n}^s \qquad \text{on } \Sigma(\mathbf{d}), \qquad (3.2f)$$

with $\mathbf{d} = [\mathbf{d}^m, \mathbf{d}^r]$ and fluid normal $\mathbf{n}^f = -\mathbf{n}^s = \mathbf{n}$.

Notice that the fluid domain Ω^f (and thus the FS interface Σ) depends explicitly on the structures displacement $\mathbf{d}$ through its definition (3.1). In FSI problems this condition represents the so-called *geometric coupling* between the fluid and the structure domains.

In System (3.2), Eq. (3.2a) and (3.2b) are the non-linear incompressible Navier-Stokes equations, Eq. (3.2c) is the linearized elastodynamic equation, and Eq. (3.2d) is the harmonic extension for the movement of Ω_r. Eq. (3.2e) and (3.2f) are the no-slip coupling conditions imposed on the interface Σ guaranteeing the continuity of velocity (*kinematic coupling*) and of tractions (*dynamic coupling*), respectively. We remark that a *no-slip condition* implies that all three components of the fluid and solid velocity are equal at the FS interface; on the contrary, a *slip condition* enforces the equivalence in the normal direction to the interface, while it allows for potential slip in tangential direction. We adopted the no-slip kinematic condition because experimental evidences indicate that for Newtonian fluids slip can occur at length scales smaller than *μm* or *nm*, that are outside the scopes of this work [170].

In conclusion, the system of PDEs (3.2) has to be closed with proper initial and boundary conditions. For the fluid problem, we considered Neumann conditions both at the inlet Γ^{in} and at the outlet Γ^{out} to represent the pressure difference acting over the pump. We also applied an homogeneous Dirichlet condition (no-slip) at the pump walls Γ^w. Finally, as anticipated in Section 3.1.1, we impose Dirichlet conditions on Γ^m and Γ^r to model the forced oscillations on the membrane and on the magnet imposed by the pump actuator. In summary, we have:

$$\mathbf{T}^f(\mathbf{u}, p)\, \mathbf{n} = -P^{in}\, \mathbf{n} \qquad \text{on } \Gamma^{in}, \qquad (3.3a)$$

$$\mathbf{T}^f(\mathbf{u}, p)\, \mathbf{n} = P^{out}\, \mathbf{n} \qquad \text{on } \Gamma^{out}, \qquad (3.3b)$$

$$\mathbf{u} = \mathbf{0} \qquad \text{on } \Gamma^w, \qquad (3.3c)$$

$$\mathbf{d} = \boldsymbol{\varphi} \qquad \text{on } \Gamma^m \cup \Gamma^r, \qquad (3.3d)$$

$$\mathbf{u} = \dot{\boldsymbol{\varphi}} \qquad \text{on } \Gamma^m \cup \Gamma^r, \qquad (3.3e)$$

where P^{in} and P^{out} represent the pressure values at the pump inlet and outlet, respectively, such that $P^{in} = P^{out} - H$, with $H > 0$ being a given head pressure value. Since the forced oscillations are nearly sinusoidal [256], we assume the field displacement

$\boldsymbol{\varphi}(t)$ to be a sinusoid, along the axial coordinate, with input frequency f and amplitude $\Phi/2$, being Φ the *stroke* parameter. Hence, we have

$$\boldsymbol{\varphi}(t) = \frac{\Phi}{2} \sin(2\pi f t) \, \mathbf{e}_z \qquad t \in (0, T), \tag{3.4}$$

where $\mathbf{e}_z$ represents the axial direction. We refer to the triplet of parameters (H, f, Φ) from Eq. (3.3b)-(3.4) as the *Operating Point* (OP) of the pump device.

At time $t = 0$, we finally imposed the initial conditions to solve the first order time derivaive of the blood velocity and the second order time derivative for the membrane displacement, that are

$$\mathbf{u}(\mathbf{x}, 0) = \mathbf{u}_0 \qquad \text{in } \Omega^f(0), \tag{3.5a}$$
$$\mathbf{d}^m(\mathbf{x}, 0) = \mathbf{d}_0^m \qquad \text{in } \Omega^m(0), \tag{3.5b}$$
$$\dot{\mathbf{d}}^m(\mathbf{x}, 0) = \mathbf{w}_0^m \qquad \text{in } \Omega^m(0), \tag{3.5c}$$

In our application, we considered null initial conditions for all unknowns, *i.e.* $\mathbf{u}_0 = \mathbf{0}$, $\mathbf{d}_0^m = \mathbf{0}$, and $\mathbf{w}_0^m = \mathbf{0}$.

3.1.3 Weak formulation of the FSI problem

We define the following functional spaces:

$$\begin{aligned}
\mathbf{V}_{\boldsymbol{\psi}}(t) &= \left\{ \mathbf{v} \in \left[H^1(\Omega^f(t))\right]^3 : \mathbf{v}|_{\Gamma^m(t) \cup \Gamma^r(t)} = \boldsymbol{\psi}, \quad \mathbf{v}|_{\Gamma^w} = \mathbf{0} \right\}, \\
\mathbf{Q}(t) &= \left\{ q \in \left[L^2(\Omega^f(t))\right] \right\}, \\
\mathbf{W}_{\boldsymbol{\psi}}^m &= \left\{ \widehat{\mathbf{w}}^m \in \left[H^1(\widehat{\Omega}^m)\right]^3 : \widehat{\mathbf{w}}^m|_{\widehat{\Gamma}^m} = \widehat{\boldsymbol{\psi}} \right\}, \\
\mathbf{W}_{\boldsymbol{\psi}}^r &= \left\{ \mathbf{w}^r \in \left[H^1(\Omega^r)\right]^3 : \mathbf{w}^r|_{\Gamma^r} = \boldsymbol{\psi} \right\},
\end{aligned} \tag{3.6}$$

for the fluid velocity, for the fluid pressure, the membrane displacement and the magnet ring displacement, respectively. Notice that the Dirichlet conditions (3.3d)-(3.3e) have been integrated in the definition of the spaces.

Thus, denoting by $(\cdot, \cdot)_\Omega$ the L^2 product in Ω, the weak formulation of the FSI problem (3.2)-(3.3) reads as follows:

Weak Formulation of FSI Problem in WMBP

Find, for any $t \in (0, T]$, the fluid velocity $\mathbf{u}(t) \in \mathbf{V}_{\dot{\boldsymbol{\varphi}}}$, the fluid pressure $p(t) \in Q$, the membrane displacement $\widehat{\mathbf{d}}^m(t) \in \mathbf{W}_{\boldsymbol{\varphi}}^m$ and the magnet ring displacement

$\mathbf{d}^r(t) \in \mathbf{W}^r_{\boldsymbol{\varphi}}$, such that $\mathbf{u} = \partial_t \mathbf{d}^m$ on Σ, and

$$
\begin{aligned}
&\rho_f \left(\partial_t \mathbf{u}, \mathbf{v} \right)_{\Omega^f(t)} + a^f(\mathbf{u}, \mathbf{v}) + b(p, \mathbf{v}) - b(q, \mathbf{u}) + c(\mathbf{u}, \mathbf{u}, \mathbf{v}) \\
&+ \rho_m \left(\partial_{tt} \widehat{\mathbf{d}}^m, \widehat{\mathbf{w}}^m \right)^m_{\widehat{\Omega}} + a^s(\widehat{\mathbf{d}}^m, \widehat{\mathbf{w}}^m) + a^r(\mathbf{d}^r, \mathbf{w}^r) = f^f(\mathbf{v}),
\end{aligned} \tag{3.7}
$$

for all test functions $\left(\mathbf{v}, q, \widehat{\mathbf{w}}^m, \mathbf{w}^r \right) \in \mathbf{V_0} \times Q \times \mathbf{W}^m_0 \times \mathbf{W}^r_0$ such that $\mathbf{v}| = \mathbf{w}^m|$ on Σ.

In the presented weak formulation, we have introduced the following forms, defined in $\mathbf{V} = \left[H^1(\Omega^f(t)) \right]^3$, $Q = \left[L^2(\Omega^f(t)) \right]$, $\mathbf{W}^m = \left[H^1(\widehat{\Omega}^m) \right]^3$, $\mathbf{W}^r = \left[H^1(\Omega^r) \right]^3$:

- the fluid bilinear form for the viscous term $a^f : \mathbf{V} \times \mathbf{V} \to \mathbb{R}$, such that

$$
a^f(\mathbf{u}, \mathbf{v}) = 2\mu_f \left(\mathbf{D}(\mathbf{u}), \mathbf{D}(\mathbf{v}) \right)_{\Omega^f(t)};
$$

- the fluid bilinear form for the pressure term $b : Q \times \mathbf{V} \to \mathbb{R}$, such that

$$
b(p, \mathbf{v}) = - \left(p, \nabla \cdot \mathbf{v} \right)_{\Omega^f(t)};
$$

- the fluid trilinear form for the convective term $c : \mathbf{V} \times \mathbf{V} \times \mathbf{V} \to \mathbb{R}$, such that

$$
c(\mathbf{z}, \mathbf{u}, \mathbf{v}) = \rho_f \left(\mathbf{z} \cdot \nabla \mathbf{u}, \mathbf{v} \right)_{\Omega^f(t)};
$$

- the membrane structure bilinear form $a^s : \mathbf{W}^m \times \mathbf{W}^m \to \mathbb{R}$, such that

$$
a^s(\widehat{\mathbf{d}}^m, \widehat{\mathbf{w}}^m) = \left(\widehat{\mathbf{T}}^s(\widehat{\mathbf{d}}^m), \widehat{\nabla} \widehat{\mathbf{w}}^m \right)_{\widehat{\Omega}^m};
$$

- the magnet ring structure bilinear form $a^r : \mathbf{W}^r \times \mathbf{W}^r \to \mathbb{R}$, such that

$$
a^r(\mathbf{d}^r, \mathbf{w}^r) = \left(\nabla \mathbf{d}^r, \nabla \mathbf{w}^r \right)_{\Omega^r(t)};
$$

- the forcing term $f^f : \mathbf{V} \to \mathbb{R}$, such that

$$
f^f(\mathbf{v}) = \left(P^{out} \mathbf{n}, \mathbf{v} \right)_{\Gamma^{out}} - \left((P^{out} - H) \mathbf{n}, \mathbf{v} \right)_{\Gamma^{in}}.
$$

We remark that in Eq. (3.7) the geometric coupling resides in the L^2 product over the fluid domain $\Omega^f(t)$ varying in time, depending on the displacement solution. Instead, unlike the kinematic condition (3.2e) that is explicitely reported in the weak formulation, the dynamic condition is hidden and implicitely used to cancel the corresponding fluid and structure terms at the FS interface, as explained in [238].

Shortly, we will refer to this weak formulation as

$$
\mathcal{A}^{FSI} \left(\mathbf{u}, p, \widehat{\mathbf{d}}^m, \mathbf{d}^r; \mathbf{v}, q, \widehat{\mathbf{w}}^m, \mathbf{w}^r \right) = 0,
$$
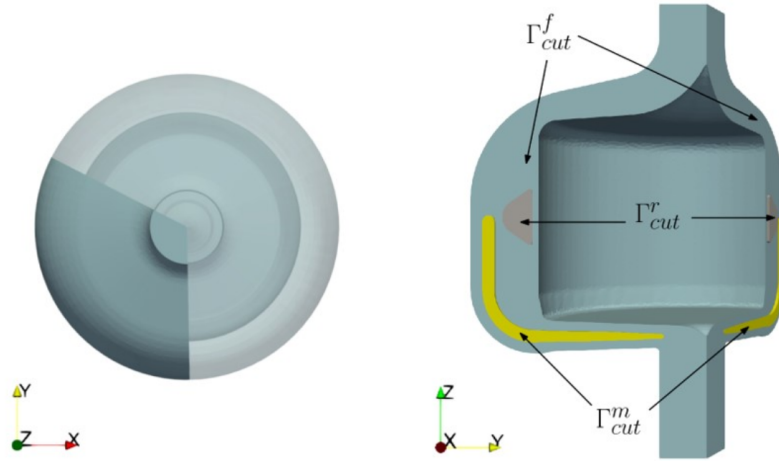
FIGURE 3.3: Reduction of pump axi-symmetric geometry to a 120-degree section. Left: View from above. Right: Cross-sectional view and definition of artificial cut boundaries Γ^f_{cut}, Γ^m_{cut} and Γ^r_{cut}.

where $\mathcal{A}$ includes all the terms from Eq. (3.7), including the right-hand side with the opposite sign.

3.1.4 FSI simulations in reduced geometry

Numerical solution of the FSI problem (3.2) can be very challenging and time-consuming. In view of the optimization of the computational cost, we can exploit the axi-symmetry of the pump domain and consider a reduced geometry to decrease the degrees of freedom of the system. In particular, we restricted the domain to a 120-degree section (see Figure 3.3, left), thereby carrying out the simulation in one third of the overall pump domain [193]. Notice that this is a simplifying assumption since anti-symmetric behaviors may arise during the pump functioning at certain operating conditons. Accordingly, in this work we consider both this simplified configuration and the complete one.

The construction of the reduced geometry introduces the artificial *cut surfaces* Γ^f_{cut}, Γ^m_{cut} and Γ^r_{cut} on the fluid, membrane, and ring domains (see Figure 3.3, left). Here, we prescribed typical symmetry conditions on the fluid and membrane unknowns and the same Diriclet condition (3.3d) on the displacement of the magnet ring, as the latter is a rigid structure. Such conditions translate to the following set of additional boundary conditions:

$$\mathbf{u} \cdot \mathbf{n}^f = 0 \quad \text{on } \Gamma^f_{cut}, \qquad \mathbf{T}^f(\mathbf{u}, p)\mathbf{n}^f \times \mathbf{n}^f = \mathbf{0} \quad \text{on } \Gamma^f_{cut}; \qquad (3.8)$$

$$\mathbf{d}^m \cdot \mathbf{n}^s = 0 \quad \text{on } \Gamma^m_{cut}, \qquad \mathbf{T}^s(\mathbf{d}^m)\mathbf{n}^s \times \mathbf{n}^s = \mathbf{0} \quad \text{on } \Gamma^m_{cut}; \qquad (3.9)$$

$$\mathbf{d}^r = \boldsymbol{\varphi} \quad \text{on } \Gamma^r_{cut}. \qquad (3.10)$$

with $\boldsymbol{\varphi}$ defined as in (3.4).

In case of reduced geometry approximation, the results computed from the integration over the boundary Γ^{in} or Γ^{out}, such as the volume flow rate at the outlet, are multiplied by 3 to recover the full-angle representation of the quantity.

3.2   Fluid-Structure Interaction model with contact

3.2.1   Motivation for a contact model in WMBPs

In WMBPs, the oscillatory motion of the wave membrane may, in principle, lead to a contact with the pump head flanges (see Figure 2.2-2.5). In fact, as mentioned in Section 2.2.3, the contact-derived dynamics are essential for an optimal functioning of the valveless wave membrane technology, because they allow for better propagation and isolation of the fluid pockets. Furthermore, as the membrane approaches to the pump walls, it compresses the interstitial fluid, causing an increase in the local pressure field and thereby contributing to blood propulsion into the outlet channel [193].

Nevertheless, it is still unclear if a physical membrane-wall collision actually occurs and no experimental evidences have been produced to demonstrate such phenomenon. In addition, repeated dry contacts (*i.e.*, with no fluid in-between) should be avoided in clinical practice to secure membrane integrity and increase device durability. For such reasons, we speak of contact configuration to refer to the general situation of the membrane approaching very closely to the pump flanges, which triggers repulsion forces typical of contact dynamics.

From a theoretical perspective, the conditions considered in the system (3.2) should prohibit dry contact. Indeed, according to previous studies [148, 60], the combination of the incompressibility of the fluid in Eq. (3.2b) with the no-slip kinematic condition (3.2e) should make physical contact impossible when an immersed moving body approaches to a wall because the interstitial fluid cannot slip away and allow for actual collision. Therefore, unless the fluid is compressible or slip is permitted either at the interface or at the pump wall, there is no need of contact model from a strictly mathematical point of view.

However, this theoretical result holds true also in numerical applications only provided that the discretization is infinitesimal in both time and space, that is unpracticable for computational reasons. As a consequence, in most cases, a contact model should be added to reproduce the repulsion that the blood opposes to the membrane, when the latter approaches to the wall [193]. Otherwise, as shown in Figure 3.4a, the wave membrane may exit from the fluid computational domain and lead to obviously non-physical configurations. Nonetheless, the contact model can still be omitted for a certain range of "low" operating conditions, such as for low stroke and/or frequency parameters, that result in a wave propagation that is too damped by the fluid to risk for a contact with the pump head flanges (see Figure 3.4b) [194].
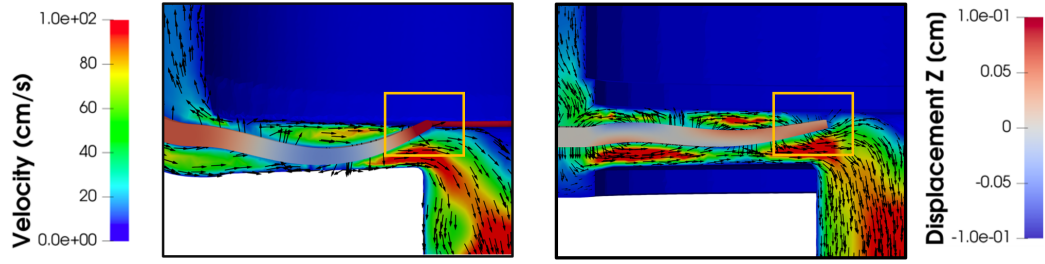
FIGURE 3.4: Cross-sectional view of FSI simulations with no contact model a) when the wave membrane exits from the fluid domain (large stroke parameter) and (b) when the deformation is too small to penetrate out from the fluid boundary (small stroke parameter).

3.2.2 Modeling the contact

We first consider a general contact problem featuring an immersed elastic body Ω^s, with FS interface Σ, moving against a fixed fluid boundary Γ^w with external wall normal $\mathbf{n}_w$. In this scenario, represented at the moment of contact in Figure 3.5A, the mechanics are represented by the classical inequality conditions from Karush-Kuhn-Tucker [4, 307, 68], that are

$$\Delta \geq 0 \qquad \text{on } \Sigma, \tag{3.11a}$$

$$\chi \geq 0 \qquad \text{on } \Sigma, \tag{3.11b}$$

$$\chi \Delta = 0 \qquad \text{on } \Sigma, \tag{3.11c}$$

where Δ denotes the gap distance of the moving body from the wall and χ corresponds to the normal component of the contact traction at the interface. In particular, Eq. (3.11a) represents the *non-penetration condition*, ensuring that the structure cannot cross the wall boundary; Eq. (3.11b) introduces the *contact force condition*, that corresponds to the non-negativeness constraint for the normal component of the contact traction (with wall normal oriented externally); finally, Eq. (3.11c) is the *complementarity condition* that guarantees that at least one of the former two constraints is null. In summary, either there is contact with boundary $\Gamma^c = \Sigma \cap \Gamma^w$ ($\Delta = 0$) and a repulsive contact force is activated ($\chi > 0$), or there is no contact ($\Delta > 0$, $\chi = 0$), *i.e.* $\Gamma^c = \emptyset$. In order to integrate such contact constraints in the FSI model, the system of inequalities (3.11) can be reduced in a consistent way to a single non-linear equality [68, 69], as

$$\chi = \gamma_c \left[-\Delta + \frac{1}{\gamma_c} \chi \right]_+ , \tag{3.12}$$

with $\gamma_c > 0$ being an arbitrary positive parameter. Notice that, since we consider *frictionless contact*, the tangential component of the contact force is assumed to be null [52, 317].

In this work, we applied a relaxation on the non-penetration contact conditions, as suggested by Burman et al. [52], by assuming that contact can occur within a distance
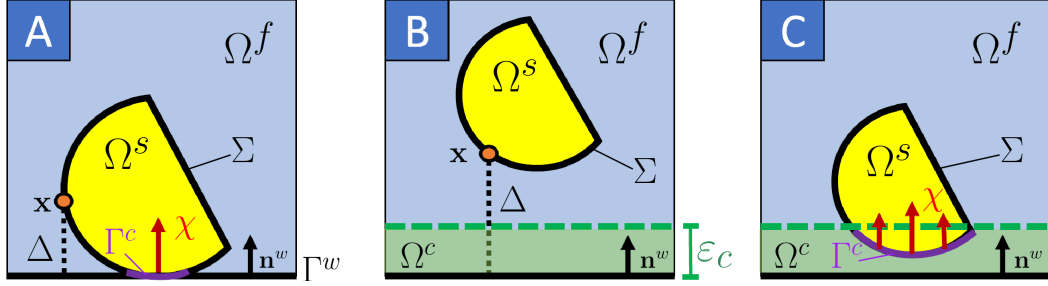
FIGURE 3.5: Schematic representation of contact in FSI problems. A) Dry contact of structure Ω^s with fluid boundary Γ^w. B) Contact layer Ω^c of relaxed contact approach, with width ε_c. C) Application of contact force χ on contact boundary $\Gamma^c = \Sigma \cap \Omega^c$.

ε_c from the wall boundary. Hence, the contact equation (3.12) is modified into

$$\chi = \gamma_c \left[(\varepsilon_c - \Delta) + \frac{1}{\gamma_c} \chi \right]_+ . \tag{3.13}$$

In other words, we assumed that there is an infinitesimal layer of fluid $\Omega^c \subsetneq \Omega^f$ with thickness $\varepsilon_c \to 0$, said *contact layer*, that always separates the FS interface from the wall boundary, ensuring the non-penetration of the moving body (see Figure 3.5B). In this framework, the contact boundary Γ^c, where the contact force χ is applied in the direction of the wall normal $\mathbf{n}_w$, corresponds to the portion of the FS interface that penetrates into the contact layer, *i.e.* $\Gamma^c = \Sigma \cap \Omega^c$ (see Figure 3.5C).

As done by Formaggia et al. [103], the definition of the contact force χ in Eq. (3.13) is simplified into the non-consistent form

$$\chi(\mathbf{x}) = \begin{cases} \gamma_c \left(\varepsilon_c - \Delta(\mathbf{x}) \right) & \text{if} \quad \Delta(\mathbf{x}) < \varepsilon_c, \\ 0 & \text{if} \quad \Delta(\mathbf{x}) \geq \varepsilon_c, \end{cases} \tag{3.14}$$

for $\mathbf{x} \in \Sigma$. Hence, the repulsive contact force is assumed to act as a spring force whose intensity is directly proportional to the degree of penetration of the structure in the contact layer.

Notice that, since this is a non-consistent approach, the penalty parameter γ_c has to be high enough to ensure numerical stability, possibly leading to an ill-conditioned matrix [103]. Alternatively, the consistent definition of the contact force (Eq. (3.13)) can be introduced in the formulation using the Nitsche's method as in [52], thereby achieving numerical stability even at lower penalty coefficient.

3.2.3 Strong and weak formulations of the FSI model with contact

In this section, we integrate the FSI problem in WMBPs defined in Eq. (3.2) with the penalization contact model discussed in Section 3.2.2 to include the potential membrane-wall contact dynamics in the pump head. As a result to the relaxation of the contact model, the membrane is assumed to be in contact when it penetrates into the contact layer. Therefefore, the portion Γ^c of the FS interface Σ receives a

repulsive contact force in the direction to the pump wall normal $\mathbf{n}^w$. For this reason, the contribution of the contact dynamics has to be taken into account for the balance of stresses at the interface.

Since the wave membrane oscillates between two pump walls, the inferior and superior pump head flanges (see Figure 2.3), we need to take into account potential collisions with both the surfaces. Thus, the contact force χ is a combination of the contact terms χ^{sup} and χ^{inf} from the superior and inferior pump head flanges, *i.e.*

$$\chi(\mathbf{x}) = \chi^{sup}(\mathbf{x})\,\mathbf{n}_w^{sup}(\mathbf{x}) + \chi^{inf}(\mathbf{x})\,\mathbf{n}_w^{inf}(\mathbf{x}), \tag{3.15}$$

each applied along the direction of the corresponding wall normals $\mathbf{n}_w^{sup}$ and $\mathbf{n}_w^{inf}$. Contact terms χ^{sup} and χ^{inf} are both defined as in Eq. (3.14) with respect to corresponding gap functions Δ^{sup} and Δ^{inf}. We denote by Γ_{sup}^c and Γ_{inf}^c the portions of the FS interface Σ that are in contact with the superior and inferior pump head flanges, respectively.

As a result, for a given $T > 0$, the strong formulation of the Fluid-Structure-Contact Interaction problem (FSCI) reads as follows:

Fluid-Structure-Contact Interaction Model in WMBP

For each time $t \in (0, T]$, find the fluid velocity $\mathbf{u}(t) : \Omega^f(t) \to \mathbb{R}^3$, the fluid pressure $p(t) : \Omega^f(t) \to \mathbb{R}$, the membrane deformation $\widehat{\mathbf{d}}^m : \widehat{\Omega}^m \to \mathbb{R}^3$, and the magnet ring displacement $\mathbf{d}^r(t) : \Omega^r(t) \to \mathbb{R}^3$, such that:

$$\rho_f\left(\partial_t \mathbf{u} + \mathbf{u} \cdot \nabla \mathbf{u}\right) - \nabla \cdot \mathbf{T}^f(\mathbf{u}, p) = \mathbf{0} \qquad \text{in } \Omega^f(\mathbf{d}), \tag{3.16a}$$

$$\nabla \cdot \mathbf{u} = 0 \qquad \text{in } \Omega^f(\mathbf{d}), \tag{3.16b}$$

$$\rho_m \partial_{tt} \widehat{\mathbf{d}}^m - \nabla \cdot \widehat{\mathbf{T}}^s(\widehat{\mathbf{d}}^m) = \mathbf{0} \qquad \text{in } \widehat{\Omega}^m, \tag{3.16c}$$

$$\Delta \mathbf{d}^r = \mathbf{0} \qquad \text{in } \Omega^r, \tag{3.16d}$$

$$\mathbf{u} = \partial_t \mathbf{d}^m \qquad \text{on } \Sigma(\mathbf{d}^m), \tag{3.16e}$$

$$\mathbf{T}^f(\mathbf{u}, p)\,\mathbf{n} - \mathbf{T}^s(\mathbf{d}^m)\,\mathbf{n} = -\chi \qquad \text{on } \Sigma(\mathbf{d}^m), \tag{3.16f}$$

where χ is the contact force defined as in Eq. (3.14)-(3.15).

We can observe that the previous formulation naturally reduces to the non-contact variant in case of no contact, *i.e.* $\chi = \mathbf{0} \ \forall \ \mathbf{x} \in \Sigma$ or, alternatively, $\Gamma_{sup}^c \cup \Gamma_{inf}^c = \emptyset$, and the classical dynamic condition (3.2f) holds true again. We remark that the numerical solution of the FSCI problem is more stiff because of the additional non-linearity coming from the definition of the contact force, that needs to be addressed numerically.

The proposed relaxed model is in agreement with the non-collision theoretical results for no-slip conditions from [148, 60] and with the target membrane dynamics, *i.e.* without dry contacts, that are potentially harmful for the membrane integrity. Furthermore, observe that, by projecting Eq. (3.16f) along the direction of the wall

normal, we obtain

$$\chi^i = -\mathbf{n}_w^i \left(\mathbf{T}^f(\mathbf{u}, p) - \mathbf{T}^s(\mathbf{d}^m) \right) \mathbf{n} \qquad \text{on } \Gamma_i^c \subset \Sigma(\mathbf{d}^m), \qquad (3.17)$$

for $i \in \mathcal{W} = \{sup, inf\}$. Hence, for instance, χ^{sup} is either equal to the difference of normal tractions acting on Γ_{sup}^c, in case of contact with the superior wall, or to 0, otherwise. Notice that the impossibility of dry contact allows to always define the normal fluid traction $\mathbf{n}_w^i \mathbf{T}^f \mathbf{n}$ and consequently the definition in Eq. (3.17) is well-defined [52].

By using the definition of the contact force χ in Eq. (3.14)-(3.15), the weak formulation of the FSCI problem (3.16) reads as:

Weak Formulation of the FSCI Problem

Find, for any $t \in (0, T]$, the fluid velocity $\mathbf{u}(t) \in \mathbf{V}_{\dot{\varphi}}(t)$, the fluid pressure $p(t) \in Q(t)$, the membrane displacement $\widehat{\mathbf{d}}^m \in \mathbf{W}_{\varphi}^m$ and the magnet ring displacement $\mathbf{d}^r(t) \in \mathbf{W}_{\varphi}^r$, such that $\mathbf{u} = \partial_t \mathbf{d}^m$ on $\Sigma(t)$, and

$$\mathcal{A}^{FSI} \left(\mathbf{u}, p, \widehat{\mathbf{d}}^m, \mathbf{d}^r; \mathbf{v}, q, \widehat{\mathbf{w}}^m, \mathbf{w}^r \right) + \sum_{i \in \mathcal{W}} \gamma_c \left(\varepsilon_c - \Delta^i, \mathbf{w}^m \cdot \mathbf{n}_w^i \right)_{\Gamma_i^c(t)} = 0, \quad (3.18)$$

with $\mathcal{W} = \{sup, inf\}$, for all test functions $\left(\mathbf{v}, q, \widehat{\mathbf{w}}^m, \mathbf{w}^r \right) \in \mathbf{V_0} \times Q \times \mathbf{W_0}^m \times \mathbf{W_0}^r$ such that $\mathbf{v}| = \mathbf{w}^m|$ on $\Sigma(t)$.

Notice that the non-linearity of the contact problem is here hidden in the integration over the unknown boundaries Γ_{inf}^c and Γ_{sup}^c.

3.3   Extended Finite Element Method

3.3.1   Unfitted mesh methods

The FSI problem in WMBPs belongs to the class of numerical problems featuring a membrane immersed in a fluid. Similar problems arise in a wide variety of engineering applications, from the aircrafts to hydro-turbines, from sailing boats to valve leaflets. For this type of problems, the numerical methods are divided in two main categories: *fitted mesh methods* and *unfitted mesh methods*.

In fitted mesh methods, the fluid and the structure meshes are fitted and conforming at their interface (see Figure 3.6, left) and move together in time to automatically satisfy the geometric coupling condition. One of the most well-known fitted mesh method is the *Arbitrary Lagrangian-Eulerian* (ALE) method, introduced for the first time in [150] to model the fluid dynamics in a moving domain and subsequently extended for FSI applications in [88, 155]. Specifically, in the ALE approach, the displacement induced by the structure at the FS interface is applied to the interface points of the

fluid mesh, so that the latter deforms following the motion of the structure, and then extended to the inner fluid domain. Thus, the ALE formulation introduces an additional unknown, the fluid mesh displacement field $\widehat{\mathbf{d}}^f$, that has to be computed in the fluid domain $\widehat{\Omega}^f$ (Lagrangian coordinates), typically by means of an harmonic extension, and integrated in the Eulerian frame of the fluid equations. Thanks to the simplicity of its implementation, the ALE approach has been widely employed in many numerical FSI applications, especially in hemodynamics. For instance, it has been used to study the FSI in blood vessels, both in combination with the Finite Element Method (FEM) as in [85, 102, 144], and with the High-Order Spectral Methods, as in [224, 43, 61]. However, the ALE strategy is not recommended in case of large structure displacements or in contact problems. Indeed, in such cases, the deformation of the fluid mesh might lead to ill-shaped elements, thereby undermining the accuracy of the solution. In some cases, local remeshing can be applied to recover accuracy, but this procedure can be very computationally expensive and introduce artificial errors in the interpolation to the new fluid mesh [299, 233].

Unfitted mesh methods are specifically designed to avoid remeshing issues by using fixed background mesh for the fluid and an overlapping mesh for the structure moving on the foreground. In the unfitted mesh framework, the main issues consist in the detection of the FS interface and in the prescription of the interface conditions. Therefore, the different unfitted techniques differ on the way pursued to tackle these problems. In particular, the most important unfitted methods are: the *Immersed Boundary* (IB), the *Fictitious Domain* (FD) and the *Cut Finite Element Method* (CutFEM).

In the IB approach [226, 32, 314], the structure is represented in Lagrangian coordinates as a forcing term for the fluid problem and the FS interface is spatially defined by means of a discrete Dirac function, that is non-zero on the fluid nodes next to the structure boundary. For this reason, the IB method is known as a *"diffused" interface* method. In FD technique [124, 125, 27], the physical fluid domain is extended in the region occupied by the solid domain and the kinematic interface condition is weakly imposed via Lagrange multipliers defined at the FS interface. Both these methods solve the fluid problem in Eulerian coordinates in the whole domain Ω, and not only in the physical domain Ω^f.

Instead, in the CutFEM [54, 9], the fluid solution is represented only in the portion of the background mesh that is not overlapped by the foreground structure mesh, as depicted in the 2D example in Figure 3.7. Indeed, in this framework, as the structure
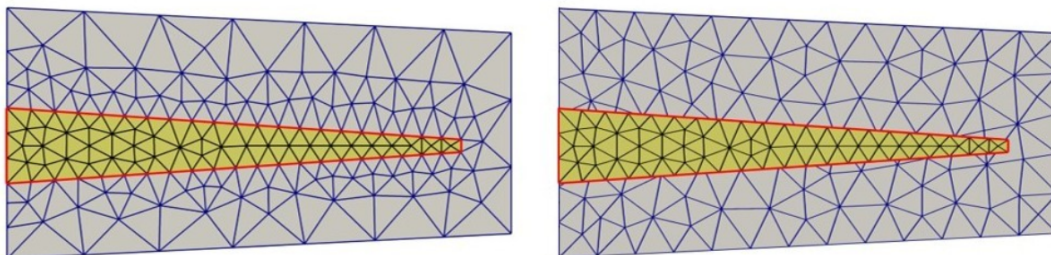
FIGURE 3.6: Bidimensional example of fitted (left) and unfitted (right) fluid and solid meshes.
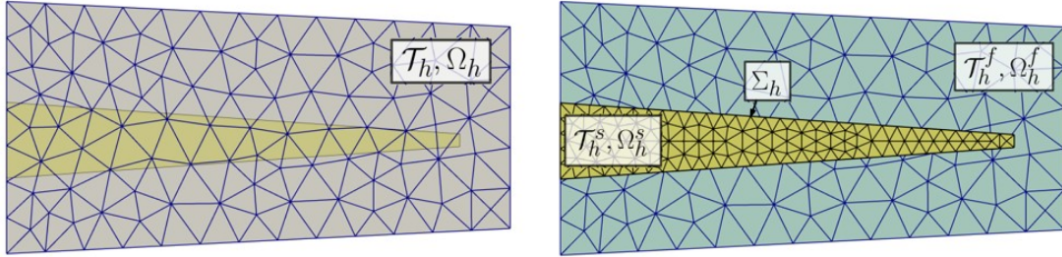
FIGURE 3.7: Bidimensional example of CutFEM mesh setting. Left: Background mesh $\mathcal{T}_h$ which covers the whole domain Ω_h (gray). The element in red is a split element. Right: Foreground solid mesh $\mathcal{T}_h^s$ on solid domain Ω_h^s (yellow). The fluid mesh $\mathcal{T}_h^f$ corresponds to the polyhedral cut-mesh, *i.e.* the non-overlapped portion of $\mathcal{T}_h$, that covers the physical fluid domain Ω_h^f (light blue).

mesh $\mathcal{T}_h^s$ moves on the foreground, it cuts the underlying background mesh $\mathcal{T}_h$ in different positions, thereby covering (or uncovering) sub-portions of the background mesh. Thus, the fluid mesh $\mathcal{T}_h^f$ contains elements of arbitrary shape (*i.e.* polygons, in 2D, or polyheadra, in 3D) that correspond to the visible physical portions of the background elements. In such context, the FS interface is sharply captured during its motion, because it corresponds to the union of the faces of the fluid mesh that are generated by the cut of the structure.

However, the formulation of the problem using the CutFEM can be challenging. Indeed, in case of thin structures, the background elements may be cut in such a way that multiple disjoint fluid sub-portions, said *sub-elements*, are visible. As a consequence, these background elements, called *split elements*, require a specific treatment of the discontinuity created across the structure. For this reason, the *Extended Finite Element Method* (XFEM) [22, 141, 51], which belongs to the class of CutFEM, was proposed to specifically address the formulation of the solution on the split elements. Indeed, the XFEM is based on an enrichment of the numerical approximation that allows to represent discontinuities within the same element, by means of the same shape functions and degrees of freedom (dofs) defined on the original mesh. Specifically, in XFEM the dofs of the split elements are enriched so that the fluid solution can be integrated independently in the different physical sub-elements using separate sets of dofs, thereby allowing to have a discontinuity within the fluid element itself. Therefore, the enrichment of the dofs corresponds to their doubling in case of two fluid sub-elements, triplication in case of three sub-elements, and so on. Notice that, from the fluid point of view, such discontinuity can either be represented as a level-set function defining a curve (surface) embedded in a 2D (3D) domain, as in the original formulations of XFEM in [23, 141, 109], or by the structure mesh itself, as done in [315]. In both cases, a numerical approximation $u_h(\mathbf{x})$ on a split element with two fluid sub-elements can be thought as the sum of two contributions: the standard Finite Element part, with standard (*i.e.* built on the un-cut background element) basis functions $\varphi_i(\mathbf{x})$ and dof u_i, and the enrichment term, consisting in the enriched (*i.e.*, doubled) dof e_i and in the same standard basis

functions $\varphi_i(\mathbf{x})$ multiplied by the enrichment function $\Upsilon_i(\mathbf{x})$, namely

$$u_h(\mathbf{x}) = \sum_{i \in I^{std}} u_i \varphi_i(\mathbf{x}) + \sum_{i \in I^{enr}} e_i \varphi_i(\mathbf{x}) \Upsilon_i(\mathbf{x}),$$

where I^{std} and I^{enr} are the sets of standard and enriched dof, respectively, and $\Upsilon_i(\mathbf{x})$ is the sign function restricted on the two fluid sub-elements. Notice that, this approximation can be generalized to the case of split elements with three or more fluid sub-elements. We noticed that in the literature, other, more general, definitions of XFEM have been provided [109]. Here we will refer to XFEM only when the duplication of the dofs is considered.

An alternative is provided by the Polygonal Discontinuous Galerkin (polyDG) approach where basis functions (usually of DG-spectral type) are built directly on the sub-elements thus not requiring the dofs enrichment [10].

In our computational study, we employed the XFEM strategy to solve the FSCI problem in WMBPs. The XFEM-based numerical discretization of the problem will be discussed in detail in Section 3.4, while the advantages and disadvantages of the XFEM with respect to other fitted or unfitted techniques are discussed in Sect. 3.5. Before that, in the next paragraph we report the state of the art of the XFEM-based applications in literature.

3.3.2   State of the art in XFEM

The main feature of XFEM consists in enabling modeling of discontinuities in the standard finite element framework, without need of remeshing procedures. Such discontinuities are normally encountered in problems with moving interfaces, that may lead to jumps, kinks or singularities within the finite elements [109]. According to [315], the nature of the discontinuity can either be geometric or physical: indeed, in the former case, the source of discontinuity is a change in the material properties, such as in case of cracks [291, 158] or holes [276]; in the second case, the discontinuity comes from a specific physical interaction, such as in a multi-phase [110, 59] or multi-fluid flows [159], in case of contact [87, 103], or in fluid-structure interaction applications [298, 51, 5].

As example of set of problems with geometric discontinuities, XFEM is frequently applied in fracture problems, where the propagation and the growth of a crack are studied to predict potential fracture failures in several applications [158]. Examples of these problems can be found in several fields, such as geotechnical, hydraulic and biomedical engineering. Particularly, we mention the following examples of fracture problems in cardiovascular applications, solved with XFEM: in [222], the atherosclerotic plaque disruption, caused by the shear stress on the artery walls, was numerically investigated combining the XFEM technique with patient-specific tomography data and with the Paris' Law to describe the fatigue crack growth; in [48], an XFEM-based cohesive segment method was used to model the initiation and the early propagation of the intimal tear along the aorta and study the influence of different geometric parameters on aortic dissection; finally, in [161], a virtual crack
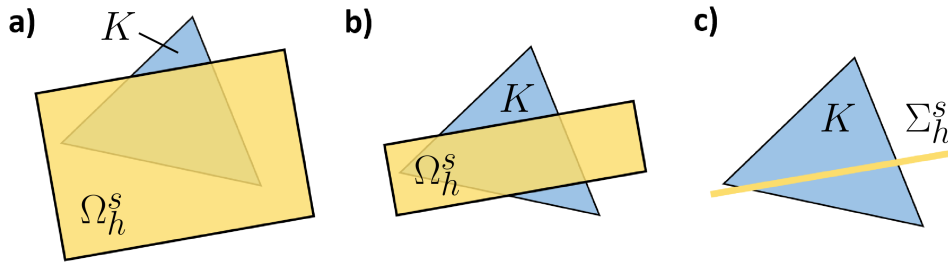
FIGURE 3.8: Different scenarios of FSI applications depending on thickness of the structure foreground domain Ω^s, that can be either larger (a) or smaller (b) than the size of the background fluid element K. In case of a very thin structure, it can be represented with a zero-thickness membrane Σ^s_h (c).

method, based on XFEM, was employed to investigate the relation between crack propagation in the atherosclerotic artery and spontaneous coronary artery dissection. The capabilities of the XFEM-based approach to simulate fatigue tear growth in complex crack fronts were validated against experimental data in [100], showing very good correlation regarding crack shape and number of cycles to failure.

When unfitted mesh methods are considered, FSI applications are typical examples of problems with physical discontinuities, because the immersed structure cuts the fluid domain and generates a jump in the solution at the interface. In some cases, the thickness of the structure is larger than the characteristic size of the fluid mesh, as shown in Figure 3.8a. Hence, a CutFEM method is sufficient because no dof enrichment is required. This is the case of [51] in two dimensions, or [196, 198] in three-dimensions. In the opposite case, see Figure 3.8c, the structure is subtle enough to approximate it with a zero-thickness immersed surface. In this case, dof enrichment of XFEM is needed on the fluid elements crossed by the FS interface, as done in [206, 143]. In the intermediate case, the thickness of the structure is comparable or smaller than the characteristic size of the background mesh elements (see Figure 3.8b). This represents the most challenging scenario, as the structure mesh intersects the fluid grid, potentially leading to the formation of split elements. As a consequence, there are fewer examples in literature that address this type of problem, that are *e.g.* [116, 115] in 2D and [315, 293] for 3D problems.

A particular issue in FSI applications consists in the way of prescribing the coupling conditions at the interface. One possible approach is to employ Lagrange multipliers, as done in [115, 114]. However, this approach adds an unknown to the problem, resulting in a higher computational cost. Alternatively, the solution at the FS interface can be coupled via *Discontinuous Galerkin* (DG) mortaring (or *Nitsche's method*) [11], a penalization method that ensures the consistency of the problem [146]. In such case, we refer to this approach as to the *XFEM-DG technique*. Nitsche's mortaring was applied in [142, 70] for zero-thickness problems and in [315, 293] for thin and thick structures.

In particular, Zonca et al. [315] applied the XFEM-DG approach to solve the time-dependent FSI problem in ideal aortic valves, to simulate the large deformations of the three leaflets during the opening and the closure of the valve. The numerical model was further developed in [103] with the integration of the penalization relaxed

contact model described in Section 3.2.2, used to reproduce the contact with a fluid boundary or between two deformable solids. The main limitations of these works are the simple computational geometries and the moderate Reynolds numbers of the numerical tests (~ 10).

In this thesis, we could overcome such limitations by testing the XFEM-DG approch in the complex 3D geometry of WMBPs, for flows with higher Reynolds number (200-2000), even though still not in the turbulent regime.

3.4 XFEM-based numerical discretization

3.4.1 Domain discretization

In the framework of unfitted mesh methods, the different components of the WMBP system are discretized independently, with no conformity constraints at the interface. In Figure 3.9 we show a possible domain discretization for the three-dimensional domain of a WMBP, in the particular case of the 120-degree reduced geometry introduced in Section 3.1.4. We denote by $\mathcal{T}_h$ the background mesh that extends over the whole pump domain Ω_h, see Figure 3.9a, where pedex h refers to the space discretization step $h > 0$. Notice that the spatial elements are tetrahedra and that the size of the discretization step may be varied depending on the pump region or on the local curvature of the domain. In Figure 3.9b, the structure meshes $\mathcal{T}_h^m$ and $\mathcal{T}_h^r$ are represented on the foreground for the membrane domain Ω_h^m and the magnet ring domain Ω_h^r, respectively. In order to simplify the notation in some formulations, we denote by Ω_h^s the ensemble of both structure domains, *i.e.* $\Omega_h^s(t) = \Omega_h^m(t) \cup \Omega_h^r(t)$.

In analogy with the definition of the fluid domain in the continuum problem from Eq. (3.1), the fluid mesh $\mathcal{T}_h^f$ is defined as follows:

$$\mathcal{T}_h^f(t) = \mathcal{T}_h \setminus \left(\mathcal{T}_h^m(t) \cup \mathcal{T}_h^r(t) \right), \tag{3.19}$$

where the operator $\setminus$ has to be interpreted as the geometric cut difference between the meshes. Hence, the resulting fluid mesh $\mathcal{T}_h^f$, called also *cut-mesh*, corresponds to the non-overlapped portion of the background mesh and covers only the physical fluid domain Ω_h^f, as shown in Figure 3.9c. Notice that in Eq. 3.19 the time dependancy is not present for the background mesh $\mathcal{T}_h$ that is fixed in time, while the foreground meshes are free to move and cut $\mathcal{T}_h$ in different positions during their motion.

As a result, the fluid cut-mesh has to be updated at each time instant, computing the new intersections generated by the motion of the structure mesh. In order to reduce the complexity of the computation of the mesh intersections, we first need to detect which fluid elements are more likely to intersect the overlapping structure elements, so that the intersection points can be calculated over a reduced set of entities, using a similar approach as in [195]. In this regards, we specifically employed the *Alternating Digital Tree* (ADT) algorithm [33], that is a spatial tree-based search algorithm, which is built upon a hierarchical organization of the mesh elements
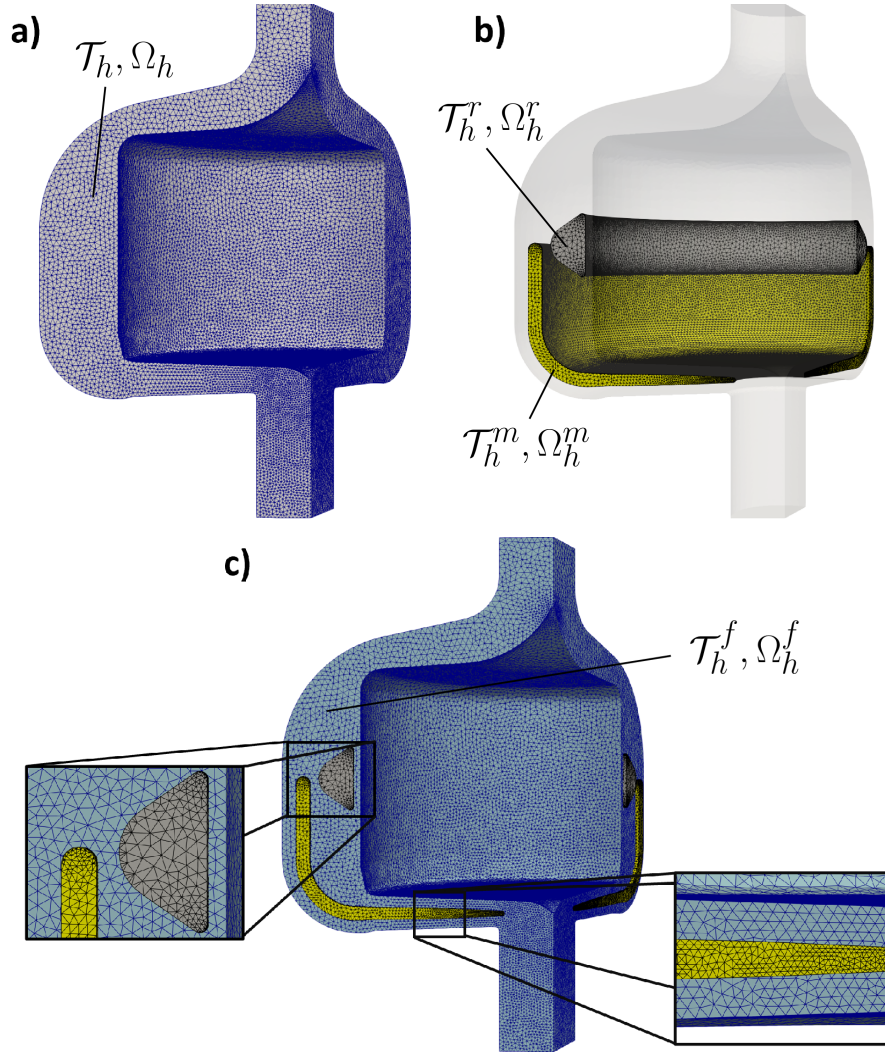
FIGURE 3.9: Unfitted domain discretization in a 120-degree section of WMBPs. a) Background mesh $\mathcal{T}_h$. b) Foreground meshes of membrane $\mathcal{T}_h^m$ (yellow) and magnet ring $\mathcal{T}_h^r$ (gray). c) Fluid cut-mesh $\mathcal{T}_h^f$ (light blue) and zoom on the non-fitted interfaces with magnet and memebrane meshes.

according to their spatial location. Therefore, this approach is particularly suitable for our problem, where the search can be confined to specific sub-regions of the fluid mesh. In case of more complex interface detection problems, it is possible to consider alternative approaches to ADT for 3D geometric mesh search, such as the *no binary* search [213] or the *dynamic cell-based* search algorithm [305].

The fluid cut-mesh $\mathcal{T}_h^f$ is, in general, made of polyhedra, because the background elements may be overlapped, partially or totally, by the structures meshes. Specifically, referring to the 2D example in Figure 3.10a, we can identify three different types of background elements in the neighborood to the FS interface Σ_h:

- *hidden elements*, which correspond to the background elements that are completely overlapped by the structure, such as the green element in Figure 3.10a; they are not visible and thereby not included in the fluid cut-mesh;

- *cut elements*, that are the background elements partially overlapped but with only one connected portion which is visible, as in the blue element in Figure 3.10a; in this case, only the visible portion is considered to be part of the fluid cut-mesh;

- *split elements*, that present multiple non-connected visible portions after the cut between meshes, as in the red element in Figure 3.10a; similarly to the cut elements, all the visible portions of the split elements, called *sub-elements* (P_1^K and P_2^K in the example), are included in the fluid mesh. We denote by N^K the number of fluid sub-elements for the split element K.
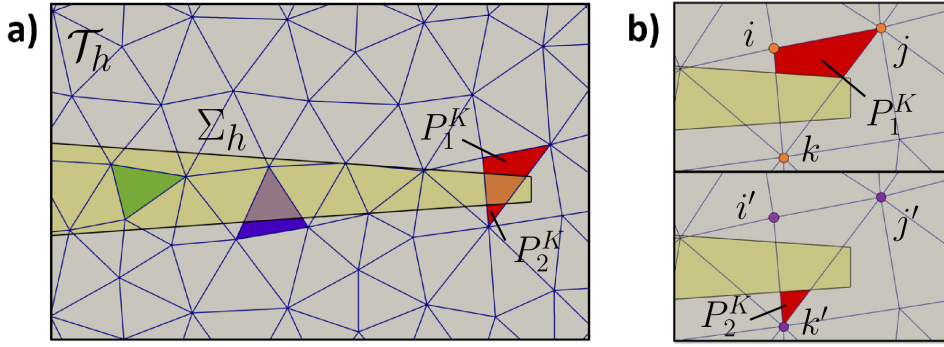
FIGURE 3.10: Left: Different fluid elements in XFEM: completely overlapped element (green), partially overlapped cut element (blue) and split element (red). Right: Dof enrichment in a split element with $N^K = 2$ sub-elements: the same basis functions are applied on P_1^K and P_2^K, but different sets of dof $\mathcal{I} = \{i, j, k\}$ and $\mathcal{I}' = \{i', j', k'\}$ are used for each sub-element.

Among these types, the split elements ($N_K > 1$) require a particular treatment because they are characterized by an internal discontinuity caused by the presence of the intermediate structure between the sub-elements. Hence, the representation of the solution in the split elements needs to be addressed in the XFEM enrichment strategy. Specifically, the degrees of freedom (dofs) of the split elements are enriched (*i.e.* doubled for $N_K = 2$, tripled for $N_K = 3$, and so on) so that the fluid solution can be computed independently over all the fluid sub-portions using separate sets of dofs for the integration. Therefore, taking as a reference the case illustrated in Figure 3.10 with $N_K = 2$, the dofs are doubled so that the set of dofs $\mathcal{I} = \{i, j, k\}$ is used to represent the solution on sub-element P_1^K, while the the set of dofs $\mathcal{I}' = \{i', j', k'\}$ is used to represent the solution on sub-element P_2^K. The same approach can be easily extended to the case of any number N_K of split non-connected fluid sub-elements, provided that the number of dofs is multiplied N_K times.

Notice that the cut elements ($N_K = 1$) do not require dof enrichment, because the solution can be normally computed with a single set of dofs by restricting the solution on the visible sub-element. Instead, the dofs of the hidden elements are excluded from the integration needed to build the Finite Elements matrices, because they do not belong to the physical fluid domain.

According to the previous discussion, we can define the subset $\mathcal{G}_h$ of the split elements in $\mathcal{T}_h$ as follows:

$$\mathcal{G}_h(t) = \left\{ K : K \in \mathcal{T}_h, \, K \cap \Omega_h^s(t) \neq 0, \, K \cap \Omega_h^f(t) \text{ is not connected} \right\}, \qquad (3.20)$$
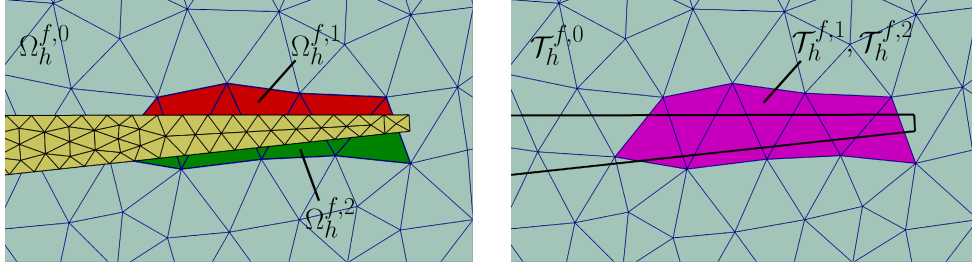
FIGURE 3.11: Left: Standard fluid domain $\Omega_h^{f,0}$ and extended sub-domains $\Omega_h^{f,1}$ and $\Omega_h^{f,2}$. Right: Standard background fluid mesh $\mathcal{T}_h^{f,0}$ and meshes $\mathcal{T}_h^{f,1}$ and $\mathcal{T}_h^{f,2}$, where dof enrichment is applied.

where dof enrichment is applied, and the complementary fluid sub-domain $\Omega^{f,0}$ and mesh $\mathcal{T}_h^0$ as

$$\Omega_h^{f,0} = \Omega_h^f \setminus \bigcup_{K \in \mathcal{G}_h} K, \qquad \mathcal{T}_h^{f,0} = \{K \in \mathcal{T}_h : K \notin \mathcal{G}_h\}, \tag{3.21}$$

where dof enrichment is not required.

Moreover, we can denote by $\mathcal{G}_h^P$ the set of fluid sub-elements, such that

$$\mathcal{G}_h^P(t) = \left\{ P_i^K, \text{ for } i = 1, \ldots, N^K, K \in \mathcal{G}_h(t) \right\} \subset \mathcal{G}_h(t) \tag{3.22}$$

and identify a set of connected sub-domains $\left\{ \Omega_h^{f,i} \right\}_{i=1}^{N^f}$, with $N^f = \max_K N^K$, such that

$$\mathcal{G}_h^P = \bigcup_{i=1}^{N^f} \Omega_h^{f,i}, \quad \Omega_h^{f,i} \cap \Omega_h^{f,j} = \emptyset \quad \text{if } i \neq j. \tag{3.23}$$

Hence, we can define the corresponding grids $\left\{ \mathcal{T}_h^{f,i} \right\}_{i=1}^{N^f}$ as

$$\mathcal{T}_h^{f,i} = \left\{ K \in \mathcal{G}_h : K \cup \Omega_h^{f,i} \neq \emptyset \right\}. \tag{3.24}$$

We remark that, by this definition, each split element $K \in \mathcal{G}_h$ belongs to N^K different meshes $\mathcal{T}_h^{f,i}$, thereby indicating that the solution of the weak formulation can be discontinuous in it. Figure 3.11 displays the standard and enriched domains (left) and meshes (right) in a 2D example.

Finally, in order to address the possible discontinuities and instabilities in the proximity to the FS interface, we can identify four different sets of element faces in the fluid cut-mesh:

- the faces $\mathcal{F}_h^\Sigma$ of the cut elements at the FS interface Σ_h, such that $\cup_F \mathcal{F}_h^\Sigma = \Sigma_h$, where coupling conditions are applied to glue the fluid and solid solution via Nitsche's method;

- the faces $\mathcal{F}_h^{p,i}$ of the physical fluid sub-elements in $\mathcal{T}_h^{f,i}$, for $i = 1, \ldots, N^f$ (see Figure 3.12, left), where the continuity is weakly imposed at the fluid-fluid interfaces via DG method;

- the faces $\mathcal{F}_h^s$ of the interior background elements, where the Continuous Interior Penalty (CIP) stabilization will be applied to handle spurious pressure and velocity instabilities due to equal order Finite Elements and to convection dominating regimes, see [53];

- the faces $\mathcal{F}_h^g$ of the cut elements that cross the FS interface (see Figure 3.12, right), where *ghost-penalty* stabilization will be enforced to add stability with respect to the mesh cuts, see [50].

We remark that the weak continuity at the fluid faces in $\mathcal{F}_h^{p,i}$ is strictly needed only on the faces between fluid elements that have different dof multiplicity, where strong continuity may be impossible to enforce [316]. Here, for simplicity, we extend this treatment to all physical faces $\mathcal{F}_h^{p,i}$, where dof enrichment is applied. Notice also that the stabilization set faces $\mathcal{F}_h^s$ and $\mathcal{F}_h^g$ include also the $\mathcal{F}_h^{s,i}$ and $\mathcal{F}_h^{g,i}$ duplicated faces of the split elements in $\mathcal{T}_h^{f,i}$, for $i = 1, \ldots, N^f$.
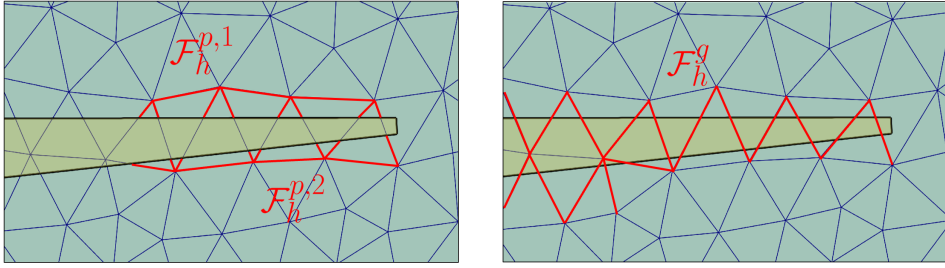
FIGURE 3.12: Sets of faces of the cut elements used for formulation of the fluid problem. Left: Physical cut faces $\mathcal{F}_h^{p,1}$ and $\mathcal{F}_h^{p,2}$ where fluid-fluid DG mortaring is applied. Right: Faces $\mathcal{F}_h^\Sigma$ of background elements crossing the FS interface, where ghost-penalty stabilization is applied.

3.4.2 Full discretization of the FSI problem

We introduce the following Finite Element spaces for the standard and extended elements in the fluid domain as

$$
\begin{aligned}
X_h^{f,std} &= \left\{ v_h \in C^0(\Omega_h^{f,0}) : v_h|_K \in \mathbb{P}_1(K) \quad \forall K \in \mathcal{T}_h^{f,0} \right\}, \\
X_h^{f,X,i} &= \left\{ v_h \in L^2(\Omega_h^{f,i}) : v_h|_K \in \mathbb{P}_1(K) \quad \forall K \in \mathcal{T}_h^{f,i} \right\},
\end{aligned}
\tag{3.25}
$$

for $i = 1, \ldots, N^f$, where N^f is the maximum number N_K of fluid sub-elements per split element in $\mathcal{G}_h$. Hence, we can define the finite element space for the fluid as the

direct sum of the standard and enriched spaces:

$$X_h^f = X_h^{f,std} \bigoplus_{i=1}^{N^f} X_h^{f,X,i}. \tag{3.26}$$

We highlight that the functional space of the fluid domain X_h^f does not require the continuity of the solution over the whole fluid domain Ω^f. In fact, we impose the continuity just in $\Omega_h^{f,0}$, *i.e.* over the fluid elements that do not require dof enrichment, while we apply the DG approach on the split elements in $\Omega_h^{f,i}$. Therefore, in order to address the discontinuities at the cut element faces, we need to introduce the α-weighted mean operator $\{\cdot\}_F$ and the jump operator $[\![\cdot]\!]_F$, defined over an element face F as:

$$\begin{aligned} \{q\}_F = \alpha q_+ + (1-\alpha)q_-, \quad [\![q]\!]_F = q_+ - q_-, \\ \{\mathbf{v}\}_F = \alpha \mathbf{v}_+ + (1-\alpha)\mathbf{v}_-, \quad [\![\mathbf{v}]\!]_F = \mathbf{v}_+ - \mathbf{v}_-, \end{aligned} \tag{3.27}$$

where q is a scalar function that assumes values q_+ and q_- on the two sides of face F and $\mathbf{v}$ is a vector function with values $\mathbf{v}_+$ and $\mathbf{v}_-$ at the sides of face F.

Since we consider equal order finite element spaces for velocity and pressure, we apply a stabilization term to satisfy the inf-sup condition for the solution of the Navier-Stokes equations. Specifically, we employ the Continuous Interior Penalty stabilization [53], that additionally handles possible instabilities due to convection dominating regimes. Furthermore, we apply the ghost-term penalty stabilization [50] to add robustness to the method with respect to the mesh cuts, see below.

For the structural problem, standard linear finite element spaces are used:

$$\begin{aligned} X_h^m = \left\{ \widehat{v}_h \in C^0(\widehat{\Omega}_h^m) : \widehat{v}_h|_{\widehat{K}} \in \mathbb{P}_1(\widehat{K}) \quad \forall \widehat{K} \in \widehat{\mathcal{T}}_h^m \right\}, \\ X_h^r = \left\{ v_h \in C^0(\Omega_h^r) : v_h|_K \in \mathbb{P}_1(K) \quad \forall K \in \mathcal{T}_h^r \right\}, \end{aligned} \tag{3.28}$$

for the membrane and the magnet ring, respectively.

Thus, analogously to what done in Eq. (3.6), the discrete spaces for the approximation of the velocity, the pressure and the displacements of the two structures can be defined as follows:

$$\begin{aligned} \mathbf{V}_{h,\psi} &= \left\{ \mathbf{v}_h \in [X_h^f]^3 : \mathbf{v}_h = \psi \ \text{ on } \Gamma^m \cup \Gamma^r, \ \mathbf{v}_h = \mathbf{0} \ \text{ on } \Gamma^w \right\}, \\ \mathbf{Q}_h &= \left\{ q_h \in X_h^f \right\}, \\ \mathbf{W}_{h,\psi}^m &= \left\{ \widehat{\mathbf{w}}_h \in [X_h^m]^3 : \widehat{\mathbf{w}}_h = \widehat{\psi} \ \text{ on } \widehat{\Gamma}^m \right\}, \\ \mathbf{W}_{h,\psi}^r &= \left\{ \mathbf{w}_h \in [X_h^r]^3 : \mathbf{w}_h = \psi \ \text{ on } \Gamma^r \right\}, \end{aligned} \tag{3.29}$$

where index ψ indicates the function that is prescribed in a strong way on the Dirichlet boundary of each domain.

We then consider a temporal discretization of the time interval $(0, T)$ based on the

timestep parameter $\Delta t > 0$ such that $t^n = n\Delta t$ for $n = 1, 2, \dots N_t$ with $N_t = \frac{T}{\Delta t}$. We consider the Backward Differentiation Formula of order 1 for the time discretization of both the fluid and solid problems, with a semi-implicit treatment of the fluid non-linear term. Therefore, the space-time approximation of the fluid velocity $\mathbf{u}(t^n)$ is denoted as $\mathbf{u}_h^n$, but to simplify the notation we will omit the current temporal index $n + 1$ (which is then understood) for the variables and the domains (*i.e.*, $\mathbf{u}_h = \mathbf{u}_h^{n+1}$, $\Omega_h^f = \Omega_h^{f,n+1}$)

In view of the full discretization of the FSI problem, we introduce the following discrete forms:

- the fluid form $\mathcal{A}_h^f(\mathbf{u}_h^*, \mathbf{u}_h, p_h; \mathbf{v}_h, q_h)$, defined as

$$
\begin{aligned}
\mathcal{A}_h^f \left(\mathbf{u}_h^*, \mathbf{u}_h, p_h; \mathbf{v}_h, q_h \right) = {}&\frac{\rho_f}{\Delta t} \left(\mathbf{u}_h, \mathbf{v}_h \right)_{\Omega_h^f} + \rho_f \left(\mathbf{u}_h^* \cdot \nabla \mathbf{u}_h, \mathbf{v}_h \right)_{\Omega_h^f} \\
&+ 2\mu_f \left(\mathbf{D}(\mathbf{u}_h), \mathbf{D}(\mathbf{v}_h) \right)_{\Omega_h^f} - \left(p_h, \nabla \cdot \mathbf{v}_h \right)_{\Omega_h^f} \\
&+ \left(q_h, \nabla \cdot \mathbf{u}_h \right)_{\Omega_h^f} + c_h(\mathbf{u}_h^*, \mathbf{u}_h; \mathbf{v}_h) \\
&+ s_h(\mathbf{u}_h, p_h; \mathbf{v}_h, q_h) + g_h(\mathbf{u}_h; \mathbf{v}_h),
\end{aligned}
\tag{3.30}
$$

which collects the terms of the weak formulation of the stabilized Navier-Stokes equations with convective velocity $\mathbf{u}_h^*$. In our simulations, we used a semi-implicit approach for the convective term by taking a first order extrapolation of the velocity, *i.e.* $\mathbf{u}_h^* = \mathbf{u}_h^n$.

The term $c_h(\mathbf{u}_h^*, \mathbf{u}_h; \mathbf{v}_h)$ is the correction of the convective term, defined over the cut faces in $\mathcal{F}_h^{p,i}$ (see Figure 3.12, left)) as

$$
\begin{aligned}
c_h(\mathbf{u}_h^*, \mathbf{u}_h; \mathbf{v}_h) = {}&\frac{\rho_f}{2} \left((\nabla \cdot \mathbf{u}_h^*)\, \mathbf{u}_h, \mathbf{v}_h \right)_{\Omega_h^f} \\
&- \sum_{i=1}^{N^f} \sum_{F \in \mathcal{F}_h^{p,i}} \rho_f \left(\{\mathbf{u}_h^*\}_F \cdot \mathbf{n} [\![\mathbf{u}_h]\!]_F, \{\mathbf{v}_h\}_F \right)_F \\
&- \sum_{i=1}^{N^f} \sum_{F \in \mathcal{F}_h^{p,i}} \frac{\rho_f}{2} \left([\![\mathbf{u}_h^*]\!]_F \cdot \mathbf{n}, \{\mathbf{u}_h \cdot \mathbf{v}_h\}_F \right)_F .
\end{aligned}
\tag{3.31}
$$

Such correction is used to recover the null condition of the convective term $(\mathbf{z} \cdot \nabla \mathbf{v}, \mathbf{v})_{\Omega^f} = 0 \quad \forall \mathbf{v} \in \mathbf{V}, \mathbf{z} \in \{\mathbf{v} \in \mathbf{V} : \nabla \cdot \mathbf{v} = 0\}$ in the discrete space [281, 315].

The stabilization term $s_h(\mathbf{u}_h, p_h; \mathbf{v}_h, q_h)$ corresponds to the *Continuous Interior Penalty* (CIP) stabilization [53, 258], introduced to handle spurious instabilities due to equal order of Finite Elements for velocity and pressure, and have better control on the convective term and on the incompressibility condition. It was defined over the computational faces in the set $\mathcal{F}_h^s$, as done in [315]:

$$s_h(\mathbf{u}_h, p_h; \mathbf{v}_h, q_h) = \gamma_v \sum_{F \in \mathcal{F}_h^s} \xi\left(Re_F\right) h_F^2 \, ||\mathbf{u}_h^* \cdot \mathbf{n}||_{\infty,F} \left(\llbracket \nabla \mathbf{u}_h \cdot \mathbf{n} \rrbracket_F, \llbracket \nabla \mathbf{v}_h \cdot \mathbf{n} \rrbracket_F\right)_F$$
$$+ \gamma_{div} \sum_{F \in \mathcal{F}_h^s} \xi_F\left(Re_F\right) h_F^2 ||\mathbf{u}_h^*||_{\infty,F} \left(\llbracket \nabla \cdot \mathbf{u}_h \rrbracket_F, \llbracket \nabla \cdot \mathbf{v}_h \rrbracket_F\right)_F$$
$$+ \gamma_p \sum_{F \in \mathcal{F}_h^s} \xi\left(Re_F\right) \frac{h_F^2}{||\mathbf{u}_h^*||_{\infty,F}} \left(\llbracket \nabla p_h \rrbracket_F, \llbracket \nabla q_h \rrbracket_F\right)_F,$$

$$(3.32)$$

where γ_v, γ_{div} and γ_p are positive penalty parameters for stabilization of velocity, divergence and pressure, respectively; Re_F is the local Reynolds number over face F defined as $Re_F = \frac{\rho_f \, h_F \, ||\mathbf{u}_h^*||_{\infty,F}}{\mu_f}$, and $\xi(x)$ is the minimum function such that $\xi(x) = \min(1, x)$.

The ghost-penalty stabilization $g_h(\mathbf{u}_h; \mathbf{v}_h)$ [50] is added to guarantee robustness of the method with respect to the cut elements, by preventing possible instabilities caused by the arbitrarily small dimension of the generated cut elements, as done in [315, 103]. Thus, the ghost-penalty term is defined over the set of faces crossed by the interface $\mathcal{F}_h^g$ (see Figure 3.12, right) as:

$$g_h(\mathbf{u}_h; \mathbf{v}_h) = \gamma_g \sum_{F \in \mathcal{F}_h^g} \mu_f h_F \left(\llbracket \nabla \mathbf{u}_h \rrbracket_F \mathbf{n}^F, \llbracket \nabla \mathbf{v}_h \rrbracket_F \mathbf{n}^F\right)_F, \qquad (3.33)$$

with $\gamma_g > 0$.

- the membrane structure form $\mathcal{A}_h^m(\widehat{\mathbf{d}}_h^m; \widehat{\mathbf{w}}_h^m)$, defined as

$$\mathcal{A}_h^m(\widehat{\mathbf{d}}_h^m; \widehat{\mathbf{w}}_h^m) = \frac{\rho_m}{\Delta t^2} \left(\widehat{\mathbf{d}}_h^m, \widehat{\mathbf{w}}_h^m\right)_{\widehat{\Omega}_h^m} + \lambda^m \left(\nabla \cdot \widehat{\mathbf{d}}_h^m, \nabla \cdot \widehat{\mathbf{w}}_h^m\right)_{\widehat{\Omega}_h^m}$$
$$+ 2\mu_m \left(\mathbf{D}(\widehat{\mathbf{d}}_h^m), \mathbf{D}(\widehat{\mathbf{w}}_h^m)\right)_{\widehat{\Omega}_h^m}. \qquad (3.34)$$

- the magnet ring structure form $\mathcal{A}_h^r(\mathbf{d}_h^r; \mathbf{w}_h^r)$, defined as

$$\mathcal{A}_h^r(\mathbf{d}_h^r; \mathbf{w}_h^r) = \left(\mathbf{D}(\mathbf{d}_h^r), \mathbf{D}(\mathbf{w}_h^r)\right)_{\Omega_h^r}. \qquad (3.35)$$

- the form $\mathcal{I}_h(\mathbf{u}_h, p_h, \mathbf{d}_h^m; \mathbf{v}_h, q_h, \mathbf{w}_h^m)$ of the coupling terms, where the weak continuity is applied over the fluid-structure interface Σ_h to glue the fluid-solid

solution via DG mortaring:

$$
\mathcal{I}_h(\mathbf{u}_h, p_h, \mathbf{d}_h^m; \mathbf{v}_h, q_h, \mathbf{w}_h^m) = \left(\alpha \mathbf{T}^f(\mathbf{u}_h, p_h)\mathbf{n}^f + (1 - \alpha)\, \mathbf{T}^s(\mathbf{d}_h^m)\mathbf{n}^s, \mathbf{v}_h - \mathbf{w}_h^m \right)_{\Sigma_h}
$$

$$
+ \left(\mathbf{u}_h - \frac{\mathbf{d}_h^m}{\Delta t}, \alpha \mathbf{T}^f(\mathbf{v}_h, q_h)\mathbf{n}^f + (1 - \alpha)\, \mathbf{T}^s(\mathbf{w}_h^m)\mathbf{n}^s \right)_{\Sigma_h}
$$

$$
- \frac{\gamma_\Sigma \mu_f}{h} \left(\mathbf{u}_h - \frac{\mathbf{d}_h^m}{\Delta t}, \mathbf{v}_h - \mathbf{w}_h^m \right)_{\Sigma_h},
\tag{3.36}
$$

where $\gamma_\Sigma > 0$ is the penalty parameter associated with the interface Σ. For the α-weighted mean terms in $\mathcal{I}_h$, we have taken $\alpha = 1$ for the fluid-structure mortaring, as done in [51, 5].

- the form $\mathcal{D}_h(\mathbf{u}_h, p_h; \mathbf{v}_h, q_h)$, to handle the weak continuity (in a DG sense) for the fluid problem among the interfaces defined over the set $\mathcal{F}_h^{p,i}$ of the physical cut faces (see Figure 3.12, left), as done in the DG approach [11, 315]:

$$
\mathcal{D}_h(\mathbf{u}_h, p_h; \mathbf{v}_h, q_h) = \sum_{i=1}^{N^f} \sum_{F \in \mathcal{F}_h^{p,i}} \left(\{\mathbf{T}^f(\mathbf{u}_h, p_h)\}_F\, \mathbf{n}^F, [\![\mathbf{v}_h]\!]_F \right)_F
$$

$$
+ \sum_{i=1}^{N^f} \sum_{F \in \mathcal{F}_h^{p,i}} \left([\![\mathbf{u}_h]\!]_F, \{\mathbf{T}^f(\mathbf{v}_h, -q_h)\}_F\, \mathbf{n}^F \right)_F
\tag{3.37}
$$

$$
- \sum_{i=1}^{N^f} \sum_{F \in \mathcal{F}_h^{p,i}} \frac{\gamma_{dg} \mu_f}{h_F} \left([\![\mathbf{u}_h]\!]_F, [\![\mathbf{v}_h]\!]_F \right)_F,
$$

with interior penalty parameter $\gamma_{dg} > 0$. For the mean operator in $\mathcal{D}_h^f$ we have used $\alpha = \frac{1}{2}$, as indicative of homogeneous coupling, in agreement with [71].

Notice that whereas strong continuity for the fluid problem is prescribed in a standard way for the interfaces far from the structure by using continuous Finite Elements, a DG approach has been preferred for the faces of the split elements. Indeed, in some scenarios, it is not possible to enforce strong continuity at interfaces between adjacent fluid elements that have different dof multiplicity, see [316].

- the form $\mathcal{F}_h(\mathbf{u}_h^n, \mathbf{d}_h^{m,n}, \mathbf{d}_h^{m,n-1}; \mathbf{v}_h, q_h, \mathbf{w}_h^m)$ of the terms resulting from the integration over the boundaries Γ^{out} and Γ^{in} and discretization of the time derivatives:

$$
\begin{aligned}
\mathcal{F}_h(\mathbf{u}_h^n, \mathbf{d}_h^{m,n}, \mathbf{d}_h^{m,n-1}; \mathbf{v}_h, q_h, \mathbf{w}_h^m) = {} & \frac{\rho_f}{\Delta t}\left(\mathbf{u}_h^n, \mathbf{v}_h\right)_{\Omega_h^f} + \frac{\rho_m}{\Delta t^2}\left(2\widehat{\mathbf{d}}_h^{m,n} - \widehat{\mathbf{d}}_h^{m,n-1}, \widehat{\mathbf{w}}_h^m\right)_{\widehat{\Omega}_h^m} \\
& + \left(P^{out}\,\mathbf{n}^f, \mathbf{v}_h\right)_{\Gamma^{out}} - \left((P^{out}-H)\,\mathbf{n}^f, \mathbf{v}_h\right)_{\Gamma^{in}} \\
& + \left(\frac{\mathbf{d}_h^{m,n}}{\Delta t}, \alpha\mathbf{T}^f(\mathbf{v}_h, q_h)\mathbf{n}^f + (1-\alpha)\,\mathbf{T}^s(\mathbf{w}_h^m)\mathbf{n}^s\right)_{\Sigma_h} \\
& - \frac{\gamma_\Sigma \mu_f}{h}\left(\frac{\mathbf{d}_h^{m,n}}{\Delta t}, \mathbf{v}_h - \mathbf{w}_h^m\right)_{\Sigma_h}.
\end{aligned}
$$
(3.38)

To address the integration over the unknown domains Ω_h^f and Σ_h in Eq. (3.30)-(3.36)-(3.38), we considered an explicit treatment of the geometric coupling by taking the first order extrapolation from the previous timestep, *i.e.* $\Omega_h^f \simeq \Omega_h^{f,n} = \Omega_h^f(\mathbf{d}_h^{m,n}, \mathbf{d}_h^{r,n})$ and $\Sigma_h \simeq \Sigma_h^n = \Sigma_h(\mathbf{d}_h^{m,n})$.

As a consequence, the velocity approximation at previous time step $\mathbf{u}_h^n$, appearing in Eq. (3.31) and (3.38), is defined in $\Omega^{f,n-1}$, but evaluated in $\Omega^{f,n}$ as the test function $\mathbf{v}_h$. Notice that, passing from time $n-1$ to time n, the moving structures may (i) cover new portions or new entire elements of the fluid mesh, where the old solution $\mathbf{u}_h^n$ was defined, and (ii) uncover areas that were previously overlapped, where the old solution $\mathbf{u}_h^n$ did not exist. Thus, in order to define $\mathbf{u}_h^n$ in $\Omega^{f,n}$, we introduce the new quantity $\Pi^n \mathbf{u}_h^n$, such that

$$
\Pi^n \mathbf{u}_h^n(\mathbf{x}) = \begin{cases} \mathbf{u}_h^n(\mathbf{x}) & \text{if } \mathbf{x} \in \Omega^{f,n}, \quad \mathbf{x} \in \Omega^{f,n-1}, \\ E^n(\mathbf{u}_h^n(\mathbf{x})) & \text{if } \mathbf{x} \in \Omega^{f,n}, \quad \mathbf{x} \notin \Omega^{f,n-1}, \\ \text{not defined} & \text{if } \mathbf{x} \notin \Omega^{f,n}, \end{cases}
$$
(3.39)

where $E^n(\mathbf{u}_h^n(\mathbf{x}))$ represents the "natural extension" of the piecewise linear solution $\mathbf{u}_h^n$ into $\Omega^{f,n}$. For instance, if we consider a 1D background element $K^i = \left[x^i, x^{i+1}\right)$, the extension $E^n(\mathbf{u}_h^n)$ into the new uncovered portion of sub-element $P_K^n \subset K^i$ is obtained via linear extrapolation of the solution $\mathbf{u}_h^n$ defined in $P_K^{n-1} \subset K^i$ (see Figure 3.13). The same approach can be applied on the entire elements K that were hidden at time $n-1$ and become visible at time n, by extending the solution from adjacent elements $\tilde{K}$ that were visible at time $n-1$.

Finally, the full discretization of problem (3.2) reads as follows:

Full discretization of the FSI problem

For $n = 0, 1, \ldots, N_t - 1$, find $\left(\mathbf{u}_h, p_h, \mathbf{d}_h^m, \mathbf{d}_h^r\right) \in \mathbf{V}_{h,\dot{\varphi}} \times \mathbf{Q}_h \times \mathbf{W}_{h,\varphi}^m \times \mathbf{W}_{h,\varphi}^r$ such that $\mathbf{u}_h^0 = \mathbf{0}$, $\mathbf{d}_h^{m,0} = \mathbf{0}$, $\mathbf{d}_h^{m,-1} = \mathbf{0}$:
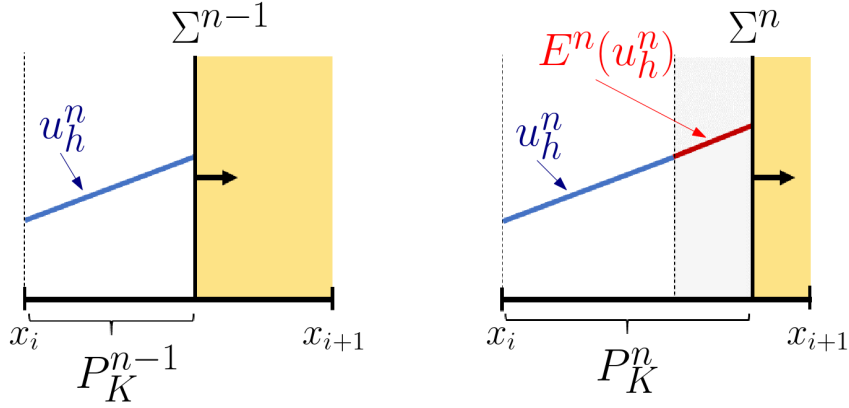
FIGURE 3.13: One-dimensional example of natural extension $E^n(\mathbf{u}_h^n)$ (red) of the solution $\mathbf{u}_h^n$ (blue), defined in sub-element $P_K^{n-1} \subset [x^i, x^{i+1})$, into the new uncovered portion (gray) of sub-element $P_K^n \subset [x^i, x^{i+1})$. Image re-edited from [316].

$$\mathcal{A}_h^f(\Pi^n \mathbf{u}_h^n, \mathbf{u}_h, p_h; \mathbf{v}_h, q_h) + \mathcal{A}_h^m(\mathbf{d}_h^m; \mathbf{w}_h^m) + \mathcal{A}_h^r(\mathbf{d}_h^r; \mathbf{w}_h^r) - \mathcal{D}_h^f(\mathbf{u}_h, p_h; \mathbf{v}_h, q_h)$$
$$- \mathcal{I}_h(\mathbf{u}_h, p_h, \mathbf{d}_h^m; \mathbf{v}_h, q_h, \mathbf{w}_h^m) = \mathcal{F}_h(\Pi^n \mathbf{u}_h^n, \mathbf{d}_h^{m,n}, \mathbf{d}_h^{m,n-1}; \mathbf{v}_h, q_h, \mathbf{w}_h^m) \quad (3.40)$$

$$\forall \left(\mathbf{v}_h, q_h, \mathbf{w}_h^m, \mathbf{w}_h^r\right) \in \mathbf{V}_{h,\mathbf{0}} \times \mathbf{Q}_h \times \mathbf{W}_{h,\mathbf{0}}^m \times \mathbf{W}_{h,\mathbf{0}}^r.$$

We remark that the integration over the cut elements in the fluid mesh is carried over by means of an intermediate sub-tetrahedralization procedure, that allows to write each sub-element as a sum of tetrahedra. Hence, the integration over the sub-elements is obtained as the sum of the contributions from each sub-tetrahedron, where the standard Gaussian quadrature rule can be normally applied. For more details on the computational implementation of this integration strategy, we refer the reader to [315, 316].

3.4.3 Discretization of the contact term

The solution of the FSCI problem given by Eq. (3.18) requires the discretization of the additional terms modeling the contact with the superior and inferior pump head flanges.

The discretized version of the contact term active on the pump head boundary $\Gamma_{i,h}^c$ is

$$\int_{\Gamma_{i,h}^c} \gamma_{c,h} \left(\varepsilon_c(h) - \Delta_h^i(\mathbf{x})\right) \qquad \text{for } i = \{sup, inf\}, \qquad (3.41)$$

with $\varepsilon_c(h) = \mathcal{O}(h)$ and $\gamma_{c,h} = \gamma_c^0 h^{-1}$, where γ_c^0 is a positive penalty constant and h represents the local mesh size of the fluid mesh. Notice that at the current time step, the *discrete current gap* Δ_h^i is unknown. Therefore, in order to compute it, we need to write it as an explicit function of the membrane displacement $\mathbf{d}_h^m$. Hence, according
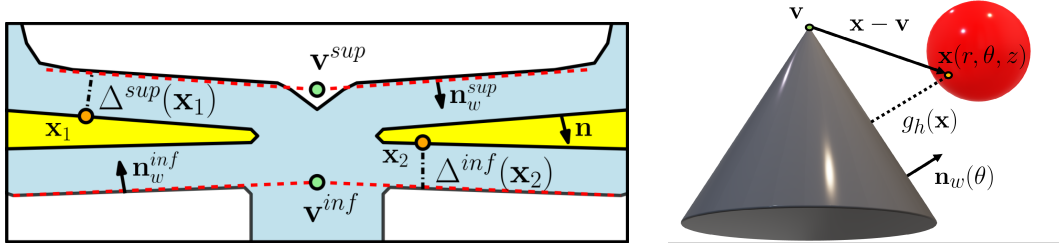
FIGURE 3.14: Left: Approximation of pump head flanges with conic surfaces. Right: Schematic 3D representation of cone-structure distance computation.

with [103], we took

$$\Delta_h^i = g_h^i - \mathbf{d}_h^m \cdot \mathbf{n}_w^i \tag{3.42}$$

where g_h^i is the *discrete initial gap* from the pump head wall i and $\mathbf{n}_w^i$ is the corresponding wall external normal.

As mentioned in Section 2.2.2, the pump head flanges are slightly inclined, so that the gap of the pump head region decreases, almost linearly, while moving radially towards the central axis. In order to compute the initial gaps g_h^{inf} and g_h^{sup} in a practical way, we approximated the pump head flanges with two conic surfaces, co-axial with the pump, with two virtual cone vertices denoted by $\mathbf{v}^{sup}$ and $\mathbf{v}^{inf}$, respectively (see Figure 3.14, left). Therefore, we can define the discrete initial gap with respect to the pump head flange i as

$$g_h^i(\mathbf{x}) = \left(\mathbf{x} - \mathbf{v}^i\right) \cdot \mathbf{n}_w^i(\mathbf{x}) \qquad \text{for } \mathbf{x} \in \Sigma. \tag{3.43}$$

Notice that the conic approximation allows to (i) compute the normal distance from all points $\mathbf{x}$ using the unique reference point $\mathbf{v}^i$ and (ii) easily find out the direction of minimal distance, that coincides with the wall normal direction corresponding to the angular coordinate θ of $\mathbf{x}$ (see Figure 3.14, right).

As a consequence, we can now define the contact bilinear form $C_h(\mathbf{d}_h^m; \mathbf{w}_h^m)$ as

$$
\begin{aligned}
C_h(\mathbf{d}_h^m; \mathbf{w}_h^m) = &\frac{\gamma_c^0}{h} \left(\mathbf{d}_h^m \cdot \mathbf{n}_w^{sup}, \mathbf{w}_h^m \cdot \mathbf{n}_w^{sup}\right)_{\Gamma_{sup,h}^c} \\
&+ \frac{\gamma_c^0}{h} \left(\mathbf{d}_h^m \cdot \mathbf{n}_w^{inf}, \mathbf{w}_h^m \cdot \mathbf{n}_w^{inf}\right)_{\Gamma_{inf,h}^c},
\end{aligned}
\tag{3.44}
$$

and the form of the corresponding terms at the right-hand side $\mathcal{F}_h^c(\mathbf{w}_h^m)$ as

$$
\begin{aligned}
\mathcal{F}_h^c(\mathbf{w}_h^m) = &\frac{\gamma_c^0}{h} \left(g_h^{sup} - \varepsilon_c, \mathbf{w}_h^m \cdot \mathbf{n}_w^{sup}\right)_{\Gamma_{sup,h}^c}, \\
&+ \frac{\gamma_c^0}{h} \left(g_h^{inf} - \varepsilon_c, \mathbf{w}_h^m \cdot \mathbf{n}_w^{inf}\right)_{\Gamma_{inf,h}^c},
\end{aligned}
\tag{3.45}
$$

Analogously to what done for the geometric coupling of the FSI problem, the unknown active contact boundaries $\Gamma_{sup,h}^c$ and $\Gamma_{inf,h}^c$ in Eq. (3.44)-(3.45) are extrapolated from

the previous timestep, *i.e.*, $\Gamma_{i,h}^c \simeq \Gamma_{i,h}^{c,n} = \Gamma_{i,h}^c(\mathbf{d}_h^{m,n})$ for $i = \{sup, inf\}$.

In conclusion, the discrete formulation of the FSCI problem (3.18) reads as follows:

Full discretization of the FSCI problem

For $n = 0, 1, \ldots, N_t - 1$, find $(\mathbf{u}_h, p_h, \mathbf{d}_h^m, \mathbf{d}_h^r) \in \mathbf{V}_{h,\dot\varphi} \times \mathbf{Q}_h \times \mathbf{W}_{h,\varphi}^m \times \mathbf{W}_{h,\varphi}^r$ such that $\mathbf{u}_h^0 = \mathbf{0}$, $\mathbf{d}_h^{m,0} = \mathbf{0}$, $\mathbf{d}_h^{m,-1} = \mathbf{0}$:

$$
\mathcal{A}_h^f(\Pi^n \mathbf{u}_h^n, \mathbf{u}_h, p_h; \mathbf{v}_h, q_h) + \mathcal{A}_h^m(\mathbf{d}_h^m; \mathbf{w}_h^m) + \mathcal{A}_h^r(\mathbf{d}_h^r; \mathbf{w}_h^r)
$$
$$
- \mathcal{D}_h^f(\mathbf{u}_h, p_h; \mathbf{v}_h, q_h) - \mathcal{I}_h(\mathbf{u}_h, p_h, \mathbf{d}_h^m; \mathbf{v}_h, q_h, \mathbf{w}_h^m) + \mathcal{C}_h(\mathbf{d}_h^m; \mathbf{w}_h^m)
$$
$$
= \mathcal{F}_h(\Pi^n \mathbf{u}_h^n, \mathbf{d}_h^{m,n}, \mathbf{d}_h^{m,n-1}; \mathbf{v}_h, q_h, \mathbf{w}_h^m) + \mathcal{F}_h^c(\mathbf{w}_h^m) \quad (3.46)
$$

$\forall \left(\mathbf{v}_h, q_h, \mathbf{w}_h^m, \mathbf{w}_h^r\right) \in \mathbf{V}_{h,\mathbf{0}} \times \mathbf{Q}_h \times \mathbf{W}_{h,\mathbf{0}}^m \times \mathbf{W}_{h,\mathbf{0}}^r.$

We remind the reader that, unlike in the model from [52], the contact term considered in this work is not fully consistent, with the advantage that the contact method does not depend on the material properties of the deformable structure [112]. Nevertheless, the parameter γ_c^0 should be taken large enough to recover the numerical stability of the formulation, as done in [103].

3.4.4 Numerical solver

The algebraic linear system associated to the FSCI problem described in Section 3.4.3 has the form of

$$
A\,\mathbf{x} = \mathbf{F}, \quad (3.47)
$$

where the vector of unknowns $\mathbf{x} \in \mathbb{R}^{N^T}$ collects all the N^T degrees of freedom (dof) of the fluid variables (both standard and enriched) and structure variables, and matrix $A \in \mathbb{R}^{N^T \times N^T}$ and vector $\mathbf{F} \in \mathbb{R}^{N^T}$ are obtained via XFEM approximation of the terms in the weak formulation (3.46).

Specifically, vector $\mathbf{x}$ is shaped as a 4×1 block vector such that

$$
\mathbf{x} = \begin{bmatrix} \mathbf{U} \\ \mathbf{P} \\ \mathbf{D}^m \\ \mathbf{D}^r \end{bmatrix}, \quad (3.48)
$$

where $\mathbf{U} \in \mathbb{R}^{3N_{h,f}}$ contains the dof associated to fluid velocity $\mathbf{u}_h$, $\mathbf{P} \in \mathbb{R}^{N_{h,f}}$ includes the dof associated to fluid pressure p_h, $\mathbf{D}^m \in \mathbb{R}^{3N_{h,m}}$ collects the dof associated to membrane displacement $\mathbf{d}_h^m$, and $\mathbf{D}^r \in \mathbb{R}^{3N_{h,r}}$ contains the dof associated to membrane displacement $\mathbf{d}_h^r$. Hence, we have that $N^T = 4N_{h,f} + 3N_{h,m} + 3N_{h,r}$. Notice that $N_{h,f}$ is the sum of the number of standard dof $N_{h,f}^{std}$ from classical Finite Element approximation and the total number $N_{h,f}^X$ of additional enriched dof coming

from XFEM duplication. In particular, we assume that the indices of the fluid dof vectors are sorted in such a way that the ones associated to the standard nodes, called *standard indices*, precede the ones associated to the enriched dofs, called *enriched indices*, *i.e.* $i = 1, 2, \ldots N_{h,f}^{std}, N_{h,f}^{std} + 1, \ldots, N_{h,f}^{std} + N_{h,f}^{X}$.

We introduce the scalar basis functions $\{\varphi_i\}_{i=1}^{N_{h,f}^{std}} \in X_h^f$, $\{\psi_j\}_{j=1}^{N_{h,f}^{std}} \in X_h^f$, $\{\eta_k\}_{k=1}^{N_{h,m}} \in X_h^m$, and $\{\omega_t\}_{t=1}^{N_{h,t}} \in X_h^r$. Moreover, we can consider the corresponding vectorial basis functions $\{\boldsymbol{\varphi}_i\}_{i=1}^{3N_{h,f}^{std}}$ for the velocity, defined such that

$$
\boldsymbol{\varphi}_i = \begin{cases}
\begin{bmatrix} \varphi_i, & 0, & 0 \end{bmatrix}^T & \text{if } i = 1, 2, \ldots, N_{h,f}^{std}, \\[2mm]
\begin{bmatrix} 0, & \varphi_{i-N_{h,f}^{std}}, & 0 \end{bmatrix}^T & \text{if } i = N_{h,f}^{std} + 1, N_{h,f}^{std} + 2, \ldots, 2N_{h,f}^{std}, \\[2mm]
\begin{bmatrix} 0, & 0, & \varphi_{i-2N_{h,f}^{std}} \end{bmatrix}^T & \text{if } i = 2N_{h,f}^{std} + 1, 2N_{h,f}^{std} + 2, \ldots, 3N_{h,f}^{std}.
\end{cases}
\tag{3.49}
$$

Analogous definitions hold true for vectorial basis functions $\{\boldsymbol{\eta}_k\}_{k=1}^{3N_{h,m}}$ and $\{\boldsymbol{\omega}_t\}_{t=1}^{3N_{h,r}}$.

Notice that the fluid basis functions are defined only for the standard indices, corresponding to all actual vertices of the fluid domain, including the ones of the split elements (but counted only once per geometric node). Indeed, the basis functions of the nodes of the split elements are common to all associated dof, regardless they are standard or enriched dof. However, when the enriched dof are considered for the integration, the basis functions active on the split elements are multiplied by an *enrichment function* Υ, that discriminates between the different sub-elements of the split element. For instance, in case of a split element with two fluid sub-elements (*i.e.*, $N_K = 2$) a suitable enrichment function is the sign function, which assumes 1 in P_1^K and -1 in P_2^K, that is able to represent the jump of the solution across the structure.

Hence, the approximated solutions for problem (3.46) can be written as

$$
\mathbf{u}_h(\mathbf{x}) = \sum_{i=1}^{3N_{h,f}^{std}} U_i\, \boldsymbol{\varphi}_i(\mathbf{x}) + \sum_{i=3N_{h,f}^{std}+1}^{3(N_{h,f}^{std}+N_{h,f}^{X})} U_i\, \boldsymbol{\varphi}_{\xi(i)}(\mathbf{x})\, \Upsilon_i(\mathbf{x}),
\tag{3.50a}
$$

$$
p_h(\mathbf{x}) = \sum_{j=1}^{N_{h,f}^{std}} P_j\, \psi_j(\mathbf{x}) + \sum_{j=N_{h,f}^{std}+1}^{N_{h,f}^{std}+N_{h,f}^{X}} P_j\, \psi_{\xi(j)}(\mathbf{x})\, \Upsilon_j(\mathbf{x}),
\tag{3.50b}
$$

$$
\mathbf{d}_h^m(\mathbf{x}) = \sum_{k=1}^{3N_{h,m}} D_k^m\, \boldsymbol{\eta}_k(\mathbf{x}),
\tag{3.50c}
$$

$$
\mathbf{d}_h^r(\mathbf{x}) = \sum_{t=1}^{3N_{h,t}} D_t^r\, \boldsymbol{\omega}_t(\mathbf{x}),
\tag{3.50d}
$$

where $\xi(\cdot)$ is a function that associates an enriched index (for which no basis function is defined) to the standard index of the corresponding node in the split element.

We remark that the formulation of the XFEM approximation of the fluid variables in Eq. (3.50a)-(3.50b) is inspired on the classical definition from the literature, *e.g* see [109]. From an operative point of view, in our implementation, the enrichment function is applied to both the standard and the enriched dof of the split elements and it is a boolean function that is activated or not depending on the region of integration.

Now, we can define the matrix A and the vector $\mathbf{F}$ appearing in the linear system in Eq. (3.47). Indeed, by substituting the XFEM approximations from Eq. (3.50) into the weak formulation (3.46) and taking the basis functions as test functions, we obtain 4×4 block matrix A and 4×1 block right-hand side vector $\mathbf{F}$, shaped as

$$A = \begin{bmatrix} \mathcal{F} & \mathcal{B} & \mathcal{E} & 0 \\ \mathcal{B}^T & \mathcal{P} & \mathcal{H} & 0 \\ \mathcal{E}^T & \mathcal{H}^T & \mathcal{S} & 0 \\ 0 & 0 & 0 & \mathcal{R} \end{bmatrix}, \qquad \mathbf{F} = \begin{bmatrix} \mathbf{F^u} \\ \mathbf{F}^p \\ \mathbf{F^d} + \mathbf{F}_c \\ \mathbf{0} \end{bmatrix}. \tag{3.51}$$

In particular, the blocks in the definition of matrix A correspond to the following group of matrices coming from standard XFEM discretization:

$$\mathcal{F} = \Delta t^{-1} M^f + A^f + C + S^{\mathbf{uu}} + G + E^{\mathbf{uu}} + D^{\mathbf{uu}}, \tag{3.52}$$

$$\mathcal{B} = B^T + E^{\mathbf{up}} + D^{\mathbf{up}}, \tag{3.53}$$

$$\mathcal{E} = E^{\mathbf{ud}}, \tag{3.54}$$

$$\mathcal{P} = S^{\mathbf{pp}}, \tag{3.55}$$

$$\mathcal{H} = E^{\mathbf{pd}}, \tag{3.56}$$

$$\mathcal{S} = \Delta t^{-2} M^m + \mu_m A^m + \lambda_m L + E^{\mathbf{dd}} + N, \tag{3.57}$$

$$\mathcal{R} = A^r, \tag{3.58}$$

where:

- $M^f_{i,j} = \int_{\Omega^f_h} \boldsymbol{\varphi}_j \cdot \boldsymbol{\varphi}_i d\Omega,$ is the fluid mass matrix (analogously for $M^m_{i,j}$);

- $A^f_{i,j} = \int_{\Omega^f_h} \left(\nabla \boldsymbol{\varphi}_j + \nabla \boldsymbol{\varphi}^T_j \right) : \left(\nabla \boldsymbol{\varphi}_i + \nabla \boldsymbol{\varphi}^T_i \right) d\Omega,$ is the fluid stiffness matrix (analogously for $A^m_{i,j}$ and $A^r_{i,j}$);

- $C_{i,j} = \int_{\Omega^f_h} \left(\Pi^n \mathbf{u}^n_h \cdot \nabla \right) \boldsymbol{\varphi}_j \cdot \boldsymbol{\varphi}_i d\Omega,$ is the linearized convective matrix;

- $B_{i,j} = - \int_{\Omega^f_h} \psi_j \nabla \cdot \boldsymbol{\varphi}_i d\Omega;$

- $L_{i,j} = \int_{\Omega^m_h} \left(\nabla \cdot \boldsymbol{\eta}_j \right) \left(\nabla \cdot \boldsymbol{\eta}_i \right) d\Omega;$

- $S^{\mathbf{uu}}_{i,j} = s^u_h(\boldsymbol{\varphi}_j; \boldsymbol{\varphi}_i),$ $S^{pp}_{i,j} = s^p_h(\psi_j; \psi_i),$ are the stabilization matrices associated to the Continuous Interior Penalty term $s_h = s^u_h + s^p_h$ defined in Eq. (3.32);

- $G_{i,j} = g_h(\boldsymbol{\varphi}_j; \boldsymbol{\varphi}_i),$ is the stabilization matrix associated to the ghost-penalty term g_h defined in Eq. (3.33);

- $E^{\mathbf{uu}}_{i,j} = \mathcal{I}^{\mathbf{uu}}_h(\boldsymbol{\varphi}_j; \boldsymbol{\varphi}_i),$ $E^{\mathbf{up}}_{i,j} = \mathcal{I}^{\mathbf{up}}_h(\psi_j; \boldsymbol{\varphi}_i),$ $E^{\mathbf{ud}}_{i,j} = \mathcal{I}^{\mathbf{ud}}_h(\boldsymbol{\eta}_j; \boldsymbol{\varphi}_i),$

$E_{i,j}^{p\mathbf{d}} = \mathcal{I}_h^{p\mathbf{d}}(\boldsymbol{\eta}_j; \psi_i)$, $\quad E_{i,j}^{\mathbf{dd}} = \mathcal{I}_h^{\mathbf{dd}}(\boldsymbol{\eta}_j; \boldsymbol{\eta}_i)$, $\quad$ are the matrices coming from the interface term $\mathcal{I}_h = \mathcal{I}_h^{\mathbf{uu}} + \mathcal{I}_h^{\mathbf{u}p} + \mathcal{I}_h^{\mathbf{ud}} + \mathcal{I}_h^{p\mathbf{d}} + \mathcal{I}_h^{\mathbf{dd}}$ for the DG mortaring at the fluid-strucure interface (see Eq. (3.36));

- $D_{i,j}^{\mathbf{uu}} = \mathcal{D}_h^{\mathbf{uu}}(\boldsymbol{\varphi}_j; \boldsymbol{\varphi}_i)$, $\quad D_{i,j}^{\mathbf{u}p} = \mathcal{D}_h^{\mathbf{u}p}(\psi_j; \boldsymbol{\varphi}_i)$, $\quad$ are the matrices obtained from the approximation of the DG term $\mathcal{D}_h = \mathcal{D}_h^{\mathbf{uu}} + \mathcal{D}_h^{\mathbf{u}p}$ for the weak continuity at the fluid-fluid interface of split elements (see Eq. (3.37));

- $N_{i,j} = C_h(\boldsymbol{\eta}_j, \boldsymbol{\eta}_i)$, $\quad$ is the contact matrix from Eq. (3.44).

Analogously, we can define the blocks for the vector $\mathbf{F}$ as:

- $\mathbf{F}^{\mathbf{u}} = \mathcal{F}_h^{\mathbf{u}}(\boldsymbol{\varphi}_i)$, $\quad \mathbf{F}^p = \mathcal{F}_h^p(\psi_i)$, $\quad \mathbf{F}^{\mathbf{d}} = \mathcal{F}_h^{\mathbf{d}}(\boldsymbol{\eta}_i)$ $\quad$ including all the terms from Eq. (3.38), such that $\mathcal{F}_h = \mathcal{F}_h^{\mathbf{u}} + \mathcal{F}_h^p + \mathcal{F}_h^{\mathbf{d}}$;

- $\mathbf{F}_c = \mathcal{F}_c(\boldsymbol{\eta}_i)$ $\quad$ coming from the right-hand side term of the contact model in Eq. (3.45).

Notice that the structure of matrix A in Eq. (3.51) highlights that the mechanics of the magnet ring are not coupled with the rest of the pump system in this model. Indeed, the mechanic coupling of the magnet ring with the membrane as well as the coupling with the fluid are surrogated with the Dirichlet condition Eq. (3.3d)-(3.3e). Nonetheless, the geometric coupling between the fluid domain and the magnet ring displacement, that is not directly visible in matrix A, still holds true.

At each time iteration, the linear system given by Eq. (3.47) is solved in a monolithic approach using the Generalized Minimum Residual Method (GMRES) iterative solver. Since GMRES is a Krylov sub-space method, the solution corresponds to the minimizer of the residual $\mathbf{r}$ of the linear system projected on the Krylov sub-spaces

$$K^l(A, \mathbf{r}) = \text{span}\left\{\mathbf{r}, A\mathbf{r}, \dots, A^{l-1}\mathbf{r}\right\} \qquad \text{with} \quad \mathbf{r} = \mathbf{F} - A\mathbf{x}^0,$$

with $\mathbf{X}^0$ being an initial guess. Thus, we have that

$$\mathbf{x} = \min_{\mathbf{x}^l \in K^l} ||\mathbf{F} - A\mathbf{x}^l||. \tag{3.59}$$

As the convergence rate of the minimization problem (3.59) highly depends on the condition number of the matrix A, a preconditioner matrix P is applied to the linear system, *i.e.*

$$P A \mathbf{x} = P \mathbf{F}. \tag{3.60}$$

Specifically, we used the block Gauss-Seidel preconditioner, proposed in [113] that is

$$P^{GS} = \begin{bmatrix} \mathcal{F} & \mathcal{B} & \mathcal{E} & 0 \\ \mathcal{B}^T & \mathcal{P} & \mathcal{H} & 0 \\ 0 & 0 & \mathcal{S} & 0 \\ 0 & 0 & 0 & \mathcal{R} \end{bmatrix}, \tag{3.61}$$

which neglects the coupling term blocks in the third row $\mathcal{E}^T$ and $\mathcal{H}^T$.

3.5   Why XFEM?

Numerical solution of the fluid-structure interaction dynamics in Wave Membrane Blood Pumps (WMBPs) is particularly demanding for three main reasons: i) the pump system presents a large and complex geometry, including multiple moving structures; ii) the wave membrane, located in the narrow pump head area, undergoes to displacements that are the same order of magnitude of the dimension of the local fluid region; iii) during such wave motion, potential contact of the elastic membrane may occur with pump walls, depending on the operating conditions of the device and the elasticity properties of the membrane. In addition, being an industrial problem, the computational times should be minimized as much as possible to be compliant with typical industrial timeframes and produce relevant insight for pump design and development. For such reasons, the numerical approach used to handle such a problem should be robust with respect to the issues above.

In most FSI problems, the Arbitrary Lagrangian-Eulerian (ALE) fitted mesh method represents the golden standard numerical technique, thanks to its accuracy, efficiency, ease of implementation, and validation in many real-life engineering fields [154, 167, 234]. Indeed, it allows to simply handle the geometric coupling at the FS interface as well as the imposition of the physical coupling conditions. However, in case of WMBPs, the deformation of the fluid mesh induced by the wave membrane motion would cause high distortion of the fluid elements in the pump head and consequently it would require frequent application of remeshing procedures. Notice that remeshing is not only computationally expensive, but it may introduce also interpolation errors during the data-mapping of the fluid solution from old mesh to the new mesh. Moreover, the ALE formulation may fail in case of dry contact (*i.e.*, with no interstitial fluid) because of the zero-volume elements locally generated when the membrane is in contact with the fluid boundary.

Being an unfitted mesh method, XFEM avoids the issues linked to element distortion or contact by using a fixed background mesh. Moreover, the generation of unfitted meshes is also more practical, especially in case of complex geometries, because internal boundaries do not have to be considered. Compared with other unfitted techniques, such as Immersed Boundary (IB) or Ficticious Domain (FD), XFEM is more capable to sharply capture the fluid-structure interface boundary by means of geometric cuts between meshes and to represent the consequent discontinuities without loss of accuracy. Indeed, thanks to the enrichment of specific features of the standard Finite Element Method (FEM), the XFEM approach can handle a wider variety of physical problems than FEM, possibly characterized by discontinuities, local deformations and complex geometries [182].

However, XFEM technique is generally more difficult to implement than other unfitted approaches, due to the geometric complications underneath the cut mesh operations, especially in three dimensions. Indeed, at each time step, this technique requires the computation of the intersections between the solid and the background meshes, that can be particularly challenging in parallel environments where each processor stores a local sub-portion of the different meshes. Moreover, the implementation should also handle the integration of the solution in the generated sub-elements, either by means

of an interface-fitted sub-tethahedralization, as in [315], or, in case of particularly irregular geometries, using higher order Gaussian quadrature, as in [254]. Notice that, as the cut of the structure is purely arbitrary, the sub-elements may have infinitesimal volume or a very complex shape, thereby challenging the online meshers used for the sub-tetrahedralization. Finally, the data structure for the background mesh should be organized very efficiently to easily enable dof dropping on the hidden elements and dof enrichment on the split elements.

Given the novelty of the XFEM numerical technique, there are fewer examples of its applications than for other established methods such as ALE. For instance, to our knowledge, the XFEM strategy is employed in this study for the first time on a real industrial 3D problem. In addition, it is still unclear how to extend the XFEM formulation to higher order degree Finite Elements [316].

In this work, we specifically refered to the implementation of the XFEM-DG environment proposed in [315, 316], that was developed within the C++ Library of Finite Elements (LIFEV) [26]. The code was previously tested in several 3D scenarios with simple physical geometries and the accuracy of the results were successfully compared with ALE method in [315]. However, the bottleneck of this computational XFEM framework is represented by the mesh intersection step: indeed, although the FSI problem is solved in a multi-thread environment, the mesh intersections are computed serially. On the one hand, this approach ensures that all processors store the same fluid cut-mesh; on the other hand, it increases computational time and memory usage. In our experience, computational times ranged between 1 to 4 weeks, depending on operating conditions, discretization parameters and computational resources. Nonetheless, we believe that a fully parallel implementation of the XFEM approach may result in an accurate, verstatile and relatively efficient tool for numerical simulations in WMBPs.

Another topic that could be addressed in future works in order to improve efficiency is the development of a suitable, *ad hoc* preconditioner for the problem

Chapter 4

Results

In this chapter, we present three numerical tests performed in the Wave Membrane Blood Pump (WMBP):

- **Test I: FSI in flat WMBP** (Section 4.2). A Fluid-Structure Interaction (FSI) problem solved in the flat membrane pump design of WMBP, see Design A in Figure 2.6. Validation results against experimental data are provided.

- **Test II: FSCI in J-shape WMBP** (Section 4.3). A Fluid-Structure-Contact Interaction (FSCI) problem solved in the J-shape membrane pump design, see Design B in Figure 2.6. More realistic operating conditions are considered and the relaxed contact model from Section 3.2.2 is added to handle the potential contact between the wave membrane and the pump walls. This test addresses the comparison of the performance between the two pump designs and a parametric analysis over the operating conditions of the device with respect to hydraulic output and hemocompatibility.

- **Test III: Membrane anti-symmetries** (Section 4.4). A preliminary investigation on the development of secondary non axi-symmetric deformations, said *anti-symmetries*, in the wave membrane for a specific operating point of the WMBP.

Before reporting the results for each test, we present in Section 4.1 the pipeline for the generation of the unfitted computational meshes and the convergence study.

4.1 Meshing in WMBPs

4.1.1 Pre-processing meshing pipeline

The generation of the computational meshes can be particularly challenging in WMBPs due to the complex geometry of the domain and the presence of multiple immersed thin structures. In the unfitted framework of Extended Finite Element Method (XFEM), the meshing step is simplified with respect to fitted mesh methods, because the meshes can be generated independently for each component of the pump system, without any constraint of fitting with internal surfaces.

In this work, we pursued the following pipeline to create the computational meshes for the numerical simulations in WMBPs:

1. The developing company provided surface geometries for the main components of the WMBP system, derived from computer-assisted-design (CAD) models. Specifically, Standard Triangle Language (STL) files were generated for the pump chamber (background) and for the two main structures (foreground), the wave membrane and the magnet ring. In this process, some boundaries of the pump housing were smoothen and, as discussed in Sect. 3.1.1, the fixation system that mechanically connects the membrane to the magnet ring was omitted from the computational domain.

2. The STL files were remeshed using GMSH software [118] to construct a more refined triangulation of the boundaries of the domains, using the MeshAdapt method [118]. In this step, the mesh boundaries were reclassified to assign proper tags with respect to the different boundary conditions to prescribe on the pump system (*e.g.*, 1 for the inlet, 2 for the outlet, 3 for the walls, etc.). The output of this step is a MSH file for each component of the system.

3. Volume meshes of tetrahedral elements were constructed starting from the surface reparametrization of Point 2 using the Delaunay algorithm [243] of GMSH. The characteristic length h of the elements may be varied in space using designed geometric filters, said *fields*, based on element location or local curvature, to further improve mesh quality. Output files are again in MSH format.

4. Finally, the format of the 3D meshes was converted from MSH to MESH format using Python, in order to be compliant with the requirements of the finite element library LIFEV [26].

4.1.2   Meshes for flat and J-shape pump designs

The unfitted 3D meshes for the numerical simulations were derived using the procedure described in paragraph 4.1 for both the flat membrane pump design and the J-shape membrane pump design, introduced in Section 2.3.

The 3D meshes for the flat pump design are shown in a perspective and a cross-sectional view in Figure 4.1a. In this case, we can observe a uniform discretization, i.e. with fixed mesh size $\tilde{h}$[1], for the background mesh $\mathcal{T}_h$, that counts $1.2M$ elements. Instead, the characteristic length of the membrane mesh $\mathcal{T}_h^m$, counting $280k$ elements, was varied in space using a distance-based field based on the radial distance of the elements (see Figure 4.1b). In particular, as the thickness of the membrane disc decreases in radial direction towards the center, the mesh discretization was set in such a way to obtain at least 3 elements spanning its thickness, in order to guarantee a correct propagation of the progressive waves along the elastic medium. Finally, in Figure 4.1c, we report the magnet ring mesh $\mathcal{T}_h^r$, which has $250k$ elements. Notice

---

[1]The value of mesh step $\tilde{h}$ is not specified for confidentiality reasons, as it could be used to reconstruct the dimensions of the pump geometry.
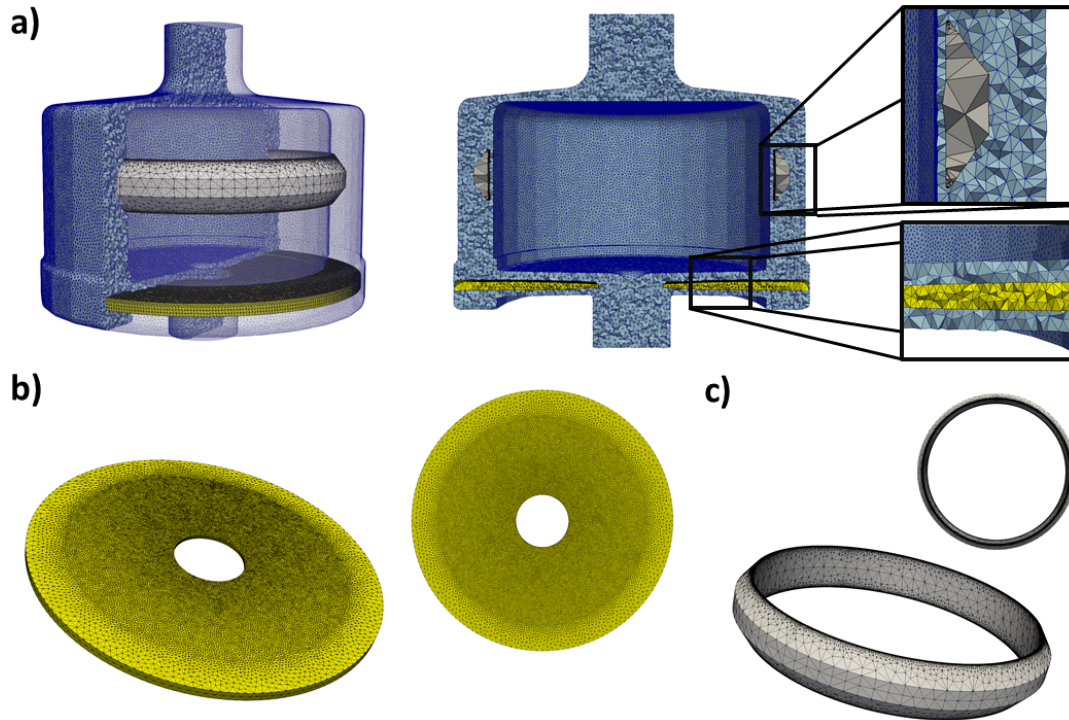
FIGURE 4.1: Volume meshes for flat membrane pump design. a) Perspective and cross-sectional view of the unfitted meshes, with focus on the magnet and pump head regions. b) Flat membrane mesh. c) Magnet ring mesh.

that the quality of the mesh inside the magnet domain is not relevant, as the latter is modeled as a rigid structure and we are not interested in its internal stresses.

In the J-shape pump design (Figure 4.2), all the meshes were locally refined using geometric fields in regions with high curvature or of interest for the pump dynamics. Specifically, in the background mesh $\mathcal{T}_h$ ($1.65M$ elements), the mesh size in the magnet region was set to be similar to the one used for the flat mesh ($h \simeq \tilde{h}$), while it was halfed in the pump head region ($h \simeq \tilde{h}/2$), where the wave membrane propagation occurs, and doubled at the inlet region ($h \simeq 2\tilde{h}$), where the dynamics are less disturbed. In the membrane mesh $\mathcal{T}_h^m$ ($935k$ elements), the mesh size is decreased in radial directon, as for the flat design, and at the high-curvature membrane edge, while it is higher in the remaining part of the membrane periphery, corresponding to the rigid membrane holder region. Finally, the magnet mesh $\mathcal{T}_h^r$ ($380k$ elements) presents a higher refinement on the boundary with respect to the flat pump design because of the more curved and larger geometry of the ring. Notice that the meshes in the J-shape design have a higher number of elements than the corresponding ones in the flat design, mainly due to the larger geometries of each component (wider flow channels, vertical elongations of the membrane holder, larger magnet ring). Moreover, the membrane mesh was further refined, reaching a minimum of 4 elements through its thickness, to ensure a correct wave propagation also at the high oscillating conditions and avoid element inversions. Indeed, as will be specified in Section 4.3, the J-shape membrane will be simulated for higher oscillating conditions (*i.e.* higher stroke parameter, lower frequency) and different elasticity parameters, resulting in larger deformations of the flexible wave membrane than the ones observed in the flat membrane.

a)

b)

c)
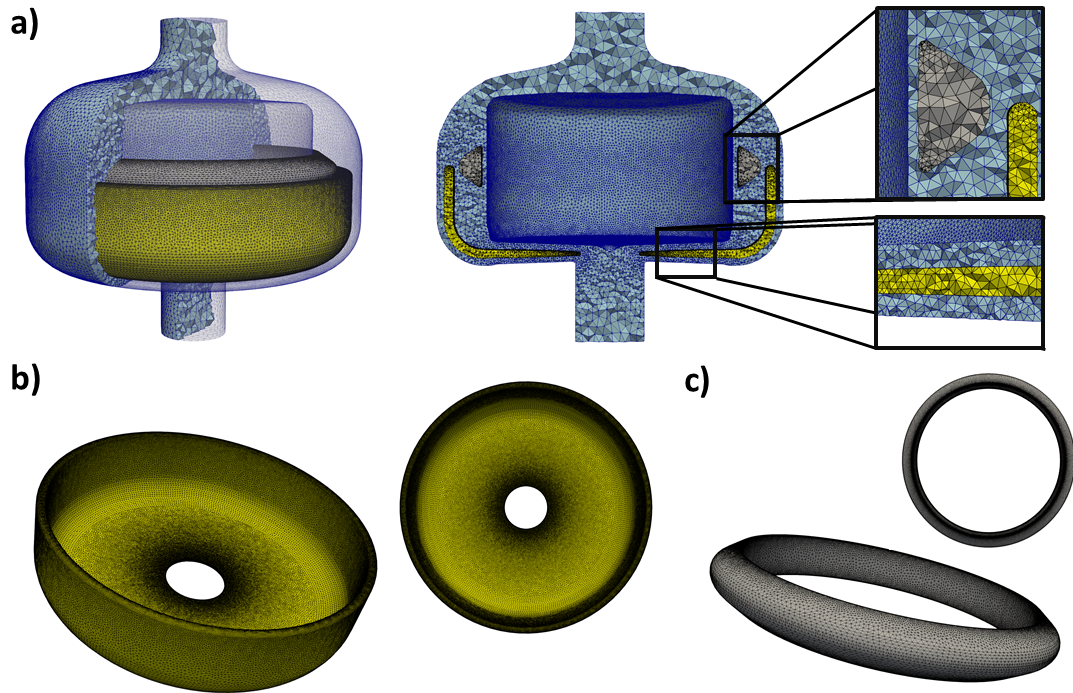
FIGURE 4.2: Volume meshes for J-shape membrane pump design. a) Perspective and cross-sectional view of the unfitted meshes, with focus on the magnet and pump head regions. b) J-shape membrane mesh. c) Magnet ring mesh.

As the meshes for the J-shape design have a high number of elements, we decided to adopt a reduced geometry approximation by taking the 120-degree section of the pump domain, as explained in Section 3.1.4. Thus, the meshes for the J-shape pump design, shown in Figure 4.3 were generated in the reduced geometry, with similar characteristic lenghts. Indeed, the resulting meshes present roughly one third of the elements compared with the full meshes ($\mathcal{T}_h$: 520k, $\mathcal{T}_h^m$: 390k, $\mathcal{T}_h^r$: 140k). Notice that, in Figure 3.1.4a, the pump domain presents an additional geometric detail at the inlet, consisting of a curved deviation, that we refer to as *inlet cuspid*. The introduction of the inlet cuspid in the pump design will be studied in Section 4.3.1. Such variation motivates the smaller mesh size in the inlet region in the mesh in Figure 3.1.4a than the one in Figure 4.2. The detail of the structure meshes is reported in Figure 3.1.4b. The application to the reduced geometry approximation allowed to significantly reduce the memory usage and the computational time, with a speed-up of 5, allowing to carry over three-dimensional simulations in less than a week.

We can observe that in both pump designs there is a very small gap between the magnet mesh and the side wall of the actuator, said *magnet clearance gap*. In such region, the use of the unfitted meshes allowed us to avoid high distortion of the interstitial fluid elements during vertical oscillations of the magnet ring. Similar discussion can be addressed to the narrow gap in the pump head region dividing the flexible wave membrane from the pump walls, said pump head flanges.
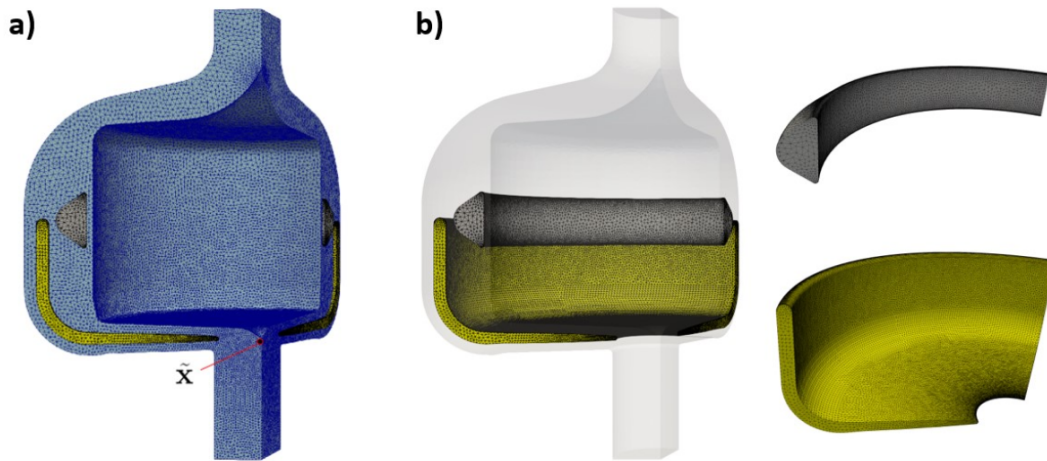
FIGURE 4.3: Volume meshes in the 120-degree J-shape pump geometry. a) Perspective visualization of the unfitted meshes. Point $\tilde{\mathbf{x}} = [0, 0, 1.4]$ used for convergence analysis. b) Focus on the structure meshes.
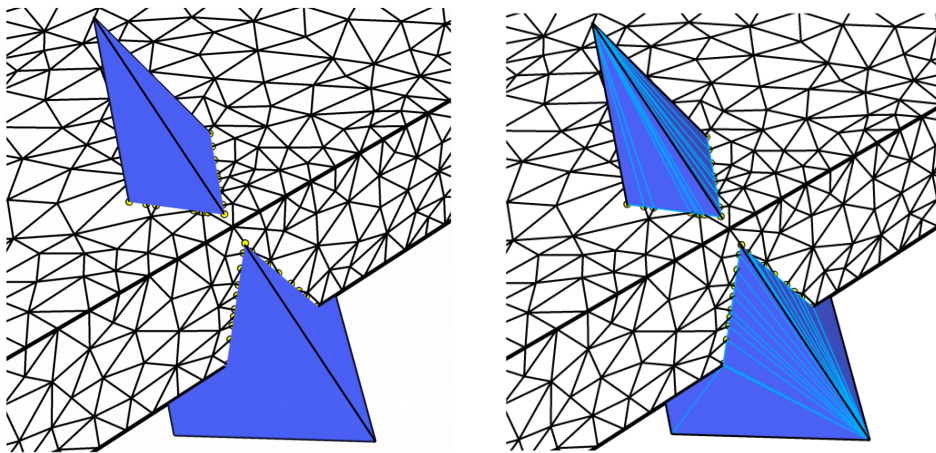
FIGURE 4.4: Cut mesh operations on a split element (blue). Left: Identification of intersection points (yellow dots). Right: Inteface-fitted sub-tetrahedralization on both sub-elements. Figures are taken from [315].

4.1.3 Issues in fluid cut-mesh generation

We remind the reader that in the XFEM framework the fluid mesh is obtained at each time step by cutting the background mesh at the intersections with the structure meshes. Such arbitrary cut operations can lead to a variety of undesired geometric configurations in case of complex geometries, such as in WMBPs. For instance, the generated sub-elements, that are in general polyhedra, can be convex or concave, with a stretched shape or with very small volume. In our work, we found that, in order to reduce the instances of similar degenerated configurations, the quality of the input meshes (both the background and the structure meshes) should be optimized. Specifically, we employed Netgen optimizer tools in GMSH aimed at correcting the improve the aspect ratio of elements with quality index lower than 0.3-0.5.

A second major issue in the generation of the fluid cut-mesh was the sub-tetrahedralization
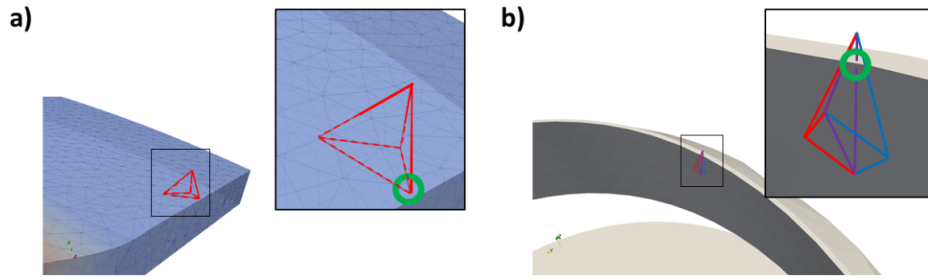
FIGURE 4.5: Examples of sub-tetrahedralization error for small volume partition (green circle) at the interface with the membrane holder (a) or with the magnet ring (b). Volumes are magnified for sake of visualization.

step, that in our implementation of XFEM is required in order to carry over the integration over the visible (*i.e.* not overlapped) sub-portions of the background element. In this step, each sub-element is divided in a sum of sub-tetrahedra where the fluid solution can be easily integrated using the standard Gaussian quadrature rule. Notice that the sub-tetrahedralization is constrained by requiring that the intersection points between the background elements and the structure mesh are vertices of the sub-grid (see Figure 4.4), to ensure the conformity between facing elements, as explained in [315]. However, the sub-tetrahedralization procedure, that was initially delegated to external libraries Triangle [263], for 2D meshing, and TetGen [264], for 3D meshing, may fail in case of particularly complex volumes or configurations, generating sub-tetrahedra with zero or negative volume. For instance, in Figure 4.5 we report two scenarios where the sub-tetrahedralization was not successful due to the small volume of the input partition generated by the cut, because the cut occurs either very close to a vertex (as at the interface with the membrane holder in Figure 4.5a) or in correspondance to a sharp angle of the structure (as at the interface with a magnet edge in Figure 4.5b). In our experience, the likelihood of success of TetGen meshing increased by iteratively changing the input seed for the internal randomized operations or the approximations of the input coordinates. Nonetheless, it was still not robust enough to handle the iterative automatic meshing in our working scenario. Therefore, we employed a second in-house sub-meshing algorithm, that is the *advancing front algorithm* [197, 240] (ADF), in combination with TetGen: indeed, for each sub-element, ADF was used first, while TetGen was called only in case of failure of ADF. Such combined approach has allowed to significantly increase the robustness of the sub-tetrahedralization and overcome issues such as the ones depicted in Figure 4.5.

Finally, an automatic perturbation procedure was implemented to handle the few remaining instances of sub-tetrahedralization failure. Indeed, when both ADF and TetGen algorithms fail the sub-meshing of a specific sub-element, the displacement of the structure that generates the cut is perturbed, locally or globally, so that the shape of that sub-element can be potentially solved during the sub-tetrahedralization step. Notice that magnitude of the solution perturbation is of 1 nm, corresponding to $\sim 10^{-6}$ of membrane displacement. In our experience, the perturbation approach always solved the issues in the cut-mesh operations, that were not handled by the traditional tools described above.

4.1.4 Convergence study

The meshes presented in Section 4.1.2 for the different pump designs were selected because they showed positive convergence results with respect to the solutions computed on further refined meshes. Specifically, we report the details of the mesh convergence study in the reduced pump meshes, shown in Figure 4.3. The simulation parameters for this convergence study were: $H = 60$ mmHg, $f = 50$ Hz, $\Phi = 1.5$ mm, $P^{out} = 120$ mmHg, $\gamma_\Sigma = 10^5$, $\gamma_{dg} = 10^3$, $\gamma_v = 0.05$, $\gamma_{div} = 0.5$, $\gamma_p = 0.01$, $\gamma_g = 1$, $\gamma_c^0 = 1 \cdot 10^5$, and $\varepsilon_c = 0.01$ cm. The results were studied across four different grids with decreasing mesh size h, with a fixed timestep $\Delta t = 0.0004$ s. The refinement ratio $r_i = h_{i-1}/h_i$, with h_i being a representative fluid mesh discretization parameter for the $i - th$ mesh, was computed for each grid i. The indices used for the convergence analysis were typical quantities to evaluate the performance in blood pumps, that are (i) the time-averaged flow rate Q at the outlet Γ^{out}, (ii) the mean pressure $p^{\tilde{\mathbf{x}}}$ and (iii) a scalar representation $\sigma^{\tilde{\mathbf{x}}}$ of the mean stress at a point $\tilde{\mathbf{x}} \in \Omega^f(t)$. Specifically, we took $\tilde{\mathbf{x}} = [0.0, 0.0, 1.4]$, which is located along the pump longitudinal axis, at the center of the pump head (see Figure 4.3a).

Table 4.1 reports the values of such quantities and the corresponding approximated relative differences. The fluid mesh with $520k$ elements (mesh index $i = 3$) showed good convergence properties, since the relative errors are lower than 2% on hydraulic quantities (e_4^Q, e_4^p) and less than 5% for the hemocompatibility index (e_4^σ) [193].

Mesh i	N_i	r_i	Q_i [l/min]	e_i^Q	$p_i^{\tilde{\mathbf{x}}}$ [mmHg]	e_i^p	$\sigma_i^{\tilde{\mathbf{x}}}$ [Pa]	e_i^σ
1	323k	·	1.24	·	121.50	·	0.41	·
2	440k	1.17	3.33	0.627	122.76	0.021	1.145	0.64
3	520k	1.05	3.09	0.077	123.09	0.005	1.025	0.12
4	700k	1.11	3.15	0.019	122.95	0.002	1.079	0.05

TABLE 4.1: Mesh sensitivity analysis. N_i and r_i are the number of fluid mesh tetrahedra and the refinement ratio, respectively. The values of convergence indices $\psi = \{Q_i, p_i^{\mathbf{x}}, \sigma_i^{\tilde{\mathbf{x}}}\}$ are presented for each mesh i, together with the corresponding approximated relative difference $e_i^\psi = |\psi_i - \psi_{i-1}|/|\psi_i|$.

Similarly, the effect of time discretization was studied by varying the timestep parameter Δt. As the choice for the timestep depends on the frequency of oscillation f, we set the frequency for this analysis to the typical value for the J-shape pump design, *i.e.* $f = 60$ Hz, and we tested the variation on the results when Δt is halved from 0.0004 s (42 time points per cycle) to 0.0002 s (84 time points per cycle). The other parameters for these simulations were: $H = 80$ mmHg, $\Phi = 1.8$ mm, $P^{out} = 120$ mmHg, $\gamma_\Sigma = 10^5$, $\gamma_{dg} = 10^3$, $\gamma_v = 0.1$, $\gamma_{div} = 0.5$, $\gamma_p = 0.01$, $\gamma_g = 1$, $\gamma_c^0 = 5 \cdot 10^5$, and $\varepsilon_c = 0.2$ mm. Analogously to what done for the grid sensitivity, Table 4.2 reports the convergence indices and the corresponding relative errors for flow rate, pressure and scalar stress. The results, featuring a maximum relative difference of 6.6%, indicate that it is sufficient to select the timestep so that 42 time points are taken for each period of oscillation [193]. Hence, for the operating points tested in this work, the timestep Δt was fixed to 0.0004 s when $f \leq 60$ Hz, and halved to 0.0002 s for the simulations when $f = 120$ Hz.

Time i	Δt [s]	N^τ	Q_i [l/min]	e_i^Q	$p_i^{\tilde{\mathbf{x}}}$ [mmHg]	e_i^p	$\sigma_i^{\tilde{\mathbf{x}}}$ [Pa]	e_i^σ
1	0.0004	42	4.83	·	131.7	·	2.25	·
2	0.0002	84	5.03	0.04	135.8	0.03	2.11	0.066

TABLE 4.2: Time sensitivity analysis. The timestep Δt is halved from 0.0004 s to 0.0002 s. N_τ indicates the number of timesteps per period of oscillation, for $f = 60$ Hz. The values of convergence indices $\psi = \{Q_i, p_i^{\mathbf{x}}, \sigma_i^{\tilde{\mathbf{x}}}\}$ are presented for each time index i, together with the corresponding approximated relative difference e_i^ψ.

Analogous conclusions were reached for the space and time discretizations in the case of the flat pump design, but, for sake of simplicity, the convergence study was carried out in a smaller geometry, limited to the lower pump head region [194]. For the operating condition studied in the flat design, *i.e.* $f = 120$ Hz, $\Phi = 1.06$ mm, no significant changes have been observed in the flow rate or in the membrane displacement by further refining the mesh. In fact, the simulation results on such meshes showed very good agreement with experimental data, as will be described in Section 4.2.

4.2   Test I: FSI in flat WMBP

In this section, we report the three-dimensional numerical results obtained by solving the Fluid-Structure Interaction (FSI) problem given by (3.40) in the flat membrane pump design (see Design A in Figure 2.6).

We remind to the reader that in WMBPs the operating conditions of the device are defined by the following parameters:

a) the head pressure H between the outlet and the inlet ports;

b) the frequency f of membrane oscillation;

c) the oscillation stroke Φ, corresponding to twice the amplitude of the membrane vibration.

In this scenario, we fixed the oscillating parameters of the magnet ring and the membrane holder to frequency $f = 120$ Hz and stroke $\Phi = 1.06$ mm and we studied the pump performance at different pressure conditions. Specifically, we considered different values of head pressure $H = P^{out} - P^{in} = \{50, 55, 60\}$, indicating the hydraulic resistance inside the pump, and we fixed the pressure at the outlet P^{out} to 120 mmHg, corresponding to the systolic aortic pressure. The physical parameters used for the FSI simulations are detailed in Table 4.3.

The background and structure meshes for these simulations are shown in Figure 4.1 and the timestep Δt is fixed to 0.0002 s, as discussed in Section 4.1.4. The numerical parameters that are common to all the simulations in this section are: $\gamma_\Sigma = 10^6$, $\gamma_{dg} = 10^3$, and $\gamma_g = 1$. We remind the reader that the contact model is not employed in this section, since the oscillating parameters do not lead to collisions with the pump head flanges, see Section 3.2.1.

Physical parameter	Value	Unit
ρ_f : Blood mass density	1050	$[Kg/m^3]$
μ_f : Blood dynamic viscosity	0.0035	$[Pa \cdot s]$
ρ_m : Membrane mass density	1125	$[Kg/m^3]$
λ_m : Membrane first Lamé's parameter	2772	$[MPa]$
μ_m : Membrane second Lamé's parameter	56.6	$[MPa]$

TABLE 4.3: Values of the physical parameters of the main components of the pump system used in the numerical experiments. Test I: FSI in flat WMBP.

The main objective of these simulations is twofold: first, we want to better understand the pumping principle in membrane-based blood pumps via numerical investigation and provide quantitative information on the hydraulic performance and the potential for blood trauma in the flat membrane pump design; second, we aim at validating the numerical approach based on XFEM-DG strategy, by comparing the simulation results against experimental data [194].

4.2.1 Flow field analysis and volume conservation

In this section, we study the simulation results in the flat WMBP when the head pressure is set to $H = 50$ mmHg. We simulated the pump system for $T = 0.025$ s, which is equivalent to three periods of oscillation for the magnet ring and the membrane holder, which corresponds to the rigid external part of the membrane disc. The Continuous Interior Penalty (CIP) parameters used for this simulation were: $\gamma_v = 0.05$, $\gamma_{div} = 0.5$, $\gamma_p = 0.05$.

A view of the simulation results is reported in Figure 4.6, where the fluid velocity (a) and pressure (b) fields are shown in a cross-section of the pump domain at time $t = 0.0188$ s, together with the vertical displacement of the immersed structures. Zooms of the fluid dynamics around the magnet ring and the membrane are reported in the right panel of Figure 4.6. The time instant corresponds to the moment when the membrane holder reaches its top dead center (*i.e.* the point of maximum amplitude of oscillation) during the third cycle of oscillation. Such results confirm that the propelling action derived from the progressive wave propagation along the membrane succeeds in generating positive outflow (see Figure 4.6, left), despite the adverse pressure difference existing between the endings of the pump domain. In particular, referring to Figure 4.6b, we can identify three sub-regions in the pressure field: i) a low-pressure area (region A), extending from the inlet down to the membrane holder; ii) a high-pressure area (region B), in proximity to the outlet channel; and the so-called *fluid pocket* (region C), consisting of the fluid portion enclosed between the wave membrane and the pump head flange. The propagation of the fluid pockets in the pump head is at the core of wave pumping mechanism: indeed, by means of the progressive wave, the membrane actively transports the fluid pocket from region A to region B, going against the direction of the pressure gradient (see Figure 4.6b, right). In addition, by looking at the pressure field in the remaining part of the pump domain, outside the pump head region, we can see that the pressure gradient favors blood propulsion through the pump: specifically, in region A, blood flows from the

a)

b)
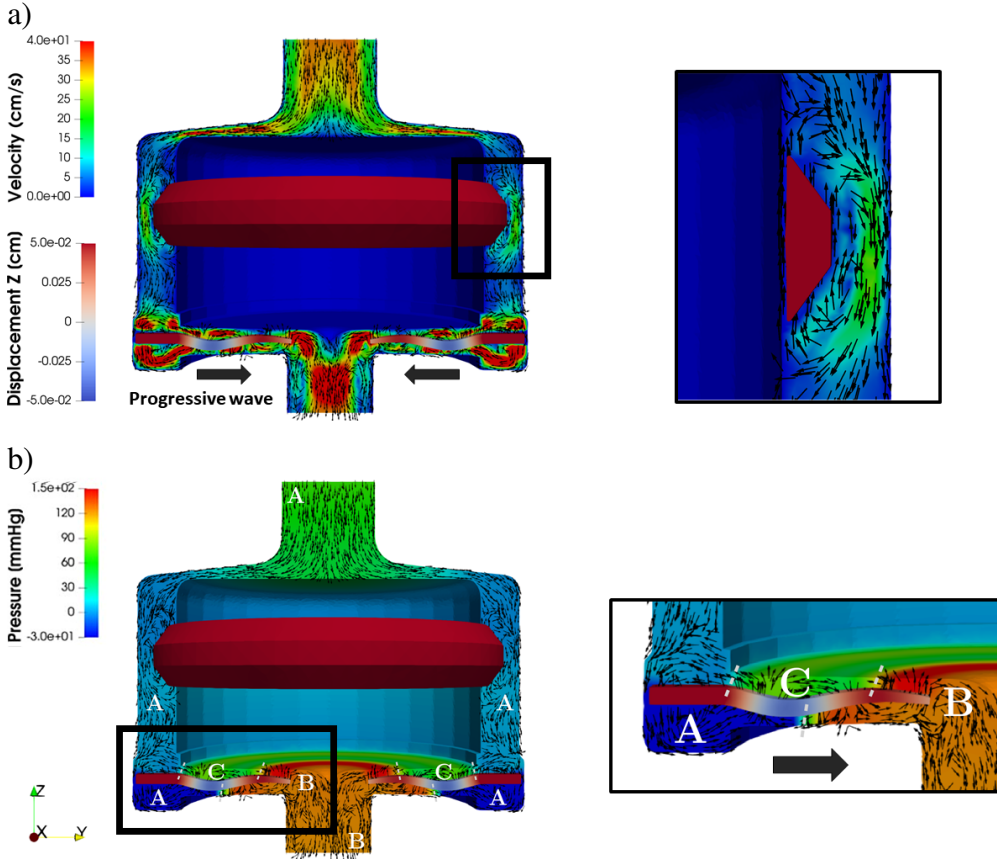
FIGURE 4.6: Cross-sectional view of the fluid-structure interaction results in the three-dimensional flat pump domain at time $t = 0.0188$ s. a) Fluid velocity field and vertical displacement of the flexible membrane, with focus on the magnet ring region. b) Fluid pressure field divided in regions A, B, and C, with zoom on the pump head. Test I: FSI in flat WMBP.

inlet (green) down to the membrane holder (blue); while, in region B, it is propelled from the membrane tip (red) into the outlet channel (orange).

The success of the wave membrane pumping technology is also confirmed by the analysis of the volume balance reported in Figure 4.7, left, where we showed the evolution in time of the incoming and outcoming blood volumes V_{in} and V_{out}, representing the volumes of blood entering in and exiting from the pump domain, respectively. These volume quantities were computed integrating the corresponding volumetric flow rate using the trapezoidal rule. Hence, we have $V_{\beta}^n = \frac{\Delta t}{2}(Q_{\beta}^n + Q_{\beta}^{n-1})$, $\beta = \{in, out\}$, where Q_{in} and Q_{out} are the computed pump inflow and outflow rates, respectively. Notice that, after a short interval of adaptation, the two curves V_{in} and V_{out} start oscillating with the same period of the membrane vibrations, *i.e.* with period $\tau = f^{-1} = 0.0083$ s. Since the contribution of the divergence of the velocity is very small ($< 3 \cdot 10^{-4}$ cm^3), the small discrepancy between V_{in} and V_{out} is due to the slight incremental variation of the structure volume $\Delta V_s^n = |\Omega_h^{m,n}| - |\Omega_h^{m,n-1}|$, with $\Omega_h^{m,n}$ being the discretized membrane domain at time $t^n = n\Delta t$. (Notice that since the magnet ring is a rigid structure, it was not considered in the volume balance). Indeed, we have $V_{out}^n - V_{in}^n \simeq \Delta V_s^n$ for all n. We remark that, as we impose the Discontinuous Galerkin (DG) approach on the faces of the fluid split elements at the interface (see Eq. 3.37),
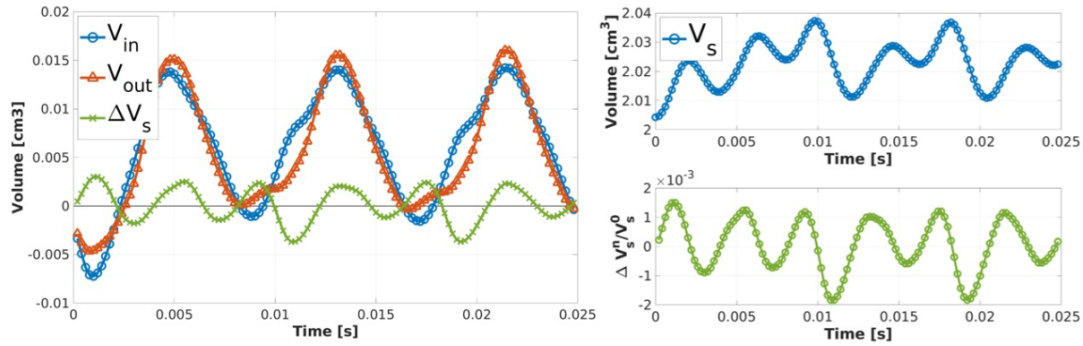
FIGURE 4.7: Left: Volume conservation through time. Right: Time evolution of structure volume V_s (above) and of the incremental deformation ΔV_s relative to the initial volume V_s^0. Test I: FSI in flat WMBP.

there are potential losses of volume due to the weak continuity of the solution that formally need to be considered for the balance, but that we found to be negligible ($< 5 \cdot 10^{-5}$ cm^3).

By looking at the trend in time of the structure volume V_s (Figure 4.7, right), we can observe the variation of the membrane volume corresponds to a relative incremental change of less than 2‰ of the initial volume of the membrane V_s^0. This small variation is explained by the not complete incompressibility of the membrane ($\nu_m = 0.49$) and by the numerical approximation. Nevertheless, we verified that such volume variation decreases when the mesh size h is reduced.

We conclude our analysis of the flow field in Figure 4.6 by noticing recirculation regions around the magnet ring (in region A) and nearby the outlet channel (in region B). In view of a clinical analysis of the pump, the effect of recirculation regions needs to be closely investigated, because it may lead to local thrombus formation, especially if it comes with flow stagnation [66, 104]. However, in this case, the flow in the recirculation areas is continuously disturbed, making the risk of thrombogenesis very low. Nonetheless, as we will see in Section 4.3, the design of the WMBP was updated to the J-shape design with the aim to reduce the risk of recirculations and improve hemocompatibility.

4.2.2 Study of wave membrane deformation

Since the propulsion effect in WMBPs is caused by the wave propagation in the flexible membrane, we studied the displacement in time of three key points of the membrane section (Figure 4.8, center): the leading edge (blue), extracted from the membrane holder, the trailing edge (red), in correspondence to the membrane tip, and a third point in-between in the membrane section (green), see Figure 4.8, left. Since the motion of the membrane holder is governed by (3.4), the leading edge oscillates between -0.53 mm and 0.53 mm with an excitation frequency equal to 120 Hz. The displacement curves of the midpoint and the trailing edge also become periodic, with the same frequency of the leading edge. In particular, we can notice that the midpoint shows an oscillation amplitude that is smaller than the one of the leading
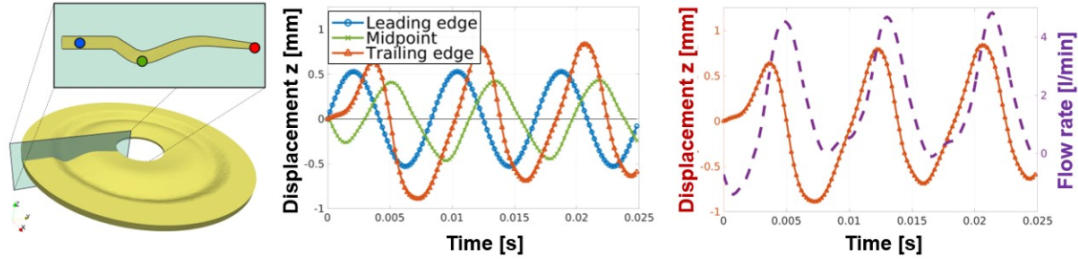
FIGURE 4.8: Left: The three points of the membrane section: the leading edge (blue), the trailing edge (red) and a midpoint in between (green). Center: Vertical displacement of the three points of the membrane through time. Right: Time trend of trailing edge displacement (red) and pump volume outflow (purple, dashed). Test I: FSI in flat WMBP.

edge, that is likely due to the damping effect of the surrounding viscous fluid on the membrane motion. However, the trailing edge actually is the point that undergoes to the highest displacement, because the most internal portion of the membrane is thinner and therefore it offers less inertial resistance to the wave elastic motion. In fact, the cross-section of the membrane is designed to make the membrane tip to approach as much as possible to the pump head flanges, allowing for the isolation of the fluid pockets and for the blockage of possible backflows. Accordingly, in Figure 4.8, right, we highlight the link between the displacement of the trailing edge and the flow rate signal at the pump outlet: the latter follows the dynamics of the trailing edge with a small delay due to the time needed for the propagation of the blood from the pump head throughout the outlet channel.

Furthermore, membrane deformation was analyzed by constructing the *membrane envelope*, which is obtained by reducing the membrane cross-section to its centerline (see Figure 4.9, left) and plotting its displacement during one cycle of oscillation. The black lines in Figure 4.9, right, indicate the relative distance of the centerline from the pump head flanges, taking into account the increasing thickness of the membrane disc in radial direction. The visualization of the membrane envelope confirms that the tip of the membrane is the point of the cross-section that approaches the most to the pump wall, particularly to the superior flange. More importantly, such analysis shows that, for the tested operating conditions, no point of the membrane section reaches the collision point with the pump head flanges during the whole period of oscillation, thereby validating the choice of not adding the contact model for these simulations. Finally, we can notice that, for this simulation, the envelope is not fully symmetric, suggesting that the fluid forces exerted on the membrane are different on the two sides of the membrane disc during the oscillation cycle.

4.2.3   Fluid pocket propagation

The main effect of the wave membrane deformation in the flow dynamics is represented by the propagation of the fluid pockets, which are masses of fluid that are enclosed in the space delimited by the membrane and the pump head flanges. Indeed, referring to Figure 4.6, the progressive wave along the membrane transports the fluid
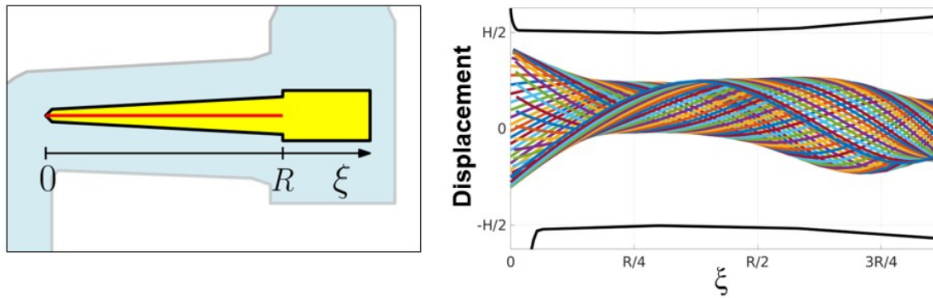
FIGURE 4.9: Left: Introduction of the radial coordinate ξ along the membrane centerline (red). Right: Membrane envelope. Black lines indicate the relative distance from the pump head flanges. The membrane radius R, the pump head height H and the membrane displacement for $\psi = R$ are not shown for confidentiality reasons. Test I: FSI in flat WMBP.

pockets from the low-pressure region at the periphery of the membrane disc to the high-pressure region at the center of the pump head, in proximity to the outlet channel.

In order to better understand the processes of formation, transportation and delivery of the fluid pockets during the work cycle of the membrane, we analyzed in Figure 4.10 the dynamics in the pump head region at four different time instants in the third period of oscillation of the membrane holder, showing for each time point the radial velocity of the flexible membrane, the blood velocity (left) and pressure (right) fields. Some comments follow.

  i) In Figure 4.10a, the membrane holder has returned back to its initial position coming from below. During this upwards vertical displacement, part of the blood coming from the inlet flows above the membrane wave, leading to the formation of an upper fluid pocket (Pocket A), while the remaining part is gathered in the low pressure area below the membrane holder. Meanwhile, in the most internal part of the pump head, another fluid pocket (Pocket B) below the membrane is transported towards the outlet channel thanks to the progressive propagation of the membrane wave. Notice that the simultaneous propagation of two fluid pockets is made possible by the high frequency of oscillation that introduces a second mode of deformation in the elastic membrane. We can also notice some recirculation areas nearby the membrane holder and in proximity to the membrane tip, caused by the flapping motion of the membrane [288].

  ii) When the membrane holder reaches the top dead center (time $t = 0.0188$ s), the formation of the upper fluid pocket (Pocket A) is completed and the blood below the membrane holder reaches its point of maximum accumulation (see Figure 4.10b). While the membrane tip is raising to reduce potential backflows, we can observe a local increase of the pressure in that area that contributes to the blood propulsion towards the outlet. Nonetheless, the ongoing vortex dynamics below the trailing edge of the membrane seems to hamper the full release of the lower fluid pocket (Pocket B) in the outlet channel, penalizing the overall outflow.

  iii) As the membrane holder moves downwards (Figure 4.10c), it compresses the fluid accumulated in the area below during the ascending phase. This causes a drastic increase of the pressure below the membrane, that strongly propels the
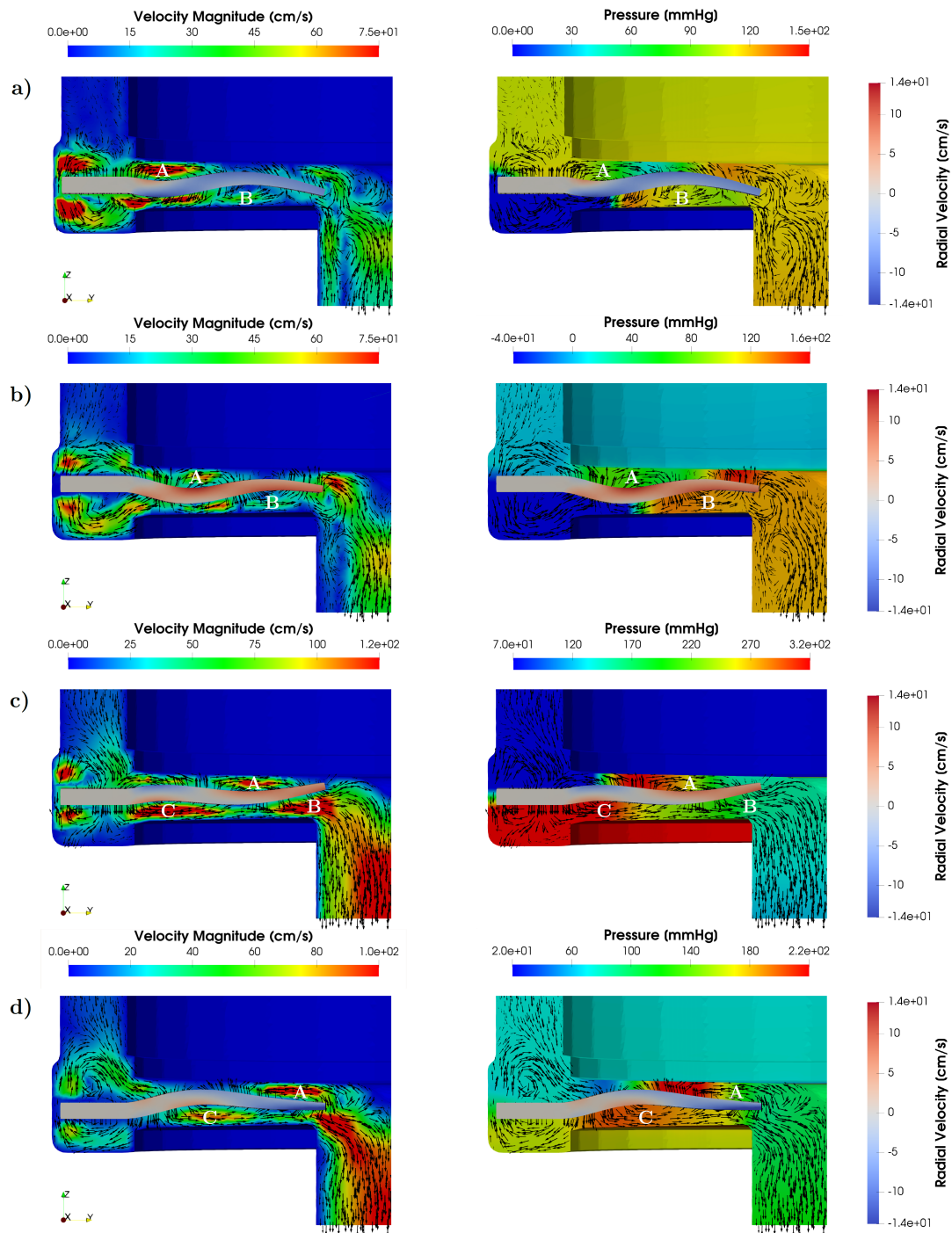
FIGURE 4.10: Visualization of the velocity field (left) and of the pressure field (right) in a vertical section of the pump head region for four different time instants: a) $t = 0.0166$ s, b) $t = 0.0188$ s, c) $t = 0.0208$ s, and d) $t = 0.0228$ s. Capital letters A, B and C indicate the fluid pockets, getting formed and transported by wave propagation. Test I: FSI in flat WMBP.

blood in the outlet direction, contributing to the formation of a new lower fluid pocket (Pocket C). Above the flexible membrane, the upper fluid pocket (Pocket A) proceeds in its radial propagation and the tip of the membrane has reached its point of minimum distance from the superior pump flange. Although we cannot consider this as a contact configuration, we can observe that the velocity values around the membrane tip are very low, indicating that potential backflows are minimized. Moreover, this configuration of the membrane tip allows to achieve the point of maximum delivery of the fluid pocket below (Pocket B). The combination of these phenomena results in successful pumping dynamics and in rapid increase of the blood outflow.

iv) Then, the membrane holder reaches the bottom dead center, completing the formation of the new fluid pocket (Pocket C) below the flexible membrane, see Figure 4.10d. Furthermore, blood from the upper pocket (Pocket A) is delivered into the outlet channel, and the cycle can restart.

4.2.4 Blood shear rate and wall shear stress analyses

As discussed in Section 1.3.3.2, high hydrodynamic stress conditions in LVADs are strictly linked to blood adverse events, because they may cause blood cells damage and consequent leak of hemoglobin (hemolysis) [12, 20, 106], or trigger von Willebrand factor (VWF) adhesion, leading to platelet aggregation and, ultimately, thrombogenesis [257, 311, 261].

As preliminary investigation of the potential for blood trauma in the flat design, we report in Figure 4.11 the values of the shear rate γ in the fluid domain and of Wall Shear Stress (WSS) at the fluid boundaries. Specifically, we chose to analyze the solution at time $t = 0.0208$ s, when the pump outflow rate is maximum and the magnet ring and the membrane holder return to their initial position with maximum velocity (see Figure 4.10c).

In Figure 4.11a, we can observe that the areas with higher shear rate ($\gamma > 1500 \ s^{-1}$) are located in the pump head region (Point 1), where the fluid pockets are transported by the membrane progressive wave with high velocity, and in the upper part of the pump domain (Point 2), where blood flows in a narrow channel. In particular, peak values of shear rate around $3500 - 4500 \ s^{-1}$ are reached under the flexible membrane, where the blood velocity is higher than 1 $^m/_s$, and, in particular, at the periphery of the membrane disc (Point 3). The same observation applies to the WSS quantity, that presents peaks of $\sim$ 10 Pa in small regions of the pump head region, corresponding overall to 0.28% of total surface area of the pump. However, the observed shear rate values are still inferior than 5000 s^{-1}, that is the threshold value for the start of VWF-mediated platelet adhesion process [257]. Moreover, since the flow is very disturbed in that area, the exposure time is very short, furtherly reducing the risk of hemolysis or thrombosis. In particular, in the right-bottom panel of Figure 4.11a, we checked the evolution in time of the shear rate at the side of the membrane holder, by looking at the maximum and the mean values achieved in this area (see red box in Point 3) during the third period of membrane oscillation. The plot highlights that the trend of the shear rate is periodic and that the maximum value in this region, i.e.
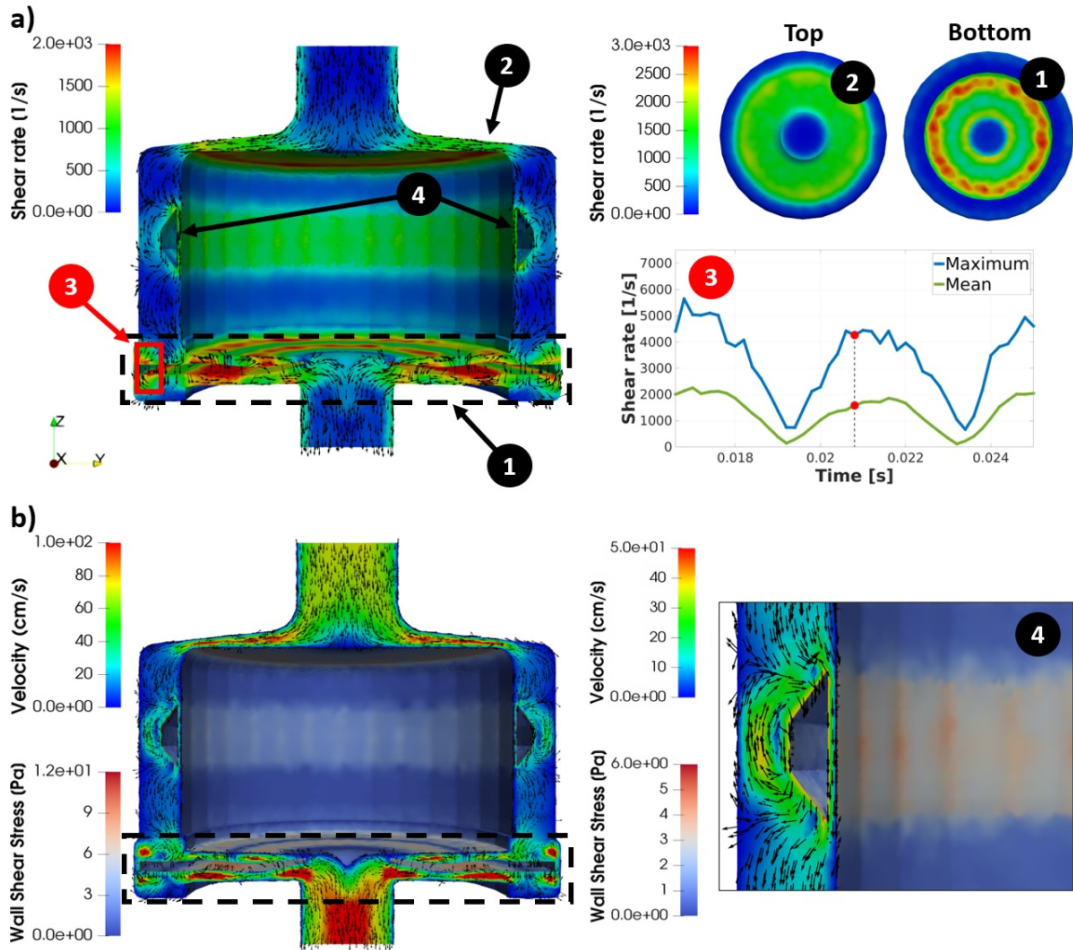
FIGURE 4.11: Study of the blood shear rate and Wall Shear Stress (WSS) at time $t = 0.0208$ s. a) Visualization of the shear rate at the cross section (left panel) and on the superior and inferior external pump surfaces (right superior panel). The points of interest are: 1) pump head region, 2) superior pump housing surface, 3) side of membrane holder, and 4) magnet clearance gap. In particular for Point 3, we show the trend in time of the maximum and the mean values of shear rate in the control volume highlighted by the red box (right inferior panel). b) Cross-sectional view of WSS (left), with focus on the magnet ring region (right). Test I: FSI in flat WMBP.

$\gamma^{max} = 5640 \ s^{-1}$, is reached during the upward displacement of the membrane holder at time $t = 0.0166$ s (see Figure 4.10a). Nevertheless, this value is still one order of magnitude smaller than the reference critical value of $42000 \ s^{-1}$, that corresponds to the areal strain limit for red blood cells [20].

Another region of interest for shear analysis is the gap between the magnet ring and the pump walls (Point 4). In this area, shear rate is actually smaller than $1000 \ s^{-1}$, in accordance with the lower magnitude of fluid velocity, and the local average of WSS amounts to 3.32 Pa (see Figure 4.11b, right). Moreover, we observed that the shear rate decreases to less than $300 \ s^{-1}$ when the magnet reaches the top or the bottom dead center (zero velocity). Nevertheless, the size of the magnet clearance gap has been enlarged in the J-shape design, considered for the analysis in Section 4.3, with the aim to further minimize any risk of hemolitic impact.

4.2.5 Validation against experimental measures

In this section, we report results about the validation of the proposed numerical model applied to the flat pump configuration. To this aim, we compared our FSI simulation results with experimental measurements obtained when testings the wave membrane blood pump working at the same operating conditions.

In particular, the hydraulic performance of the blood pump was assessed by means of *in-vitro* testings perfomed in a pump characterization bench, consisting of a reservoir and tubing in which the hydraulic resistance can be set by adding centrifugal pumps in a series circuit with the WMBP. A glycerin-water solution at 39% concentration in volume (37 °C) was used to mimic blood. The system for pump characterization is equipped with a polycarbonate hose-barb pressure sensor (PendoTECH, France), to measure the pressure difference arisen between the outlet and the inlet ports of the pump, and with an ultrasonic flowmeter (Sonotec, Germany) clamped adjacent to the LVAD outlet, to measure the pump outflow volume rate. Therefore, for any given operating point of the wave membrane, we can combine such measurements in pressure-flow data curves, called *HQ curves*, which describe the hydraulic performance of the pump when exposed to different pressure conditions. Specifically, we have at our disposal the HQ curve of the flat WMBP when the operating point of the membrane is fixed to $f = 120$ Hz and $\Phi = 1.06$ mm, which are the oscillating parameters considered in this section.

In view of the comparison with the experimental HQ curve, we extended the numerical analysis to different pressure conditions, varying the value of the head pressure H in $\{50, 55, 60\}$ mmHg. Such values are taken from the pressure data in the available HQ curve and are compliant with the range of standard head pressure conditions used for *in-vitro* and *in-vivo* tests in other blood pumps, as in [304, 205]. For this set of simulations, we used $T = 0.02$ s. Table 4.4 reports the values of the penalty parameters used for this set of simulations to ensure stability for each flow regime.

	$H = 50$ mmHg	$H = 55$ mmHg	$H = 60$ mmHg
γ_v	0.05	0.05	0.5
γ_{div}	0.5	0.5	5
γ_p	0.05	0.1	0.1

TABLE 4.4: Penalty stability parameters for different pressure conditions. Test I: FSI in flat WMBP.

In Figure 4.12, left, we report the trends in time of the volume flow rate at the outlet for each tested head pressure value. Notice that the main physical principle in pump functioning is respected in the numerical simulations: for a fixed operating point of the device, as the pressure difference H acting over the pump between outlet and inlet increases, the hydraulic resistance in the pump gets stronger and, consequently, LVAD output gets smaller. Indeed, in our results, the amplitude of the outflow volume rate curves is lower for larger values of head pressure H. Notice that, although in all the cases there are time intervals with negative outflow rate, the average in time of the flow rate at the outlet is always positive, as required by the correct functioning of the pump.
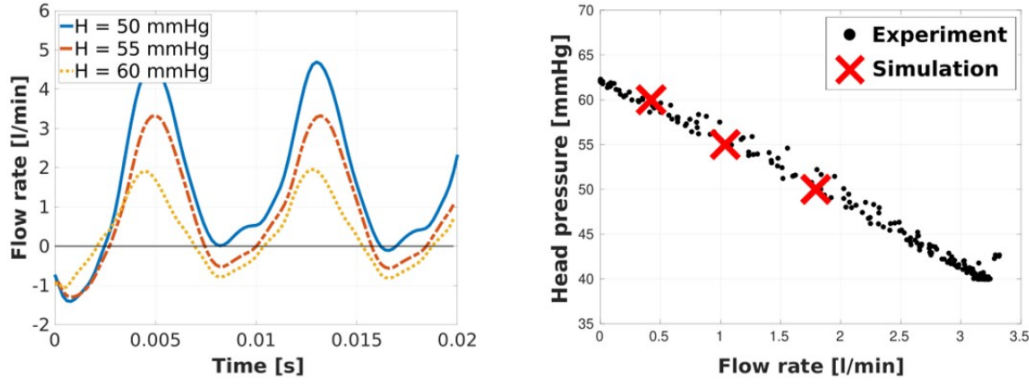
FIGURE 4.12: Left: Time profile of the outflow volume rate for three different head pressure conditions H.   Right: Validation of the model results (red crosses) against the *in-vitro* experimental data (black dots). Test I: FSI in flat WMBP.

The comparison of the numerical results with the experimental data is reported in the plot in Figure 4.12, right. Each black dot corresponds to a data point $\left(Q^{data}, H^{data}\right)$ of the HQ curve, where H^{data} is obtained as the average in time of the head pressure in the pump and Q^{data} is the corresponding measured ouflow rate. The slope of the curve is similar to the one of other reference HQ curves of centrifugal LVADs found in literature (see Figure 1.11, right), indicating that, for this operating point, the sensitivity of the pump is in line with the standards in the LVAD community. The red crosses in the plot are the numerical outflow flow rate Q^{sim} corresponding to the pressure differences $H \in \{50, 55, 60\}$ mmHg. Specifically, the flow rate was computed as the average in time of the flow rate at the outlet during the last simulated period of oscillation, *i.e.*

$$Q^{sim} = \frac{1}{\tau} \int_{T-\tau}^{T} \int_{\Gamma^{out}} \mathbf{u}(\mathbf{x}, t) \cdot \mathbf{n} \, d\mathbf{x} dt, \tag{4.1}$$

where the integrals are computed using the trapezoidal rule. Thus, in Figure 4.12, right, we can observe a very good agreement between numerical results and experimental findings.

In addition, in Table 4.5 we reported the comparison between the estimated flow rate Q^{sim} with the experimental data $\tilde{Q}^{data}$, where the latter corresponds to the measurement associated to the data point that minimizes the gauge $|\tilde{H}^{data} - H|$.

	$H = 50$ mmHg	$H = 55$ mmHg	$H = 60$ mmHg
$\tilde{Q}^{data}$	1.834 l/min	1.091 l/min	0.352 l/min
Q^{sim}	1.792 l/min	1.039 l/min	0.400 l/min
$|\tilde{Q}^{data} - Q^{sim}|$	0.042 l/min	0.052 l/min	0.048 l/min

TABLE 4.5: Experimental and simulation data for the model validation against experimental mesures. $\tilde{Q}^{data}$ values correspond to the outflow measurements of the data points with the closest pressure to H. Test I: FSI in flat WMBP.

These results highlight a very good quantitative agreement with the experimental findings, meaning that the numerical model is able to quantitatively reproduce the pump dynamics with good confidentiality for the analyzed pressure conditions. Indeed, the prediction errors are small for all considered head pressure values; in particular, the relative error is lower than 5% for $H = \{50, 55\}$ mmHg, that are the working conditions corresponding to higher pump flow support.

We can conclude that the proposed computational model is able to predict with excellent accuracy the behavior of the WMBP for the tested operating parameters, despite the simplifications underneath its modeling. Nevertheless, we note that the operating conditions of the pump considered for the model validation do not correspond neccesarily with those required for the final application of the pump. Indeed, in the next section, we will employ operating parameters that are closer to the clinical application of WMBPs.

4.3 Test II: FSCI in J-shape WMBP

In this section, the numerical simulations are performed in the J-shape design of WMBP, which differs from the older flat design considered in Section 4.2 especially in the geometry of the membrane holder, see Figure 2.6. The pump system is here tested on a wider range of operating conditions, that may potentially lead to contact between the wave membrane and the pump walls. For this reason, we solve the Fluid-Structure-Contact Interaction (FSCI) problem given by (3.46), which includes the penalization contact model proposed in [103]. Unless differently specified, the contact parameters employed for the simulations were $\varepsilon_c = 0.01$ cm and $\gamma_c^0 = 10^5$. The results of these simulations were presented in [193].

Thus, the goals of the numerical study in the J-shape WMBPs are summarized in the following list:

1. compare the pump performance of WMBPs in the new J-shape design with the one in the flat design (Sect. 4.3.1);

2. illustrate the effect of the added relaxed contact model (see Sect. 3.2.2) in the numerical results (Sect. 4.3.2)

3. perform a parametric analysis to study the sensitivity of the solution on each operating parameter, both addressing hydraulic performance and potential for hemocompatibility (Sect. 4.3.3);

4. study of a new operating point at diastolic head pressure (*nominal operating condition*), in view of potential WMBP application in human patients (Sect. 4.3.4).

Notice that the numerical simulations were carried out in the 120-degree pump meshes shown in Figure 4.3. We observed that using the reduced geometry approximation we get a mean prediction error of 4.9% in flow and of 8.5% in membrane centerline displacement with respect to the corresponding results in the full geometry, but with a speed-up in computational times of 5 times.
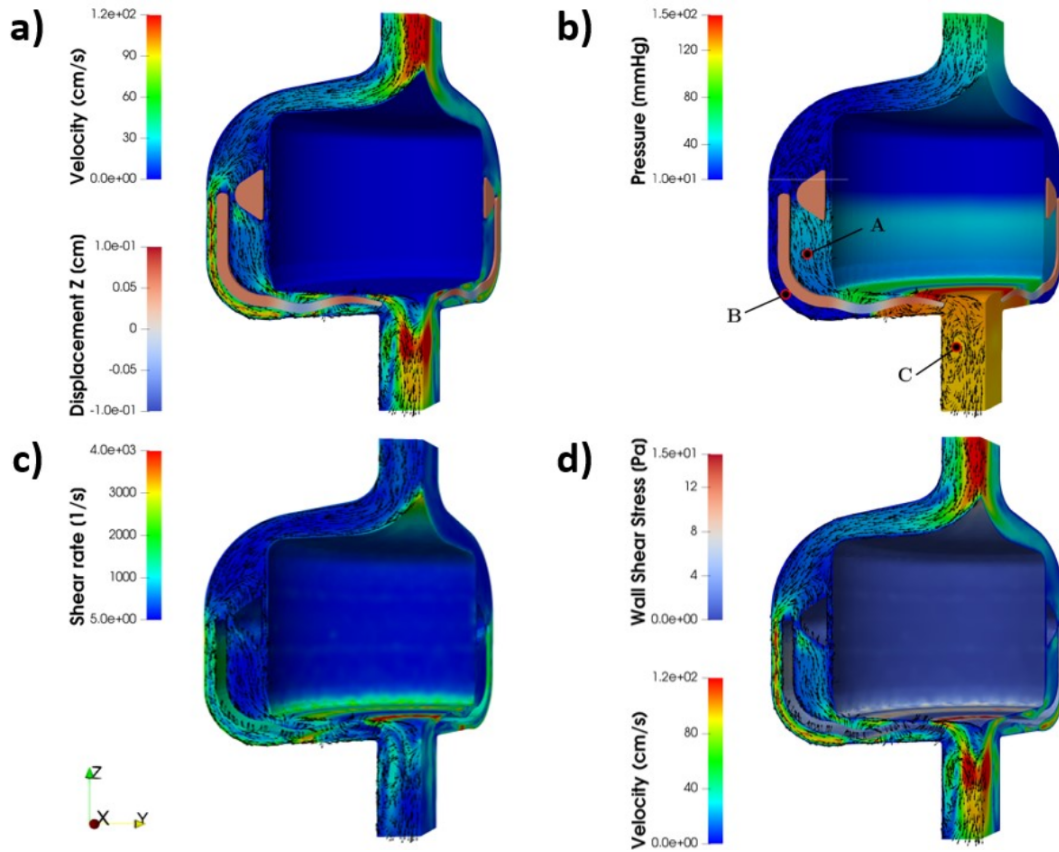
FIGURE 4.13: Visualization of membrane displacement, blood velocity (a), pressure (b), shear rate (c) and wall shear stress (d) fields at time $t = 0.0188$ s (instant of maximum oscillation) in the J-shape pump for $H = 50$ mmHg. Test II: FSCI in J-shape WMBP.

4.3.1   Design comparison

The performance of WMBP with J-shape and flat pump designs was compared when the two devices operate at the same working conditions. Hence, similarly to what done for the flat design in Section 4.2.5, we simulate the pump system with the J-shape design for oscillating parameters $f = 120$ Hz and $\Phi = 1.06$ mm and head pressure $H = \{50, 60\}$ mmHg. We will refer to this set of operating points as High-Frequency (HF) points. For sake of comparison, we also employed the same set of physical parameters (Table 4.3) and of numerical parameters used in Section 4.2. In particular, the total simulation time is set to $T = 0.025$ s, corresponding to three periods of oscillation, with a fixed timestep equal to $\Delta t = 0.0002$ s.

In Figure 4.13 we report the results of membrane displacement and blood velocity (a), pressure (b), shear rate (c) and wall shear stress (d) fields for $H = 50$ mmHg, at the time instant $t = 0.0188$ s of maximum membrane oscillation (top dead center). As observed for the flat pump design, the membrane undulations generate a favorable pressure gradient from the pump flanges and the outlet, that overcomes the adverse pressure gradient between inlet and outlet. In addition, WMBPs work as displacement pumps that transport the fluid pockets from low-pressure region to the high-pressure outlet channel. However, we can notice two important differences with the results in the flat design: i) the magnitude of the blood velocity in the J-shape design

(Figure 4.13a) exceeds the values that were found in the flat design (see Figure 4.6, left), and, ii) unlike the results in the flat membrane case, no recirculation areas were found nearby the edges of the membrane holder and the magnet ring in the J-shape design. Indeed, referring to Figure 4.13b the flow coming from the inner vein of the membrane (region A) is drawn into the outer vein (region B) following the direction of the pressure gradient. The vortex located in the outlet channel (region C) is continuously disturbed at high velocities, thus prohibiting the local formation of thrombus.

As a consequence of the larger velocity scales achieved in the J-shape design, the shear stress and the Wall Shear Stress (WSS) reached higher values than in the flat pump design (see Figure 4.11). The peak values of 4000 s^{-1} for the shear rate and of 15 Pa for the WSS were found on the pump head flanges, around the membrane tip region, whereas in the flat design the maxima were achieved nearby the membrane holder. In particular, the maximum shear rate γ^{max} in time and space amounted to 17156.2 s^{-1} (vs. γ^{max} = 5640 s^{-1} in the flat design). Thus, even though, at identical operating conditions, the shear rate conditions are higher in the new design due to the increase in the flow conditions, they are still significantly lower than the critical threshold of 42000 s^{-1} [12]. Furthermore, the WSS was specifically analyzed on the boundary close to the magnet ring and shown in Figure 4.14 for both the pump designs at the time instant of maximum magnet velocity (t = 0.0208 s). The results highlighted that the extension of the clearance gap between the magnet and the wall in the new pump design allowed to reduce the average of the local WSS from 3.32 Pa in the flat design, to 2.67 Pa in the J-shape design.
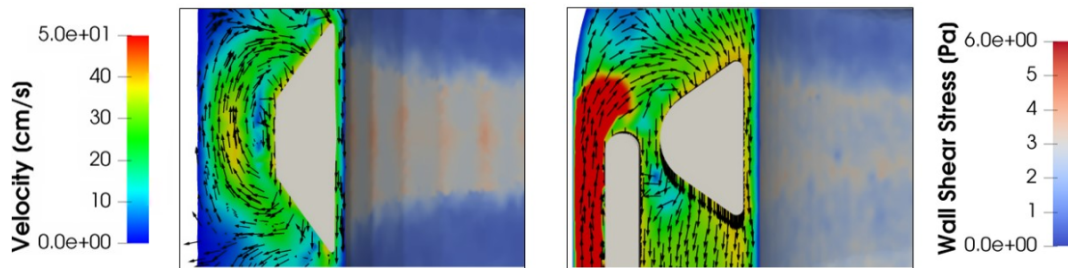
FIGURE 4.14: Comparison of wall shear stress at the wall boundary in proximity to the magnet in the flat pump design (left) and in the J-shape pump design (right) at time t = 0.0208 s (maximum magnet velocity). Test I and Test II.

Head pressure	Flat design	J-shape design
H = 50 mmHg	Q = 1.792 l/min	Q = 3.62 l/min
	W = 0.19 W	W = 0.40 W
H = 60 mmHg	Q = 0.400 l/min	Q = 2.62 l/min
	W = 0.05 W	W = 0.35 W

TABLE 4.6: Estimated time-averaged flow rate at the pump outlet (Q) and hydraulic power (W) for flat pump design and J-shape design for different pressure conditions. Comparison Test I and Test II.

In Table 4.6 we quantitatively compared the hydraulic performance in the two designs reporting the flow rate Q and the hydraulic power $W = Q H$, for $H = \{50, 60\}$ mmHg.

From these results we can observe the improved hydraulic outputs featured in the J-shape design, in terms of both outflow rate and generated power, in accordance with the experimental evidences showed in Figure 2.7. Such drastic improvement in hydraulic power could be ascribed mainly to the curved and elongated membrane geometry that allowed to separate the flow across the two sides of the membrane holder, reducing flow recirculations around the magnet (see recirculation areas in Figure 4.14) and thereby decreasing the dissipation of hydraulic energy. We also noticed that the addition of the inlet cuspid in the design of the flow path in the new pump domain has not shown evident signs of improvement in pump performance. Indeed, the comparison of the fluid dynamics in the inlet area in Figure 4.15 when the cuspid is excluded (left) or included (right) highlights only light reductions in flow recirculation, that are local in both time and space and do not affect significantly the global pump operation.
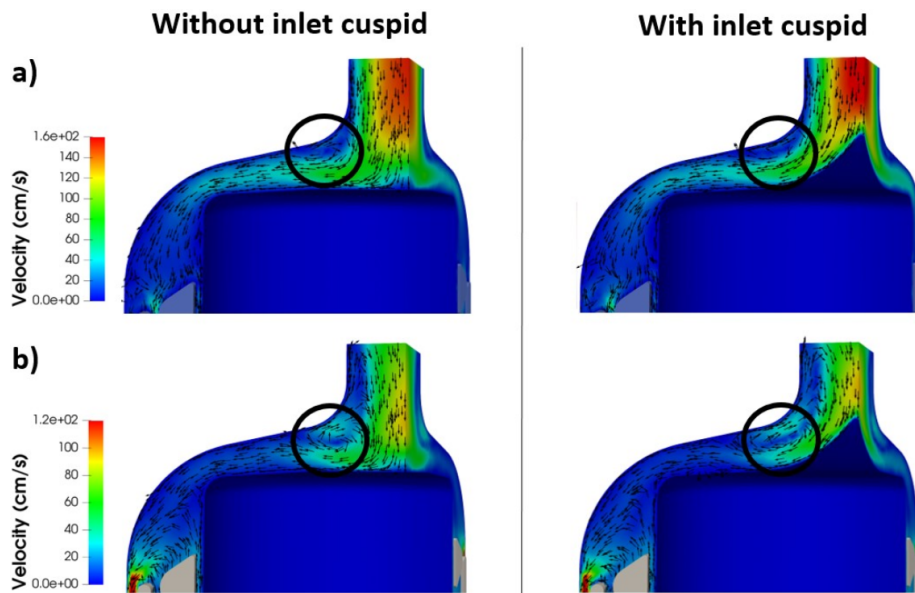
FIGURE 4.15: Comparison of fluid dynamics in J-shape pump domain without (left) and with (right) inlet cuspid at time instants of zero velocity (a) and maximum velocity (b). Black circles identify the local recirculation regions. Test II: FSCI in J-shape WMBP.

As the magnitude of the membrane deformation is limited for the HF operating conditions and very similar to what seen in the membrane envelope analysis for the flat design in Figure 4.9, the contact model was not strictly needed for these simulations. Indeed, we noticed that the relaxed contact model was never activated, because the membrane oscillations were not wide enough to enter inside the contact layer.

4.3.2   Effect of the contact model

The contact model described in Section 3.2.2 was introduced to handle at the numerical level the potential recurring impingement between the wave membrane and the pump head flanges at high oscillations. Indeed, if the membrane deformation is particularly high, as a result of high stroke or different elasticity parameters, the
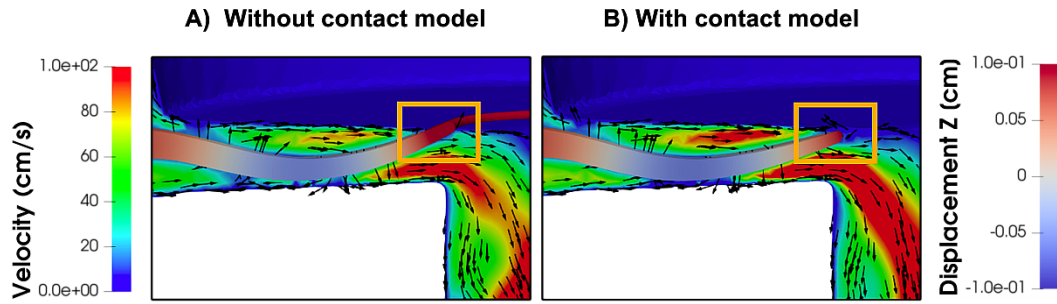
FIGURE 4.16: Snapshot of numerical simulation without (A) and with contact model (B) at time t = 0.044 s. The orange box identifies the region of highest membrane deformation, that causes the exit of the membrane from the pump fluid domain when no contact model is considered. Contact parameters for case B are: ε_c = 0.02 cm, $\gamma_c^0 = 10^5$. Test II: FSCI in J-shape WMBP.

wave membrane may exit from the pump domain if no contact model is considered. For instance, in Figure 4.16A, we show the membrane tip exiting from the superior pump head flange, when the stroke parameter is Φ = 1.5 mm, that is 41.5% larger than the corresponding value in the HF operating points considered for Section 4.3.1. This results in a non-physical configuration that causes a sudden drop in the flow rate at the outlet. Instead, in presence of the contact model, the repulsive contact force χ, defined in (3.15), is activated, prohibiting the membrane from exiting the fluid domain and penetrating into the wall (see Figure 4.16B).

The effectiveness of the contact model depends on two parameters: the thickness of the contact layer ε_c and the penalty constant γ_c^0, see (3.14). If ε_c is too narrow or if γ_c^0 is too low, the contact force enabled in the contact layer cannot push the membrane away, obtaining a result very similar to that reported in Figure 4.16A. Moreover, as discussed in Section 3.2.2, γ_c^0 should be taken sufficiently large to ensure numerical consistency. However, at the same time, too high values of ε_c and γ_c^0 should be avoided as well, because the contact model may interfere with the natural wave propagation of the membrane deformation. Indeed, in Figure 4.17, we can see that for $\gamma_c^0 = 10^6$ the wave propagation between subsequent time instants may be significantly affected, causing artificial tilting and vibration effects, thereby violating the validity of the results. As a result, in our work, the contact parameters were selected for each set of oscillating parameters following a conservative approach, taking the smallest ones in these ranges that guaranteed non-penetration of the moving structure.

In our simulations, we used $\varepsilon_c \in [0.005, 0.02]$ cm and $\gamma_c^0 \in \left[5 \cdot 10^4, 5 \cdot 10^5\right]$, depending on the magnitude of the oscillation parameters. Parameter values in the cited ranges allowed proper representation of the contact dynamics, with a variability in the mean flow at the pump outlet below 5%. Notice that values of contact parameters outside the given ranges may still be admissible, but have not been investigated in this work. Nevertheless, different choices of contact parameters are not expected to significantly affect the flow results, as long as non-physical phenomena, such as mesh penetration or abrupt deviations from regular wave propagation, are avoided.
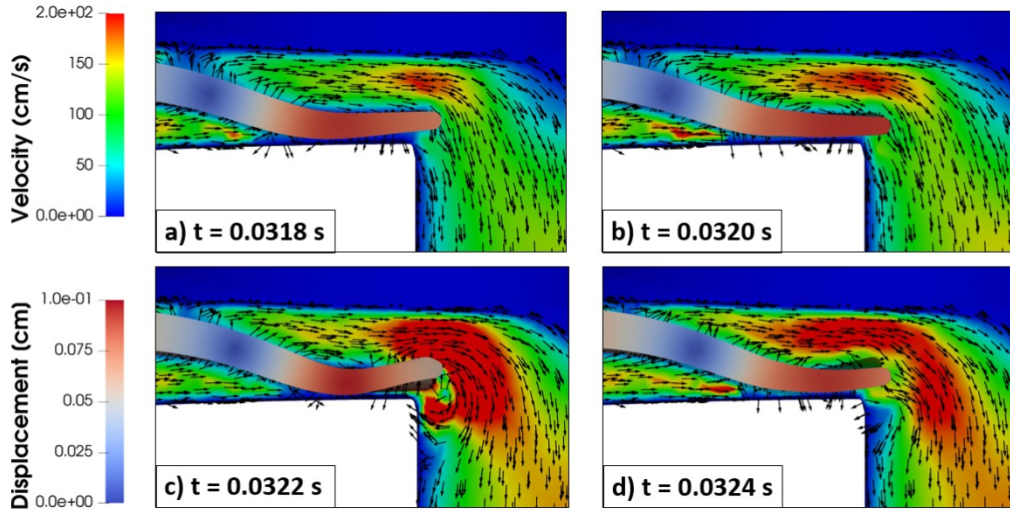
FIGURE 4.17: Undesired effect of contact model with $\gamma_c^0 = 10^6$ on membrane wave propagation through four subsequent time instants $t = 0.0318$ s (a), $t = 0.0321$ s (b), $t = 0.0324$ s (c), and $t = 0.0327$ s (d). As the membrane tip approaches to the inferior pump head flange (a), it enters in the contact layer (b), and then receives a very strong repulsive contact force which causes an artificial tilting (c). At the next time step (d), the membrane tip descends again, starting local vibrations around the contact layer. The shadows in panels (c) and (d) indicate the position of the membrane tip at previous time step. Test II: FSCI in J-shape WMBP.

4.3.3 Parametric analysis

In this section, we report the results obtained for different operating points (OPs) of WMBPs, set by changing the head pressure (P-analysis), the frequency (F-analysis), and the stroke (S-analysis), see Table 4.7. Notice that the oscillation parameters shifted to lower frequencies and higher strokes than what was observed in Section 4.3.1, because an increased hydraulic performance was found in this range for the J-shape design.

OP	Head pressure (H)	Frequency (f)	Stroke (Φ)
P1	50 mmHg	44 Hz	1.5 mm
P2	60 mmHg	44 Hz	1.5 mm
F1	60 mmHg	44 Hz	1.5 mm
F2	60 mmHg	50 Hz	1.5 mm
F3	60 mmHg	60 Hz	1.5 mm
S1	60 mmHg	50 Hz	1.5 mm
S2	60 mmHg	50 Hz	1.6 mm
S3	60 mmHg	50 Hz	1.7 mm

TABLE 4.7: List of Operating Points (OPs) for the parametric analysis. We grouped them (possibly with overlaps) in three distinct sets: P where H is changed; F where f is changed; S where Φ is changed. Test II: FSCI in J-shape WMBP.

We fixed the timestep Δt to 0.0004 s, so that we obtain 40 to 60 time points per cycle of oscillation for each tested frequency. The fluid parameters are $\rho_f = 1050 \ Kg/m^3$ and $\mu_f = 0.0035 \ Pa \ s$. The values of the membrane parameters ρ_m, λ_m and μ_m are

based on the actual material properties of the wave membrane[2]. For all simulations, the penalty parameters are $\gamma_\Sigma = 10^5$, $\gamma_{dg} = 10^3$, $\gamma_v = 0.05$, $\gamma_{div} = 0.5$, $\gamma_p = 0.01$, and $\gamma_g = 1$.
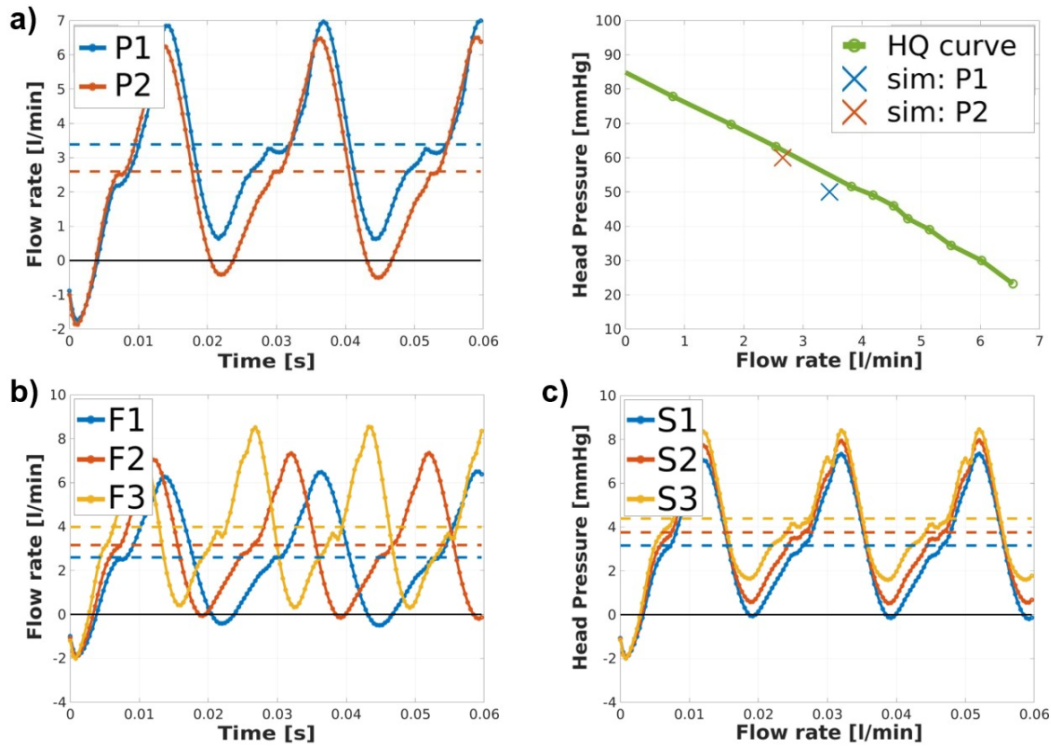
FIGURE 4.18: Outlet flow rate in time for different values of pressure (P-analysis, a), frequency (F-analysis, b) and stroke (S-analysis, c). P-analysis includes the comparison between experimental HQ curves (line) and numerical results (crosses, right). The dashed lines indicate the time-averaged values. Test II: FSCI in J-shape WMBP.

In Figure 4.18 we reported the time evolution of the flow rate Q at the outlet for the operating parameters in Table 4.7. The analysis of the flow results in the P-analysis, reported in Figure 4.18a, shows that, as expected, Q decreases when H increases, in accordance with the pump functioning. Specifically, the time-averaged ouflow amounts to 3.45 l/min at $H = 50$ mmHg (P1) and to 2.66 l/min at $H = 60$ mmHg (P2). These results are validated against the HQ data curve acquired *in-vitro*[3], see Figure 4.18a, right. For the operating points P1 and P2, the numerical model slightly underestimates the experimental output, showing a relative error of 11.6% and 6.6%, respectively. Notice that, unlike for the validation analysis in the flat pump design (see Section 4.2.5), here the penalty parameters are fixed for both OPs.

The flow results from the F-analysis (Figure 4.18b) and the S-analysis (Figure 4.18c) show that the output increases when either one of the two parameters increases. Specifically, we have that the averaged-in-time flow rate increases from 2.66 l/min for $f = 44$ Hz (F1), to 3.09 l/min for $f = 50$ Hz (F2) and further to 4.03 l/min for

---

[2]The specific values of the membrane parameters are not detailed because they are protected by confidentiality.

[3]The experimental setup for such data employs the position control system on the membrane proposed in [256], that makes the oscillation amplitude closer to a sine function, as assumed in Eq. (3.4).
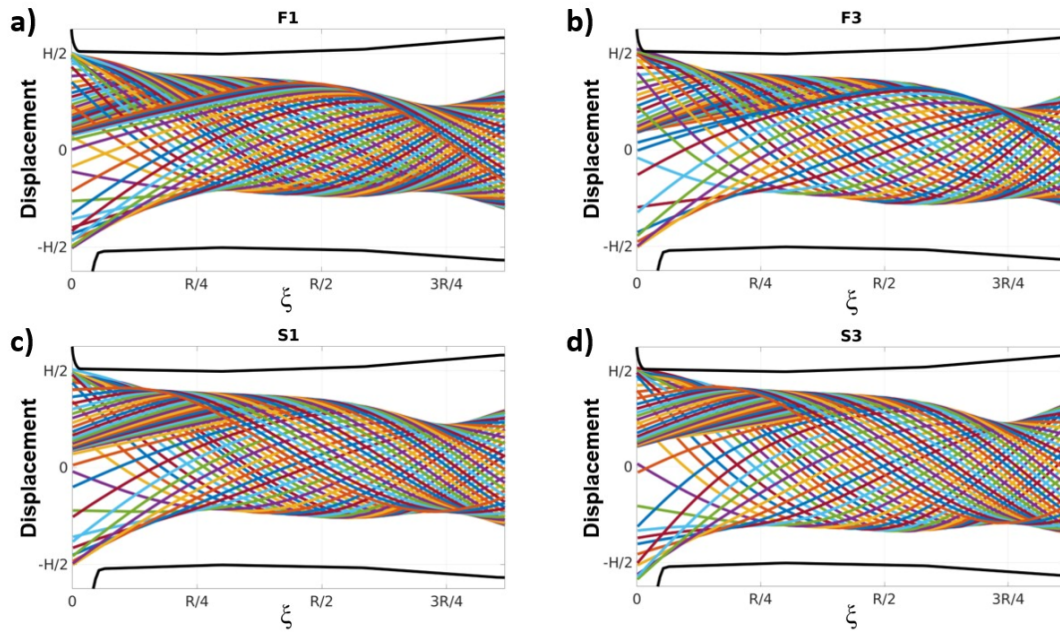
FIGURE 4.19: Membrane envelopes for different operating points of the device, at fixed head pressure $H = 60$ mmHg. The black lines represent the relative position of the pump head superior and inferior flanges, with respect to the superior and inferior edges of the membrane, respectively. The membrane radius R, the pump head height H and the membrane displacement for $\psi = R$ are not shown for confidentiality reasons. Test II: FSCI in J-shape WMBP.

$f = 60$ Hz (F3). Similarly, the averaged-in-time flow rate amounts to 3.09 $^l/_{min}$ for $\Phi = 1.5$ mm (S1), to 3.76 $^l/_{min}$ for $\Phi = 1.6$ mm (S2) and to 4.39 $^l/_{min}$ for $\Phi = 1.7$ mm (S3). Hence, we observed that the pump output increased of 0.36-0.5 $^l/_{min}$, for every increment of 5 Hz of oscillation frequency, while it increased by 0.6-0.7 $^l/_{min}$, when the stroke is increased by 0.1 mm.

The membrane deformation was studied for different oscillation parameters by looking at the *membrane envelopes*, as done for Figure 4.9 for the planar membrane. Membrane envelopes can provide important insight in terms of wave propagation and formation of fluid pockets, by analyzing its distance from the pump flange. In Figure 4.19, we reported the membrane envelopes for operating points F1, F3, S1, S3 (see Table 4.7). (F3 and S3), especially with respect to the lower flange, indicating that the fluid pockets are better isolated during their propagation towards the outlet, thus limiting backflows. In addition, in all cases the amplitude of the membrane undulations increases while moving towards the center of the pump (decreasing ξ values), probably as a result of the decreasing thickness of the membrane in the radial direction. In particular, the maximum displacement is observed at the membrane tip, where contact occurs with the pump flange, without exiting from the pump domain (as discussed in Sect. 4.3.2). Moreover, we can observe that the membrane envelopes are wider and more symmetric than the one found in the analysis for the flat pump design (see Figure 4.9, right), as a consequence of the smaller stroke and the different elasticity parameters.

OP	σ^{scalar} [Pa]		Area [%] with WSS		Volume [%] with σ^{scalar}		
	Max	Mean	< 0.1 Pa	< 0.3 Pa	< 1 Pa	> 9 Pa	> 50 Pa
P1	39.0	3.26	2.52	9.12	74.2	0.09	0
P2/F1	22.8	2.98	2.25	14.2	73.5	0.03	0
F2/S1	24.2	3.40	1.28	8.83	71.3	0.09	0
F3	27.0	4.06	1.76	8.95	66.3	0.25	0
S2	25.1	3.66	1.57	6.81	69.2	0.16	0
S3	29.1	3.90	1.96	6.82	67.2	0.22	0

TABLE 4.8: Stress statistics for each operating point. Test II: FSCI in J-shape WMBP.

In order to evaluate the risk of hemocompatibility-related adverse events in the J-shape design for the different operating conditions, we observed two hemodynamic quantities: the stress index σ^{scalar} and the Wall Shear Stress (WSS). The former is a scalar representation of the internal fluid stresses, computed starting from the shear stress tensor $\boldsymbol{\sigma} = \mu_f \dfrac{(\nabla \mathbf{u} + \nabla \mathbf{u}^T)}{2}$, and defined as

$$\sigma^{scalar} = \sqrt{\frac{k}{2} \sum_{i=1}^{3} \sum_{j=i+1}^{3} \left(\sigma_{ii} - \sigma_{jj}\right)^2 + \sum_{i=1}^{3} \sum_{j=i+1}^{3} (\sigma_{ij})^2}, \qquad (4.2)$$

with $k = 1/3$, in analogy with the Von Mises criterion for blood cells, as proposed in [30] and used in many numerical works [20, 160, 98, 63]. The WSS was considered to evaluate the risk of thrombosis at the pump contacting surfaces, as done in [242, 120].

In Table 4.8, we report the statistics of σ^{scalar} and WSS for all the operating points from Table 4.7. In particular: the 'Max' column corresponds to the highest value of σ^{scalar} during the last period of oscillation; the 'Mean' column refers to the maximum-in-time of the volumetric mean of σ^{scalar} in the pump head region; the area percentages represent the amount of wall surfaces exposed to WSS lower than 0.1 Pa and 0.3 Pa, that are reference values for potential thrombus deposition taken from [242] and [120], respectively; the volume percentages indicate the portions of pump volume with σ^{scalar} lowering 1 Pa, representative of low stress regions, or exceeding typical thresholds for hemocompatibility, *i.e.* 9 Pa for the degradation of the Von Willebrand factor [106], and 50 Pa for the activation of platelets [147]. We remark that the area and volume percentages are computed at two different instants of the oscillation cycle: the WSS statistics refer to the time point t^{min} that minimizes the volumetric mean of σ^{scalar}, when the oscillating structures have almost null velocity; while the volume percentages are calculated at the instant t^{max} of maximum stress conditions, *i.e.* at maximum oscillation velocity.

Notice that all operating points show low stress conditions, with most of the pump volume (65-75%) with fluid stress smaller than 1 Pa and no occurrence of values exceeding 50 Pa. Large peak values of stress are frequently markers for hemolysis potential, especially in case of long exposure time. As the reference thresholds for hemolysis risk typically found in literature vary from 100 to 650 Pa, depending on
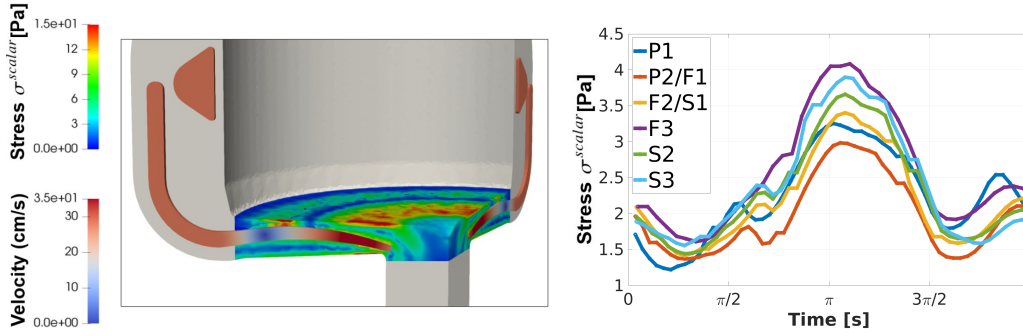
FIGURE 4.20: Left: Representation of the fluid scalar stress σ^{scalar} at time $t = 0.0568$ s for F3 in the pump head. Right: Time evolution of the volumetric mean of σ^{scalar} in the pump head for different operating points during the last period of oscillation, properly rescaled in the interval $[0, 2\pi]$. Test II: FSCI in J-shape WMBP.

the exposure time [160, 106, 245], WMBPs showed very low potential for hemolysis in our simulations.

Concerning the risk of thrombus deposition, the portions of the pump walls with low WSS (1.5-2.5% of the total surface for WSS < 0.1 Pa) are restricted to small regions below and above the magnet ring. Nonetheless, such regions are largely affected by the oscillation dynamics of the structures; indeed, in the same points, the WSS reaches physiologic values of 1-1.5 Pa [242] at time t^{max}. Additionally, certain phenomena that are connected with thrombogenesis, such as the unfolding of Von Willebrand factor protein or the activation of platelets, are triggered at high stress conditions that are very rarely achieved in the pump, *i.e.* at 9 Pa [106] and 50 Pa [147], respectively. Thus, being furterly in absence of flow stagnation due to the oscillating nature of the fluid dynamics in WMBP, the potential for thrombogenicity is also expected to be low in WMBPs for the tested operating conditions.

Moreover, in Figure 4.20, we specifically analyzed the scalar stress σ^{scalar} in the pump head, where the highest values of stresses were observed for all operating points. In particular, in the left panel, we show the case with highest frequency of oscillation (F3), that showed the largest mean value of σ^{scalar} in Table 4.8. The results highlight that the peak values are found on the pump head flanges, nearby the tip of the membrane, where the structure velocity is maximum and where the membrane approaches closely to the wall. Notice that in this area the flow is continuously disturbed and thereby the local residence time is expected to be low. Furthermore, in the right panel of Figure 4.20, we show the time evolution of the volumetric mean of σ^{scalar} in the pump head during the last period of oscillation, for all operating points. Notice that, in agreement with the statistics in Table 4.8, the fluid stresses increase for larger values of f and Φ, whereas they decrease for increasing H. The trend in time of σ^{scalar} is similar for all operating points, showing a peak at π, when membrane holder velocity is maximum.

Finally, we considered also the stress conditions in the wave membrane during its oscillatory motion. Thus, we computed the solid Von Mises stress σ^{VM} in the wave membrane to study the material resistance at different frequencies of oscillation. In particular, in Figure 4.21 we showed this quantity for operating point F3 at time

$t = 0.052$ s and its maximum and volumetric mean values for each tested frequency. We can observe that the solid stress increased with the frequency of oscillation and that the maximum was achieved at the junction with the membrane holder (gray region) during the ascending phase of the membrane oscillation.
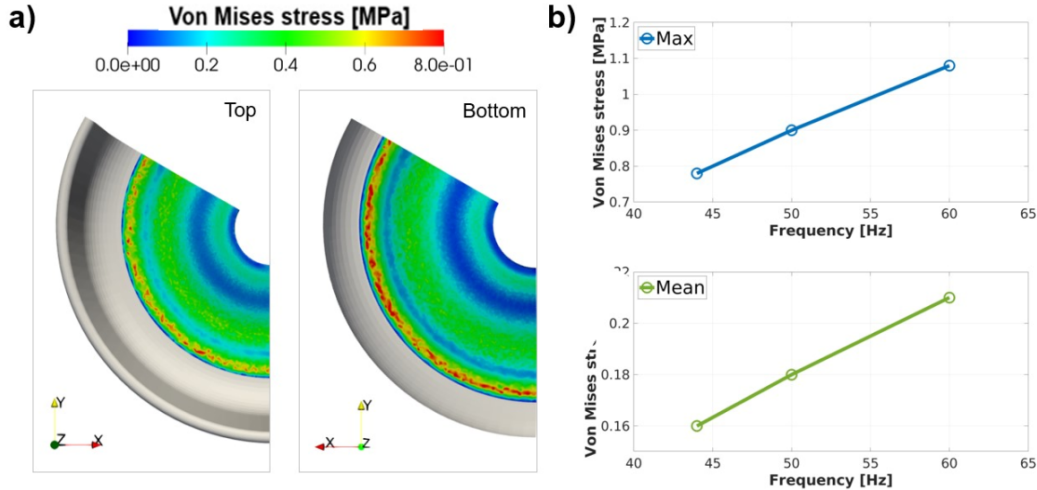
FIGURE 4.21: Von Mises stress analysis in the wave membrane. a) Visualization of the Von Mises stress on the top and the bottom surfaces of the wave membrane at time $t = 0.052$ (ascending phase). b) Plots of the maximum (above) and volumetric mean (bottom) Von Mises stress for F1, F2 and F3. Test II: FSCI in J-shape WMBP.

We remark that the analyses here reported indicate that the shift of the operating points to lower oscillation frequencies, adopted for the new J-shape design, has important beneficial effects, both on hemocompatibility (lower fluid stress) and on the fatigue life of the membrane structure (lower solid Von Mises stress).

4.3.4 Nominal operating conditions

The primary ambition of the WMBP system is to provide a physiological pulsatile flow to patients suffering of advanced heart failure. Therefore, the pump hydraulic and hemocompatibility performance should be studied over the entire heart cycle, with the head pressure H varying in time. Here, we focus our analysis to a fixed operating condition to initiate the process of prediction of pump performance using numerical models. In particular, we chose to study a typical operating condition (here refered to as *nominal operating point*, NOP) generating physiologic mean flow at head pressure $H = 80$ mmHg, with oscillation parameters $f = 60$ Hz and $\Phi = 1.8$ mm. This value of head pressure corresponds to the standard pressure difference between systemic and left ventricular pressure at diastole in a failed heart with LVAD support [205].

The pump system was simulated for $T = 0.05$ s, corresponding to three periods of oscillation, using a fixed timestep $\Delta t = 0.0002$ s. The physical and penalty parameters are set as in Section 4.3.3, except for γ_v that was doubled due to the higher flow conditions. Contact parameters $\varepsilon_c = 0.02$ cm and $\gamma_c^0 = 5 \cdot 10^5$ were increased
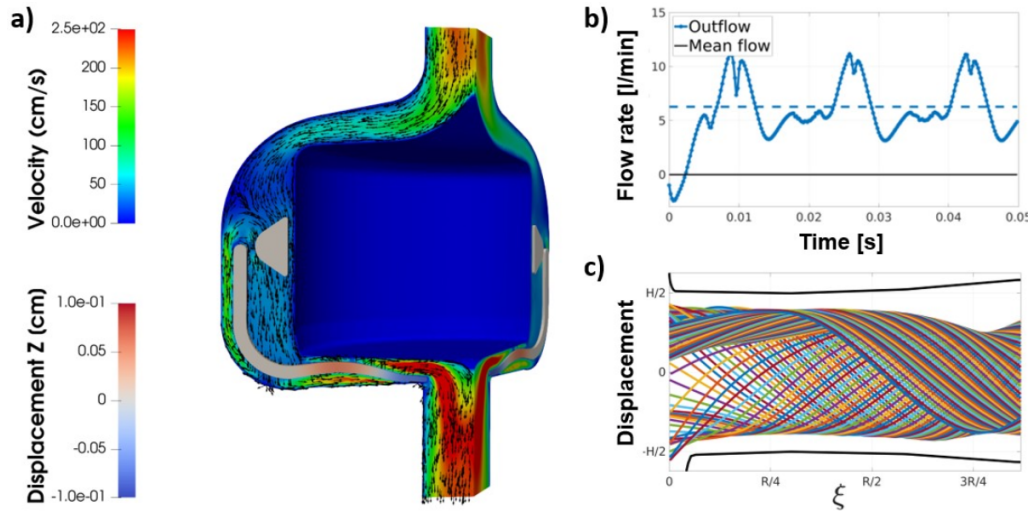
FIGURE 4.22: Nominal operating condition. a) Velocity and displacemnt field at $t = 0.0416$ s. b) Time evolution of the flow rate at the outlet. c) Visualization of the membrane envelope. Test II: FSCI in J-shape WMBP.

with respect to default values because of the larger membrane undulations observed during the simulations, probably due to the higher stroke parameter.

Figure 4.22 shows the blood velocity and membrane displacement fields at $t = 0.0416$ s (a), the trend in time of Q (b) and the membrane envelope (c) at NOP. Compared with the membrane envelopes in Figures 4.9 and 4.19, the higher oscillation parameters of NOP resulted in a more uniform membrane wave propagation that spans most of the gap in the pump head region. This indicates a better isolation of the fluid pockets during their transport towards the outlet channel, that results in a flow field with high blood velocities and no recirculation areas or stagnation points. The time-averaged LVAD output amounts to 6.25 $^l/_{min}$ at $H = 80$ mmHg, that is compliant with regular flow conditions. Nonetheless, the operating point should be tested also at different head pressures to fully characterize the HQ trend and capture the global behavior of the pulsatile pump.

In addition, maximum and volumetric mean of σ^{scalar} are plotted in time during the last period of oscillation (Figure 4.23a). The maximum value in time and space is 56.4 Pa (that is significantly lower than critical thresholds of 100-650 Pa [160, 106, 245]), achieved at $t_1 = 0.035$ s, while the volumetric mean in the pump head reaches a maximum of 5.3 Pa at time $t_2 = 0.0432$ s, *i.e.* during the descending phase of the membrane holder. The histograms in Figure 4.23b represent the volumetric distribution of the *elemental scalar stress*, i.e. the average value of σ^{scalar} in each element, for both time points. In particular, the highest elemental scalar stress (42.8 Pa at $t = t_1$) is restricted to a volume of 0.003 mm^3, close to the membrane tip. Since the mean local velocity in the element amounts to 114 $^{cm}/_s$, the residence time in the element is expected to be very low ($\sim$ 0.1 ms). Furthermore, for $t = t_2$, the stress values above 20 Pa are overall limited to less than 1 mm^3 in the pump volume.

Such results are particularly promising when compared with the hemocompatibility studies on modern LVADs working in similar flow-pressure conditions. For instance, in HeartMate II, a clinically-approved axial blood pump, 11 mm^3 of pump volume
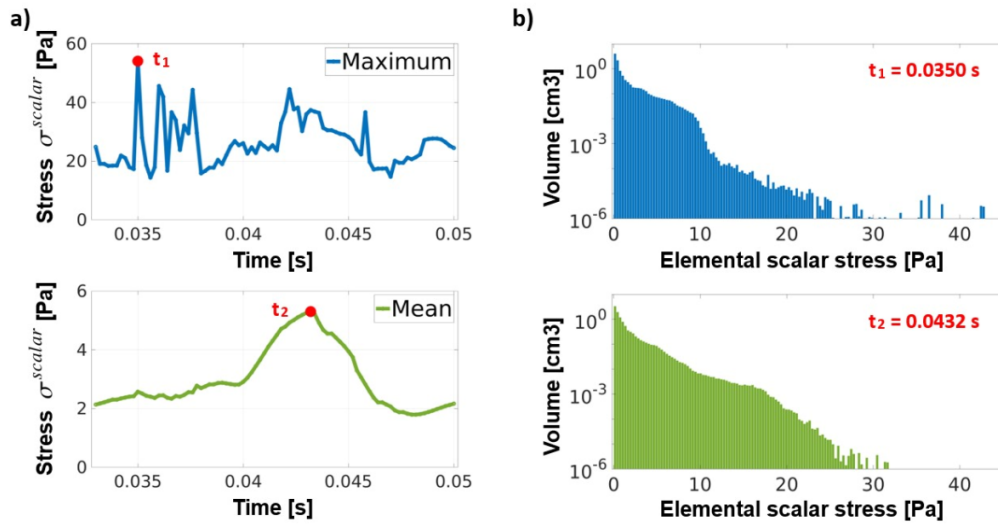
FIGURE 4.23: a) Time plot of maximum value (above) and volumetric mean in the pump head (below) of Von Mises stress analysis at nominal operating conditions. Red dots indicate the time points t_1 and t_2 of maximum value. b) Volumetric stress distributions for NOP at time istants of maximum peak stress $t_1 = 0.0350$ s (above) and of maximum mean stress $t_2 = 0.0432$ s (below). Test II: FSCI in J-shape WMBP.

was exposed to stress levels higher than 150 Pa at 5.4 l/min [42], but showed acceptable levels of plasma-free hemoglobin in experimental studies at similar operating conditions [24]. In the same experimental work [24], the centrifugal blood pump HVAD showed lower hemolysis indices than HeartMate II, even though in [63] 0.7% of its volume presented stresses values higher than 100 Pa at 5 l/min. Finally, the preclinical tests for HeartMate III [42], one of the most recently developed LVADs, showed very good performance in both *in-vitro* hemolysis testings and in *in-vivo* bovine trials, even though in the numerical simulations the scalar stress was found to be higher than 50 Pa in 52.7 mm^3 and than 150 Pa in 3.3 mm^3 (up to 350-400 Pa). Nevertheless, in future works, an hemolysis model will be developed in order to properly assess the risk of hemolysis and estimate the mean residence time in WMBP.

In conclusion, we computed the relative contribution of normal and shear stresses to the definition of σ^{scalar}, see Eq. (4.2). Figure 4.24 shows the ratio between extensional and shear stresses in the flow field at times t_1 and t_2. The results highight that the extensional stresses dominate in 45-55% of the pump volume, especially close to contact regions and in curved regions of the flow channel (ratio > 1); on the other hand, shear is higher on most part of the pump walls and at the sides of the membrane holder and the magnet (ratio < 1). When we restrict the analysis to regions with $\sigma^{scalar} > 9$ Pa, shear stress was found to be predominant in 99.2% of the corresponding volume at t_1 and 71.4% at t_2. Indeed, in the computation of σ^{scalar} the contribution of the normal stresses is penalized by a factor $k = 1/3$, as used in most numerical studies [20, 160, 98, 63]. However, other studies [89, 97] proposed that extensional stresses actually deform red blood cells more than shear stresses and, hence, other values $k > 1$ in Eq. (4.2) could be tested in the future.
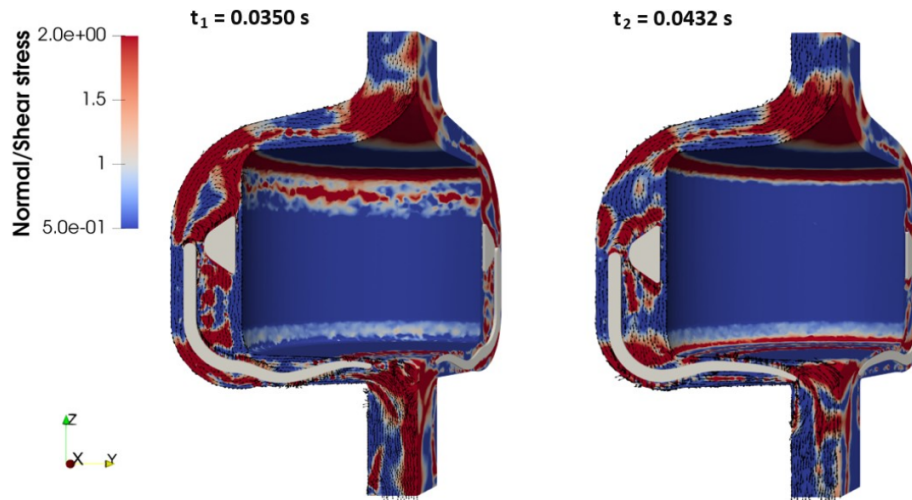
FIGURE 4.24: Ratio between normal and shear stresses in the flow field at t_1 = 0.035 s (left) and t_2 = 0.0432 s (right). Extensional stresses dominate in red regions, shear stresses dominate in blue regions. Test II: FSCI in J-shape WMBP.

4.4 Test III: Membrane anti-symmetries

In the previous sections, the wave membrane deformation was assumed to be axi-symmetric and consequently we adopted the reduced geometry approximation described in Section 3.1.4 to decrease the computational time of the three-dimensional FSCI simulations.
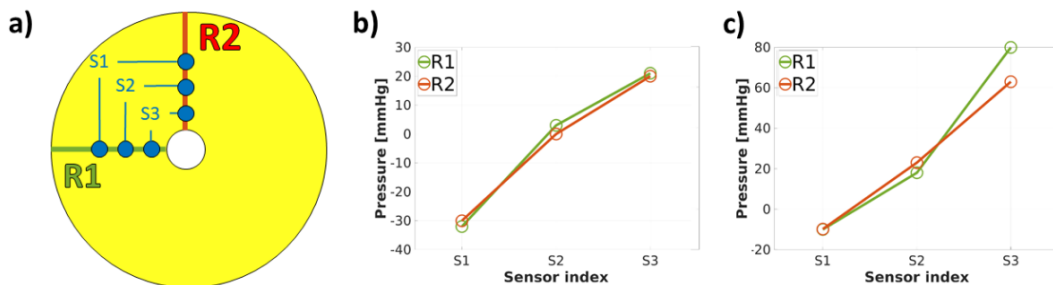
FIGURE 4.25: Experimental data for membrane anti-symmetries. a) Setup of pressure sensors {S1, S2, S3} along radii R1 and R2. b) Symmetric pressure signals. c) Anti-symmetric pressure signals. Experimental data for (b) and (c) were obtained during two distinct experimental sessions, with different setups. Test III: Membrane anti-symmetries.

However, experimental evidences have recently suggested that, for certain operating conditions of the WMBPs, secondary non axi-symmetric modes of vibration may arise in the membrane deformation. We will refer to these modes as *anti-symmetries*. Notice that the hypothesis of anti-symmetry in the membrane behavior is actually derived from non-symmetric registrations of pressure signals in the pump head. Specifically, a certain number of pressure sensors are placed in the pump head (hence in close proximity to the wave membrane) at different radial distances from the pump axis, along two orthogonal radii $R1$ and $R2$, as shown in Figure 4.25a. In this way, the pressure signals can be measured along the two radii and their comparison can highlight whether there are symmetries (similar pressure signals)
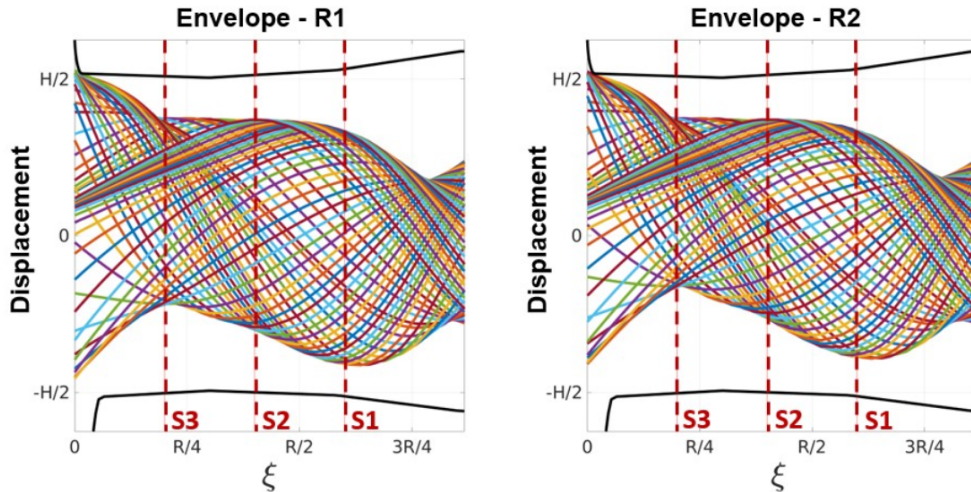
FIGURE 4.26: Membrane envelopes along perpendicular radii R1 and R2. The vertical dashed lines correspond to the position of the pressure sensors S1, S2, and S3. Test III: Membrane anti-symmetries.

or anti-symmetries (different pressure signals) in the fluid field in proximity to the wave membrane. Hence, the basic assumption is that different pressure signals indicate different behavior of the membrane along the two directions, and hence anti-symmetry. For instance, in Figure 4.25, we show an example of symmetric pressure registration (b) and an example of anti-symmetric pressure registration (c). Notice that in both cases, the pressure rises for increasing sensor indices, *i.e.* while moving towards the outlet channel, in agreement with the pressure build-up functioning of WMBP.

The cause of anti-symmetries in the membrane of WMBPs is currently unknown. It may be either due (i) to the non axi-symmetric geometry of the rigid apparatus that connects the wave membrane to the magnet ring, or (ii) to anti-symmetries in the fluid dynamics that affect the membrane displacement via fluid-structure interaction (or both).

In this section, we aim at examining, in a preliminary way, the validity of hypothesis (ii) by reproducing the fluid-structure interaction dynamics in the pump system for an operating point that demonstrated anti-symmetric pressure signals during the experiments. Therefore, we solved the FSCI problem (3.46) in the full-angle J-shape pump system (see meshes in Figure 4.2), using the operating point used to generate the experimental data in Figure 4.25c, that were pressure head H = 90 mmHg, frequency f = 48 Hz and stroke Φ = 1.37 mm. In order to reduce the computational cost of the simulation, we omitted from the computational domain the magnet ring, which has a minor effect (< 10%) on the membrane displacement, according to experimental data. The time settings for this simulation were: T = 0.035 s and Δt = 0.0003 s. Both the physical and the penalty parameters were set as in Section 4.3.3. The contact parameters were ε_c = 0.009 cm and γ_c^0 = 2 · 10^5.

Thanks to the three-dimensional nature of the FSCI simulations, we can analyze the fluid pressure and the membrane displacement along two perpendicular radii R1 and

R2 and, particularly, at the radial distances where the sensors S1, S2 and S3 were located.

In Figure 4.26, we report the membrane envelopes along the two radii R1 and R2, that represent the membrane deformation along each direction during the last period of oscillation. The difference between the two plots, particularly evident on the lower edge of the envelopes, indicates that, at the tested operating condition, the anti-symmetric behavior of the membrane emerged also in our numerical results. Additionally, the dashed lines in Figure 4.26 shows that sensors S1, S2 and S3 , which are placed at equal distance from each other along the radial coordinate ξ and they are sorted following the order of proximity to the outlet channel. Notice that the choice of the radii R1 and R2 for the numerical test was arbitrary and not related to the directions effectively used for the experimental measurements. Therefore, there might be other radii that show higher anti-symmetric behavior than what shown in the plots.
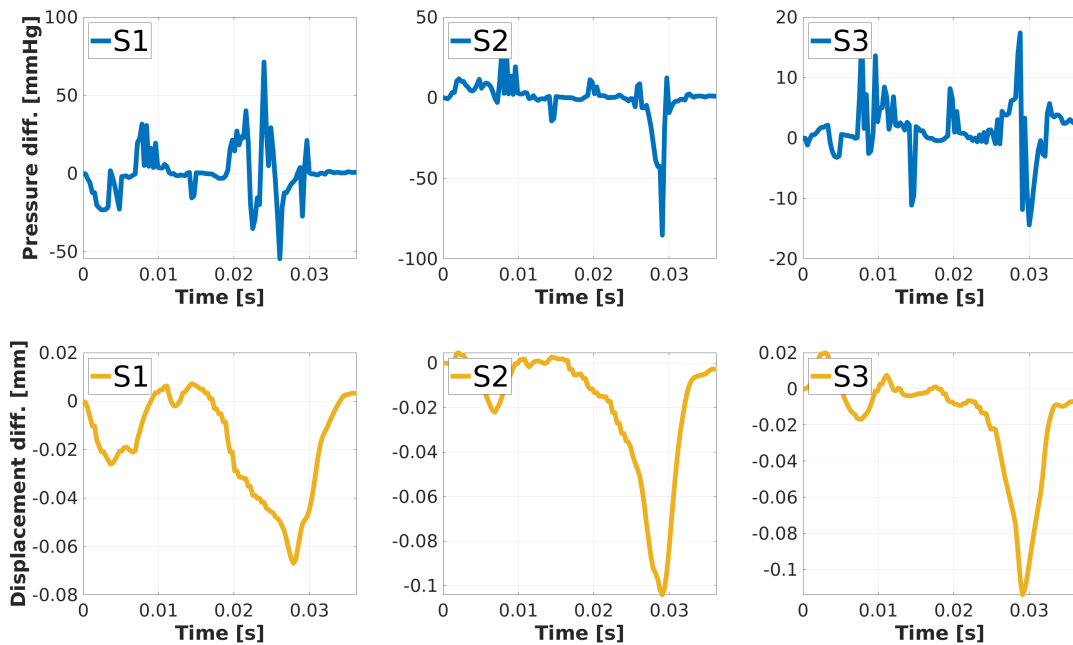
FIGURE 4.27: Differences of pressure (above) and membrane displacement (below) signals from radii R1 and R2, in correspondence to sensor positions S1 (left), S2 (center) and S3 (right). Test III: Membrane anti-symmetries.

In order to link the fluid pressure and the membrane deformation, we show in Figure 4.27 the difference of the pressure signals (above) and membrane displacement (below) from the two radii, in correspondence to sensor positions S1, S2 and S3. The largest differences in pressure were found in the time range $[0.024, 0.031]$ s, with the peaks from sensor S1 anticipating the ones of sensors S2 and S3, hence following the direction of the progressive propagation (from S1 to S3). In the same time slot, also the plot of the membrane displacement difference exhibits the highest values, confirming the assumption that the anti-symmetries in the pressure is a good indicator for anti-symmetries in the membrane behavior. Nonetheless, while the anti-symmetry in the membrane displacement increases while moving towards the outlet channel, with a maximum variation of 0.067 mm, 0.104 mm, and 0.114 mm, recorded at
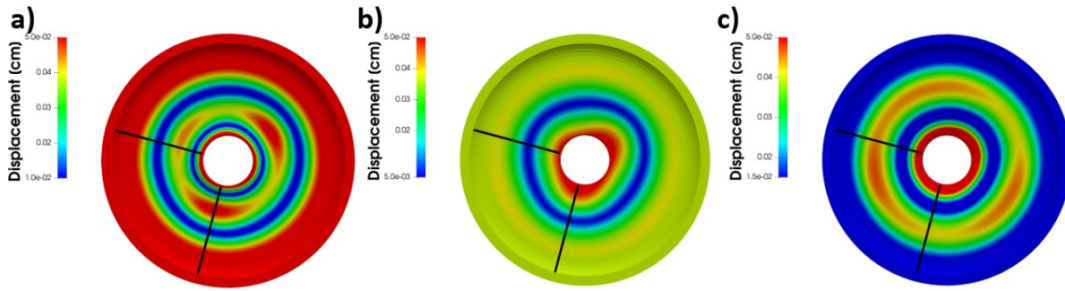
FIGURE 4.28: Visualization of the membrane anti-symmetries for operating point OPA at time $t = 0.0285$ s (left), $t = 0.0294$ s (center) and $t = 0.0306$ s (right). Black lines indicate radii R1 and R2 in the numerical test. Test III: Membrane anti-symmetries.

sensors S1, S2, and S3, respectively, the maxima of pressure difference have not the same trend, with 71.3 mmHg at S1, 85.3 mmHg at S2, and 17.4 mmHg at S3. The membrane anti-symmetries are visualized from above in Figure 4.28 at three time instants $t = 0.0285$ s (left), $t = 0.0294$ s (center) and $t = 0.0306$ s (right), where the membrane exhibits anti-symmetric behavior along the angular coordinate at different radial distances. Notice that the magnitude of the membrane anti-symmetry, corresponding to the maximum displacement difference along the angular coordinates, depends on the choice of the radii R1 and R2, that are identified by the black lines in Figure 4.28. For instance, in Figure 4.27a, the anti-symmetry magnitude is actually higher than what detected by the considered radii (~ 0.1 mm) and reaches a value of ~ 0.2 mm for other choices of R1 and R2.
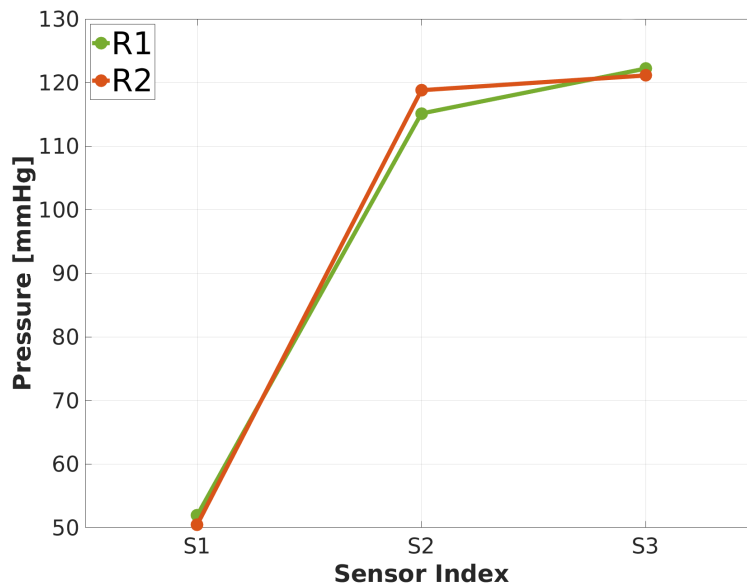
FIGURE 4.29: Predicted time-averaged pressure values in correspondence to the location of sensors S1, S2, and S3. Test III: Membrane anti-symmetries.

Nevertheless, when we compute the average of the pressure signals from each sensor over the last period of oscillation, the pressure values from radii R1 and R2 differ by a maximum of ~ 4 mmHg (see Figure 4.29). These time-averaged values, which are increasing towards the outlet channel in agreement with the experimental data, show the highest difference at sensor S2, where the anti-symmetric membrane deformation

was more remarkable (see Figure 4.28a). Indeed, in these preliminary results, the membrane anti-symmetries emerged only during a restricted time range. It is possible that for longer simulation times, the membrane anti-symmetries occur more often or permanently during the oscillation cycle, ultimately resulting in a broader pressure difference between the two radii R1 and R2. In any case, further study is required to ascertain whether these simulations accurately represent the actual membrane behavior.

Chapter 5

Conclusions and next developments

Wave Membrane Blood Pumps (WMBPs) represent a new frontier in the field of Left Ventricular Assist Devices (LVADs), which is based on an innovative technology where the propulsion of blood is obtained by the progressive undulations of an immersed elastic membrane. This novel membrane-based pumping principle has the potential to overcome the limitations of standard rotor-based LVADs, in particular by providing a physiological pulsatile flow rate to the body and reducing the risk of hemocompatibility-related adverse events, such as hemolysis or thrombosis.

In this thesis, we numerically studied the Fluid-Structure-Contact Interaction (FSCI) between the blood and the elastic membrane in WMBPs for different designs and operating conditions of the device. In this regard, three-dimensional (3D) computational simuations were performed using the unfitted mesh Extended Finite Element Method (XFEM), with a Discontinuous-Galerkin (DG) mortaring at the interface. A penalization contact model was added to handle the potential collisions between the wave membrane and the pump walls and avoid mesh penetrations in case of high oscillations.

To our knowledge, the XFEM-DG numerical strategy was here employed for the first time to address a real 3D industrial application and the corresponding numerical results in WMBPs were validated against experimental pressure-flow (HQ) data.

Specifically, the numerical investigation in WMBPs allowed us to:

- understand the effects of the progressive wave propagation in the membrane on the blood dynamics, which consist in a pressure buildup in the pump head and in the transportation of the fluid pockets towards the outlet channel against an adverse pressure gradient, ultimately resulting in blood flow generation;

- show the superior hydraulic performance of the J-shape membrane pump design to the previous flat membrane pump design at identical operating conditions;

- analyze the pump performance by varying separately the different operating parameters of the device, both in terms of hydraulic power and hemocompatibility: for instance, we observed that the increase of both the oscillation parameters (frequency and stroke) led to an higher outflow rate, but decreasing particularly the frequency can reduce the stress conditions in the pump and increase the life fatigue of the membrane;

- propose a new operating point for the WMBP which achieved physiologic flow output at diastolic pressure conditions;

- highlight for the first time the development of anti-symmetries in the wave membrane deformation and their link with the pressure signal in the pump head.

However, this work presents the following list of limitations.

1. Although in the real LVAD application the pump is exposed to variable pressure conditions during the cardiac cycle, here we restricted for each simulation the analysis of the pump performance to operating points that are fixed in time, *i.e.* for steady head pressure H, frequency f and stroke Φ. Thus, the pulsatility operating mode, where the frequency and the stroke parameters are modulated during the heartbeat to reproduce the native heart pulsatility, was not tested.

2. The domain of WMBPs presents some geometric simplifications. First, the membrane holder, that is actually a separate component embedded in the elastic membrane, is here modeled as part of the membrane assembly. In principle, this simplification may affect the membrane displacement close to the junction of the membrane holder. Second, we omitted from the computational domain other minor rigid structures, such as the membrane fixation apparatus or the suspension springs, that may deform the flow patterns around the magnet ring. In particular, the non axi-symmetric architecture of the rigid complex of titanium posts connecting the membrane to the magnet ring may play an important role in the development of anti-symmetries in the wave membrane deformation.

3. The computational cost of the 3D FSCI simulations in WMBP is rather high, resulting in long simulation times (in the order of weeks). This is mainly due to the operations of intersection and cut-mesh generation involved in the unfitted XFEM framework, which, on the other side, allows for high accuracy and geometric flexibility.

4. The hemocompatibility analysis is here limited to the observation of hemo-dynamic quantities (*e.g.* shear rate or wall shear stress) and of flow patterns (*e.g.* recirculation or stagnation areas), that offer preliminary information on the potential blood trauma in WMBPs. Thus, the exposure time to stress or the damage history of blood cells are not considered in this work.

In order to overcome such limitations and improve the numerical model, we propose the following developments of the present study.

1. The simplifications on the geometry of WMBP could be removed by re-introducing the previously omitted rigid components in the computational domain, so that we could evaluate their effect on the membrane deformation (and particularly on its anti-symmetries) and on the hemocompatibility of the device.

2. Alternative numerical approaches could be adopted to reduce the computational time, at the expense of a highly reduced accuracy, such as lumped parameter models, as in [300]. A potential strategy that could be considered for future studies consists in the coupling between a 3D complete FSCI modeling in a

region of interest (such as in the pump head) and a 0D model of the remaining portion of the pump domain.

3. The simulation time may be reduced by parallelizing the mesh intersections between the unfitted meshes and/or implementing an efficient preconditioner for the linear system.

4. A finite elasticity model can be considered to better describe the membrane dynamics and its interaction with blood.

5. The geometric and the contact non-linearities could be solved iteratively at each time step, to further improve the accuracy and reduce the risk of mesh penetrations.

6. An adaptive time step scheme could be implemented, *e.g.* to increase the accuracy in case of contact, and decrease the computational cost otherwise.

7. An hemolysis model, either Eulerian or Lagrangian, could be developed to properly assess the risk of hemolysis and estimate the mean residence time in WMBPs.

Bibliography

[1]   A. B. Abid, V. Morgenthaler, M. Aymami, E. Flecher, and P. Haigron. "A CFD based analysis of the influence of IC angulation on blood stagnation for Left Ventricular Assist Device implantation". In: *2020 IEEE-EMBS Conference on Biomedical Engineering and Sciences (IECBES)*. IEEE. 2021, pp. 218–223. DOI: 10.1109/IECBES48179.2021.9398845.

[2]   F Abraham, M Behr, and M Heinkenschloss. "Shape optimization in steady blood flow: A numerical study of non-Newtonian effects". In: *Computer Methods in Biomechanics and Biomedical Engineering* 8.2 (2005), pp. 127–137.

[3]   R. M. Adamson, A. A. Mangi, R. L. Kormos, D. J. Farrar, and W. P. Dembitsky. "Principles of HeartMate II implantation to avoid pump malposition and migration". In: *Journal of cardiac surgery* 30.3 (2015), pp. 296–299.

[4]   P. Alart and A. Curnier. "A mixed formulation for frictional contact problems prone to Newton like solution methods". In: *Computer methods in applied mechanics and engineering* 92.3 (1991), pp. 353–375.

[5]   F. Alauzet, B. Fabrèges, M. A. Fernández, and M. Landajuela. "Nitsche-XFEM for the coupling of an incompressible fluid with immersed thin-walled structures". In: *Computer Methods in Applied Mechanics and Engineering* 301 (2016), pp. 300–335.

[6]   A. C. Alba and D. H. Delgado. "The future is here: ventricular assist devices for the failing heart". In: *Expert Review of Cardiovascular Therapy* 7.9 (2009), pp. 1067–1077. DOI: 10.1586/erc.09.86.

[7]   J. Alvarez and V. Rao. "HeartMate 3—a "Step" in the right direction". In: *Journal of thoracic disease* 9.5 (2017), E457.

[8]   *Anatomy of the heart*. 2007. URL: https://qcg.com.au/patients/anatomy-heart.

[9]   M. Anselmann and M. Bause. "CutFEM and ghost stabilization techniques for higher order space-time discretizations of the Navier-Stokes equations". In: *arXiv preprint arXiv:2103.16249* (2021).

[10]   P. F. Antonietti, M. Verani, C. Vergara, and S. Zonca. "Numerical solution of fluid-structure interaction problems by means of a high order Discontinuous Galerkin method on polygonal grids". In: *Finite Elements in Analysis and Design* 159 (2019), pp. 1–14.

[11]   D. N. Arnold, F. Brezzi, B. Cockburn, and L. D. Marini. "Unified analysis of discontinuous Galerkin methods for elliptic problems". In: *SIAM journal on numerical analysis* 39.5 (2002), pp. 1749–1779.

[12]   D. Arora, M. Behr, and M. Pasquali. "Hemolysis estimation in a centrifugal blood pump using a tensor-based measure". In: *Artificial organs* 30.7 (2006), pp. 539–547.

[13] D. Arora, M. Behr, and M. Pasquali. "A tensor-based measure for estimating blood damage". In: *Artificial organs* 28.11 (2004), pp. 1002–1015.

[14] B. Balakrishnan, A. R. Tzafriri, P. Seifert, A. Groothuis, C. Rogers, and E. R. Edelman. "Strut position, blood flow, and drug deposition: implications for single and overlapping drug-eluting stents". In: *Circulation* 111.22 (2005), pp. 2958–2965.

[15] F. Ballarin, E. Faggiano, S. Ippolito, A. Manzoni, A. Quarteroni, G. Rozza, and R. Scrofani. "Fast simulations of patient-specific haemodynamics of coronary artery bypass grafts based on a POD–Galerkin method and a vascular shape parametrization". In: *Journal of Computational Physics* 315 (2016), pp. 609–628.

[16] F. Ballarin, E. Faggiano, A. Manzoni, A. Quarteroni, G. Rozza, S. Ippolito, C. Antona, and R. Scrofani. "Numerical modeling of hemodynamics scenarios of patient-specific coronary artery bypass grafts". In: *Biomechanics and modeling in mechanobiology* 16.4 (2017), pp. 1373–1399.

[17] A. T. Barker and X.-C. Cai. "Scalable parallel methods for monolithic coupling in fluid–structure interaction with application to blood flow modeling". In: *Journal of computational physics* 229.3 (2010), pp. 642–659.

[18] C. Bartoli and R. Dowling. "The Next Wave of Mechanical Circulatory Support Devices". In: *Cardiac Interventions Today* 13.1 (2019), pp. 53–59.

[19] A. A. Basri, M. Zuber, M. S. Zakaria, E. I. Basri, A. F. A. Aziz, R. M. Ali, M. Tamagawa, and K. A. Ahmad. "The hemodynamic effects of paravalvular leakage using fluid structure interaction; Transcatheter aortic valve implantation patient". In: *Journal of Medical Imaging and Health Informatics* 6.6 (2016), pp. 1513–1518.

[20] M. Behbahani, M. Behr, M. Hormes, U. Steinseifer, D. Arora, O. Coronado, and M. Pasquali. "A review of computational fluid dynamics analysis of blood pumps". In: *European Journal of Applied Mathematics* 20.4 (2009), pp. 363–397.

[21] M. Behr, D. Arora, O. M. Coronado, and M. Pasquali. "Models and finite element techniques for blood flow simulation". In: *International Journal of Computational Fluid Dynamics* 20.3-4 (2006), pp. 175–181.

[22] T. Belytschko and T. Black. "Elastic crack growth in finite elements with minimal remeshing". In: *International journal for numerical methods in engineering* 45.5 (1999), pp. 601–620.

[23] T. Belytschko, N. Moës, S. Usui, and C. Parimi. "Arbitrary discontinuities in finite elements". In: *International Journal for Numerical Methods in Engineering* 50.4 (2001), pp. 993–1013.

[24] Z. B. Berk, J. Zhang, Z. Chen, D. Tran, B. P. Griffith, and Z. J. Wu. "Evaluation of in vitro hemolysis and platelet activation of a newly developed maglev LVAD and two clinically used LVADs with human blood". In: *Artificial organs* 43.9 (2019), pp. 870–879.

[25] M. Berman, J. Parameshwar, D. P. Jenkins, K. Dhital, C. Lewis, K. Dempster, P. Lincoln, C. Sudarshan, S. R. Large, J. Dunning, et al. "Thoratec implantable ventricular assist device: the Papworth experience". In: *The Journal of thoracic and cardiovascular surgery* 139.2 (2010), pp. 466–473.

[26]   L. Bertagna, S. Deparis, L. Formaggia, D. Forti, and A. Veneziani. "The LifeV library: engineering mathematics beyond the proof of concept". In: *arXiv preprint arXiv:1710.06596* (2017).

[27]   F. Bertrand, P. A. Tanguy, and F. Thibault. "A three-dimensional fictitious domain method for incompressible fluid flow problems". In: *International Journal for Numerical Methods in Fluids* 25.6 (1997), pp. 719–736.

[28]   M. Bianchi, G. Marom, R. P. Ghosh, O. M. Rotman, P. Parikh, L. Gruberg, and D. Bluestein. "Patient-specific simulation of transcatheter aortic valve replacement: impact of deployment options on paravalvular leakage". In: *Biomechanics and modeling in mechanobiology* 18.2 (2019), pp. 435–451.

[29]   P. L. Blackshear Jr, F. D. Dorman, and J. H. Steinbach. *Some mechanical effects that influence hemolysis*. 1965.

[30]   C Bludszuweit. "Three-Dimensional numerical prediction of stress loading of blood particles in a centrifugal pump". In: *Artificial Organs* 19.7 (1995), pp. 590–596.

[31]   T. Bodnár, G. P. Galdi, and Š. Nečasová. *Fluid-structure interaction and biomedical applications*. Springer, 2014.

[32]   D. Boffi and L. Gastaldi. "The immersed boundary method: a finite element approach". In: *Computational Fluid and Solid Mechanics 2003*. Elsevier, 2003, pp. 1263–1266.

[33]   J. Bonet and J. Peraire. "An alternating digital tree (ADT) algorithm for 3D geometric searching and intersection problems". In: *International Journal for Numerical Methods in Engineering* 31.1 (1991), pp. 1–17.

[34]   J. Bonnemain, S. Deparis, and A. Quarteroni. "Connecting ventricular assist devices to the aorta: a numerical model". In: *Imagine Math*. Springer, 2012, pp. 211–224.

[35]   J. Bonnemain, A. C. I. Malossi, M. Lesinigo, S. Deparis, A. Quarteroni, and L. K. Von Segesser. "Numerical simulation of left ventricular assist device implantations: comparing the ascending and the descending aorta cannulations". In: *Medical engineering and physics* 35.10 (2013), pp. 1465–1475.

[36]   C. Botterbusch, N. Barabino, F. Cornat, N. Jem, R. Pruvost, D. Marino, S. Benoit, E. Monticone, L. Polverelli, T. Snyder, V. Loobuyck, A. Rauch, S. Susen, and A. Vincentelli. "Progress in the Development of the Pulsatile CorWave LVAD". In: *The Journal of Heart and Lung Transplantation* 40.4, Supplement (2021), S104. ISSN: 1053-2498.

[37]   C. N. Botterbusch, P. Monticone, E. Illouz, B. Burg, L. Polverelli, and T. Snyder. "Getting Past The Spin: The CorWave LVAD, a Membrane Wave Pump Providing Physiologic Pulsatility without High Shear". In: *The Journal of Heart and Lung Transplantation* 38.4 (2019), p. 5345.

[38]   C. N. Botterbusch, S. Lucquin, P. Monticone, J. B. Drevet, A. Guignabert, and P. Meneroud. *Implantable pump system having an undulating membrane*. US Patent 9,968,720. 2018.

[39]   C. Botterbusch, T. Snyder, P.-P. Monticone, L. de Lillers, A. Schmidt, and C. Rasser. "CorWave LVAD: Insight into Device Concept and Stage of Development". In: *Mechanical Support for Heart Failure*. Springer, 2020, pp. 587–597.

[40] C. Botterbusch, P Monticone, and L Polverelli. "Flow Performance of the CorWave LVAD Membrane Wave Pump". In: *The Journal of Heart and Lung Transplantation* 37.4 (2018), S259.

[41] K. Bourque, D. B. Gernes, H. M. Loree, J. S. Richardson, V. L. Poirier, N. Barletta, A. Fleischli, G. Foiera, T. M. Gempp, R. Schoeb, et al. "HeartMate III: pump design for a centrifugal LVAD with a magnetically levitated rotor". In: *ASAIO journal* 47.4 (2001), pp. 401–405.

[42] K. Bourque, C. Cotter, C. Dague, D. Harjes, O. Dur, J. Duhamel, K. Spink, K. Walsh, and E. Burke. "Design rationale and preclinical evaluation of the HeartMate 3 left ventricular assist system for hemocompatibility". In: *ASAIO journal* 62.4 (2016), pp. 375–383.

[43] N. Boustead. "The haemodynamics of aneurysms: a spectral element analysis of the effects of wall stiffness". PhD thesis. Monash University, 2012.

[44] N. L. Bragazzi, W. Zhong, J. Shu, A. Abu Much, D. Lotan, A. Grupper, A. Younis, and H. Dai. "Burden of heart failure and underlying causes in 195 countries and territories from 1990 to 2017". In: *European Journal of Preventive Cardiology* (2021).

[45] M. Brandfonbrener, M. Landowne, and N. W. Shock. "Changes in cardiac output with age". In: *Circulation* 12.4 (1955), pp. 557–566.

[46] J. G. Brink and J. Hassoulas. "The first human heart transplant and further advances in cardiac transplantation at Groote Schuur Hospital and the University of Cape Town". In: *Cardiovascular journal of Africa* 20.1 (2009), p. 31.

[47] S. C. Brozena and M. Jessup. "The new staging system for heart failure. What every primary care physician should know." In: *Geriatrics (Basel, Switzerland)* 58.6 (2003), pp. 31–6.

[48] J. Brunet, B. Pierrat, and P. Badel. "A parametric study on factors influencing the onset and propagation of aortic dissection using the extended finite element method". In: *IEEE Transactions on Biomedical Engineering* (2021). DOI: `10.1109/TBME.2021.3056022`.

[49] G. W. Burgreen, J. F. Antaki, Z. Wu, and A. J. Holmes. "Computational fluid dynamics as a development tool for rotary blood pumps". In: *Artificial organs* 25.5 (2001), pp. 336–340.

[50] E. Burman. "Ghost penalty". In: *Comptes Rendus Mathematique* 348.21-22 (2010), pp. 1217–1220.

[51] E. Burman and M. A. Fernández. "An unfitted Nitsche method for incompressible fluid–structure interaction using overlapping meshes". In: *Computer Methods in Applied Mechanics and Engineering* 279 (2014), pp. 497–514.

[52] E. Burman, M. A. Fernández, and S. Frei. "A Nitsche-based formulation for fluid-structure interactions with contact". In: *arXiv preprint arXiv:1808.08758* (2018).

[53] E. Burman, M. A. Fernández, and P. Hansbo. "Continuous interior penalty finite element method for Oseen's equations". In: *SIAM journal on numerical analysis* 44.3 (2006), pp. 1248–1274.

[54] E. Burman, S. Claus, P. Hansbo, M. G. Larson, and A. Massing. "CutFEM: discretizing geometry and partial differential equations". In: *International Journal for Numerical Methods in Engineering* 104.7 (2015), pp. 472–501.

[55] C. Capelli, G. M. Bosi, E. Cerri, J. Nordmeyer, T. Odenwald, P. Bonhoeffer, F. Migliavacca, A. M. Taylor, and S. Schievano. "Patient-specific simulations of transcatheter aortic valve stent implantation". In: *Medical & biological engineering & computing* 50.2 (2012), pp. 183–192.

[56] *Cardiac pressure Volume loop*. 2019. URL: https://quizlet.com/362331729/cardiac-pressure-volume-loop-flash-cards/.

[57] *Cardiovascular system*. 2015. URL: https://www.slideshare.net/sydpeck93/heart-cardiac-cycle-46793168.

[58] F. Castagna, E. Stöhr, A. Pinsino, J. Cockcroft, J. Willey, A. Garan, V. Topkara, P. Colombo, M. Yuzefpolskaya, and B. McDonnell. "The unique blood pressures and pulsatility of LVAD patients: current challenges and future opportunities". In: *Current hypertension reports* 19.10 (2017), p. 85.

[59] L. Cattaneo, L. Formaggia, G. F. Iori, A. Scotti, and P. Zunino. "Stabilized extended finite elements for the approximation of saddle point problems with unfitted interfaces". In: *Calcolo* 52.2 (2015), pp. 123–152.

[60] C. J. Cawthorn and N. J. Balmforth. "Contact in a viscous fluid. Part 1. A falling wedge". In: *Journal of Fluid Mechanics* 646 (2010), pp. 327–338.

[61] V. Chabannes, G. Pena, and C. Prud'Homme. "High-order fluid–structure interaction in 2D and 3D application to blood flow in arteries". In: *Journal of Computational and Applied Mathematics* 246 (2013), pp. 1–9.

[62] Z. Chen, S. K. Jena, G. A. Giridharan, S. C. Koenig, M. S. Slaughter, B. P. Griffith, and Z. J. Wu. "Flow features and device-induced blood trauma in CF-VADs under a pulsatile blood flow condition: A CFD comparative study". In: *International journal for numerical methods in biomedical engineering* 34.2 (2018), e2924.

[63] Z. Chen, S. K. Jena, G. A. Giridharan, M. A. Sobieski, S. C. Koenig, M. S. Slaughter, B. P. Griffith, and Z. J. Wu. "Shear stress and blood trauma under constant and pulse-modulated speed CF-VAD operations: CFD analysis of the HVAD". In: *Medical & biological engineering & computing* 57.4 (2019), pp. 807–818.

[64] A. Cheng, C. A. Williamitis, and M. S. Slaughter. "Comparison of continuous-flow and pulsatile-flow left ventricular assist devices: is there an advantage to pulsatility?" In: *Annals of cardiothoracic surgery* 3.6 (2014), p. 573.

[65] S. Chien. "Shear dependence of effective cell volume as a determinant of blood viscosity". In: *Science* 168.3934 (1970), pp. 977–979.

[66] W. Chiu, M. J. Slepian, and D. Bluestein. "Thrombus formation patterns in the HeartMate II VAD-clinical observations can be predicted by numerical simulations". In: *ASAIO journal (American Society for Artificial Internal Organs: 1992)* 60.2 (2014), p. 237.

[67] W.-C. Chiu, M. Xenos, Y. Alemu, G. Girdhar, B. Lynch, J. Jesty, M. Slepian, S. Einav, and D. Bluestein. "Thrombogenicity Comparison of Axial Ventricular Assist Devices by DTE Methodology: MicroMed HeartAssist 5 and Thoratec Heartmate II". In: *Summer Bioengineering Conference*. Vol. 44809. American Society of Mechanical Engineers. 2012, pp. 63–64.

[68] F. Chouly and P. Hild. "A Nitsche-based method for unilateral contact problems: numerical analysis". In: *SIAM Journal on Numerical Analysis* 51.2 (2013), pp. 1295–1307.

[69]   F. Chouly, M. Fabre, P. Hild, R. Mlika, J. Pousin, and Y. Renard. "An overview of recent results on Nitsche's method for contact problems". In: *Geometrically unfitted finite element methods and applications* (2017), pp. 93–141.

[70]   S. Claus and P. Kerfriden. "A stable and optimally convergent LaTIn-CutFEM algorithm for multiple unilateral contact problems". In: *International Journal for Numerical Methods in Engineering* 113.6 (2018), pp. 938–966.

[71]   B. Cockburn, G. Kanschat, and D. Schötzau. "A note on discontinuous Galerkin divergence-free solutions of the Navier–Stokes equations". In: *Journal of Scientific Computing* 31.1-2 (2007), pp. 61–73.

[72]   Z. J. Coffman, V. M. Bandisode, M. N. Kavarana, and J. R. Buckley. "Utilization of an Abiomed Impella Device as a Rescue Therapy for Acute Ventricular Failure in a Fontan Patient". In: *World Journal for Pediatric and Congenital Heart Surgery* 10.4 (2019), pp. 518–519.

[73]   M. Cohen, P. Urban, J. T. Christenson, D. L. Joseph, R. J. Freedman Jr, M. F. Miller, E. M. Ohman, R. C. Reddy, G. W. Stone, and J. J. Ferguson III. "Intra-aortic balloon counterpulsation in US and non-US centres: results of the Benchmark Registry". In: *European heart journal* 24.19 (2003), pp. 1763–1770.

[74]   L. H. Cohn. *Fifty years of open-heart surgery*. 2003.

[75]   W. E. Cohn, D. L. Timms, and O. H. Frazier. "Total artificial hearts: past, present, and future". In: *Nature Reviews Cardiology* 12.10 (2015), p. 609.

[76]   P Colli Franzone, L. F. Pavarino, and S Scacchi. *Mathematical Cardiac Electrophysiology*. Springer, 2014.

[77]   J. A. Cook, K. B. Shah, M. A. Quader, R. H. Cooke, V. Kasirajan, K. K. Rao, M. C. Smallfield, I. Tchoukina, and D. G. Tang. "The total artificial heart". In: *Journal of thoracic disease* 7.12 (2015), p. 2172.

[78]   D. A. Cooley. "In Memoriam: Willem Johan Kolff 1911–2009". In: *Texas Heart Institute Journal* 36.2 (2009), p. 83.

[79]   D. A. Cooley, D. Liotta, G. L. Hallman, R. D. Bloodwell, R. D. Leachman, and J. D. Milam. "Orthotopic cardiac prosthesis for two-staged cardiac replacement". In: *The American journal of cardiology* 24.5 (1969), pp. 723–730.

[80]   J. G. Copeland, A. Pavie, D. Duveau, W. J. Keon, R. Masters, R. Pifarre, R. G. Smith, and F. A. Arabia. "Bridge to transplantation with the CardioWest total artificial heart: the international experience 1993 to 1995." In: *The Journal of heart and lung transplantation: the official publication of the International Society for Heart Transplantation* 15.1 (1996), pp. 94–99.

[81]   F. Cornat, E. E. Antoine, F. Bozsak, and A. I. Barakat. "Optimizing the performance of drug-eluting stents: simulations and experiments". In: *19th European Conference on Mathematics for Industry*. 2016, p. 31.

[82]   J. Davidson, F Baumgariner, B. Omari, and J. Milliken. "Intra-aortic balloon pump: indications and complications." In: *Journal of the National Medical Association* 90.3 (1998), p. 137.

[83]   C De Lazzari, A D'Ambrosi, F Tufano, L. Fresiello, M Garante, R Sergiacomi, F Stagnitti, C. Caldarera, and N Alessandri. "Cardiac resynchronization therapy: could a numerical simulator be a useful tool in order to predict the

response of the biventricular pacemaker synchronization". In: *Eur Rev Med Pharmacol Sci* 14.11 (2010), pp. 969–978.

[84] E. S. DeMartino, N. A. Braus, D. P. Sulmasy, J. K. Bohman, J. M. Stulak, P. K. Guru, K. R. Fuechtmann, N. Singh, G. J. Schears, and P. S. Mueller. "Decisions to withdraw extracorporeal membrane oxygenation support: patient characteristics and ethical considerations". In: *Mayo Clinic Proceedings*. Vol. 94. 4. Elsevier. 2019, pp. 620–627.

[85] S. Deparis, M. Discacciati, G. Fourestey, and A. Quarteroni. "Fluid–structure algorithms based on Steklov–Poincaré operators". In: *Computer Methods in Applied Mechanics and Engineering* 195.41-43 (2006), pp. 5797–5812.

[86] S. Di Gregorio, M. Fedele, G. Pontone, A. F. Corno, P. Zunino, C. Vergara, and A. Quarteroni. "A computational model applied to myocardial perfusion in the human heart: from large coronaries to microvasculature". In: *Journal of Computational Physics* 424 (2021), p. 109836.

[87] J. Dolbow, N. Moës, and T. Belytschko. "An extended finite element method for modeling crack growth with frictional contact". In: *Computer methods in applied Mechanics and engineering* 190.51-52 (2001), pp. 6825–6846.

[88] J. Donea, S. Giuliani, and J. Halleux. "An arbitrary Lagrangian-Eulerian finite element method for transient dynamic fluid-structure interactions". In: *Computer methods in applied mechanics and engineering* 33.1-3 (1982), pp. 689–723.

[89] L. A. Down, D. V. Papavassiliou, and A. Edgar. "Significance of extensional stresses to red blood cell lysis in a shearing flow". In: *Annals of biomedical engineering* 39.6 (2011), pp. 1632–1642.

[90] M. G. Doyle. *Simulation of myocardium motion and blood flow in the heart with fluid-structure interaction*. University of Ottawa (Canada), 2011.

[91] J. B. Drevet. *Vibrating membrane fluid circulator*. US Patent 6,659,740. 2003.

[92] D. Dvir, I. M. Barbash, I. Ben-Dor, R. Torguson, S. Badr, L. K. Pendyala, J. P. Loh, A. D. Pichard, R. Waksman, et al. "Paravalvular regurgitation after transcatheter aortic valve replacement: diagnosis, clinical outcome, preventive and therapeutic strategies". In: *Cardiovascular Revascularization Medicine* 14.3 (2013), pp. 174–181.

[93] K. Dworzynski, E. Roberts, A. Ludman, and J. Mant. "Diagnosing and managing acute heart failure in adults: summary of NICE guidance". In: *BmJ* 349 (2014).

[94] H. J. Eisen. "Left ventricular assist devices (LVADS): History, clinical application and complications". In: *Korean circulation journal* 49.7 (2019), p. 568.

[95] M. Esmaily-Moghadam, T.-Y. Hsia, and A. L. Marsden. "A non-discrete method for computation of residence time in fluid mechanics simulations". In: *Physics of fluids* 25.11 (2013), p. 110802.

[96] J. D. Estep, R. C. Starling, D. A. Horstmanshof, C. A. Milano, C. H. Selzman, K. B. Shah, M. Loebe, N. Moazami, J. W. Long, J. Stehlik, et al. "Risk assessment and comparative effectiveness of left ventricular assist device and medical management in ambulatory heart failure patients: results from the ROADMAP study". In: *Journal of the American College of Cardiology* 66.16 (2015), pp. 1747–1761.

[97] M. M. Faghih and M. K. Sharp. "Deformation of human red blood cells in extensional flow through a hyperbolic contraction". In: *Biomechanics and modeling in mechanobiology* 19.1 (2020), pp. 251–261.

[98] M. M. Faghih and M. K. Sharp. "Modeling and prediction of flow-induced hemolysis: a review". In: *Biomechanics and modeling in mechanobiology* 18.4 (2019), pp. 845–881.

[99] D. Farmakis, P. Stafylas, G. Giamouzis, N. Maniadakis, and J. Parissis. *The medical and socioeconomic burden of heart failure: a comparative delineation with cancer*. 2016.

[100] "Fatigue crack propagation in complex stress fields: Experiments and numerical simulations using the Extended Finite Element Method (XFEM)". In: *International Journal of Fatigue* 103 (2017), pp. 112–121. ISSN: 0142-1123.

[101] H. Feier, C. Mekkaoui, J.-B. Drevet, Y. Sérée, C. Richomme, P.-H. Rolland, and T. G. Mesana. "A novel, valveless ventricular assist device: the FishTail pump. First experimental in vivo studies". In: *Artificial organs* 26.12 (2002), pp. 1026–1031.

[102] M. A. Fernández and M. Moubachir. "A Newton method using exact Jacobians for solving fluid–structure coupling". In: *Computers & Structures* 83.2-3 (2005), pp. 127–142.

[103] L. Formaggia, F. Gatti, and S. Zonca. "An XFEM/DG Approach for Fluid-Structure Interaction Problems with Contact". In: *Applications of Mathematics* 66.2 (2021), pp. 183–211.

[104] K. H. Fraser, T. Zhang, M. E. Taskin, B. P. Griffith, and Z. J. Wu. "Computational fluid dynamics analysis of thrombosis potential in left ventricular assist device drainage cannulae". In: *ASAIO journal (American Society for Artificial Internal Organs: 1992)* 56.3 (2010), p. 157.

[105] K. H. Fraser, M. E. Taskin, T. Zhang, J. S. Richardson, B. Gellman, K. Dasse, B. P. Griffith, and Z. J. Wu. "The effect of impeller position on CFD calculations of blood flow in magnetically levitated centrifugal blood pumps". In: *Summer Bioengineering Conference*. Vol. 44038. American Society of Mechanical Engineers. 2010, pp. 119–120.

[106] K. H. Fraser, T. Zhang, M. E. Taskin, B. P. Griffith, and Z. J. Wu. "A quantitative comparison of mechanical blood damage parameters in rotary ventricular assist devices: shear stress, exposure time and hemolysis index". In: *Journal of biomechanical engineering* 134.8 (2012), p. 081002.

[107] K. H. Fraser, M. E. Taskin, B. P. Griffith, and Z. J. Wu. "The use of computational fluid dynamics in the development of ventricular assist devices". In: *Medical Engineering and Physics* 33.3 (2011), pp. 263–280. ISSN: 1350-4533.

[108] L. Fresiello, F. Rademakers, P. Claus, G. Ferrari, A. Di Molfetta, and B. Meyns. "Exercise physiology with a left ventricular assist device: Analysis of heart-pump interaction with a computational simulator". In: *Plos one* 12.7 (2017), e0181879.

[109] T. Fries. "Overview and comparison of different variants of the XFEM". In: *PAMM* 14.1 (2014), pp. 27–30.

[110] A. Fumagalli and A. Scotti. "A numerical method for two-phase flow in fractured porous media with non-matching grids". In: *Advances in Water Resources* 62 (2013), pp. 454–464.

[111]   I. Fumagalli. "A reduced 3D-0D FSI model of the aortic valve including leaflets curvature". In: *arXiv preprint arXiv:2106.00571* (2021).

[112]   F. Gatti. "An XFEM-Nitsche approach for fluid structure interaction problems with contact". PhD Thesis. Politecnico di Milano, 2019.

[113]   M. W. Gee, U. Küttler, and W. A. Wall. "Truly monolithic algebraic multigrid for fluid–structure interaction". In: *International Journal for Numerical Methods in Engineering* 85.8 (2011), pp. 987–1016.

[114]   A. Gerstenberger and W. A. Wall. "An embedded Dirichlet formulation for 3D continua". In: *International Journal for Numerical Methods in Engineering* 82.5 (2010), pp. 537–563.

[115]   A. Gerstenberger and W. A. Wall. "An extended finite element method/Lagrange multiplier based approach for fluid–structure interaction". In: *Computer Methods in Applied Mechanics and Engineering* 197.19-20 (2008), pp. 1699–1714.

[116]   A Gerstenberger and W. Wall. "An extended finite element method based approach for large deformation fluid-structure interaction". In: *Proceedings of the European Conference on Computational Fluid Dynamics*. 2006, p. CD551.

[117]   L. Gesenhues, L. Pauli, and M. Behr. "Strain-based blood damage estimation for computational design of ventricular assist devices". In: *The International journal of artificial organs* 39.4 (2016), pp. 166–170.

[118]   C. Geuzaine and J.-F. Remacle. "Gmsh: A 3-D finite element mesh generator with built-in pre-and post-processing facilities". In: *International journal for numerical methods in engineering* 79.11 (2009), pp. 1309–1331.

[119]   B. Ghadimi, A. Nejat, S. A. Nourbakhsh, and N. Naderi. "Shape optimization of a centrifugal blood pump by coupling CFD with metamodel-assisted genetic algorithm". In: *Journal of Artificial Organs* 22.1 (2019), pp. 29–36.

[120]   M. Ghodrati, A. Maurer, T. Schlöglhofer, T. Khienwad, D. Zimpfer, D. Beitzke, F. Zonta, F. Moscato, H. Schima, and P. Aigner. "The influence of left ventricular assist device inflow cannula position on thrombosis risk". In: *Artificial organs* 44.9 (2020), pp. 939–946.

[121]   A. Gilmanov, H. Stolarski, and F. Sotiropoulos. "Flow–structure interaction simulations of the aortic heart valve at physiologic conditions: The role of tissue constitutive model". In: *Journal of biomechanical engineering* 140.4 (2018).

[122]   S. Giordan. *Contiuum mechanics and nonlinear elasticity*. Lecture notes. Department of Physics, University of Cagliari, 2011.

[123]   G. Girdhar, M. Xenos, Y. Alemu, W.-C. Chiu, B. E. Lynch, J. Jesty, S. Einav, M. J. Slepian, and D. Bluestein. "Device thrombogenicity emulation: a novel method for optimizing mechanical circulatory support device thromboresistance". In: *PloS one* 7.3 (2012), e32463.

[124]   R. Glowinski, T. Pan, and J. Periaux. "A fictitious domain method for Dirichlet problem and applications". In: *Computer Methods in Applied Mechanics and Engineering* 111.3-4 (1994), pp. 283–303.

[125]   R. Glowinski, T. Pan, and J. Periaux. "A fictitious domain method for external incompressible viscous flow modeled by Navier-Stokes equations". In: *Computer Methods in Applied Mechanics and Engineering* 112.1-4 (1994), pp. 133–148.

[126]   J. Gohean and R. Smalling. "New Mechanical Circulatory Device: TOR-VAD". In: *Mechanical Support for Heart Failure*. Springer, 2020, pp. 555–561.

[127]   A. T. Golpaygani, K. Hassani, A. Karimi, and A. N. Zaeim. "A numerical analysis on different-generation prototypes of ventricular assist device". In: *International Journal of Modeling, Simulation, and Scientific Computing* 10.05 (2019), p. 1950029.

[128]   P. D. Goodman, E. T. Barlow, P. M. Crapo, S. F. Mohammad, and K. A. Solen. "Computational model of device-induced thrombosis and thromboembolism". In: *Annals of biomedical engineering* 33.6 (2005), pp. 780–797.

[129]   M. L. Goodwin, P. H. Lee, and N. A. Mokadam. "Implantable Continuous-Flow Blood Pump Technology and Features". In: *Mechanical Support for Heart Failure*. Springer, 2020, pp. 337–358.

[130]   E. Z. Gorodeski, C. Magnelli-Reyes, L. A. Moennich, A. Grimaldi, and J. Rickard. "Cardiac resynchronization therapy-heart failure (CRT-HF) clinic: a novel model of care". In: *Plos one* 14.9 (2019), e0222610.

[131]   R. Graefe and L. Pauli. "Computational Fluid Dynamics for Mechanical Circulatory Support Device Development". In: *Mechanical Support for Heart Failure*. Springer, 2020, pp. 399–427.

[132]   R. Graefe, A. Henseler, R. Körfer, B. Meyns, and L. Fresiello. "Influence of left ventricular assist device pressure-flow characteristic on exercise physiology: Assessment with a verified numerical model". In: *The International journal of artificial organs* 42.9 (2019), pp. 490–499.

[133]   R. Graefe, C. Beyel, A. Henseler, R. Körfer, U. Steinseifer, and G. Tenderich. "The effect of LVAD pressure sensitivity on the assisted circulation under consideration of a mitral insufficiency: an in vitro study". In: *Artificial organs* 42.10 (2018), E304–E314.

[134]   G. P. Gravlee. *Cardiopulmonary bypass: principles and practice*. Lippincott Williams & Wilkins, 2008.

[135]   I. D. Gregoric, L. P. Jacob, S. La Francesca, B. A. Bruckner, W. E. Cohn, P. Loyalka, B. Kar, and O. Frazier. "The TandemHeart as a bridge to a long-term axial-flow left ventricular assist device (bridge to bridge)". In: *Texas Heart Institute Journal* 35.2 (2008), p. 125.

[136]   S. D. Gregory, D. Timms, N. Gaddum, D. G. Mason, and J. F. Fraser. "Biventricular assist devices: a technical review". In: *Annals of biomedical engineering* 39.9 (2011), p. 2313.

[137]   B. P. Griffith, R. L. Kormos, H. S. Borovetz, K. Litwak, J. F. Antaki, V. L. Poirier, and K. C. Butler. "HeartMate II left ventricular assist system: from concept to first clinical use". In: *The Annals of thoracic surgery* 71.3 (2001), S116–S120.

[138]   J. Grinstein, R. Torii, C. V. Bourantas, and H. M. Garcia-Garcia. "Left Ventricular Assist Device Flow Pattern Analysis Using a Novel Model Incorporating Left Ventricular Pulsatility". In: *ASAIO Journal* 67.7 (2021), pp. 724–732.

[139]   F. Guglietta, M. Behr, L. Biferale, G. Falcucci, and M. Sbragaglia. "On the effects of membrane viscosity on transient red blood cell dynamics". In: *Soft Matter* 16.26 (2020), pp. 6191–6205.

[140] J. E. Hall and G. AC. "Guyton and Hall textbook of medical physiology". In: *Korea: Bupmoon Education* (2017).

[141] A. Hansbo and P. Hansbo. "An unfitted finite element method, based on Nitsche's method, for elliptic interface problems". In: *Computer methods in applied mechanics and engineering* 191.47-48 (2002), pp. 5537–5552.

[142] P. Hansbo, M. G. Larson, and S. Zahedi. "A cut finite element method for a Stokes interface problem". In: *Applied Numerical Mathematics* 85 (2014), pp. 90–114.

[143] P. Hansbo, M. G. Larson, and S. Zahedi. "Characteristic cut finite element methods for convection–diffusion problems on time dependent surfaces". In: *Computer Methods in Applied Mechanics and Engineering* 293 (2015), pp. 431–461.

[144] W. Hao, P. Sun, J. Xu, and L. Zhang. "Multiscale and monolithic arbitrary Lagrangian–Eulerian finite element method for a hemodynamic fluid-structure interaction problem involving aneurysms". In: *Journal of Computational Physics* 433 (2021), p. 110181.

[145] *Heart Transplantation Rejection*. URL: https://www.ncbi.nlm.nih.gov/books/NBK537057/.

[146] B. Heinrich and S. Nicaise. "The Nitsche mortar finite-element method for transmission problems with singularities". In: *IMA journal of numerical analysis* 23.2 (2003), pp. 331–358.

[147] J. D. Hellums. "1993 Whitaker Lecture: biorheology in thrombosis research". In: *Annals of biomedical engineering* 22.5 (1994), pp. 445–455.

[148] M. Hillairet and T. Takahashi. "Collisions in three-dimensional fluid structure interaction problems". In: *SIAM Journal on Mathematical Analysis* 40.6 (2009), pp. 2451–2477.

[149] M. Hirschhorn, V. Tchantchaleishvili, R. Stevens, J. Rossano, and A. Throckmorton. "Fluid–structure interaction modeling in cardiovascular medicine–A systematic review 2017–2019". In: *Medical engineering and physics* 78 (2020), pp. 1–13.

[150] C. W. Hirt, A. A. Amsden, and J. Cook. "An arbitrary Lagrangian-Eulerian computing method for all flow speeds". In: *Journal of computational physics* 14.3 (1974), pp. 227–253.

[151] W. L. Holman, D. Acharya, F. Siric, and R. Y. Loyaga-Rendon. "Assessment and management of right ventricular failure in left ventricular assist device patients". In: *Circulation Journal* (2015), CJ–15.

[152] W. L. Holman, W. E. Pae, J. J. Teutenberg, M. A. Acker, D. C. Naftel, B. C. Sun, C. A. Milano, and J. K. Kirklin. "INTERMACS: interval analysis of registry data". In: *Journal of the American College of Surgeons* 208.5 (2009), pp. 755–761.

[153] G. A. Holzapfel and R. W. Ogden. "Modelling the layer-specific three-dimensional residual stresses in arteries, with an application to the human aorta". In: *Journal of the Royal Society Interface* 7.46 (2010), pp. 787–799.

[154] M.-C. Hsu, I. Akkerman, and Y. Bazilevs. "Wind turbine aerodynamics using ALE–VMS: Validation and the role of weakly enforced boundary conditions". In: *Computational Mechanics* 50.4 (2012), pp. 499–511.

[155] T. J. R. Hughes, W. K. Liu, and T. K. Zimmermann. "Lagrangian-Eulerian finite element formulation for incompressible viscous flows". In: *Computer methods in applied mechanics and engineering* 29.3 (1981), pp. 329–349.

[156] S. A. Hunt, E. Rose, R. E. of Mechanical Assistance for the Treatment of Congestive Heart Failure (REMATCH) Study Group, et al. "The REMATCH trial: Long-term use of a left ventricular assist device for end-stage heart failure". In: *Journal of cardiac failure* 8.2 (2002), pp. 59–60.

[157] C. T. January, L. S. Wann, H. Calkins, L. Y. Chen, J. E. Cigarroa, J. C. Cleveland Jr, P. T. Ellinor, M. D. Ezekowitz, M. E. Field, K. L. Furie, et al. "2019 AHA/ACC/HRS Focused Update of the 2014 AHA/ACC/HRS Guideline for the Management of Patients With Atrial Fibrillation: A Report of the American College of Cardiology/American Heart Association Task Force on Clinical Practice Guidelines and the Heart Rhythm Society in Collaboration With the Society of Thoracic Surgeons". In: *Circulation* 140.2 (2019), e125–e151.

[158] X. Jiang, Z. Huang, R. Luo, H. Zuo, X. Zheng, and S. Deng. "A New Method for Searching the Enrichment Element in Extended Finite Element Method". In: *International Journal of Applied Mathematics* 50.3 (2020).

[159] K. Kamran, R. Rossi, and E. Oñate. "A locally extended finite element method for the simulation of multi-fluid flows using the Particle Level Set method". In: *Computer Methods in Applied Mechanics and Engineering* 294 (2015), pp. 1–18.

[160] V. Kannojiya, A. K. Das, and P. K. Das. "Numerical simulation of centrifugal and hemodynamically levitated LVAD for performance improvement". In: *Artificial Organs* (2019).

[161] A. Karimi, R. Razaghi, and M. Koyama. "A patient-specific numerical modeling of the spontaneous coronary artery dissection in relation to atherosclerosis". In: *Computer methods and programs in biomedicine* 182 (2019), p. 105060.

[162] K. K. Khush, W. S. Cherikh, D. C. Chambers, M. O. Harhay, D. Hayes, E. Hsich, B. Meiser, L. Potena, A. Robinson, J. W. Rossano, et al. "The International Thoracic Organ Transplant Registry of the International Society for Heart and Lung Transplantation: Thirty-sixth adult heart transplantation report—2019; focus theme: Donor and recipient size match". In: *The Journal of Heart and Lung Transplantation* 38.10 (2019), pp. 1056–1066.

[163] J. K. Kirklin and D. C. Naftel. "Mechanical circulatory support: registering a therapy in evolution". In: *Circulation: Heart Failure* 1.3 (2008), pp. 200–205.

[164] W.-J. Ko, C.-Y. Lin, R. J. Chen, S.-S. Wang, F.-Y. Lin, and Y.-S. Chen. "Extracorporeal membrane oxygenation support for adult postcardiotomy cardiogenic shock". In: *The Annals of thoracic surgery* 73.2 (2002), pp. 538–545.

[165] R. L. Kormos, J. Cowger, F. D. Pagani, J. J. Teuteberg, D. J. Goldstein, J. P. Jacobs, R. S. Higgins, L. W. Stevenson, J. Stehlik, P. Atluri, et al. "The Society of Thoracic Surgeons Intermacs database annual report: evolving indications, outcomes, and scientific partnerships". In: *The Journal of Heart and Lung Transplantation* 38.2 (2019), pp. 114–126.

[166] A. Koster, M. Loebe, R. Hansen, E. V. Potapov, G. P. Noon, H. Kuppe, and R. Hetzer. "Alterations in coagulation after implantation of a pulsatile Novacor LVAD and the axial flow MicroMed DeBakey LVAD". In: *The Annals of thoracic surgery* 70.2 (2000), pp. 533–537.

[167] A. L. Kozak, K Tehrani, E Abrahamson, and A Krimotat. "Validation of the ALE Methodology by Comparison with the Experimental Data Obtained from a Sloshing Tank". In: *14th International LS-DYNA Users Conference*. 2016.

[168] T. Lassila, A. Manzoni, A. Quarteroni, and G. Rozza. "Boundary control and shape optimization for the robust design of bypass anastomoses under uncertainty". In: *ESAIM: Mathematical Modelling and Numerical Analysis* 47.4 (2013), pp. 1107–1131.

[169] C. Latrémouille, A. Carpentier, P. Leprince, J. C. Roussel., B. Cholley, E. Boissier, E. Epailly, A. Capel, P. Jansen, and D. M. Smadja. "A bioprosthetic total artificial heart for end-stage heart failure: results from a pilot study". In: *The Journal of Heart and Lung Transplantation* 37.1 (2018), pp. 33–37.

[170] E. Lauga, M. Brenner, and H. Stone. "Microfluidics: The no-slip boundary condition". In: *Springer Handbooks*. Springer, 2007, pp. 1219–1240.

[171] A. W. Lee, C. M. Costa, M. Strocchi, C. A. Rinaldi, and S. A. Niederer. "Computational modeling for cardiac resynchronization therapy". In: *Journal of cardiovascular translational research* 11.2 (2018), pp. 92–108.

[172] L. S. Lee and P. S. Shekar. "Current state-of-the-art of device therapy for advanced heart failure". In: *Croatian medical journal* 55.6 (2014), pp. 577–586.

[173] H. Leo, H. Simon, J. Carberry, S.-C. Lee, and A. Yoganathan. "A Comparison of Flow Field Structures of Two Tri-Leaflet Polymeric Heart Valves". In: *Annals of biomedical engineering* 33 (May 2005), pp. 429–43.

[174] H. Li, Z. Gou, F. Huang, X. Ruan, W. Qian, and X. Fu. "Evaluation of the hemolysis and fluid dynamics of a ventricular assist device under the pulsatile flow condition". In: *Journal of Hydrodynamics* (2018), pp. 1–11.

[175] D. Liotta. "Early clinical application of assisted circulation". In: *Texas Heart Institute Journal* 29.3 (2002), p. 229.

[176] G. Lippi and F. Sanchis-Gomar. "Global epidemiology and future trends of heart failure". In: *AME Med J* 5.15 (2020), pp. 1–6.

[177] G. Liu, D. Jin, J. Zhou, Y. Zhang, H. Chen, H. S. Sun, S. Hu, and X. Gui. "Numerical investigation of the influence of blade radial gap flow on axial blood pump performance". In: *Asaio Journal* 65.1 (2019), pp. 59–69.

[178] G.-M. Liu, H.-b. Chen, J.-f. Hou, Y. Zhang, and S.-s. Hu. "Platelet adhesion emulation: A novel method for estimating the device thrombosis potential of a ventricular assist device". In: *The International journal of artificial organs* 43.4 (2020), pp. 252–257.

[179] H. Liu, S. Liu, and X. Ma. "Varying speed modulation of continuous-flow left ventricular assist device based on cardiovascular coupling numerical model". In: *Computer Methods in Biomechanics and Biomedical Engineering* 24.9 (2021), pp. 956–972.

[180] E. Lluch, O. Camara, R. Doste, B. Bijnens, M. De Craene, M. Sermesant, V. Y. Wang, M. P. Nash, and H. G. Morales. "Calibration of a fully coupled

electromechanical meshless computational model of the heart with experimental data". In: *Computer Methods in Applied Mechanics and Engineering* 364 (2020), p. 112869.

[181]   A. Loforte, L. Botta, S. Boschi, G. Gliozzi, G. G. Cavalli, C. Mariani, S. Martin Suarez, and D. Pacini. "Durable Continuous-Flow Mechanical Circulatory Support: State of the Art". In: *Hearts* 2.1 (2021), pp. 127–138.

[182]   A. S. Lone, S. A. Kanth, A. Jameel, and G. Harmain. "A state of art review on the modeling of Contact type Nonlinearities by Extended Finite Element method". In: *Materials Today: Proceedings* 18 (2019), pp. 3462–3471.

[183]   B. Long, J. Robertson, A. Koyfman, and W. Brady. "Left ventricular assist devices and their complications: a review for emergency clinicians". In: *The American journal of emergency medicine* 37.8 (2019), pp. 1562–1570.

[184]   J. W. Long, A. G. Kfoury, M. S. Slaughter, M. Silver, C. Milano, J. Rogers, R. Delgado, and O. Frazier. "Long-term destination therapy with the HeartMate XVE left ventricular assist device: improved outcomes since the REMATCH study". In: *Congestive Heart Failure* 11.3 (2005), pp. 133–138.

[185]   G. Luraghi, F. Migliavacca, and J. F. R. Matas. "Study on the accuracy of structural and FSI heart valves simulations". In: *Cardiovascular engineering and technology* 9.4 (2018), pp. 723–738.

[186]   G. Luraghi, F. Migliavacca, A. García-González, C. Chiastra, A. Rossi, D. Cao, G. Stefanini, and J. F. R. Matas. "On the Modeling of Patient-Specific Transcatheter Aortic Valve Replacement: A Fluid–Structure Interaction Approach". In: *Cardiovascular engineering and technology* (2019), pp. 1–19.

[187]   A. M. Maceira, S. K. Prasad, M. Khan, and D. J. Pennell. "Reference right ventricular systolic and diastolic function normalized to age, gender and body surface area from steady-state free precession cardiovascular magnetic resonance". In: *European heart journal* 27.23 (2006), pp. 2879–2888.

[188]   A. Maceira, S. Prasad, M Khan, and D. Pennell. "Normalized left ventricular systolic and diastolic function by steady state free precession cardiovascular magnetic resonance". In: *Journal of Cardiovascular Magnetic Resonance* 8.3 (2006), pp. 417–426.

[189]   G. Makdisi and I.-w. Wang. "Extra corporeal membrane oxygenation (ECMO) review of a lifesaving technology". In: *Journal of thoracic disease* 7.7 (2015), E166.

[190]   J. Marcano, A. Mattar, and J. A. Morgan. "Overview of Mechanical Circulatory Support Devices and Concepts". In: *Mechanical Support for Heart Failure*. Springer, 2020, pp. 51–61.

[191]   T. D. Marco and K. Chatterjee. "Refractory Heart Failure: A Therapeutic Approach". In: *Journal of Intensive Care Medicine* 11.3 (1996), pp. 121–148.

[192]   A. L. Marsden, Y. Bazilevs, C. C. Long, and M. Behr. "Recent advances in computational methodology for simulation of mechanical circulatory assist devices". In: *Wiley interdisciplinary reviews: Systems biology and medicine* 6.2 (2014), pp. 169–188.

[193]   M. Martinolli, F. Cornat, and C. Vergara. "Computational Fluid-Structure Interaction Study of a new Wave Membrane Blood Pump". In: *MOX Report 40/2021* (2021).

[194] M. Martinolli, J. Biasetti, S. Zonca, L. Polverelli, and C. Vergara. "Extended Finite Element Method for Fluid-Structure Interaction in Wave Membrane Blood Pump". In: *International Journal for Numerical Methods in Biomedical Engineering* (2021), e3467.

[195] A. Massing, M. G. Larson, and A. Logg. "Efficient implementation of finite element methods on nonmatching and overlapping meshes in three dimensions". In: *SIAM Journal on Scientific Computing* 35.1 (2013), pp. C23–C47.

[196] A. Massing, M. Larson, A. Logg, and M. Rognes. "A Nitsche-based cut finite element method for a fluid-structure interaction problem". In: *Communications in Applied Mathematics and Computational Science* 10.2 (2015), pp. 97–120.

[197] D. J. Mavriplis. "An advancing front Delaunay triangulation algorithm designed for robustness". In: *Journal of Computational Physics* 117.1 (1995), pp. 90–101.

[198] U. M. Mayer, A. Popp, A. Gerstenberger, and W. A. Wall. "3D fluid–structure-contact interaction based on a combined XFEM FSI and dual mortar contact approach". In: *Computational Mechanics* 46.1 (2010), pp. 53–67.

[199] M. R. Mehra, N. Uriel, Y. Naka, J. C. Cleveland Jr, M. Yuzefpolskaya, C. T. Salerno, M. N. Walsh, C. A. Milano, C. B. Patel, S. W. Hutchins, et al. "A fully magnetically levitated left ventricular assist device". In: *New England Journal of Medicine* 380.17 (2019), pp. 1618–1627.

[200] M. R. Mehra, J. C. Cleveland Jr, N. Uriel, J. A. Cowger, S. Hall, D. Horstmanshof, Y. Naka, C. T. Salerno, J. Chuang, C. Williams, et al. "Primary results of long-term outcomes in the MOMENTUM 3 pivotal trial and continued access protocol study phase: a study of 2200 HeartMate 3 left ventricular assist device implants". In: *European journal of heart failure* (2021).

[201] M. Mehri, M. Fig, and M. Mousaviraad. "Patient-Specific Computational Fluid-Structure Interaction (FSI) Modeling of Full Cardiac Cycle". In: *APS Division of Fluid Dynamics Meeting Abstracts*. 2019, pp. L30–006.

[202] S. M. Mehta, W. E. Pae Jr, G. Rosenberg, A. J. Snyder, W. J. Weiss, J. P. Lewis, D. J. Frank, J. J. Thompson, and W. S. Pierce. "The LionHeart LVD-2000: a completely implanted left ventricular assist device for chronic circulatory support". In: *The Annals of thoracic surgery* 71.3 (2001), S156–S161.

[203] C. A. Milano, J. G. Rogers, A. J. Tatooles, G. Bhat, M. S. Slaughter, E. J. Birks, N. A. Mokadam, C. Mahr, J. S. Miller, D. W. Markham, et al. "HVAD: the ENDURANCE supplemental trial". In: *JACC: Heart Failure* 6.9 (2018), pp. 792–802.

[204] P. E. Miller, M. A. Solomon, and D. McAreavey. "Advanced percutaneous mechanical circulatory support devices for cardiogenic shock". In: *Critical care medicine* 45.11 (2017), p. 1922.

[205] N. Moazami, K. Fukamachi, M. Kobayashi, N. G. Smedira, K. J. Hoercher, A. Massiello, S. Lee, D. J. Horvath, and R. C. Starling. "Axial and centrifugal continuous-flow rotary pumps: a translation from pump mechanics to clinical practice". In: *The Journal of heart and lung transplantation* 32.1 (2013), pp. 1–11.

[206]   N. Moës, J. Dolbow, and T. Belytschko. "A finite element method for crack growth without remeshing". In: *International journal for numerical methods in engineering* 46.1 (1999), pp. 131–150.

[207]   P. Mohacsi and P. Leprince. *The CARMAT total artificial heart*. 2014.

[208]   A. Molteni, Z. P. H. Masri, K. W. Q. Low, H. N. Yousef, J. Sienz, and K. H. Fraser. "Experimental measurement and numerical modelling of dye washout for investigation of blood residence time in ventricular assist devices". In: *The International journal of artificial organs* 41.4 (2018), pp. 201–212.

[209]   S. Morganti, N. Brambilla, A. S. Petronio, A. Reali, F. Bedogni, and F. Auricchio. "Prediction of patient-specific post-operative outcomes of TAVI procedure: the impact of the positioning strategy on valve performance". In: *Journal of biomechanics* 49.12 (2016), pp. 2513–2519.

[210]   M. Morshuis, A. El-Banayosy, L. Arusoglu, R. Koerfer, R. Hetzer, G. Wieselthaler, A. Pavie, and C. Nojiri. "European experience of DuraHeart™ magnetically levitated centrifugal left ventricular assist system". In: *European Journal of Cardio-Thoracic Surgery* 35.6 (2009), pp. 1020–1028.

[211]   S. D. Moulopoulos, S. Topaz, and W. J. Kolff. "Diastolic balloon pumping (with carbon dioxide) in the aorta—a mechanical assistance to the failing circulation". In: *American heart journal* 63.5 (1962), pp. 669–675.

[212]   "Multi-scale, tailor-made heart simulation can predict the effect of cardiac resynchronization therapy". In: *Journal of Molecular and Cellular Cardiology* 108 (2017), pp. 17–23. ISSN: 0022-2828.

[213]   A. Munjiza and K. R. F. Andrews. "NBS contact detection algorithm for bodies of similar size". In: *International Journal for Numerical Methods in Engineering* 43.1 (1998), pp. 131–149.

[214]   E. M. Ohman, B. S. George, C. J. White, M. J. Kern, P. A. Gurbel, R. J. Freedman, C. Lundergan, J. R. Hartmann, J. D. Talley, and M. J. Frey. "Use of aortic counterpulsation to improve sustained coronary artery patency during acute myocardial infarction. Results of a randomized trial. The Randomized IABP Study Group." In: *Circulation* 90.2 (1994), pp. 792–799.

[215]   A. F. Osorio, R. Osorio, A. Ceballos, R. Tran, W. Clark, E. A. Divo, I. R. Argueta-Morales, A. J. Kassab, and W. M. DeCampli. "Computational fluid dynamics analysis of surgical adjustment of left ventricular assist device implantation to minimise stroke risk". In: *Computer Methods in Biomechanics and Biomedical Engineering* 16.6 (2013), pp. 622–638.

[216]   R. Osuna-Orozco, V. K. Chivukula, and A. Aliseda. "Numerical modeling of platelet margination and its impact on left ventricular assist device thrombogenicity". In: *Bulletin of the American Physical Society* 63 (2018).

[217]   C. Ozturk, I. B. Aka, and I. Lazoglu. "Effect of blade curvature on the hemolytic and hydraulic characteristics of a centrifugal blood pump". In: *The International journal of artificial organs* 41.11 (2018), pp. 730–737.

[218]   F. Pagani, C. Milano, A. Tatooles, G Bhat, M. Slaughter, E. Birks, S. Boyce, S. Najjar, V Jeevanandam, A. Anderson, et al. "HeartWare HVAD for the treatment of patients with advanced heart failure ineligible for cardiac transplantation: results of the ENDURANCE destination therapy trial". In: *J Heart Lung Transplant* 34.4 (2015), S9.

[219] L. Papamanolis, H. J. Kim, C. Jaquet, M. Sinclair, M. Schaap, I. Danad, P. van Diemen, P. Knaapen, L. Najman, H. Talbot, et al. "Myocardial perfusion simulation for coronary artery disease: A coupled patient-specific multiscale model". In: *Annals of biomedical engineering* 49.5 (2021), pp. 1432–1447.

[220] C. A. Papanastasiou, K. G. Kyriakoulis, C. A. Theochari, D. G. Kokkinidis, T. D. Karamitsos, and L. Palaiodimos. "Comprehensive review of hemolysis in ventricular assist devices". In: *World Journal of Cardiology* 12.7 (2020), pp. 334–341.

[221] D. Papantonis. "Numerical prediction of the shear stresses and of the mean stay time for radial flow impellers". In: *Proceedings of the International Workshop on Rotary blood pumps*. 2nd Univ–Dept. of Surgery. 1991, pp. 63–9.

[222] P. K. Paritala, P. K. Yarlagadda, J. Wang, Y. Gu, and Z. Li. "Numerical investigation of atherosclerotic plaque rupture using optical coherence tomography imaging and XFEM". In: *Engineering Fracture Mechanics* 204 (2018), pp. 531–541.

[223] L. Pauli, J. Nam, M. Pasquali, and M. Behr. "Transient stress-based and strain-based hemolysis estimation in a simplified blood pump". In: *International journal for numerical methods in biomedical engineering* 29.10 (2013), pp. 1148–1160.

[224] G. Pena and C. Prud'Homme. "Spectral Element Approximation of Fluid-Structure Interaction in Hemodynamics". In: *ECCM 2010-4th European Conference on Computational Mechanics*. 2010.

[225] M. Perschall, J. B. Drevet, T. Schenkel, and H. Oertel. "The progressive wave pump: numerical multiphysics investigation of a novel pump concept with potential to ventricular assist device application". In: *Artificial organs* 36.9 (2012).

[226] C. Peskin. "Flow patterns around heart valves: a digital computer method for solving the equations of motion". In: *IEEE Transactions on Biomedical Engineering* 4 (1973), pp. 316–317.

[227] S. J. Pettit. "HeartMate 3: real-world performance matches pivotal trial". In: *European Heart Journal* 41.39 (2020), pp. 3810–3812.

[228] I. L. Pieper, S. J. Sonntag, B. Meyns, H. Hadi, and A. Najar. "Evaluation of the novel total artificial heart RealHeart in a pilot human fitting study". In: *Artificial organs* 44.2 (2020), pp. 174–177.

[229] R. Piersanti, P. C. Africa, M. Fedele, C. Vergara, L. Dedè, A. F. Corno, and A. Quarteroni. "Modeling cardiac muscle fibers in ventricular and atrial electrophysiology simulations". In: *Computer Methods in Applied Mechanics and Engineering* 373 (2021), p. 113468.

[230] M. Pinotti and E. S. Rosa. "Computational prediction of hemolysis in a centrifugal ventricular assist device". In: *Artificial Organs* 19.3 (1995), pp. 267–273.

[231] L. Polverelli, L. Maine, C. N. Botterbusch, S. Lucquin, J.-b. Drevet, A. Guignabert, P. Meneroud, A. Schmidt, and P.-P. Monticone. *Implantable pump system having an undulating membrane with improved hydraulic performance*. US Patent 10,188,779. 2019.

[232] P. Ponikowski, A. A. Voors, S. D. Anker, H. Bueno, J. G. F. Cleland, A. J. S. Coats, V. Falk, J. R. González-Juanatey, V.-P. Harjola, E. A. Jankowska, M. Jessup, C. Linde, P. Nihoyannopoulos, J. T. Parissis, B. Pieske, J. P. Riley, G. M. C. Rosano, L. M. Ruilope, F. Ruschitzka, F. H. Rutten, P. van der Meer, and E. S. D. Group. "2016 ESC Guidelines for the diagnosis and treatment of acute and chronic heart failure: The Task Force for the diagnosis and treatment of acute and chronic heart failure of the European Society of Cardiology (ESC) developed with the special contribution of the Heart Failure Association (HFA) of the ESC". In: *European Heart Journal* 37.27 (May 2016), pp. 2129–2200. ISSN: 0195-668X.

[233] A. Pont, R. Codina, and J. Baiges. "Interpolation with restrictions between finite element meshes for flow problems in an ALE setting". In: *International Journal for Numerical Methods in Engineering* 110.13 (2017), pp. 1203–1226.

[234] S. Pozzi, M. Domanin, L. Forzenigo, E. Votta, E Zunino, A. Redaelli, and C. Vergara. "A surrogate model for plaque modeling in carotids based on Robin conditions calibrated by cine MRI data". In: *Int. J. Numer. Methods Biomed. Eng.* (2021), e3447.

[235] R. O. Prather, M. W. Ni, E. Divo, A. J. Kassab, and W. M DeCampli. "Pulsatile multiscale fluid-structure interaction modeling for optimal left ventricular assist device implantation". In: *ASTFE Digital Library*. Begel House Inc. 2018.

[236] R. Prather, E. Divo, A. Kassab, and W. DeCampli. "Computational Fluid Dynamics Study of Cerebral Thromboembolism Risk in Ventricular Assist Device Patients: Effects of Pulsatility and Thrombus Origin". In: *Journal of Biomechanical Engineering* 143.9 (May 2021).

[237] A. Quarteroni and G. Rozza. "Optimal control and shape optimization of aorto-coronaric bypass anastomoses". In: *Mathematical Models and Methods in Applied Sciences* 13.12 (2003), pp. 1801–1823.

[238] A. Quarteroni, L. Dedè, A. Manzoni, and C. Vergara. *Mathematical Modelling of the Human Cardiovascular System - Data, Numerical Approximation, Clinical Applications*. Cambridge University Press, 2019.

[239] V. Rao. "HeartMate 3: Better... but not perfect". In: *The Journal of thoracic and cardiovascular surgery* 154.1 (2017), pp. 179–180.

[240] A Rassineux. "3D mesh adaptation. Optimization of tetrahedral meshes by advancing front technique". In: *Computer Methods in Applied Mechanics and Engineering* 141.3-4 (1997), pp. 335–354.

[241] A. K. Ravichandran, J. Parker, E. Novak, S. M. Joseph, J. D. Schilling, G. A. Ewald, and S. Silvestry. "Hemolysis in left ventricular assist device: a retrospective analysis of outcomes". In: *The Journal of Heart and Lung Transplantation* 33.1 (2014), pp. 44–50.

[242] V. Rayz, L Boussel, L Ge, J. Leach, A. Martin, M. Lawton, C McCulloch, and D Saloner. "Flow residence time and regions of intraluminal thrombus deposition in intracranial aneurysms". In: *Annals of biomedical engineering* 38.10 (2010), pp. 3058–3069.

[243] S. Rebay. "Efficient unstructured mesh generation by means of Delaunay triangulation and Bowyer-Watson algorithm". In: *Journal of computational physics* 106.1 (1993), pp. 125–138.

[244] F. Regazzoni, M. Salvador, P. C. Africa, M. Fedele, L. Dedé, and A. Quarteroni. "A cardiac electromechanics model coupled with a lumped parameters model for closed-loop blood circulation. Part II: numerical approximation". In: *arXiv preprint arXiv:2011.15051* (2020).

[245] N. Roberts, U. Chandrasekaran, S. Das, Z. Qi, and S. Corbett. "Hemolysis associated with Impella heart pump positioning: In vitro hemolysis testing and computational fluid dynamics modeling". In: *The International journal of artificial organs* 43.11 (2020), pp. 710–718.

[246] J. G. Rogers, F. D. Pagani, A. J. Tatooles, G. Bhat, M. S. Slaughter, E. J. Birks, S. W. Boyce, S. S. Najjar, V. Jeevanandam, A. S. Anderson, et al. "Intrapericardial left ventricular assist device for advanced heart failure". In: *New England Journal of Medicine* 376.5 (2017), pp. 451–460.

[247] E. A. Rose, A. C. Gelijns, A. J. Moskowitz, D. F. Heitjan, L. W. Stevenson, W. Dembitsky, J. W. Long, D. D. Ascheim, A. R. Tierney, R. G. Levitan, et al. "Long-term use of a left ventricular assist device for end-stage heart failure". In: *New England Journal of Medicine* 345.20 (2001), pp. 1435–1443.

[248] C. Russ, R. Hopf, S. Hirsch, S. Sündermann, V. Falk, G. Székely, and M. Gessat. "Simulation of transcatheter aortic valve implantation under consideration of leaflet calcification". In: *35th Annual International Conference of the IEEE Engineering in Medicine and Biology Society (EMBC)*. IEEE. 2013, pp. 711–714.

[249] S. Salvadori, S. Della Gatta, P. Adami, and L Betolazzi. "Development of a cfd procedure for the axial thrust Evaluation in multistage centrifugal pumps". In: *Proceedings of 7th European Conference on Turbomachinery*. 2007.

[250] M. Sampson and A. McGrath. "Understanding the ECG. Part 1: Anatomy and physiology". In: *British Journal of Cardiac Nursing* 10.11 (2015), pp. 548–554.

[251] L. E. Samuels, E. C. Holmes, P. Garwood, and F. Ferdinand. "Initial experience with the Abiomed AB5000 ventricular assist device system". In: *The Annals of thoracic surgery* 80.1 (2005), pp. 309–312.

[252] R. A. Santa-Cruz, M. G. Cohen, and E. M. Ohman. "Aortic counterpulsation: a review of the hemodynamic effects and indications for use". In: *Catheterization and cardiovascular interventions* 67.1 (2006), pp. 68–77.

[253] G. Savarese and L. H. Lund. "Global public health burden of heart failure". In: *Cardiac failure review* 3.1 (2017), p. 7.

[254] T. Sawada and A. Tezuka. "LLM and X-FEM based interface modeling of fluid–thin structure interactions on a non-interface-fitted mesh". In: *Computational Mechanics* 48.3 (2011), pp. 319–332.

[255] S. Scardulla, S. Pasta, L. D'Acquisto, S. Sciacca, V. Agnese, C. Vergara, A. Quarteroni, F. Clemenza, D. Bellavia, and P. M. "Shear Stress Alterations in the Celiac Trunk of Patients with Continuous-Flow Left Ventricular Assist Device by In-Silico and In-Vitro Flow Analysis". In: *Journal of Heart and Lung Transplantation* 36(8) (2017), pp. 906–913.

[256] M. Scheffler, N. Mechbal, E. Monteiro, M. Rebillat, and R. Pruvost. "Implementation and Evaluation of a Sensorless, Nonlinear Stroke Controller for an Implantable, Undulating Membrane Blood Pump". In: *IFAC-PapersOnLine* 53.2 (2020), pp. 8683–8688.

[257] S. Schneider, S. Nuschele, A. Wixforth, C Gorzelanny, A Alexander-Katz, R. Netz, and M. F. Schneider. "Shear-induced unfolding triggers adhesion of von Willebrand factor fibers". In: *Proceedings of the National Academy of Sciences* 104.19 (2007), pp. 7899–7903.

[258] B. Schott and W. A. Wall. "A new face-oriented stabilized XFEM approach for 2D and 3D incompressible Navier–Stokes equations". In: *Computer Methods in Applied Mechanics and Engineering* 276 (2014), pp. 233–265.

[259] R. Schramm, A. Zittermann, M. Morshuis, M. Schoenbrodt, E. von Roessing, V. von Dossow, A. Koster, H. Fox, K. Hakim-Meibodi, and J. F. Gummert. "Comparing short-term outcome after implantation of the HeartWare® HVAD® and the Abbott® HeartMate 3®". In: *ESC heart failure* 7.3 (2020), pp. 908–914.

[260] B. P. Selgrade and G. A. Truskey. "Computational fluid dynamics analysis to determine shear stresses and rates in a centrifugal left ventricular assist device". In: *Artificial organs* 36.4 (2012), E89–E96.

[261] M. Selmi, W. Chiu, V. Chivukula, G. Melisurgo, J. A. Beckman, C. Mahr, A. Aliseda, E. Votta, A. Redaelli, M. J. Slepian, et al. "Blood damage in Left Ventricular Assist Devices: Pump thrombosis or system thrombosis?" In: *The International journal of artificial organs* 42.3 (2019), pp. 113–124.

[262] C. S. Semenzin, B. Simpson, S. D. Gregory, and G. Tansley. "Validated Guidelines for Simulating Centrifugal Blood Pumps". In: *Cardiovascular Engineering and Technology* (2021), pp. 1–13.

[263] J. R. Shewchuk. "Triangle: Engineering a 2D Quality Mesh Generator and Delaunay Triangulator". In: *Applied Computational Geometry: Towards Geometric Engineering*. Ed. by M. C. Lin and D. Manocha. Vol. 1148. Lecture Notes in Computer Science. From the First ACM Workshop on Applied Computational Geometry. Springer-Verlag, May 1996, pp. 203–222.

[264] H. Si. "TetGen, a Delaunay-based quality tetrahedral mesh generator". In: *ACM Transactions on Mathematical Software (TOMS)* 41.2 (2015), pp. 1–36.

[265] K. D. Sjauw, A. E. Engström, M. M. Vis, R. J. van der Schaaf, J. Baan Jr, K. T. Koch, R. J. de Winter, J. J. Piek, J. G. Tijssen, and J. P. Henriques. "A systematic review and meta-analysis of intra-aortic balloon pump therapy in ST-elevation myocardial infarction: should we change the guidelines?" In: *European heart journal* 30.4 (2009), pp. 459–468.

[266] N. P. Smith, D. P. Nickerson, E. J. Crampin, and P. J. Hunter. "Multiscale computational modelling of the heart". In: *Acta Numerica* 13 (2004), pp. 371–431.

[267] W. Smith, P Allaire, J Antaki, K. Butler, W Kerkhoffs, T Kink, H Loree, and H Reul. "Collected nondimensional performance of rotary dynamic blood pumps". In: *ASAIO journal* 50.1 (2004), pp. 25–32.

[268] J. M. Smits, E. de Vries, M. De Pauw, A. Zuckermann, A. Rahmel, B. Meiser, G. Laufer, H. Reichenspurner, and M. Strueber. "Is it time for a cardiac allocation score? First results from the Eurotransplant pilot study on

a survival benefit–based heart allocation". In: *The Journal of Heart and Lung Transplantation* 32.9 (2013), pp. 873–880.

[269] T. Snyder, A. Bourquin, F. Cornat, B. Burg, J. Biasetti, and C. N. Botterbusch. "CorWave LVAD Development Update". In: *The Journal of Heart and Lung Transplantation* 38.4 (2019), pp. 5341–5342.

[270] X Song, H. Wood, and D. Olsen. "Transient computational fluid dynamics study of an axial blood pump". In: *Asaio Journal* 49.2 (2003), p. 144.

[271] R. C. Starling, J. D. Estep, D. A. Horstmanshof, C. A. Milano, J. Stehlik, K. B. Shah, B. A. Bruckner, S. Lee, J. W. Long, C. H. Selzman, et al. "Risk assessment and comparative effectiveness of left ventricular assist device and medical management in ambulatory heart failure patients: the ROADMAP study 2-year results". In: *JACC: Heart Failure* 5.7 (2017), pp. 518–527.

[272] J. T. Strauch, D. Spielvogel, P. L. Haldenwang, R. K. Correa, A. d. Richard, P. E. Seissler, D. A. Baran, A. L. Gass, and S. L. Lansman. "Recent improvements in outcome with the Novacor left ventricular assist device". In: *The Journal of heart and lung transplantation* 22.6 (2003), pp. 674–680.

[273] M. Strueber, G. O'Driscoll, P. Jansz, A. Khaghani, W. C. Levy, and G. M. Wieselthaler. "Multicenter Evaluation of an Intrapericardial Left Ventricular Assist System". In: *Journal of the American College of Cardiology* 57.12 (2011), pp. 1375–1382. ISSN: 0735-1097.

[274] F. Sturla, M. Ronzoni, M. Vitali, A. Dimasi, R. Vismara, G. Preston-Maher, G. Burriesci, E. Votta, and A. Redaelli. "Impact of different aortic valve calcification patterns on the outcome of transcatheter aortic valve implantation: a finite element study". In: *Journal of biomechanics* 49.12 (2016), pp. 2520–2530.

[275] B. Su, L. P. Chua, and X. Wang. "Validation of an axial flow blood pump: Computational fluid dynamics results using particle image velocimetry". In: *Artificial organs* 36.4 (2012), pp. 359–367.

[276] N. Sukumar, D. L. Chopp, N. Moës, and T. Belytschko. "Modeling holes and inclusions by level sets in the extended finite-element method". In: *Computer methods in applied mechanics and engineering* 190.46-47 (2001), pp. 6183–6200.

[277] L.-B. Tan, S. G. Williams, D. K. Tan, and A. Cohen-Solal. "So many definitions of heart failure: are they all universally valid? A critical appraisal". In: *Expert review of cardiovascular therapy* 8.2 (2010), pp. 217–228.

[278] M. E. Taskin, K. H. Fraser, T. Zhang, B. Gellman, A. Fleischli, K. A. Dasse, B. P. Griffith, and Z. J. Wu. "Computational characterization of flow and hemolytic performance of the UltraMag blood pump for circulatory support". In: *Artificial organs* 34.12 (2010), pp. 1099–1113.

[279] M. E. Taskin, K. H. Fraser, T. Zhang, C. Wu, B. P. Griffith, and Z. J. Wu. "Evaluation of Eulerian and Lagrangian models for hemolysis estimation". In: *ASAIO journal* 58.4 (2012), pp. 363–372.

[280] C. A. Taylor and C. A. Figueroa. "Patient-Specific Modeling of Cardiovascular Mechanics". In: *Annual Review of Biomedical Engineering* 11 (2009), pp. 109–134.

[281] R. Temam. *Navier–Stokes equations and nonlinear functional analysis*. Vol. 66. Siam, 1995.

[282]   B. Thamsen, B. Blümel, J. Schaller, C. O. Paschereit, K. Affeld, L. Gou-bergrits, and U. Kertzscher. "Numerical analysis of blood damage potential of the HeartMate II and HeartWare HVAD rotary blood pumps". In: *Artificial organs* 39.8 (2015), pp. 651–659.

[283]   G. B. Thurston. "Rheological parameters for the viscosity viscoelasticity and thixotropy of blood". In: *Biorheology* 16.3 (1979), pp. 149–162.

[284]   D. Timms, J. Fraser, M. Hayne, J. Dunning, K. McNeil, and M. Pearcy. "The BiVACOR rotary biventricular assist device: concept and in vitro investigation". In: *Artificial organs* 32.10 (2008), pp. 816–819.

[285]   S. R. Topper, M. A. Navitsky, R. B. Medvitz, E. G. Paterson, C. A. Siedlecki, M. J. Slattery, S. Deutsch, G. Rosenberg, and K. B. Manning. "The use of fluid mechanics to predict regions of microscopic thrombus formation in pulsatile VADs". In: *Cardiovascular engineering and technology* 5.1 (2014), pp. 54–69.

[286]   H. A. Tran, T. L. Pollema, J. Silva Enciso, B. H. Greenberg, D. D. Barnard, E. D. Adler, and V. G. Pretorius. "Durable biventricular support using right atrial placement of the HeartWare HVAD". In: *Asaio Journal* 64.3 (2018), pp. 323–327.

[287]   M. Triep, C. Brücker, W. Schröder, and T. Siess. "Computational fluid dynamics and digital particle image velocimetry study of the flow through an optimized micro-axial blood pump". In: *Artificial organs* 30.5 (2006), pp. 384–391.

[288]   T. Tronchin. "Experimental and numerical characterization of vortex mechanisms of lift generation on a wing in flapping motion". In: (June 2013).

[289]   N. Uriel, S.-W. Pak, U. P. Jorde, B. Jude, S. Susen, A. Vincentelli, P.-V. Ennezat, S. Cappleman, Y. Naka, and D. Mancini. "Acquired von Willebrand syndrome after continuous-flow mechanical device support contributes to a high prevalence of bleeding during long-term support and at the time of transplantation". In: *Journal of the American College of Cardiology* 56.15 (2010), pp. 1207–1213.

[290]   E. Van Brummelen. "Partitioned iterative solution methods for fluid–structure interaction". In: *International Journal for Numerical Methods in Fluids* 65.1-3 (2011), pp. 3–27.

[291]   G. Ventura, E Budyn, and T Belytschko. "Vector level sets for description of propagating cracks in finite elements". In: *International Journal for Numerical Methods in Engineering* 58.10 (2003), pp. 1571–1592.

[292]   C. Vergara and P. Zunino. "Multiscale boundary conditions for drug release from cardiovascular stents". In: *Multiscale Modeling & Simulation* 7.2 (2008), pp. 565–588.

[293]   C. Vergara and S. Zonca. "Extended finite elements method for fluid-structure interaction with an immersed thick non-linear structure". In: *Mathematical and Numerical Modeling of the Cardiovascular System and Applications*. Springer, 2018, pp. 209–243.

[294]   F. Viola, V. Meschini, and R. Verzicco. "Fluid-Structure-Electrophysiology interaction (FSEI) in the left-heart: a multi-way coupled computational model". In: *European Journal of Mechanics-B/Fluids* 79 (2020), pp. 212–232.

[295] S. S. Virani, A. Alonso, E. J. Benjamin, M. S. Bittencourt, C. W. Callaway, A. P. Carson, A. M. Chamberlain, A. R. Chang, S. Cheng, F. N. Delling, et al. "Heart disease and stroke statistics—2020 update: a report from the American Heart Association". In: *Circulation* 141.9 (2020), e139–e596.

[296] F. Vitale, J. Nam, L. Turchetti, M. Behr, R. Raphael, M. C. Annesini, and M. Pasquali. "A multiscale, biophysical model of flow-induced red blood cell damage". In: *AIChE Journal* 60.4 (2014), pp. 1509–1516.

[297] P. Vranckx, D. P. Foley, P. J. d. Feijter, J. Vos, P. Smits, and P. W. Serruys. "Clinical introduction of the TandemHeart, a percutaneous left ventricular assist device, for circulatory support during high-risk percutaneous coronary intervention". In: *International journal of cardiovascular interventions* 5.1 (2003), pp. 35–39.

[298] G. J. Wagner, N. Moës, W. K. Liu, and T. Belytschko. "The extended finite element method for rigid particles in Stokes flow". In: *International Journal for Numerical Methods in Engineering* 51.3 (2001), pp. 293–313.

[299] W. A. Wall, A. Gerstenberger, P. Gamnitzer, C. Förster, and E. Ramm. "Large deformation fluid-structure interaction–advances in ALE methods and new fixed grid approaches". In: *Fluid-structure interaction*. Springer, 2006, pp. 195–232.

[300] Y. Wang, P. Shen, M. Zheng, P. Fu, L. Liu, J. Wang, and L. Yuan. "Influence of Impeller Speed Patterns on Hemodynamic Characteristics and Hemolysis of the Blood Pump". In: *Applied Sciences* 9.21 (2019), p. 4689. ISSN: 2076-3417.

[301] P. A. Watterson, J. C. Woodard, V. S. Ramsden, and J. A. Reizes. "VentrAssist hydrodynamically suspended, open, centrifugal blood pump". In: *Artificial Organs* 24.6 (2000), pp. 475–477.

[302] S. Westaby, A. P. Banning, R. Jarvik, O. H. Frazier, D. W. Pigott, X. Y. Jin, P. A. Catarino, S. Saito, D. Robson, A. Freeland, et al. "First permanent implant of the Jarvik 2000 Heart". In: *The Lancet* 356.9233 (2000), pp. 900–903.

[303] L. Wiegmann, S. Boës, D. De Zélicourt, B. Thamsen, M. S. Daners, M. Meboldt, and V. Kurtcuoglu. "Blood pump design variations and their influence on hydraulic performance and indicators of hemocompatibility". In: *Annals of biomedical engineering* 46.3 (2018), pp. 417–428.

[304] L. Wiegmann, B. Thamsen, D. De Zélicourt, M. Granegger, S. Boës, M. Schmid Daners, M. Meboldt, and V. Kurtcuoglu. "Fluid dynamics in the HeartMate 3: influence of the artificial pulse feature and residual cardiac pulsation". In: *Artificial organs* 43.4 (2019), pp. 363–376.

[305] J. R. Williams, E. Perkins, and B. Cook. "A contact algorithm for partitioning N arbitrary sized objects". In: *Engineering Computations* (2004).

[306] L. A. Woodworth, B. Cansız, and M. Kaliske. "A numerical study on the effects of spatial and temporal discretization in cardiac electrophysiology". In: *International Journal for Numerical Methods in Biomedical Engineering* 37.5 (2021), e3443.

[307] P. Wriggers. "Computational contact mechanics". In: *Computational Mechanics* 49.6 (2012), p. 685.

[308] J. Wu, J. F. Antaki, W. R. Wagner, T. A. Snyder, B. E. Paden, and H. S. Borovetz. "Elimination of adverse leakage flow in a miniature pediatric centrifugal blood pump by computational fluid dynamics-based design optimization." In: *ASAIO journal* 51 5 (2005), pp. 636–43.

[309] W. Wu, D. Pott, C. Chiastra, L. Petrini, G. Pennati, G. Dubini, U. Steinseifer, S. Sonntag, M. Kuetting, and F. Migliavacca. "Fluid–Structure Simulation of a Transcatheter Aortic Valve Implantation: Potential Application to Patient-Specific Cases". In: *Computer Methods in Biomechanics and Biomedical Engineering*. Springer, 2018, pp. 93–98.

[310] W.-T. Wu, F. Yang, J. Wu, N. Aubry, M. Massoudi, and J. F. Antaki. "High fidelity computational simulation of thrombus formation in Thoratec Heart-Mate II continuous flow ventricular assist device". In: *Scientific reports* 6.1 (2016), pp. 1–11.

[311] W.-T. Wu, M. A. Jamiolkowski, W. R. Wagner, N. Aubry, M. Massoudi, and J. F. Antaki. "Multi-constituent simulation of thrombus deposition". In: *Scientific reports* 7.1 (2017), pp. 1–16.

[312] W.-T. Wu, M. Zhussupbekov, N. Aubry, J. F. Antaki, and M. Massoudi. "Simulation of thrombosis in a stenotic microchannel: The effects of vWF-enhanced shear activation of platelets". In: *International Journal of Engineering Science* 147 (2020), p. 103206.

[313] K. Yamazaki, S. Saito, H. Tomioka, M. Miyagishima, A. Kawai, S. Aomi, O. Tagusari, T. Nakatani, S. Kitamura, S. Kyo, et al. "Next generation LVAD "EVAHEART": current status of Japanese clinical trial". In: *Journal of Cardiac Failure* 12.8 (2006), S158.

[314] L. T. Zhang and M. Gay. "Immersed finite element method for fluid-structure interactions". In: *Journal of Fluids and Structures* 23.6 (2007), pp. 839–857.

[315] S. Zonca, C. Vergara, and L. Formaggia. "An unfitted formulation for the interaction of an incompressible fluid with a thick structure via an XFEM/DG approach". In: *SIAM Journal on Scientific Computing* 40.1 (2018), B59–B84.

[316] S. Zonca. "Unfitted numerical methods for fluid-structure interaction arising between an incompressible fluid and an immersed thick structure". PhD Thesis. Politecnico di Milano, 2018.

[317] S. Zonca, P. F. Antonietti, and C. Vergara. "A Polygonal Discontinuous Galerkin formulation for contact mechanics in fluid-structure interaction problems". In: (2020).

List of Figures

List of Tables